Wayne State University Dissertations

1-1-2011

The study of weak ferromagnetism by andreev reflection spin spectroscopy and development of bimorph electro-thermal actuators

Pushkal Thapa
Wayne State University,

Follow this and additional works at: http://digitalcommons.wayne.edu/oa_dissertations

Part of the Condensed Matter Physics Commons

Recommended Citation

Thapa, Pushkal, "The study of weak ferromagnetism by andreev reflection spin spectroscopy and development of bimorph electro-thermal actuators" (2011). *Wayne State University Dissertations*. Paper 398.

THE STUDY OF WEAK FERROMAGNETISM BY ANDREEV REFLECTION SPIN SPECTROSCOPY AND DEVELOPMENT OF BIMORPH ELECTRO-THERMAL ACTUATORS

by

PUSHKAL THAPA

DISSERTATION

Submitted to the Graduate School

of Wayne State University,

Detroit, Michigan

in partial fulfillment of the requirements

for the degree of

DOCTOR OF PHILOSOPHY

2011

MAJOR: PHYSICS

Approved by:

Advisor   Date

DEDICATION

To my Parents

And

Late Grandparents

ACKNOWLEDGEMENTS

I would like to express my gratitude to everyone who helped me directly or indirectly in my research. My special appreciation and a bunch of thanks go to my advisor Prof. Boris Edward Nadgorny whose vision, broad knowledge, passion, compassion, encouragement, and all kinds of supports led me to accomplish my research and this dissertation. For co-advising, serving as a member in my dissertation committee, and for providing every facility of his optoelectronics lab in ECE department, I thank Prof. Ivan Avrutsky. I offer a bunch of thanks to Prof. Gavin Lawes for accepting to be a committee member, for letting me share his lab especially SQUID for magnetic measurements, for suggesting valuable research matters, and for teaching me material characterization and advanced solid state courses during my graduate studies at Wayne State. As the chair of Physics department and member of my dissertation committee Prof. Ratna Naik always showed her concern and care in everyday progress in my research and studies, and provided departmental support. My sincere gratitude and big thanks go to Prof. Naik and to Prof. Jogindra Mohan Wadehra for awarding me for the American Association of Physics Teacher (AAPT) Award in 2011. Professor Wadehra gave all necessary instructions for choosing the right courses on right time, and he advised about different administrative procedures as graduate coordinator throughout my graduate studies at Wayne State.

Dr. Raghava Panguluri is the one who exposed me to various experimental techniques such as PCAR, deposition techniques, PPMS, SQUID etc as a postdoctoral associate in our group before he moved to an industrial position. On the days of failure of experiments he would cheerfully say, "This is just one of those bad days, we will try it next". I adore and thank him for his technical helps and in analyzing data, always available attitude, and inducing passion in me in getting good results while doing experiments. I would like to thank Dr. Scott Payson for his

confidence in me and appreciation of my teaching, and for understanding my time constraints while making teaching schedules. I would like to thank Prof. J. J. Chang for teaching me Math Physics and solid state Physics, Prof. Paul Keys for teaching me soft condensed matter Physics, Prof. Sergei Voloshin for teaching me Statistical Mechanics, Prof. J. M. Wadehra for teaching me Electricity and Magnetism, Professor Alexy Petrov for teaching me Quantum mechanics, and Prof. Asish Mukhopadhaya for teaching me Thermal Physics. I thank office secretary Mrs. De Cowen for her administrative support. I thank Dr. Zhixian Zhou for letting me use AFM in his lab and friend Ming-Wei Lin for assisting me to use it. I am thankful to other faculty and staff in the department for their help and encouragement for my success.

For providing MnBi and Pt thin film samples, I would like to thank our collaborators Prof. David Sellmyer and Dr. Parashu Kharel from NCMN; and Prof. Norman Birge from Michigan State University for supplying PdNi thin film samples. I thank Dr. Fabrizio Carbone from Ecole Polytechnique Fédérale de Lausanne (EPFL), Switzerland for sending MnSi single crystals. My acknowledgment goes to Dr. John Muth and MEMS Exchange for fabricating micro electromechanical structures.

I thank Dr. Ambesh Dixit for sharing and discussing on different issues in research and collaborating in InN and In_2O_3 studies. I thank senior colleagues in my group Dr. Mohammad Muzummal Faiz and Dr. Xiangdong Liu for sharing ideas. I am thankful to colleagues Girfan Shamsutdinov, Rupam Mukharjee and new postdoctoral fellow Dr. Debabrata Mishra in our present group for their accompanionship in and around our spintronic lab.

Last but not least at all, I appreciate the patience, encouragement, help and hope of my wife Bharti Thapa and daughter Tarangana Thapa for better and brighter future.

TABLE OF CONTENTS

LIST OF TABLES

LIST OF FIGURES

PART I
DEVELOPMENT OF BIMORPH ELECTRO-THERMAL ACTUATORS

This part of dissertation confined in Chapter One through Five describes a study of torsion phenomena observed for the first time in freestanding micromechanical mirrors made of silicon nitride and coated with thin films of metals such as nickel, gold, and silver while passing electric current. Such micromechanical freestanding silicon nitride mirrors were fabricated by photolithography and selective etching. The torsion produced on passing current was found to be proportional to the square of the dc current passed with the torsion direction independent of the current direction. The torsion angles as a function of current were measured for nickel-deposited, gold-deposited, and silver-deposited micromirrors of different dimensions. The measurements were done using optical technique by monitoring the differential voltage output from a split photodiode, with the data taken by the standard lock-in technique. Calibrations were performed using a rotation stage. The torsion angles were measured for several sets of micromirrors with the dimensions of 150µm×150µm; and 175 µm long beams with different widths of 8, 10, 12, 16 and 20 µm. The results indicate that the torsion angles are proportional to the square of the dc current and are dependent on the beam widths. Switching time for such micromirrors was found to be ~ 1ms. Large torsion angle of 26.3 degrees corresponding to 38 mA of a dc current with less than 1 V of applied voltage was measured in the case of Au-deposited structure of 390 µm × 290µm with the beam size of 100 µm×7µm. Large torsion angles achieved in such micromirrors may find potential applications in various actuators for MEMS and display technologies.

The second part of this dissertation starting from chapter six will focus on the study of various weak ferromagnetic materials by using Andreev reflection spectroscopy. Such materials have spintronic applications and have scientifically interesting and important material properties.

CHAPTER 1

TORSION MEASUREMENTS OF MICROMECHANICAL MIRRORS COATED WITH NICKEL, GOLD AND SILVER

1.1 Introduction

Famous Stern-Gerlach experiment in 1921 showed that the electrons have just two possible orientations of magnetic moment even though the origin of magnetic moment of the electrons with zero orbital angular momentum ($l = 0$) was not known to them. Four years later in 1925, Samuel Goudsmit and George Uhlenbeck made a remarkable discovery that an electron has intrinsic angular momentum that doesn't depend on the orbital characteristic [Uhlenbeck et al., 1925]. They used the term "spin" to describe such intrinsic angular momentum of electrons. The property that the electrons have charge has been widely used to develop electronic industries.

Mott (1936) was the first to consider the study of spin polarized transport which helped to understand tunneling experiments in the early days [Mott et al., 1936]. Tunneling measurements on junctions between very thin superconducting aluminum films and ferromagnetic Nickel films in a high magnetic field show that the tunneling current is spin dependent [Tedrow et al., 1971]. The study of the spin polarized tunneling current in ferromagnet in F/N/F junctions, where N and F stand for nonmagnetic and ferromagnetic, has potential application as spin filters. A giant magnetoresistance, which is much larger than anisotropy (difference in resistivity $\Delta R = R\perp - R_{ll}$ for currents flowing parallel (R_{ll}) and perpendicular ($R\perp$) to the magnetization) was found in F/AF/F layers (e.g. Fe-Cr-Fe) where F is ferromagnetic and AF is antiferromagnetic interlayer [Binasch et al., 1989; Baibich et al., 1988]. An appreciable increase of the electrical resistivity was found in the case of antiparallel alignment of magnetizations in the double magnetic layers. The origin of this effect was believed to be due to spin flip scattering of the electrons as spin

polarized electrons in one ferromagnet propagate through the structure. The effect called GMR (Giant Magnetic Resistance) was discovered independently in 1988 and 1989 by Baibich *et al*. and Binasch G. respectively. A. Fert and P. Grunberg were awarded Nobel Prize in Physics in 2007 for the discovery of spin dependent transmission of the conduction electrons between Fe layers through Cr layers. This research was promising for application to magnetoresistance sensors. In 1994 J.M. Daughton *et al*. developed the first GMR sensor as commercial electron spin product [Daughton et al., 1995].

After their discovery of GMR, continuous improvements have been made in reproducibility, increase of efficiency, and reduction of coercivity [Parkin et al., 1991; Dieny et al., 1991; Daughton et al., 1992]. GMR and spin dependent tunneling (SDT) structure are now being used in magnetic field sensors. Spin valves are used in read heads for hard drives and galvanic isolators. Spin valves and SDT are being used in non volatile random access memory development [Daughton et al, 1999]. Another interesting concept is a bipolar spin switch that was fabricated in 1993 by Mark Johnson *et al*. [Johnson et al., 1993]. When spin polarized electrons go from one layer to another in a FM-NM-FM GMR structure, the electrons have to change their spin if the magnetization of two FM layers are not parallel. This causes the change in angular momentum of the polarized electrons which, in turn, causes mechanical torque. This spin transfer torque was predicted independently by Slonczewski [Slonczewski et al., 2000] and Berger [Berger et al., 1996]. Later J.A Katine *et al*. were able to facilitate the large current density induced magnetic domain realignment in Co/Cu multilayer nanostructure in 1999 [Katine et al., 2000]. Effect of spin polarized current on various electrodeposited single contacted nanowires was studied by J.E. Wegrowe *et al*. in 2002 [Wegrowe et al., 2002] and they proposed that exchange torque and spin transfer are the two mechanisms of magnetization change. In

2003, Li. e*t al*. analyzed the consequence of the spin torque on the dynamics of the local moment of a spin valve structure. They found that the magnetic energy oscillates as a function of time even for a steady-state current. For pulsed current, the minimum width and amplitude of the spin torque for achieving current-driven magnetization reversal have been determined quantitatively [Li et al., 2003]. Microwave frequency dynamics in nanomagnets propelled by spin polarized current was studied by Kiselec et al. in 2003. They found that the spin transfer could produce several kinds of magnetic excitations, and magnetic layers are able to convert DC currents into high frequency magnetic rotation [Kiselec et al., 2003]. In 2004, Yamanouchi *et al*. demonstrated that, in a ferromagnetic semiconductor structure, magnetization reversal through domain wall switching can be induced in the absence of a magnetic field using current pulses with low current densities (below 10^{-5} A cm^{-2}). Though the switching speed was low, their approach could provide a route to magnetic information storage applications [Yamanouchi et al., 2004].

In 1998 P. Fulde proposed that the measure of spin transfer induced mechanical torque of a hybrid FM/NM wire would be the measure of the magnetic polarization of the conduction electrons in ferromagnets. This may yield new information on the transport properties of the narrow band electrons in itinerant ferromagnets [Fulde et al., 1998a]. Measurement of the mechanical torque will give the spin polarization of ferromagnet being used in the composite structure. X. Li attempted to fabricate the composite FM/NM wire to measure spin torsion by using an optical system [Li et al., 2005]. Li has also observed the torsion even when the current was passed through a single magnetic microwire of Nickel.

In order to increase reproducibility and to understand the origin of the observed effects we have studied the spin torsion in micro electro mechanical (MEM) structure. An optical system was used to measure the torsion angle produced on such micromirrors coated with

ferromagnetic material (Ni) or non-magnetic material Au or Ag. The measurement of torsion angle will be done by passing DC and AC (to get enhanced oscillations, if any, at resonance). Understanding the reason of torsion in a FM structure will reveal a new dimension on the dynamics of spin when they are influenced by current. In addition, such devices, which are easier to fabricate than composite structures, will have several possible technological applications. Quantification of such torsion angle as a function of current is essential for its controlled practical use. Also, whether the torsion is produced in nonmagnetic metal coated structure will be tested. This project is directed toward this goal that will be quite useful for spintronics device applications, as well as a variety of MEMS applications. Sample fabrication and optical technique to measure spin transfer torque directly will be discussed in the next section.

1.2 Spin and prediction of Spin Torque

Apart from the orbital angular momentum associated with the motion of an electron, an electron has an intrinsic angular momentum $\vec{S}$ whose magnitude is $S = \dfrac{\sqrt{3}}{2}\hbar$. Just like charge or mass of an electron, the spin angular momentum is also its intrinsic property. There are two possible values of its z-components viz., $S_z = m_s\hbar$, where the spin magnetic quantum numbers are $m_s = \pm\dfrac{1}{2}$, which are also referred to as spin up and spin down. When electrons go from a ferromagnetic layer to a non-ferromagnatic layer, they transfer their angular momentum to this layer. As a result of this, angular momentum transfer will be translated into a mechanical torque of the device [Fulde et al., 1998b].

1.2.1 Torque and spin Polarization

The measurement of the torque at an FM/NM interface would allow one to determine the relative contributions of different types of electrons (e.g., s and d in the case of Fe) to the current

[Aharoni et al., 1996; Fulde et al., 1973c].   Each spin flip results in a change in angular momentum $\Delta L = \hbar$. Let the number of electrons that pass through the interface in time interval Δt be ΔN while passing current I. Then, the total charge $\Delta N e$ passes in time Δt. So, $I = \dfrac{\Delta N e}{\Delta t}$, which gives the number of electrons passing as $\Delta N = \dfrac{I \Delta t}{e}$. Assuming α to be the degree of magnetic polarization of electrons contributing to the current in the ferromagnet, the fraction $\dfrac{\alpha}{2}$ of the electrons will flip their spin at the interface between FM and NM when current I is passed through the wire. Total change in angular momentum of $\dfrac{\Delta N \alpha}{2}$ electrons is $\dfrac{\alpha}{2} \Delta N \hbar$. Hence, the torque which is the rate of change of angular momentum is $\dfrac{\hbar}{2} \alpha \dfrac{I}{e} \hat{x}$, where $\hat{x}$ is the unit vector along the wire axis. Thus torque, which increases linearly with the applied current, is a direct measure of the spin polarization of the itinerant electrons in the ferromagnet [Mohanty et al., 2004]. Other factors such as Wiedemann effect, general magnetostriction effect also contribute for the torsion of the wire but these contributions are too small compared to the spin transfer torque [Li et al., 2005]. The effect of temperature on torsion angle is relatively weak, and at room temperature, at least at resonance, the torsion angles exceed the thermal torsional fluctuations [Fulde et al., 1998].

To provide a better understanding of the degree of electric transport contribution of especially d electrons in ferromagnetic transition metals like Fe, Co, Ni, scientists have given theoretical predictions for the measurement of spin flip torsion produced in the interface of the FM and NM wires as shown in Figure 1.1. However, the torsion effect has been observed in a single Ni wire [Li et al., 2005] and micro electro mechanical mirror structures.
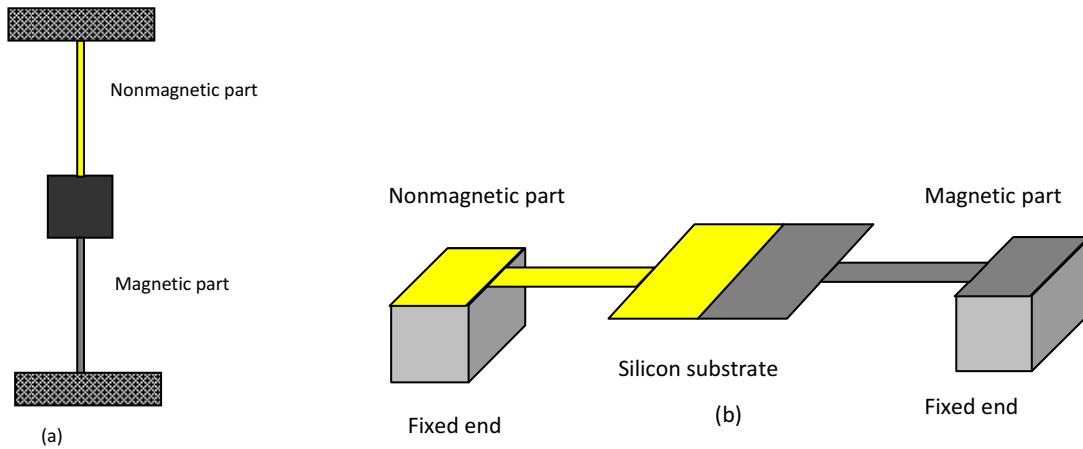
Fig. 1.1 Two types of composite structures (a) wire structure, and (b) micromechanical structure (After Xin Li et al., 2005)

1.2.2   Prediction of torsion in micromechanical structure

The micro electro mechanical structure with a mirror consists of freestanding rectangular thin film of a Silicon Nitride substrate as shown in Fig. 1.2. The beams that support the structure are fixed to the silicon wafer. Optical photolithography is used for the sample fabrication. The mirror and the beam structure are coated with Ni by electron beam deposition method.   The structure with thin layer of Ni on it (about 50 nm) is excited by either dc or ac electric current. The structure displays torsion even though it is different than the composite structure we have originally planned to study (see Figure 1.2). The effect is so large that the torsion can be seen by the naked eyes, or for small currents in an optical microscope. In addition to the magnitude of the current, the torsion depends on the geometry of the mirror namely the moment of inertia of the structure. The ferromagnetic Ni layer is much thinner than the silicon wafer (the mirror structure) so that the mechanical behavior of the mirror is dominated by the Silicon Nitride structure even after the deposition of a thin layer of Ni.

1.2.3 Moment of inertia (J) calculations for the microstructure, and the resonance frequency

These calculations are shown in Appendix A(I).

CHAPTER 2

EXPERIMENTAL TECHNIQUES FOR MEASUREMENT OF SMALL TORSIONAL ANGLE AND FABRICATION OF MICROSTRUCTURES

2.1 Different optical techniques to measure small angle

In order to measure very small torsion angles as a function of the applied current we have employed a highly sensitive optical system. Different other sensitive optical set-ups have been used by many people for research in optics.

2.1.1 Remo's correlated –optical detection approach

Remo *et al*. developed a correlated–optical detection approach (Fig. 2.1) which provides a high level of precision and resolution for linear and angular displacements [Remo et al., 1997]. A digital piezotranslator (DPT) with displacement precision of less than 1 nm is used to displace the fiber optic (FO) so that the photons supplied by a given FO aperture impinge on both segments of the dual photodiode (DPD) surface. The differential voltage as a function of displacement of piezotranslator is used as calibration standard to convert relative voltage change to displacement. This approach seems more suitable for the measurement of displacement than rotation angle.
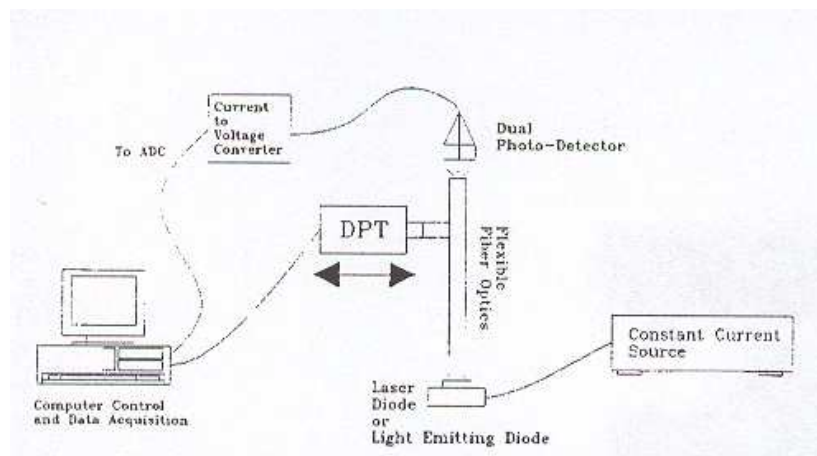
Fig. 2.1 Remo's displacement measurement set up [Remo et al., 1997]

2.1.2 Guo's surface-plasmon resonance-heterodyne interferometry (SPRHI)

Guo *et al*. have developed another method of angle measurement using surface-plasmon resonance-heterodyne interferometry (SPRHI) [Guo et al., 1998]. Their experimental set up is shown in Figure 2.2. They claim that the phase difference between p and s polarization states when surface Plasmon resonance (SPR) takes place is very sensitive to the angle of incidence. They employed heterodyne interferometry to measure this phase difference and thus to measure small angle.
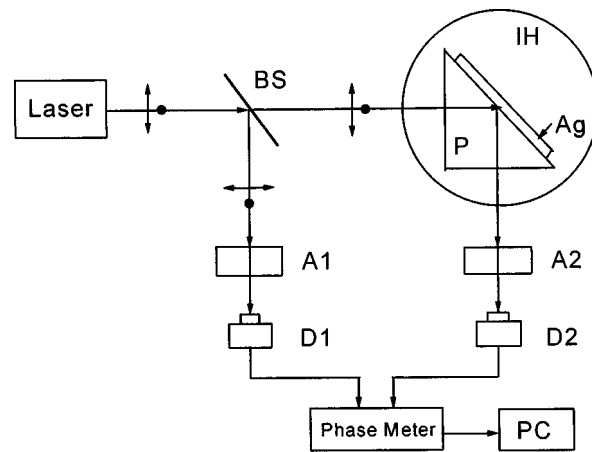
Fig. 2.2 Guo's angle measurement set up [Guo et al., 1998]

A beam of laser (He-Ne, 632.8 nm) is split into two paths by a beam splitter (BS). One part of the beam passes through analyzer A_1 and reaches the photo detector D_1. The output from D_1 is used as a reference signal. The other part of the beam reaches the prism (P) and is reflected from the hypotenuse side of the prism coated with silver. On the reflecting surface of the prism, SPR takes place so that the reflected light passes through the analyzer A_2 and reaches the photo detector D_2. It will have a phase difference Φ compared to the reference beam. The phase difference Φ is recorded as a function of a small change in the incident angle to be measured. Using these relations, a small angle can be measured by this technique. Even though the

measurement resolution of 2×10^{-5} degree can be achieved by this method, it is not easy to use it for our experiment.

2.1.3 Giuliani's oscillating mirror technique

As a modification of a basic self-mixing configuration [Servagent et al., 1998], Giuliani *et al*. devised a method for measuring small angle, with a high sensitivity (5×10^{-7} rad) [Giuliani et al., 2001]. In the presence of a strong feedback from the mirror, the laser diode (LD) operates in the so called coherent collapse regime. In this regime, the power for LD is modulated by a signal which accelerates the mirror. The experimental set up of this technique is shown in Figure 2.3. The requirement on the oscillating mirror in this technique is too complicated for our measurements.
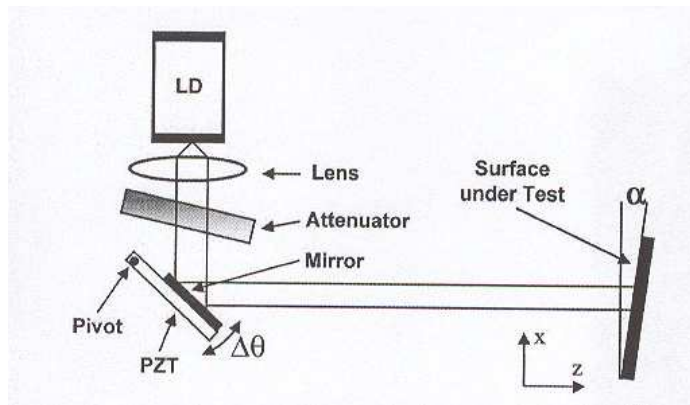
Fig. 2.3 Giuliani's angle measurement set up [Giuliani et al., 2001]

2.1.4 T. Suzuki's rotating-mirror system

Another method to measure small rotation angles was presented by Suzuki *et al*. whose experimental set up is shown in Figure 2.4 [Suzuki et al., 2001]. They calculated the angle from the relative phase shift of the viewed grating image by means of the Fourier transform (FT) method. Their set up consists of a computer-generated grating, a CCD camera with a zoom lens, a computer, and a rotating-mirror system with M_1 as a reference mirror and M_2 as an object mirror. They claim that the system does not require a coherent light source so that it is insensitive

to external disturbance and works with rough alignment. However, this method is not suitable for mounting our free standing mirror samples. Measurements of small rotation angles can also be done by interferometers and autocollimators but these techniques require an isolated environment from external disturbances, and longer measurement time respectively.
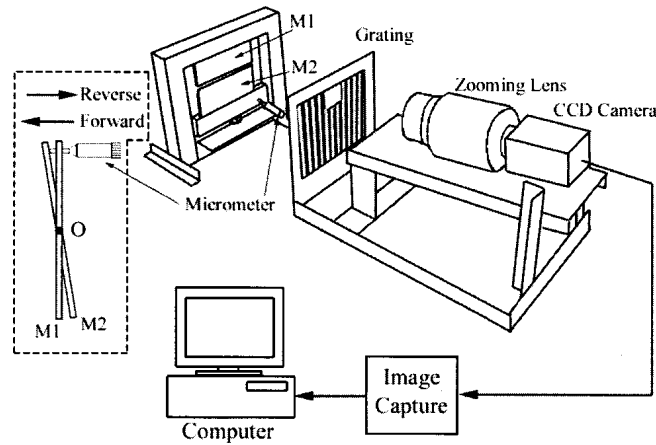
Fig. 2.4 T. Suzuki's angle measurement set up [Suzuki et al., 2001]

2.2   Our technique used for measurement of small angle /experimental set up

We have also used an optical system to measure a small torsion angle of the nano structure. The optical set up we use is shown in Figure 2.5. After attenuation of the beam of a He-Ne laser, it is directed through chopper to the reflecting surface of the mirror sample mounted vertically on a translation stage. A quadrant photodiode receives the reflected light from the sample. The signal that comes from the photodiode is measured by the lock-in technique. A chopper with a frequency around 220 Hz is used. This is the reference frequency of the signal. An oscilloscope is used to monitor the chopper frequency and the signal frequency independently. The signal from the photodiode is adjusted to zero by aligning the laser before measurements. We can do two types of measurements using this set up. DC measurement uses dc voltages taken from the Lock-in. The dc is transmitted through resistors connected in series with the mirror structure. The dc current through the sample produces torsion in the structure, so

that light reflected by it rotates and moves to a different location of the photodiode. The differential output voltages from the photodiode are synchronized with the input pulses by the LabView program, and the data are recorded in the computer that controls the Lock-in. We get the relation between the input current and the output voltages. On the other hand, the relation between the output voltages from the photodiode corresponding to different rotational positions of the sample is found by putting the sample on the rotation stage that can be controlled by the LabView program. The calibration curve is used to convert the recorded voltages to torsion angles. On the other hand, we can also pass AC currents of different frequencies from a function generator to a sample. The sample is expected to show maximum rotation when the frequency supplied by the generator is in resonance with natural oscillation frequencies of the structure.
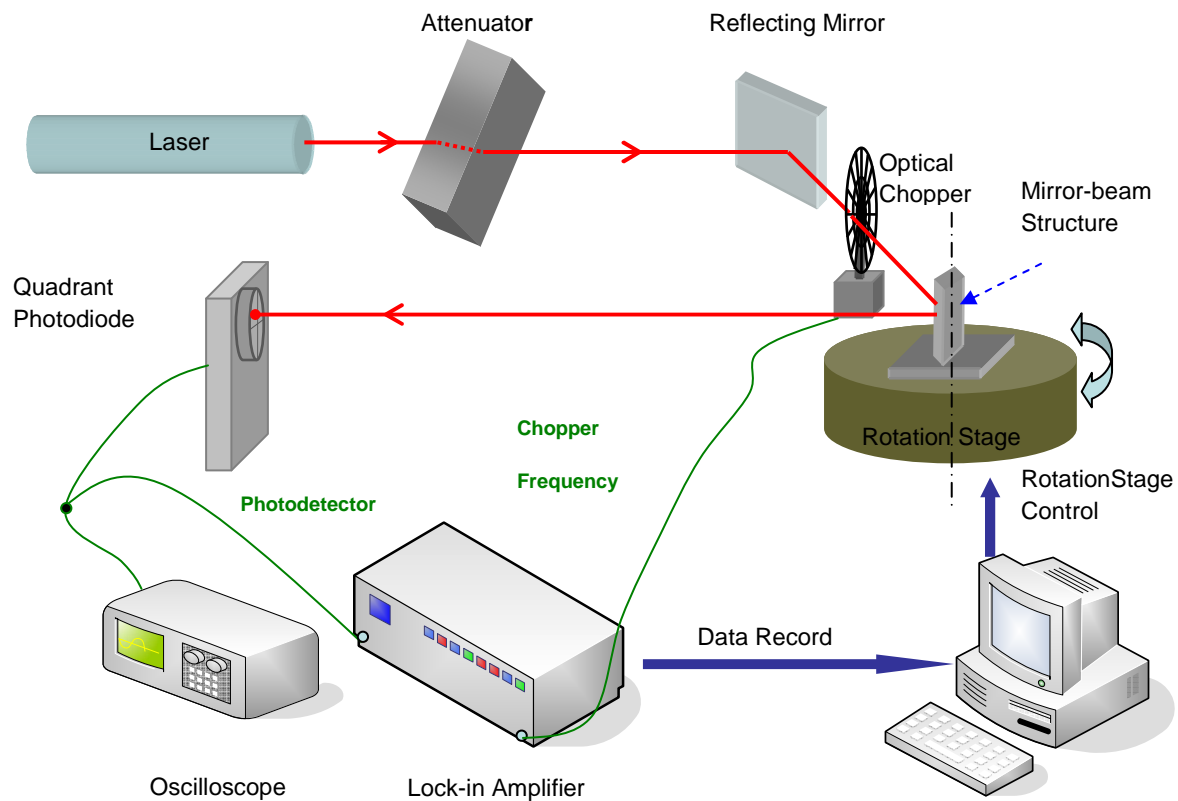
Fig. 2.5 Optical system used in our experiment

2.2.1 Split photodiode

A semiconductor photodiode QP50-6SD from Silicon Sensor Inc. has been used. It is a quadrant photodiode array with current-to-voltage amplifiers that provide X and Y difference signals. The output voltages are obtained by routing the diode element current into current to voltage amplifiers with a gain of 10^4. The four quadrants, each of these can act as a single photodiode, are formed by separating them by 42 µm gaps. The electronic assembly is shown in Figure 2.6.
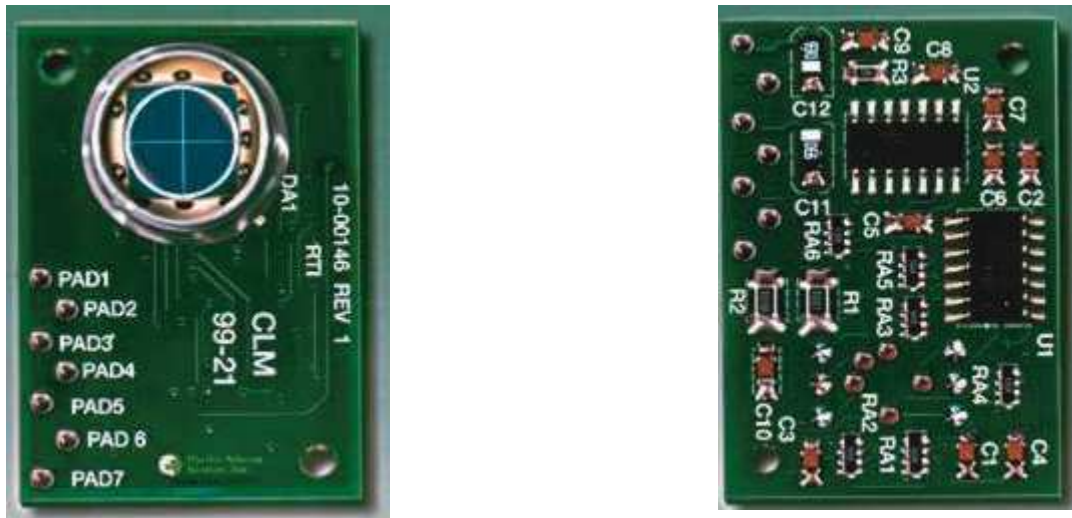
Fig.2.6. Front and back of assembly of quad photodiode

The quadrant photodiode is utilized in the principle of electron excitation that when photons (light) are incident on a PN junction of semiconductors, some electrons get exited from the valence band so that they jump to the conduction band leaving holes on the valence band. Electron hole pairs created in such a fashion are responsible for the photocurrent that depends on the power of the incident photon and the width of the depletion region of the p-n junction. The photo current is given as $I_{ph} \propto P_{in}(1-e^{-\alpha d})$, where d is the width of the depletion region and P_{in} is

the power of the incident light. The depletion region is increased and hence the photocurrent is enhanced by reverse biasing the photodiode.

Before taking any data, the output signal was zeroed by putting the light beam in the center of the photodiode. For a one-dimensional motion of the light beam we can check the difference of top and bottom, or the difference of the left and right quadrants, which is expected to be close to zero. Once this is achieved, we always get some differential voltage when the light spot moves in any direction up-down, or left-right. Figure 2.7 shows how the differential outputs are taken.
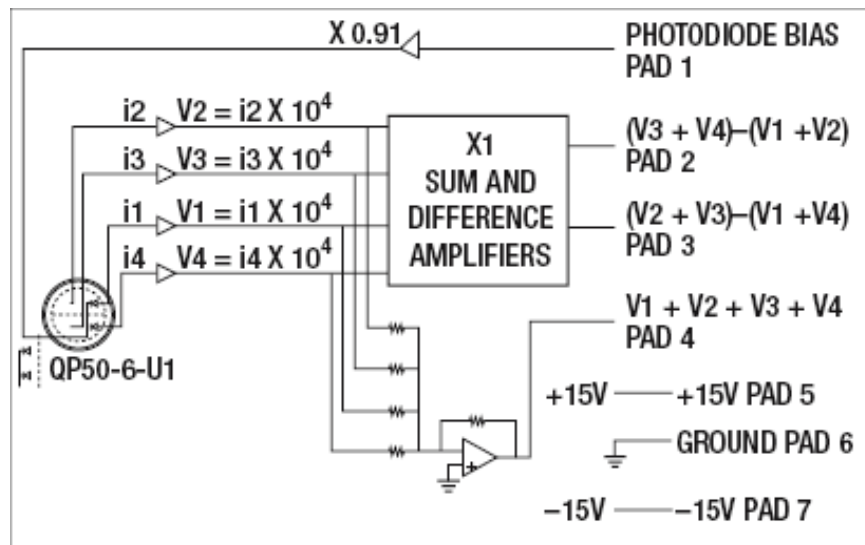
Fig 2.7 Block diagram of internal circuit of photodiode to show the output

2.2.2   Sample preparation

The momentum transfer of electrons when they pass through the interface of magnetic and nonmagnetic conductors is explained as the cause of the torque produced in the wire/composite nanostructure. However, we notice that the torsion effect is observed in a single magnetic material such as the one coated with Ni. Below we will discuss the preparation of such sample.

2.2.3 Preliminary micromirror structure

Structures of micromirrors on a silicon wafer were fabricated by photolithography. A number of similar structures were fabricated on a single Silicon wafer. One of such mirrors is shown in Figure 2.8.
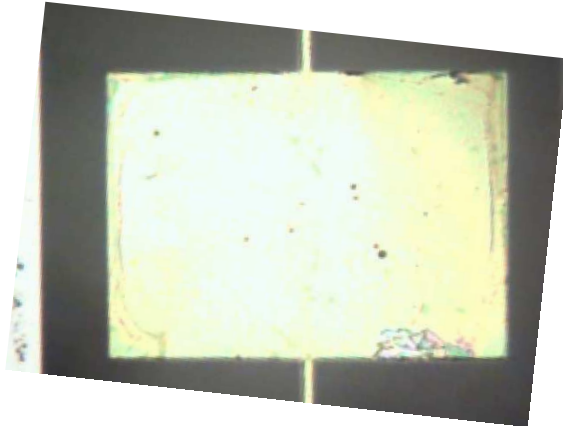
Fig. 2.8 Structure of Si mirror before Ni coating

2.2.4 Typical dimensions of the mirror-beam structure

The exact dimensions of the mirror beam structure were taken by using microscope with a CCD camera. The dimensions of the mirror and the beams supporting the mirror are shown in Figure 2.9.
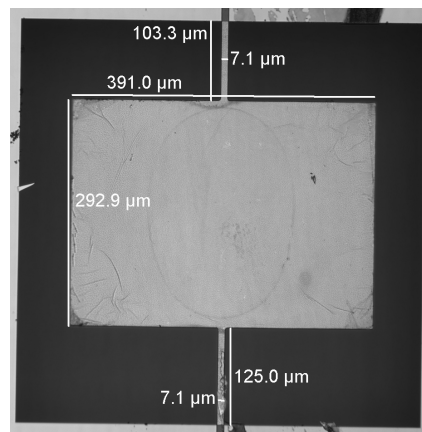
Fig. 2.9 Dimensions of the mirror beam structure

2.2.5   Ni Deposition

Nickel was chosen as one of the magnetic materials to be deposited on the mirror. Shadow masks were made for the deposition of Nickel. During the deposition we have made sure that a Nickel layer is continuous on a particular mirror and beams supporting the mirror. At the same time we made sure that individual mirrors are insulated from one another.

Nickel deposition was done by the electron beam deposition technique. In this technique, electron beam is used to melt and eventually evaporate a metal to be deposited on the wafer. For the deposition of Ni on the structures we used, the pressure of the deposition chamber has gone down to 2×10^{-6} Torr at the time of deposition. The filament current was approximately 1 A with the voltage of 8.0 KV. The deposition rate was set to be from 0.2 to 0.3Å/s. The thickness of the Nickel layer deposited in such controlled fashion was 500 Å. Fig. 2.10 shows the Si_3N_4 mirror after the Ni deposition.
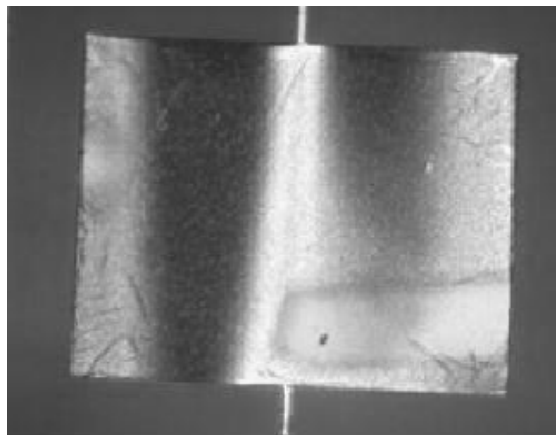
Fig. 2.10 Si mirror-beam structure after Ni deposition

2.2.6   Experiments with Nickel, and a test for the Gold deposited sample

As explained earlier, Ni-coated sample was used to see the torsion effect while passing dc current through it. The effect was observed under the microscope by applying dc current. When a current was turned on, the deflection of the mirror was seen clearly, and it was independent of the direction of the current. At this point, we assumed that the effect has magnetic origin. But it was important to check whether or not this effect is observable in nonmagnetic samples as well. For instance, rotational effect may be due to the interaction between individual electric dipoles and the ac electric field as observed by Fan *et al*. [Fan et al., 2005]. On one of the mirrors, 500Å thick layer of Au was deposited as a nonmagnetic conductor. It was difficult to make the Indium contact to the gold layer, since it was coming off easily while the surface was heated by the iron. Thin silver paste, on the other hand, allowed us to make contacts across the gold coated mirror. As in the case of Ni, gold wires were used between the contacts and the connecting wires. Using the same source meter (Keithley 2400) as a current source, dc current was passed through the structure, ranging from 0.1 μA to 2 mA. For each current the sample was observed under the microscope. In the case of Ni coating, the torsion effect was observed when dc of 1.3 mA was applied and the effect was more prominent when pulses of dc current increase. There was no torsion effect at all as we observed by naked eye in the case of gold-deposited structure for the dc current of up to about 5 mA. However, close to this value of dc current, the torsion of the structure was observed. The presence of torsion in gold deposited sample has challanged our hypothesis that the torsion in Ni-coated sample is due to magnetism alone. In fact this experiment indicated that the torsion effect in the case of Ni-deposited sample does not have magnetic origin. There are many possible sources of torques at nanoscale. Torques on MEMS are based on electrostatic forces, thermal fluctuations, circularly polarized light and angular

momentum transfer by spin polarized currents [Covalev et al., 2007]. In the context of our observation, it was important to know the reason of the torsion in the Ni deposited freestanding silicon mirrors and Au-deposited structures. It is worth noting that the torsion in the case of Ni is seen at lower currents than the torsion in the case of Gold deposited structures.

2.2.7   Taking data/experimental details

He-Ne laser was focused by lens system onto a free standing sample which was kept vertical on a stage with translational (x, y, z) and rotational degrees of freedom. Initially, the laser spot is adjusted at the center of the photodiode, so that the output signal is zero (see Figure 2.11). Once the zeroing is accomplished, current is passed through the sample. When pulses of current are passed through the mirror beam structure, torsion pulses are produced in the structure. As the mirror rotates, it rotates the reflected laser beam so that the reflected spot gets shifted on the photodiode. When a current is passed through a vertical structure the reflected light moves mostly from left to right. Output signal is taken from pad 2 which gives the differential voltage produced by the left and right opposite quadrants. Lock-in amplifier controlled by LabView program is used to execute the output signal. The output signal voltages as a function of the input voltage pulses, which is responsible for current pulses, is recorded by the LabView interface. These output voltage signals are to be converted to the corresponding torsion angles.
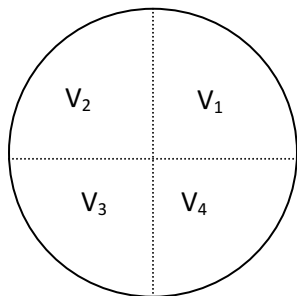
Fig. 2.11 Quadrants of the photodiode

Pad 1 Photodiode Bias

Pad 2 output = (V3+V4)- (V1+V2)

Pad 3 Output = (V2+V3)- (V1+V4)

Pad 4 Outpot = V1+V2+V3+V4

Pad 5 for +15 V

Pad 6 for GROUND

Pad 7 for –15 V

2.2.8   Lab View Programs

Lab View program was developed for controlling Lock in, generating the dc voltage in steps and run the program between +v and –v, and record the data that Lock in acquires when the micromirror actuates and the signal of laser changes on the split photodiode. Fig. 2.12 shows the front panal of the software developed.
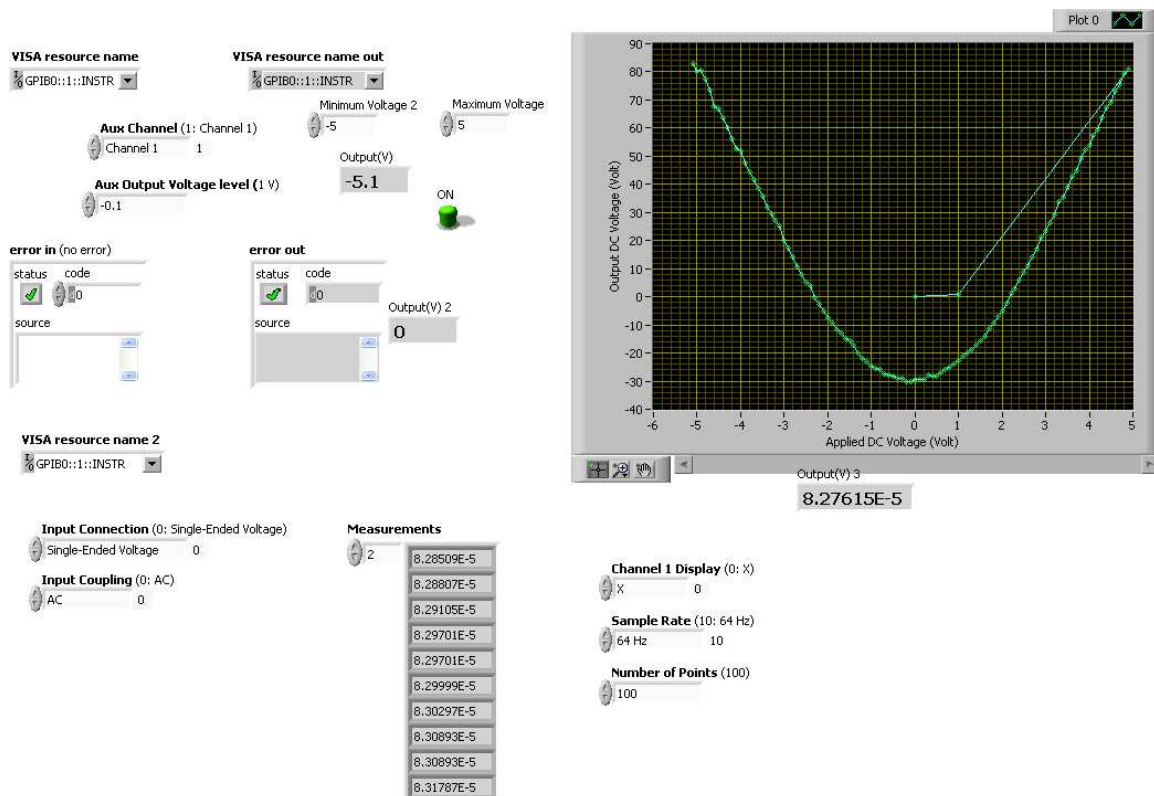
Fig. 2.12 Lab View program used to control Lock in and record data while passing dc current

2.2.9   Calibration

The calibration curves are obtained from the output voltage signals corresponding to different known angular positions of the sample structure. Such a relation is found by putting the sample in a vertical position on the rotation stage that can be rotated in a controlled fashion by LabView interface. Laser is focused on the sample. The reflected laser beam is focused on the split photodiode. As before, zeroing of Lock-in reading, which is the output signal from the

photodiode, is initially done by adjusting the position of the photodiode. The rotation stage is set to zero at this position as a reference. The rotation stage is then rotated controlling it by using the LabView program. For different positions of rotation stage, and hence the mirror-sample on it, the differential voltages as output signal from pad 2 are recorded. The distance between the sample and the photodiode layer, intensity of laser, and other parameters are kept the same during calibration as they are during the measurements. Current is not passed through the sample during calibration. A typical calibration curve is shown in Figure 2.13. It is taken up to the saturation region of the photodiode maintaining the same distance of 15 cm between the reflecting sample and the photodiode as during the measurements. While converting the actual data to the torsion angle the calibration data has been multiplied by -1 to correlate the direction of torsion of the mirror and the corresponding direction of the rotation stage. In other words, this allows the positive angle of calibration curve to represent the data for increasing currents, and negative angles to represent the data for decreasing currents.

Calibration of rotation stage for Au coated mirror

$y=-2E7x^2-43377.9x-0.0056$

Calibration of rotation stage for Ni

$y=7E14x^4+6E11X^3-9E6x^2-3377x+0.013$

(a)   (b)
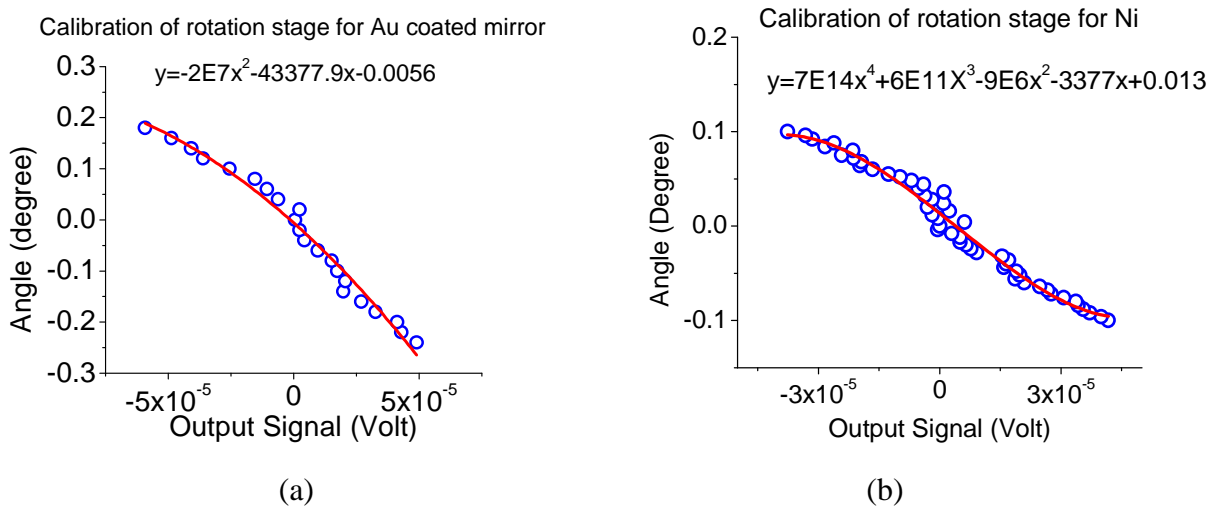
Fig. 2.13 Typical calibration curves used for (a) Gold sample (b) Ni sample

2.2.10   Some challenges in the measurements

The experimental realization of the structure is a challenge, since free-standing metallic structures on a micro and nano scale need to be fabricated and manipulated [Covalev et al., 2007]. Extra care is required in every step of such manipulation. Several problems were encountered while working with our micro scale mechanical structure. Not all the structures survive during the fabrication. Beyond that, while depositing Ni by the electron beam deposition, or gold by a thermal evaporation noticeable bending of the mirror structure was observed. The reason of bending is due to heating of the structures in the deposition chamber. Most of the time the reflecting surface with deposit Ni or Au film is convex which produces a broadened beam of light in reflection. Such reflections are very hard to focus on the photodiode. However, by introducing a small aperture some portion of light beam can still be focused in the center of the photodiode. When the structure torts while passing current, the spot of light on the photodiode moves in one direction causing the shift of power of laser spot on the photodiode. Due to slightly folded geometry of the mirrors after metal depositions in many cases, the light spot on the photodiode was found to have a complex shape. However, in average the spot could be used to measure the differential voltage between the left and right halves of the quadrant photodiode. Despite technical difficulties, optimizations of the measurement set up allow us to obtain information about the current and thermal effect on the torsion

CHAPTER 3

TORSION OF THE FIRST GENERATION MICROSTRUCTURES

3.1   Torsion with magnetic (Ni) and non-magnetic (Au) samples

As explained earlier, Ni-coated sample was used to see the torsion effect while passing dc current through it. The effect was observed under the microscope by applying pulses of dc currents. When a current was turned on, the deflection of the mirror was seen clearly, and it was independent of the direction of the current. At this point, we assumed that the effect has magnetic origin. But it was important to check whether or not this effect is observable in nonmagnetic samples as well. For instance, rotational effect may be due to the interaction between individual electric dipoles and the ac electric field as observed by Fan *et al*. [Fan et al., 2005]. Thin silver paste was used to make contacts across the gold coated mirror. Direct current ranging from 0.1 μA to 2 mA were passed through the structure. In the case of Ni coating, the torsion effect was observed when dc of 1.3 mA was applied and the effect was more prominent when pulses of dc current increase. There was no torsion effect at all as we observed by naked eye in the case of gold-deposited structure for the dc current of up to about 5 mA. However, close to this value of dc current, the torsion of the structure was observed. The presence of torsion in gold deposited sample has challanged our hypothesis that the torsion in Ni-coated sample is due to magnetism alone. In fact this experiment indicated that the torsion effect in the case of Ni-deposited sample does not have magnetic origin. There are many possible sources of torques at nanoscale. Torques on MEMS are based on electrostatic forces, thermal fluctuations, circularly polarized light and angular momentum transfer by spin polarized currents [Covalev et al., 2007]. In the context of our observation, it was important to know the reason of the torsion in the Ni deposited freestanding silicon mirrors and Au-deposited structures. It is worth noting that the torsion in the case of Ni is seen at lower currents than the torsion in the case of Gold deposited structures.

3.2 Preliminary data for dc measurements

3.2.1 Ni deposited sample

To quantify the torsion angle as a function of current in a soft magnetic material (nickel), the experiment was carried on. Figure 3.1 (a) shows that the Lock-in recorded signal from the photodiode detector in micro volts as a function of the input voltage generated from the same lock in, and applied across the micro mirror. Positive values of photo diode signal, i.e. the differential voltages between the left and right halves of the photodiode indicate that the mirror torts in the same direction irrespective of the direction of the current supporting manual observations under the microscope. When the current pulses were passed, manually by the dc current source Keithley 2400, it was clearly visible to the naked eye that the mirror would go to the same direction for both directions of the current. The data, as shown in Figure 3.1 (b) revealed that the torsion angle depends on the square of the current. The equation obtained by the second order polynomial fit, that is shown in Figure 3.1 (b) is the best representation of the data within the operating range of the photo diode.

(a) (b)
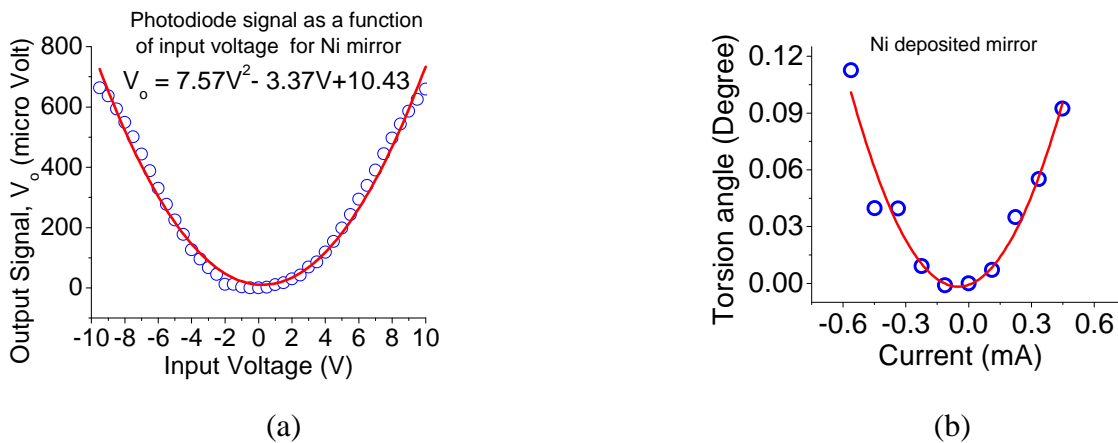
Fig.3.1 Dependence of torsion angle of Ni deposited micromirror, (a) Photodiode signal as a function of input voltage, (b) torsion angle as a function of current.

3.2.2 Au, and Ag deposited samples

The angle of torsion is not linear with the dc current passed. Rather the angle seems proportional to the square of the current as shown in Figure 3.2 (b). Also, this graph shows that the direction of rotation of the micro mirror is independent of the direction of current. This is shown by the increasing output signal within certain range of positive and negative voltage. Figure 3.2 shows the torsion angle in terms of microvolts. The parabolic region of the graph in Figure 3.2 (a) shows clearly the appropriate operating range of input voltage. Outside the parabolic region, the decreasing signal in both positive and negative input voltages indicates that for the large torsion angle of the micromirror, the laser spot moved beyond the active operating region of the photodiode. Thermal energy seems to contribute to the torsion of the micromirror. The tests done to see the contribution of thermal effect will be discussed later.

(a) (b)
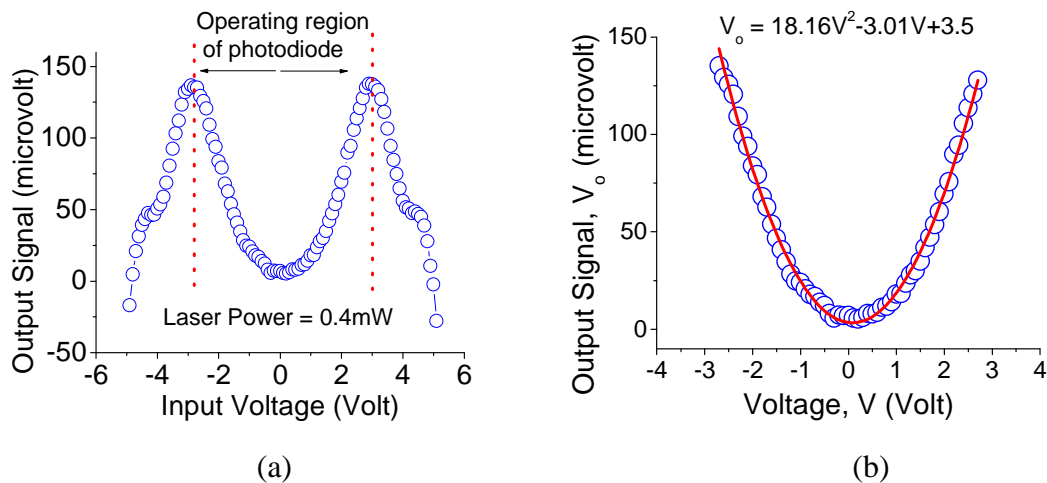
Fig.3.2 Dependence of photodiode signal on the input voltage in gold sample (a) raw data, (b) data in the operating region

The data can be converted to the units of angle as shown in Fig. 3.3 (a) and (b) for Au deposited and Ag deposited samples by using the calibration equations.
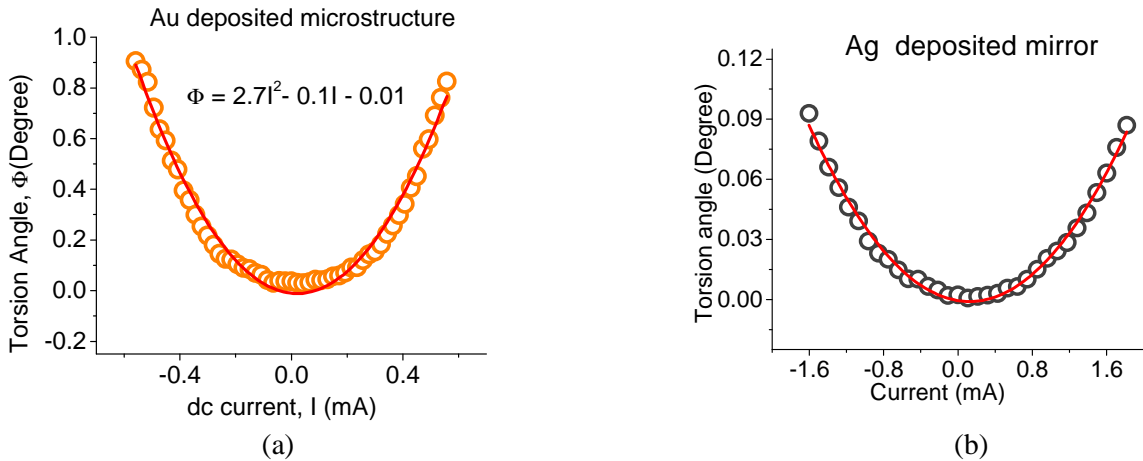
Fig. 3.3 Torsion angle as a function of direct current in (a) Gold sample, (b) Silver sample

Most of the time, it is seen that there is some hysteresis in the angle. The micromirror is allowed to actuate by passing dc current in one direction, and then the current direction is reversed. While doing so, the structure shows some hysteresis as shown in Fig. 3.4. It shows two curves one for increasing input current and the other for the decreasing input current, i.e. in the reverse direction as shown by the arrows.

3.3 Hysteresis in torsion in Au and Ni deposited samples
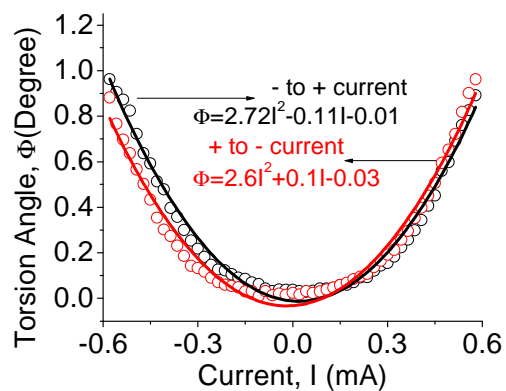
Fig.3.4 Hysteresis in reversing the direction of the current in gold sample

The nature of hysteresis in the Au samples is similar to the case of the Ni samples. In Figure 3.5, up arrow shows the data for increasing current where as the down arrow shows the

data for reverse direction of current. Gold sample and Nickel sample both show that the torsion mirror does not go back exactly to the same position for the same current when the direction is reversed. Let's consider the case when the current is decreasing from higher values to zero. Until it goes to zero, the mirror always remains little further ahead than it was for forward current direction. It is shown by higher values of photodiode signals for the reverse current until it goes down to zero. However, below zero value of current which corresponds to the initial equilibrium position of the torsion mirror, the output signals are smaller than they were for the corresponding current when it was increasing. This is shown by the lower values of the signal voltages in the negative direction of current in both the samples shown in Figures 3.4 and 3.5. The hysteresis curves suggest that it would be reasonable not to expect the micromirror position to be exactly the same for forward and reverse directions of the currents. However, the difference in positions is not large which suggests that such torsion mirrors can still be used again and again within small difference in positions for forward and reverse directions of current.
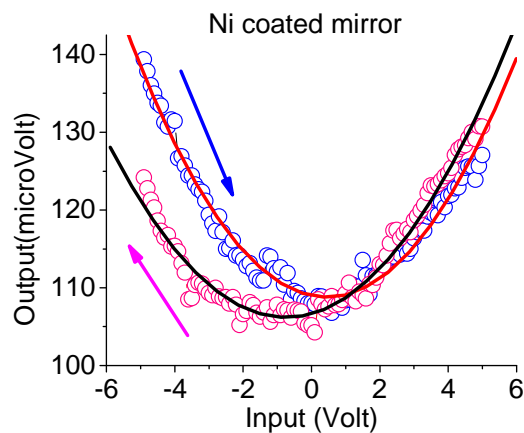
Fig. 3.5 Hysteresis in reversing the direction of current in Ni sample

3.4   The possibility of heating effect, and its test

Despite their differences regarding their magnetic properties, both nickel and gold deposited micro mirror structures showed torsion when current was passed through them. It is obvious that the beam-structures get somewhat heated when current passes through them due to their electrical resistance. Since the photodiode signals are the functions of torsion angle that depends on the applied current, they are functions of the electric power too. Figure 3.6 (a) shows how the output signals for Gold sample of resistance 20.9 Ω depend on the electric power through it. Four different lines show the output signals for increasing and decreasing current in one direction, and also increasing and decreasing currents in the reverse direction. The linear region as shown in Figure 3.6 (b), and also the linear fit of one of the curves as shown in Figure 3.6 (c) corresponds to the well behaving parabolic region of the output data. It shows that the torsion angle is proportional to the electric power applied.

(a)   (b)   (c)
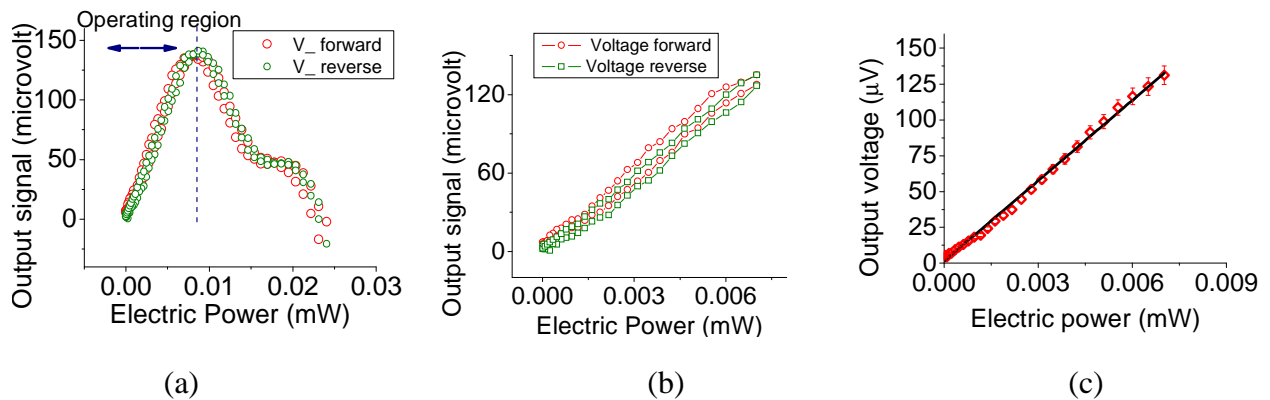
Fig. 3.6 Signal that corresponds to torsion angle; (a) as a function of electric power; (b) linear region for useful data; (c) linear fit to the average data of linear region.

It was desirable to check if there is similar pattern of output signal if the sample is heated by other thermal source in the absence of current through the sample. If there is a contribution to heating effect, a hypothesis at this point would be that the signal varies in the same fashion as in the case of electric power when the sample is heated up. A separate powerful source of green

laser was used to thermally actuate the sample. A sensitive detector was calibrated against the available power meter, and it was used to measure the low power produced by attenuating the power of green laser with the help of a set of polaroids.

Output signals were recorded after approximately every 10 seconds after the power of the green laser was changed every time to let the heat propagate through the rectangular structure to the beams supporting the structure. This would give almost the same exposure time for the sample to different power of the laser to allow equal time for its thermal expansion. Figure 3.7 shows the increase in photodiode signal indicating bigger torsion of the structure as the optical power falling on it is subjected to increase. It was also observed by the naked eye that the mirror rotated, which was confirmed by the change in the output signal on the Lock-in. This test shows that there is definitely some contribution of thermal effect to expand the metal layer which produces torsion of the micro mirror structures.
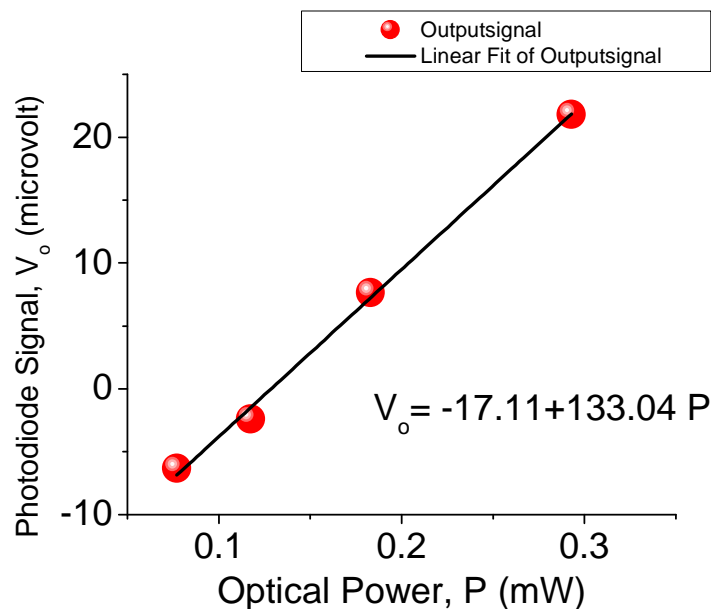
Fig. 3.7 Torsion of micromirror with Au deposit on it as a function of optical power used to heat the sample

While using green laser to heat the sample, an orange filter was used to block the reflected green laser from the sample to make sure that the green laser didn't contribute to the intensity of the laser spot focused on the photodiode. The effect of heating was also tested in another way. For different sets of data, different power of green laser was used constantly. Figure 3.8 shows the data without the green laser; and two sets of data with green laser at different power levels. These data reveal that the torsion of the mirror is higher for the higher power of the green laser used for heating. This indicates that there is definitely some contribution of thermal effect in the torsion of such micro mirrors. After the green laser, the heating source, was removed, the data was taken again with the red laser only as was done in the first experiments. The output signal didn't revert back to the original data without the green laser. This may be due to some change on the surface geometry of delicate microstructure due to heating.
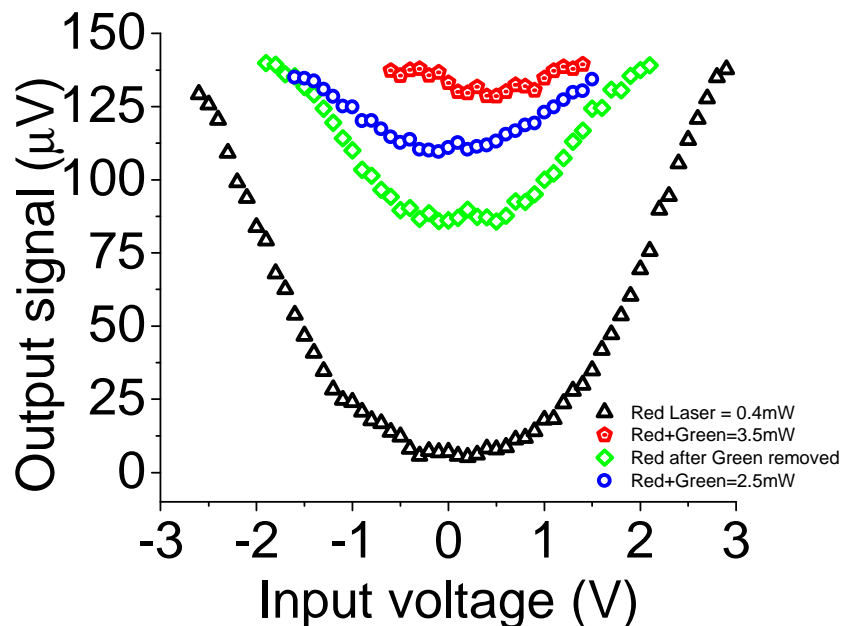
Fig.3.8 Torsion in terms of micro volts as a function of input voltage at different power levels of green laser used for heating the Au sample. Also the data before the use of green laser and after it was removed are shown

An aperture with circular shape of the diameter of about 2 mm was used right before the photodiode to form a laser spot of a regular shape on the photodiode. This hole definitely limited the laser reflected from the sample. The inflexion points at maxima seen in each curve in Fig. 3.8 are due to this effect. So, the data showing the parabolic parts are only the data that may represent the rotation of the micro mirrors. This is the reason why only the parabolic part was used earlier to find the useful relation between the rotation angle and the input current.

3.5 Higher current limits

Both Ni and Au samples have shown torsion effect. While we understand that there are some common torsion effects in both magnetic and non-magnetic samples, some of the mechanisms responsible for the origin of these effects are to be understood. Importantly, however, for the possible use of such torsion in MEMS, it is desirable to have large torsion angles. Survival of the structure is a matter of concern for such torsion because it needs to be fed higher current. Surprisingly, the Au deposited Silicon Nitride (Si_3N_4) mirror did not break up to 20 mA of direct current. The test done for higher current than 20 mA will be discussed in the next section. It would require separate calibration. While passing larger currents manually, one could hold the mirror in the position it reaches by continuing the same current. The rotation stage angle is set in the reverse direction so that the rotation stage can bring the position of the mirror back to the original position. The stage is rotated until the lock-in reading is the same as in the initial position of the mirror. The angle of rotation of the rotation stage corresponds to the angle of torsion of the mirror for the current being used. A set of data taken this way is shown in Fig. 3.9. The fit of this data can be used to predict the torsion angle for 20 mA of current up to which the mirror was strained to show torsion.
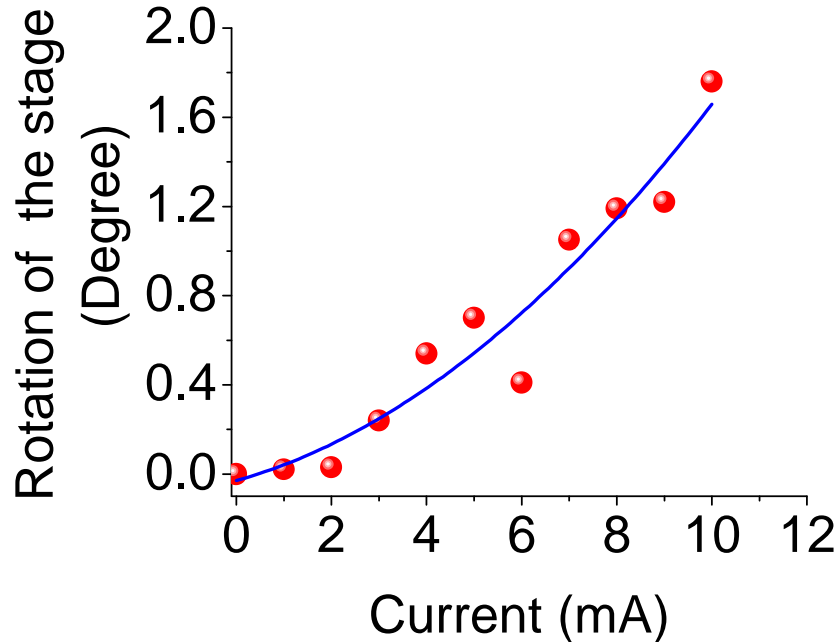
Fig.3.9 Torsion of micromirror with Au sample for higher current

Using the fit shown in the Fig. 3.9, the torsion angle for 20 mA current comes to be 5.5 degree. On the other hand, the motion of the reflected light from the sample was clearly noticeable and traceable on a sheet of paper at the same distance of 15 cm as the photodiode from the sample. One end of the light strip was monitored and projected on a white sheet of paper. The deflection of the end point was marked before and after the current was passed. It was about 2.6 cm. Considering a right angled triangle with adjacent side of 15 cm, the distance between the sample and the photodiode; and the opposite of 2.6 cm, the angle of deviation of reflected light was found to be 9.83 degree which is double of the rotation of the mirror. Hence, the rotation of the mirror was found be to be 4.9 degree which is just about 11% different than the actual measurements. This agreement supports the confidence level in the measurement of the torsion angle of the mirror.

3.6 Direct measurement of torsion angle for higher currents

As higher currents were passed through the sample, and reflected light was projected on a screen at the same distance as the photodiode, the deflection of the reflected light became more apparent to the naked eyes. When the current is turned on using a dc current source (Keithley 2400), the light (taken for one end point of the visible light strip) deflects on the screen. Initial position of this end is marked on the screen, and after the light deflects it can be brought back by rotating the rotation stage in opposite direction by the same amount as the deflection of the structure. This is done by controlling the rotation stage by the LabView interface. The restoring angle of the stage, where the sample was kept fixed vertically along its axis of rotation, corresponds to the torsion angle of the structure. Since the stage needs to be rotated in the opposite direction of the torsion, the angles can be taken as negative compared to the torsion angle. This is indicated by the negative angles shown in Fig. 3.10.
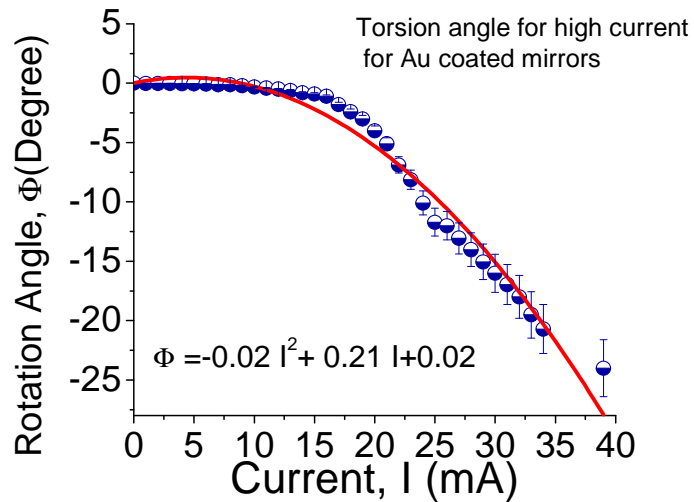
Fig.3.10 Direct measurement of torsion angle by restoring it by the rotation stage

Since the deflection of light spot on the screen for the application of low currents was too small to be observed by eyes, the initial lock-in reading was taken as the reference point which is achieved by the back rotation of the sample stage. The restoring angle of the stage is the torsion angle. In this regime, the measurements are not accurate. However, for the larger currents the deflection is clearly distinguishable, and the restoring angle is taken directly by bringing the deflected light back to the reference mark corresponding to the zero position (equilibrium position of the mirror). Thus confidence level in this regime (15-35 mA) was high. As shown in Fig. 3.11, point "A" is the position of the end of reflected light as projected on the screen before the current was turned "on", and point 'B" is the position of the corresponding point after the current is turned "on". This means that point "A" corresponds to the zero position, and point "B" corresponds to the excited state of the mirror-beam structure. For further "off' and "on" of the same amount of current, the light beam moves exactly to points A to B respectively.
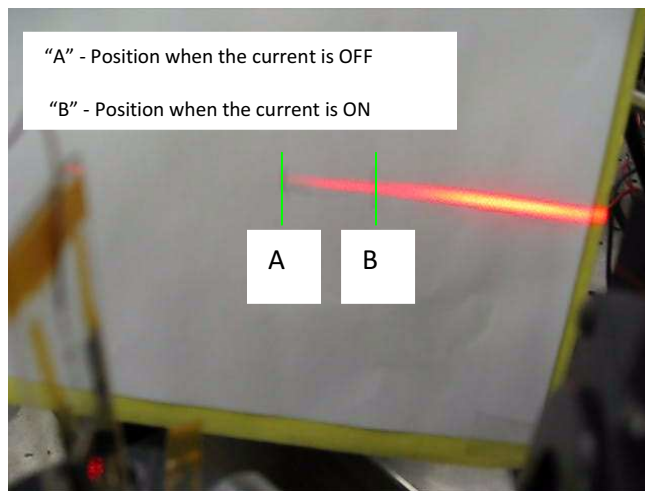
Fig.3.11 A photograph showing the initial and final positions of the tip of light

before and after 20 mA of current was turned off and on

Again, for the region of high currents (more than 35 mA), there was some distortion of the shape of the reflected light. This might be due to the slightly convex surface where the light might have been reflected from nearby points but not exactly from the same point as before. This can also be considered as the experimental limitation of aligning the sample exactly on the rotational axis of the stage. This might make the sample shift by few microns from its original position, and it might be the cause of the change of the shape of the reflected light. This caused slight deviation of the data points from the fit in this regime (35-40mA). Considering the fitting shown in the graph of Fig. 3.10, one can find the torsion angle corresponding to 20 mA of current which comes to be 5.3 degree. Compared to the earlier measured values, this value is in close agreement by 3.6% less than 5.5 degree, and 8.2% more than 4.9 degree. This shows the consistency of the measured values of torsion angles for high currents. The gold deposited structure survived well beyond this value and showed the torsion faithfully up to 40 mA of direct current. However, after the structure was cycled a couple of times by turning this current on and off, the structure lost conductivity. The current of 38 mA gave the torsion of 26.3 degree which is way above the desired angle for the applications needed for MEMS. According to these measurements the useful torsion can be produced way below the breakdown current limit demonstrating the possible use of torsion in such micromirror structures.

3.7 AC measurement technique and assumptions

From a function generator, alternating current of varying frequency is passed through the micro structure as shown in Fig. 3.12. While passing AC, the mirror beam structure is expected to oscillate, and a resonance is expected when the supplied frequency is equal to the natural oscillation frequency of the system. When the resonance takes place, the amplitude of the photodiode-output voltage goes to the maximum value.
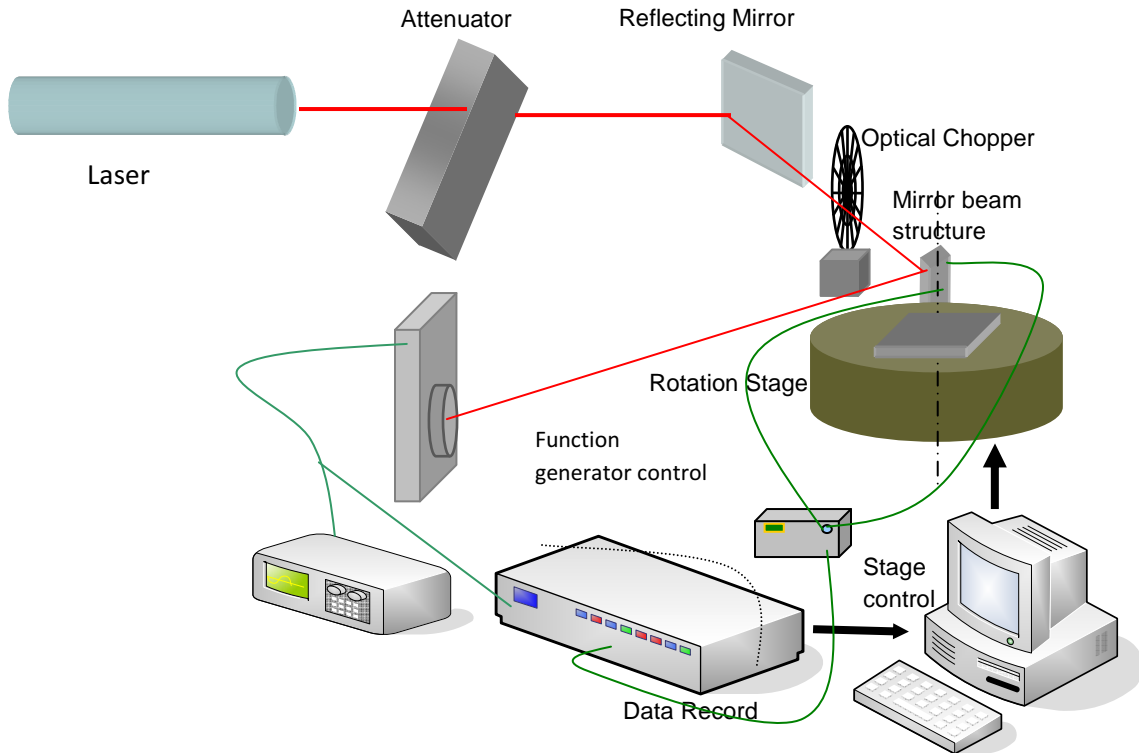
Fig.3.12 Schematic for measurement of possible resonance due to alternating current

3.8 Estimation of the resonance angle

When alternating current is passed, the oscillation is expected to be enhanced so that the torsion angle would go higher. Magnitude of this angle becomes the highest at the resonance frequency. An estimate can be made for this angle. The general expression for the torsion angle of the structure is given by the following expression. The variables appearing in this expression are explained in Appendix A (I). The torsion angle is:

$$\alpha_o(\varpi) = \frac{\dfrac{\hbar P I_o}{2q}}{\sqrt{[\dfrac{2k_1 G_{Si} h^3 b}{L} - \varpi^2(\dfrac{1}{12}\rho_{Si} BhL^3 + \dfrac{1}{24}\rho_{Si} bh^3 L_F + \dfrac{1}{24}\rho_{Si} bh^3 L_{NM})]^2 + \dfrac{KJ}{Q^2}\varpi^2}}$$

When we set the term inside square brackets to be equal to zero in resonance ($\omega = \omega_o$), we get the expression for the resonance angle when alternating current is applied.

$$\alpha_o(\varpi_o) = \frac{\dfrac{\hbar P I_o}{2q}}{\sqrt{\dfrac{KJ}{Q^2}}\ \omega_o},$$

On the other hand, when direct current is passed ($\omega = 0$), this leads to the expression for torsion angle for dc current as:

$$\alpha_{o\,dc}(\varpi = 0) = \frac{\dfrac{\hbar P I_o}{2q}}{\dfrac{2k_1 G_{Si} h^3 b}{L}},$$

From the above expressions, we get the ratio as:

$$\frac{\alpha_o(\varpi_o)}{\alpha_{o\,dc}} = \frac{Q}{\varpi_o \sqrt{KJ}}\ \frac{2k_1 G_{Si} h^3 b}{L},$$

Where $\dfrac{2\ k_1 G_{Si} h^3 b}{L} = K$ for the double torsion bar. On substituting this value, we get a simple expression relating torsion angle for dc to the torsion angle when the system is at resonance as:

$$\alpha_o(\varpi_o) = \alpha_{0\,dc}\ \frac{Q}{\varpi_o}\sqrt{\frac{K}{J}}\ , \text{ where } \varpi_o = 2\pi f_o,$$

J in the above expression can be replaced by the denominator of the following expression.

$$\omega_o = \sqrt{\frac{K}{J}} = \sqrt{\frac{\dfrac{2K_1 G_{Si} h^3 b}{L}}{\rho_{Si}\dfrac{L^3 Bh}{12} + \rho_{Si}\dfrac{h^3 LB}{12} + \rho_{Si}\dfrac{b^3 L_1 h}{6} + \rho_{Si}\dfrac{h^3 b L_1}{6}}} \quad ,$$

However, taking an approximation as b<<L, and h<<L, we can write $J = \dfrac{1}{12}\rho_{Si} BhL^3$.

Putting the values for ρ_{Si} = 2330 Kg/m^3, and for the mirror used for the Au sample B = 291.2

μm, h = 0.5 μm, and L = 388.1 μm, we get approximately, $\sqrt{J} \approx 10^{-9}$. For the structure we used,

k_1 = h/b = 0.07 for b = 6.5 μm, and G_{Si} = 65 × 10^9 N/m^2 for Silicon. If we take Q = 10, f_o=10

KHz [Li, 2005], we find that the torsion angle at resonance $\alpha_o(\varpi_o)$ is enhanced by about 100

times compared to the torsion angle due to the same amount of dc current. If we eliminate $\sqrt{K/J}$

by ϖ_o, we get a simplified relation as:

$$\alpha_o(\varpi_o) = Q\ \alpha_{o_{dc}} ,$$

If the quality factor Q is 1000, the torsion angle is enhanced by thousand times. This shows that

the alternating current can enhance the torsion angle by several orders of magnitude. So, the

micromechanical mirror can be actuated by alternating current to measure too small angles that

may not be obvious while using direct current.

3.9 Estimation of the resonant frequency

Some preliminary AC measurements were taken while working previously with the Ni

coated samples. For these samples, different parameters were taken as: k_1= 0.23; G_{Si} = 65 × 10^9

Pa; h = 5×10^{-7} m; b = 7.6×10^{-6} m; L = 3.826×10^{-4} m; ρ for Si$_3$N$_4$ = 3440 Kg/m^3; B = 2.93×10^{-4}

m; and L_1=1.039×10^{-4} m. Using these values, the resonant frequency is estimated to be about 894

Hz. For the samples with different physical parameters, we can anticipate different resonant frequencies.

Despite the expectation of resonance phenomena in actuation of microstructure while passing ac current, practically the structures were found over damped. No oscillations were observed, and it was not possible to find resonance frequency.

3.10   Conclusions for preliminary microstructures

Micromechanical free standing mirror-beam structures of Silicon Nitride have been fabricated. These structures were coated with Nickel by electron beam deposition technique to the deposition thickness of 500 Ǻ, and with Gold by thermal evaporator to about the same thickness. All of these structures show torsion when current is passed through them. The torsion direction has been found to be independent of the direction of the current. The torsion angle is typically proportional to the square of the applied direct current. A technique to measure such torsion angles has been developed. LabView programs were developed to produce auxiliary dc voltage output from the lock-in and to record the photodiode output signals through the lock-in. The torsion angles as a function of direct current have been measured for nickel and gold samples. Heating effects have been found to provide some contribution to produce torsion. On the other hand this does not seem to be the only cause of the observed effects.

CHAPTER 4

DESIGN AND FABRICATION OF MORE PRECISE, THE SECOND GENERATION OF MICROSTRUCTURES

In the previous micromechanical mirrors and the measurements as discussed earlier, we encountered a problem of mirror folding while depositing metal on them. Thinking that reduced size of mirrors would make the mirrors sturdier and remain flat on metal deposition, improved mirrors with square shape were designed and fabricated in more systematic way with smaller dimensions of 150µm×150µm. In order to see how the torsion angle depends on beam width of the mirrors, five different beam widths (8, 10, 12, 16 and 20 µm) were designed in the new fabrication of the free standing mirrors. The thickness of silicon nitride and the thickness of metal deposition were altered presumably for more systematic results in the measurements.

4.1   Design of more precise micromirrors

More systematic design of micromirror structures was necessary to understand the torsion phenomena in detail. During deposition of metal on the surface of micromirror structures in the previous design, bending of the mirrors was found every time. The convex reflecting surface caused wide reflection that always created problem in getting a sharp spot of reflected light on the photodiode during optical measurements for torsion angle. Reducing the size of micromirrors might solve this problem, thus a new design of micromirros was proposed. The layout was designed using design software named LASI. One layout of such design consists of 5 mirrors in a column with 5 rows. The mirrors are 150 µm×150µm in dimensions which are supported by beams with *different widths*, viz. 8, 10, 12, 14, and 16 µm. These freestanding mirror structures are made of silicon nitride layer, and they are suspended in KOH etched silicon wafer. The size of the top opening of the wafer is kept to be 700µm×500µm. For this opening on the top, the opening on the bottom has to be 1124 µm×924µm. The rate of etching of silicon at 54.7 degree

with the (100) plane is much faster than in other direction which is schematically shown in Fig.

4.1(a). Due to this the etching from the bottom to top of the wafer goes as four sided pyramid as

shown in Fig. 4.1 (b). The dimensions at the bottom are designed for 300 μm thick wafer.

(a)

(b)
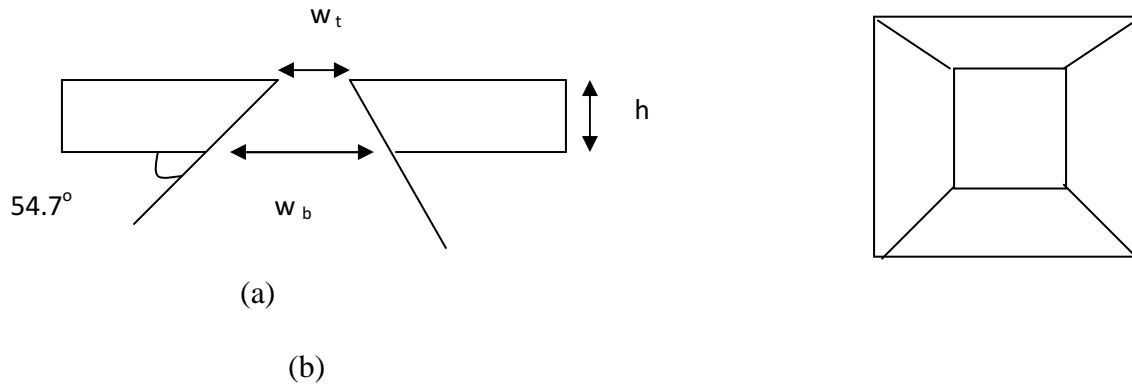
Fig. 4.1 Schematics of KOH etched hole of Si wafer (a) wider etch at the bottom than at the top of the wafer, (b) square hole with bigger opening at the botton of the wafer after etching.

If we consider the top opening with one side w_t and the corresponding side at the bottom

as w_b, then they are related to each other through the etching angle by $W_t = w_b - 2\,h \cot 54.7\,^{\circ}$,

where h is the thickness of the silicon wafer.

4.2   Mask design

For the lithography and fabrication of microstructures, four layers of masks were

designed by using *LAyout System for Individuals* (LASI) software. Each layer of mask was

designed with specific purpose which are discussed and shown in Appendix A (II). Figure 4.2

shows the unit cell of mask layers.

4.2.1 Unit cell of all layers

(a)   (b)   (c)

(d)
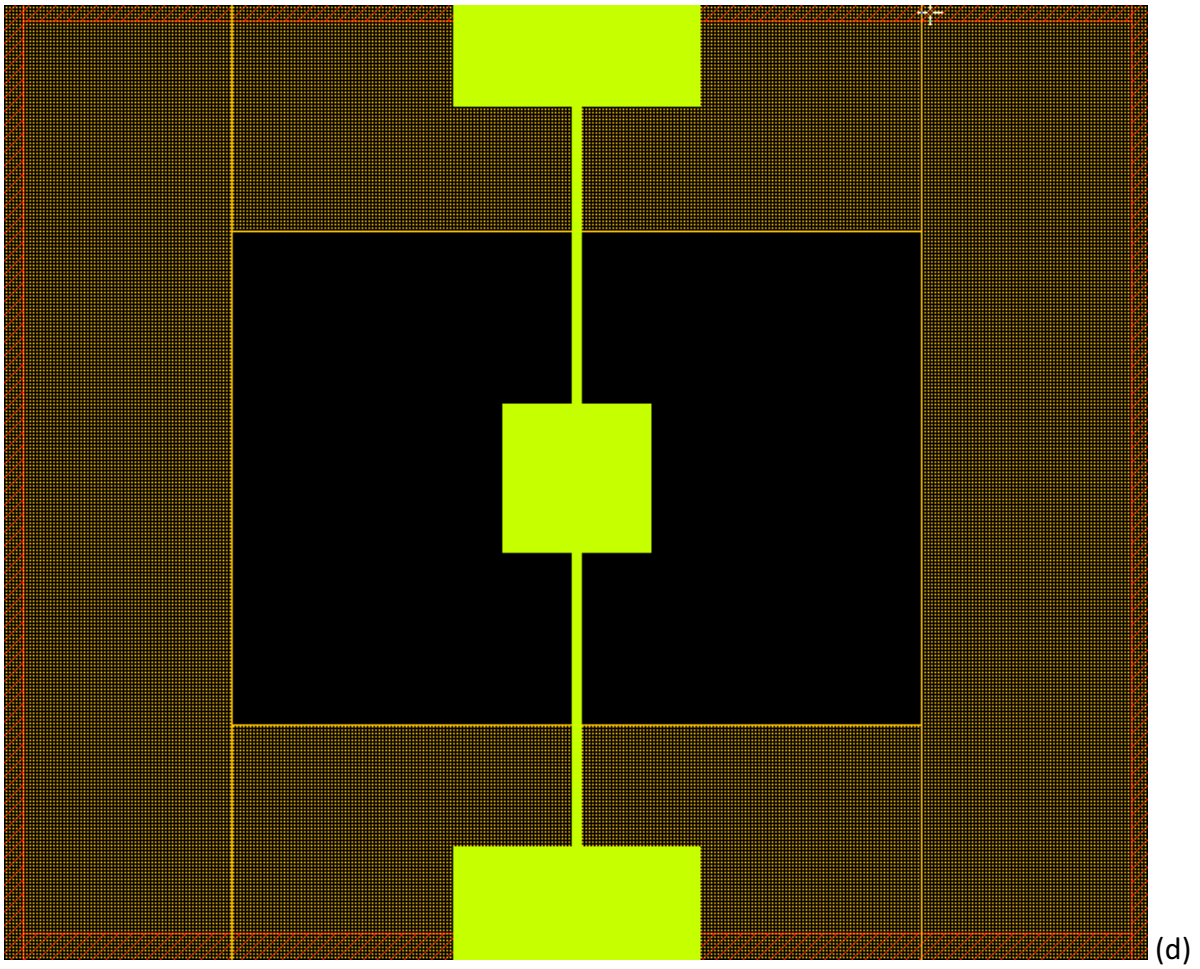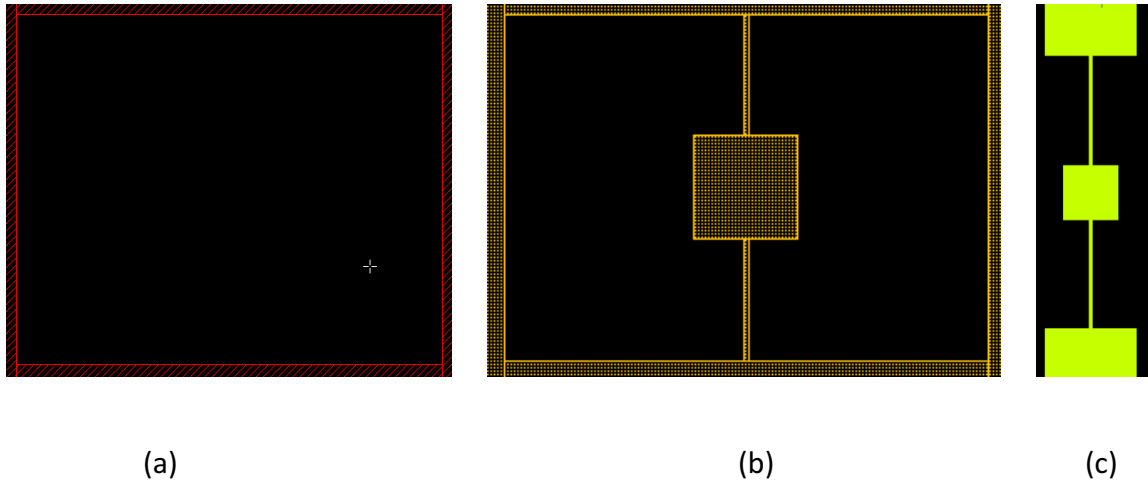
Fig. 4.2 Unit cell of design of mask (a,b and c: separate layers; and d: all layers together)

4.2.2 Design of four dies and trench

It would be useful to put four dies on single wafer from cost –viewpoint and for more yield of the micro structures. Trench between the dies would help to separate each die in the wafer so that it would be easier to handle the mirror samples. For this purpose, trenches were designed between the dies. The trenches were designed from the bottom. As shown in Fig. 4.3 the trenches were designed to be only 100 µm deep so that the remaining 200µm wafer is still strong enough for handling during processing. The width for the trench at the bottom is determined by the relation, $x = d \tan 35.3^{\circ}$, where "d" is the depth of the trench to be etched from the bottom of the wafer (we used 300 µm thick Si wafer). This calculation gives the width of the trench-opening at the bottom as 70.8µm.
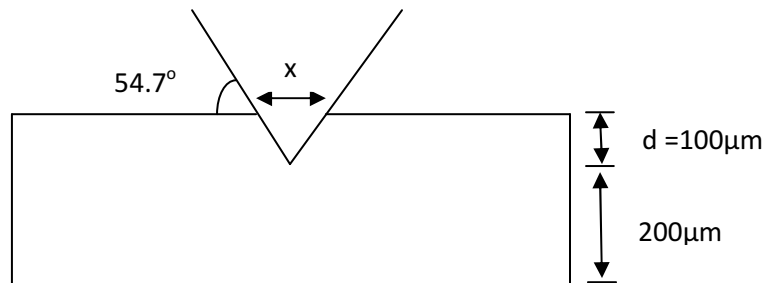
Fig.4.3 Trench design for etching from the bottom of Si wafer

4.2.3 Some important distances in the present design

The following parameters were used to use the Si wafer appropriately for the maximum yield of the micro structures, and to divide the wafer by trenches into four quadrants.

Diameter of the wafer = 4 inch = 101.6mm

Thickness of the Si wafer = 300µm

Distance between the edge to the nearest KOH etched window = 12.48mm

Distance between the trench to nearest KOH etched window = 9.36 mm

For clarity, these parameters are shown in Fig. 4.4.

9.3mm   Trench

12.4mm
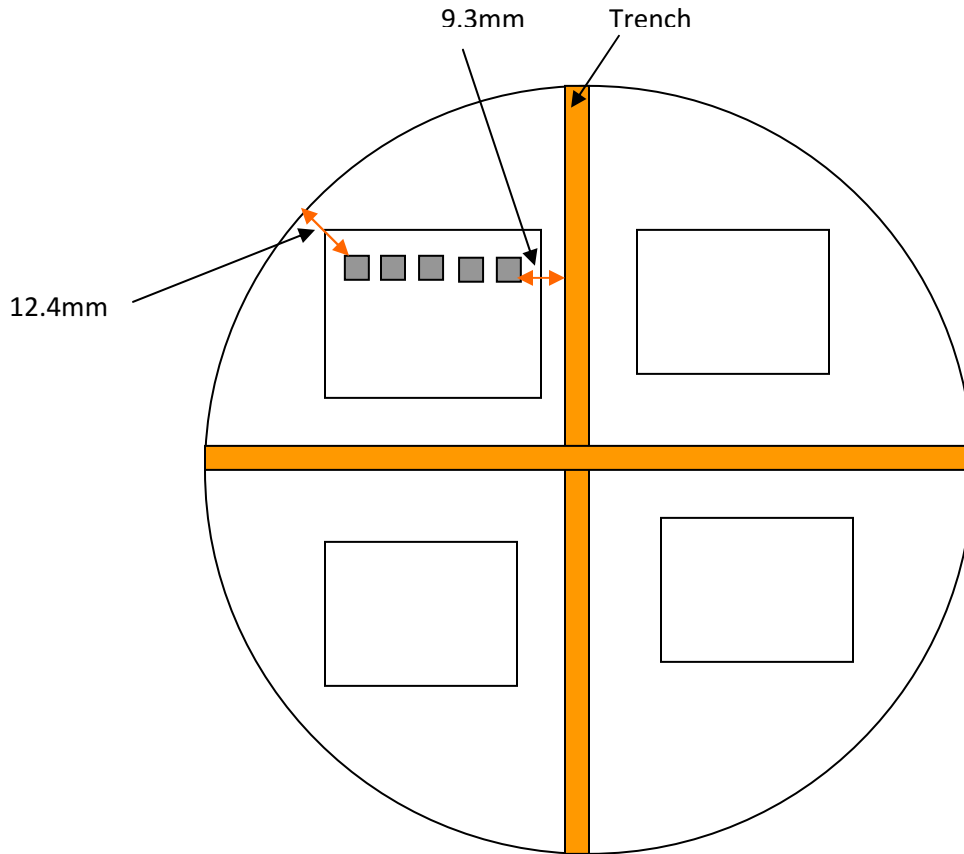
Fig. 4.4 Some important distances in the present design

4.3 Fabrication Steps of Silicon Nitride freestanding mirror-beam structures with Au deposition

Photolithography was used to fabricate the freestanding structures. Low stress silicon nitride layer was made on the front and back of Si wafer. Then Au layer was deposited on the front surface. Contact photolithography was done on the back surface to mark the areas to be etched. After this, SiN on the back on these marks was etched. Photoresist stripping was done on the front in such a way that the photoresist remains in other areas than the mirror pattern. Then Si on the back was etched by KOH to open the windows and trenches. After this step, contact photolithography was done on the front on Au surface using mask Layer 2. Gold wet etch on the front was performed afterwards to leave the Au patterns. After this, silicon nitride was etched on

the front to leave gold coated SiN freestanding mirror structures. Finally, Photoresist Stripping was done to remove photoresist remaining on the top of Au pattern. The detail of micromirror fabrication steps with schematic figures is given in Appendix A (III).

4.4 Dimensions check of the yield, and thickness measurement by AFM

Optical images of some of the microstructures after fabrication are shown in Fig. 4.5.
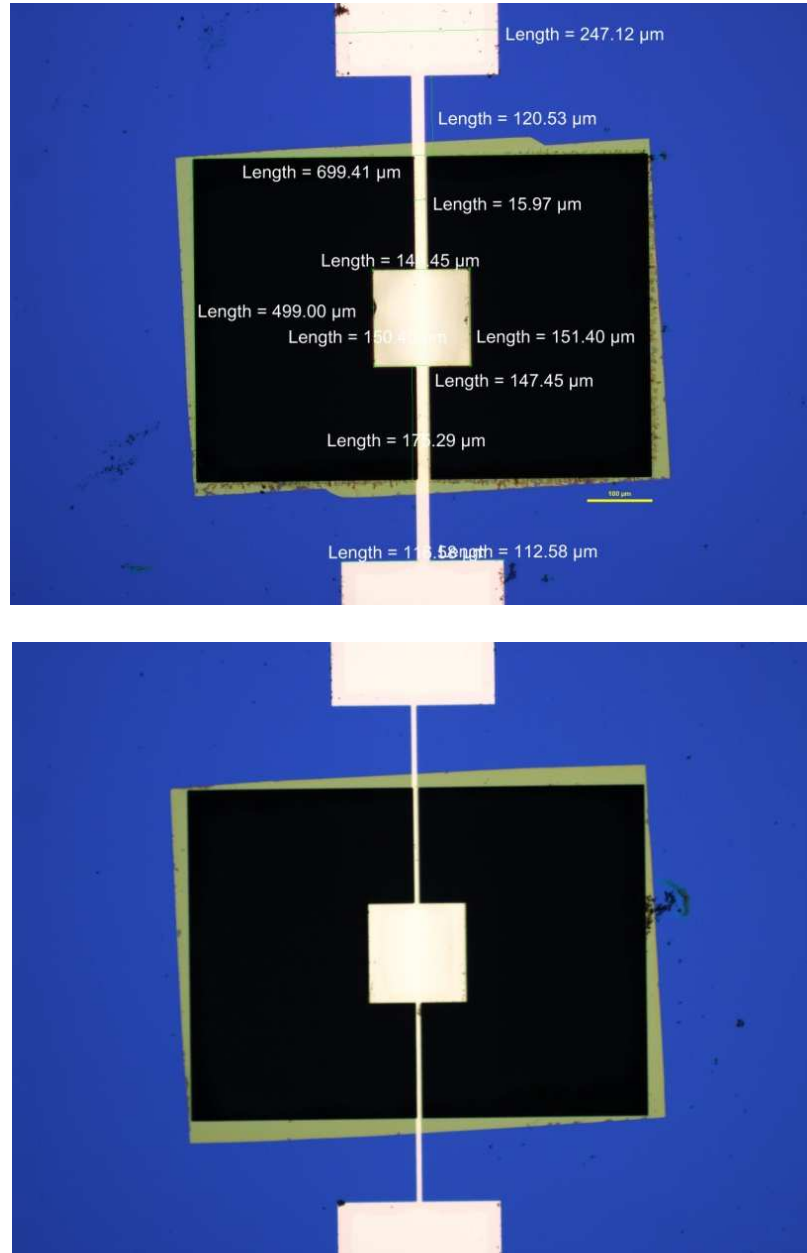
Fig.4.5 Image taken by optical microscope showing one of the micromirrors after fabrication. The figure shows the micro mirror and its supporting beams coated with Au during fabrication.

AFM was done to confirm the thickness of the Au layer. Tapping mode of AFM gave the step height of Au layer to be close to what was aimed to deposit. The Au thickness was found to be 49.53nm, i.e.495.3Å which is close to expected thickness of 500 Å. Thickness of gold was measured at different locations, e.g. on the wire, and on the contact pad. Three different thickness measured were 49.53nm, 54.63nm, and 47.72nm whose average value comes to be 50.63nm. Hence, the thickness of gold is in target thickness of 50nm within experimental errors. Fig. 4.6 shows AFM picture of thickness measurement of Au layer.
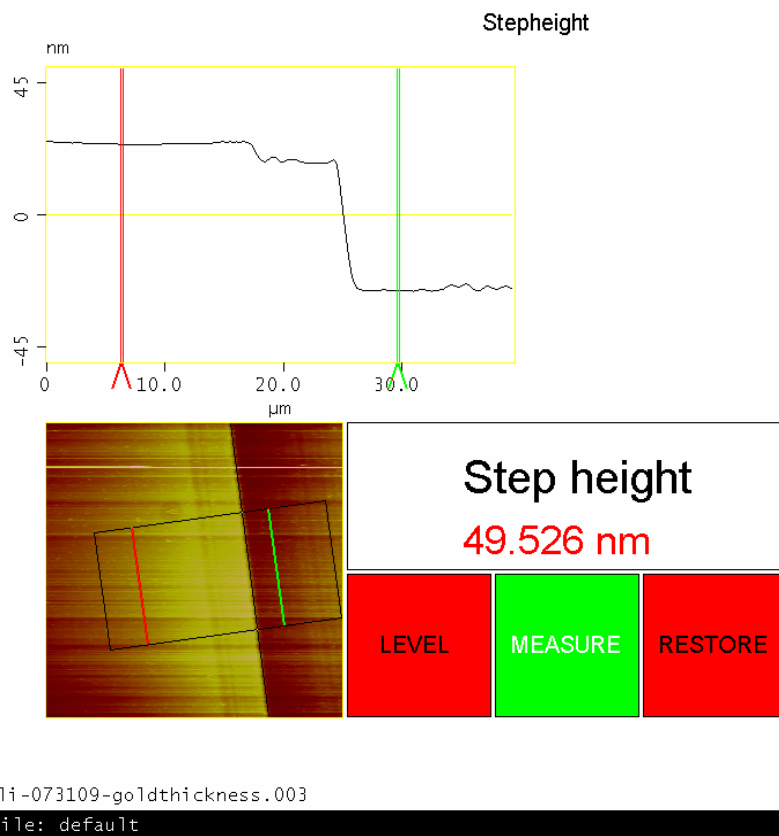
Fig. 4.6 measurement of thickness of Au layer deposition on the microstructures by using AFM

CHAPTER 5

TORSION MEASUREMENTS WITH NEWLY FABRICATED SECOND GENERATION OF MICROMIRRORS

5.1 DC voltage generation from Lock-in amplifier

An auxiliary dc output in steps was generated from Lock-in by Lab View control program. The voltage steps swinging from -3V to +3V are shown in Fig. 5.1 (a) and from +3 V to -3V are shown in Fig. 5.1 (b). The voltage goes to zero between these values.
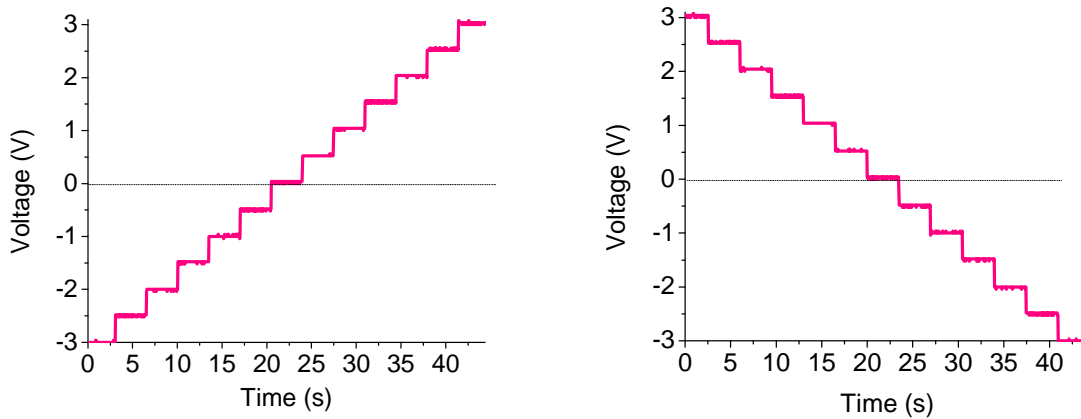
Fig. 5.1 DC voltage supplied from Lock- in at the steps of 0.5 V from (a) -3 V to +3 V; (b) +3 V to -3 V to actuate the microstructure

5.2 Response of mirrors for different input signals

Function generator was used to supply different wave forms to the microstructure to see how the output signal corresponds to the input signal type. Oscilloscope (Tektronix AFG 3021) was used to record the input and output data. Figure 5.2 shows that the output signal is square wave when the input signal, which is the actuating signal, is a square wave. This shows the proper response of photodiode signal in phase with the input signal as expected.
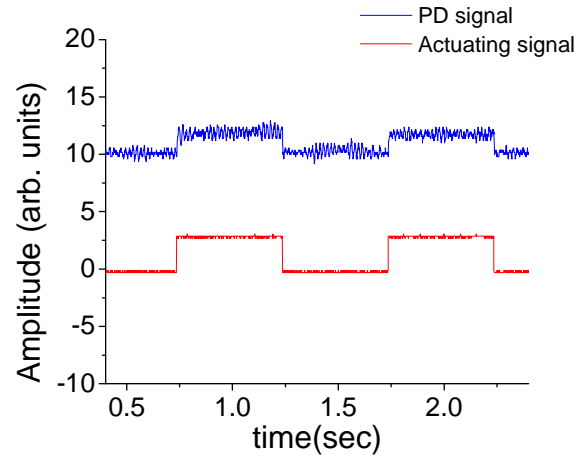
Fig. 5.2 Correlation of PD output signal due to actuation of micromirror to the actuating signal

Figure 5.3 shows that the photodiode signal when the input signal is the sine wave of frequency 1Hz from the function generator. The output signal shows that the mirror is in state 0 (Lowest voltage) when the input has zero volt. For the input voltage above zero the oscillation follows the input wave which is seen on gradual change of output signal. This means that the microstructure oscillates in correlation to the input signal as expected, and in the same direction.
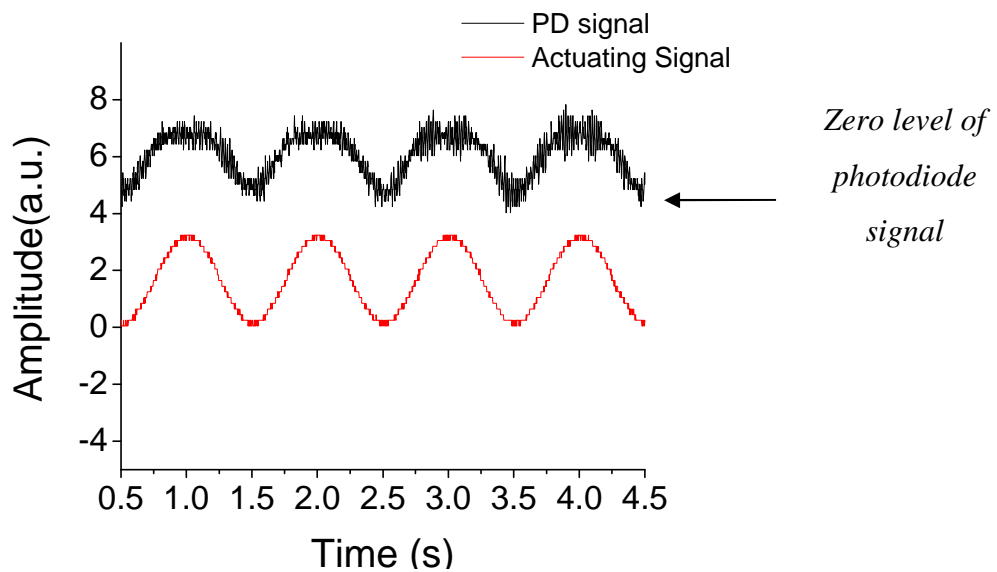
Fig.5.3 When the mirror is actuated with a sine wave, the output signal from the photodiode is in phase with with the input signal. (The input signal used has f= 1Hz)

The effect of triangular wave as actuating signal is shown in Fig. 5.4. When the input signal is at zero Volt, the mirror is in 0 state, i.e. the equilibrium state, and displaces more as the input voltage increases, and returns gradually as the input voltage decreases.
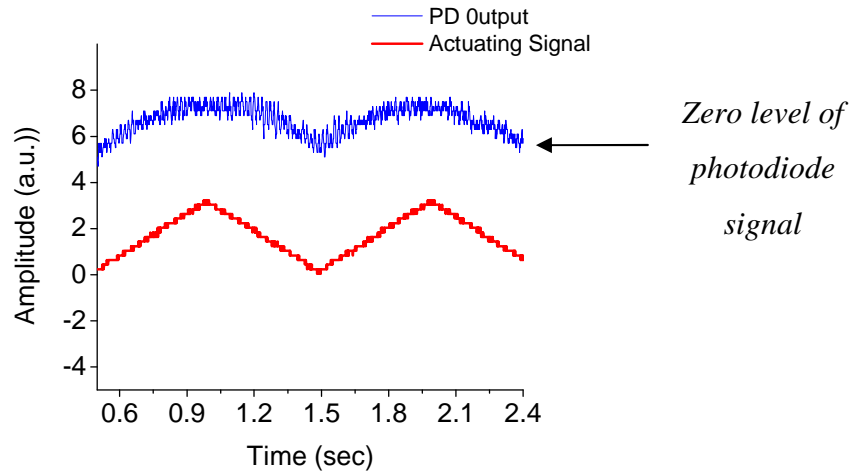
Fig. 5.4 PD signal (blue) when the actuating signal (red) is triangular wave of f = 1Hz

For the saw tooth wave as actuating signal, Fig. 5.5 shows the corresponding photodiode signal. The lowest point of output signal corresponds to zero of input signal, and for positive voltage, the rotation of mirror is represented by the output signal. These dynamical responses show that the output signals are in phase with the actuating signal.
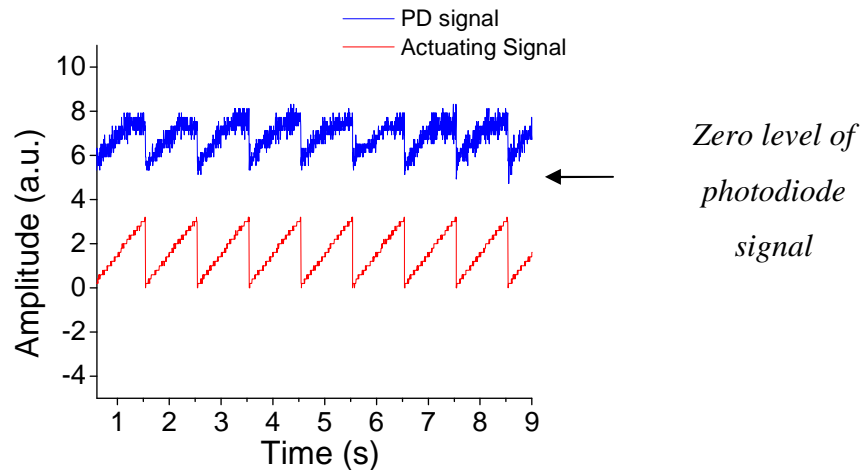
Fig. 5.5 PD signal (blue) when the actuating signal (red) is saw tooth wave of frequency, f = 1Hz

5.3 Measurements of switching time

When certain dc current is passed through the structure, it actuates from its initial state (state 0) to final state (state 1). The switching time τ of the mirror is important parameter to know. It can be hypothesized that passing current is analogous to the charging of a capacitor, and turning current off which allows the mirror go back to its initial position can be assumed analogous to discharging of a capacitor.

Experimental set up for switching time is schematically shown in Fig. 5.6. As the mirror actuates, the reflected laser from the mirror which falls on the difference photodiode is converted to electrical signal. An oscilloscope is used to record how the output voltage changes with time. Figure 5.6 is schematic for the switching time measurement.

(a)

(b)
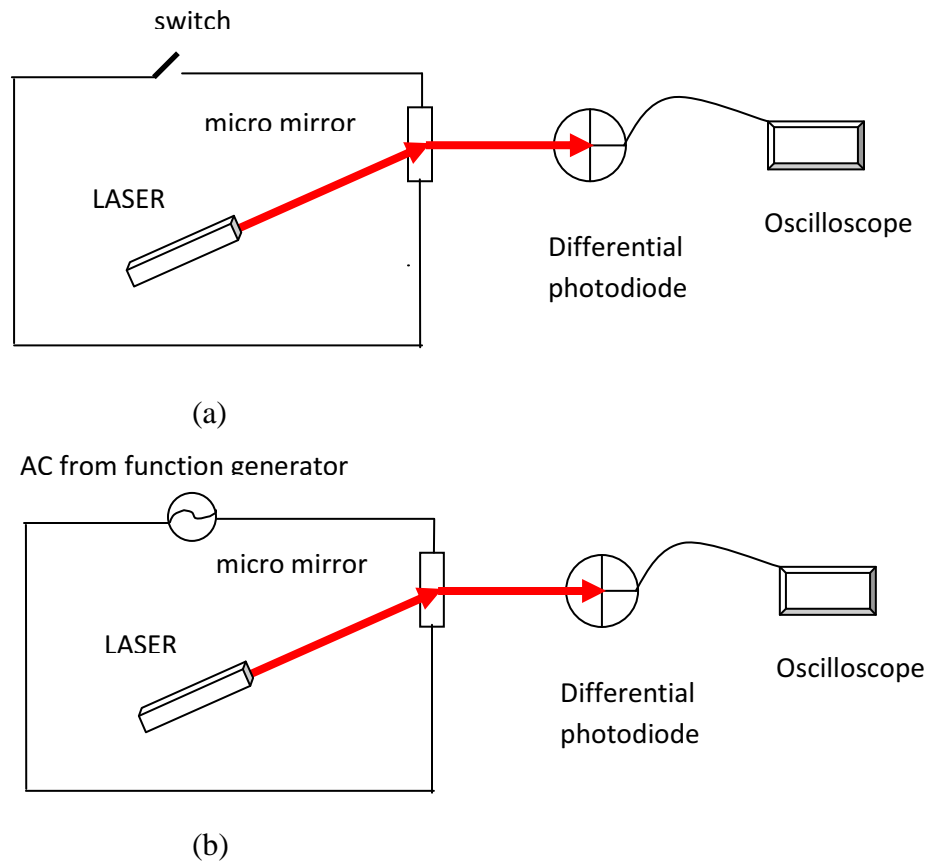
Fig. 5.6 Micromirror actuation by (a) manually, (b) ac signal from function generator

The mirror was actuated in two ways. First, it was actuated by passing dc current from current source (Keithley 2400). The data and the waveform were recorded. Again, the mirror was actuated by passing ac of certain frequency from a function generator. The data and waveforms were recorded again.

Figure 5.7 shows the output signal from the photodiode (PD) when the mirror was actuated manually. Fig 5.7 (a) shows oscilloscope screen showing the state change of the photodiode signal when the mirror goes from off (0) position to on (1) position; and Fig. 5.7 (b) shows the opposite action, i.e., from state 1 to state 0. The micromirror is stable in either state which is shown by substantially constant amplitudes in each state. Absence of oscillations after switching shows that the system is heavily/over-damped. This may be useful when 0 and 1 sate are needed by switching action in the system.

(a)   (b)
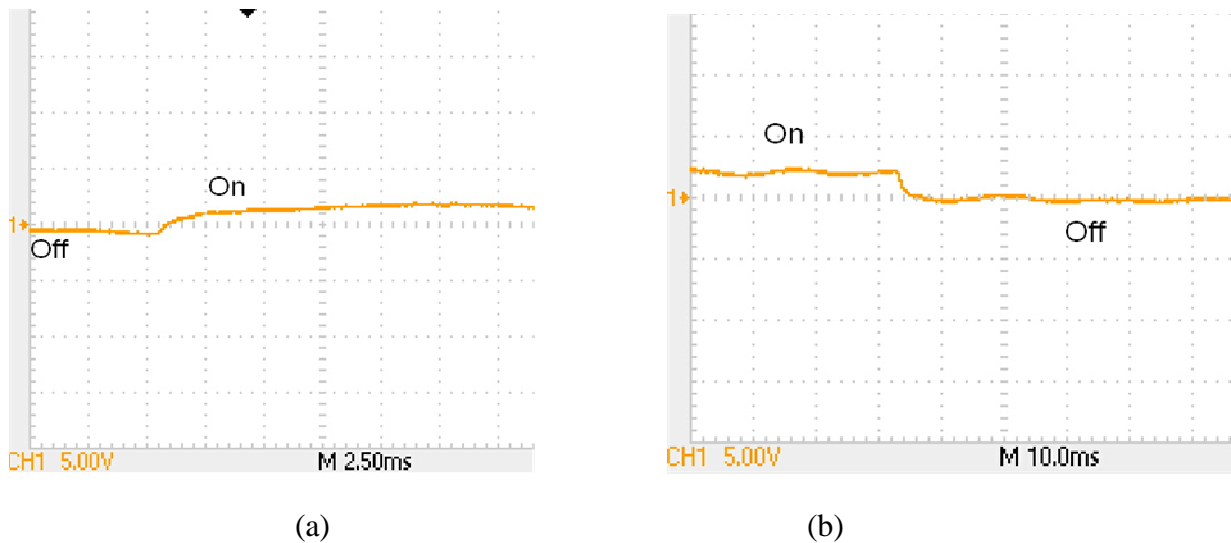
Fig. 5.7 The photodiode signal when the current supplied to actuate the micromirror is switched on and off manually, (a) when mirror goes from 0 (off) to 1 (on) position, (b) when mirror goes from 1 (on) to 0 (off) position

Switching time when the mirror actuates from 0 to 1 state can be measured quantitatively by finding the time constant of the switching action. Considering as charging a capacitor as the

mirror goes from 0 to 1 state as shown by the change in signal amplitude in Fig. 5.8, the time

constant for one of the mirrors with beam width of 20 µm is found to be 1.03ms.
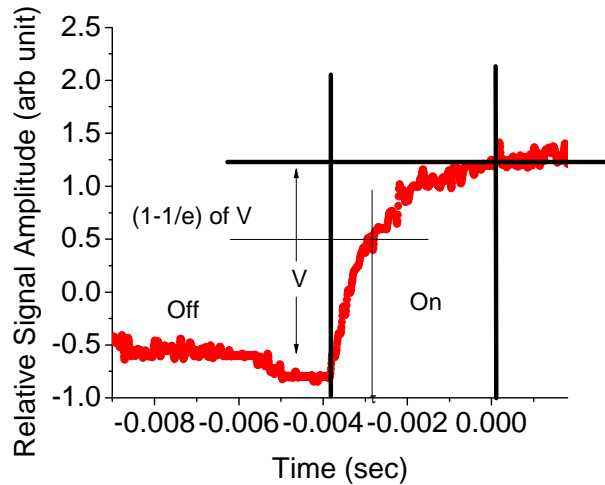
Fig. 5.8 Switching time constant of electrically actuated micromirror (beam width = 20µm) when the current is supplied turning the switch on or off manually

As a cross check, the time constant was measured by actuating the microstructure by

passing actuating signal of 1Hz from the function generator (FG). Fig. 5.9 shows the input and

output signals with the measured value of time constant of 1.17 ms.
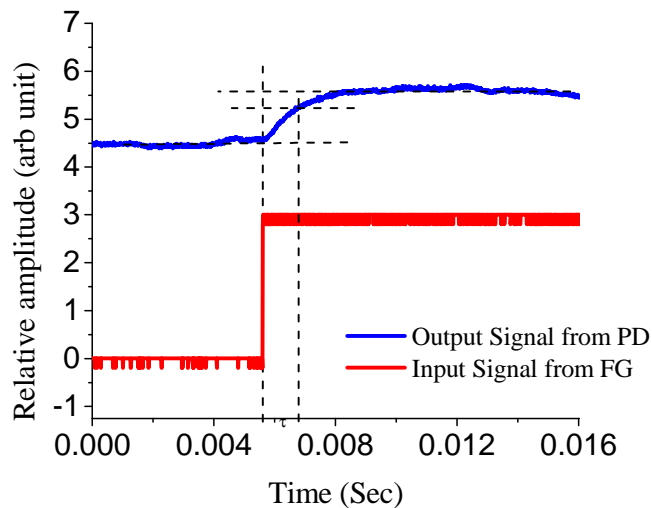
Fig. 5.9 Switching time constant of electrical actuation of micro mirror (beam width = 20 µm), while using actuating signal of 1 Hz from the function generator, time const, $\tau = 1.17$ms

5.4 Torsion angles as function of current for different micromirrors with different beam widths
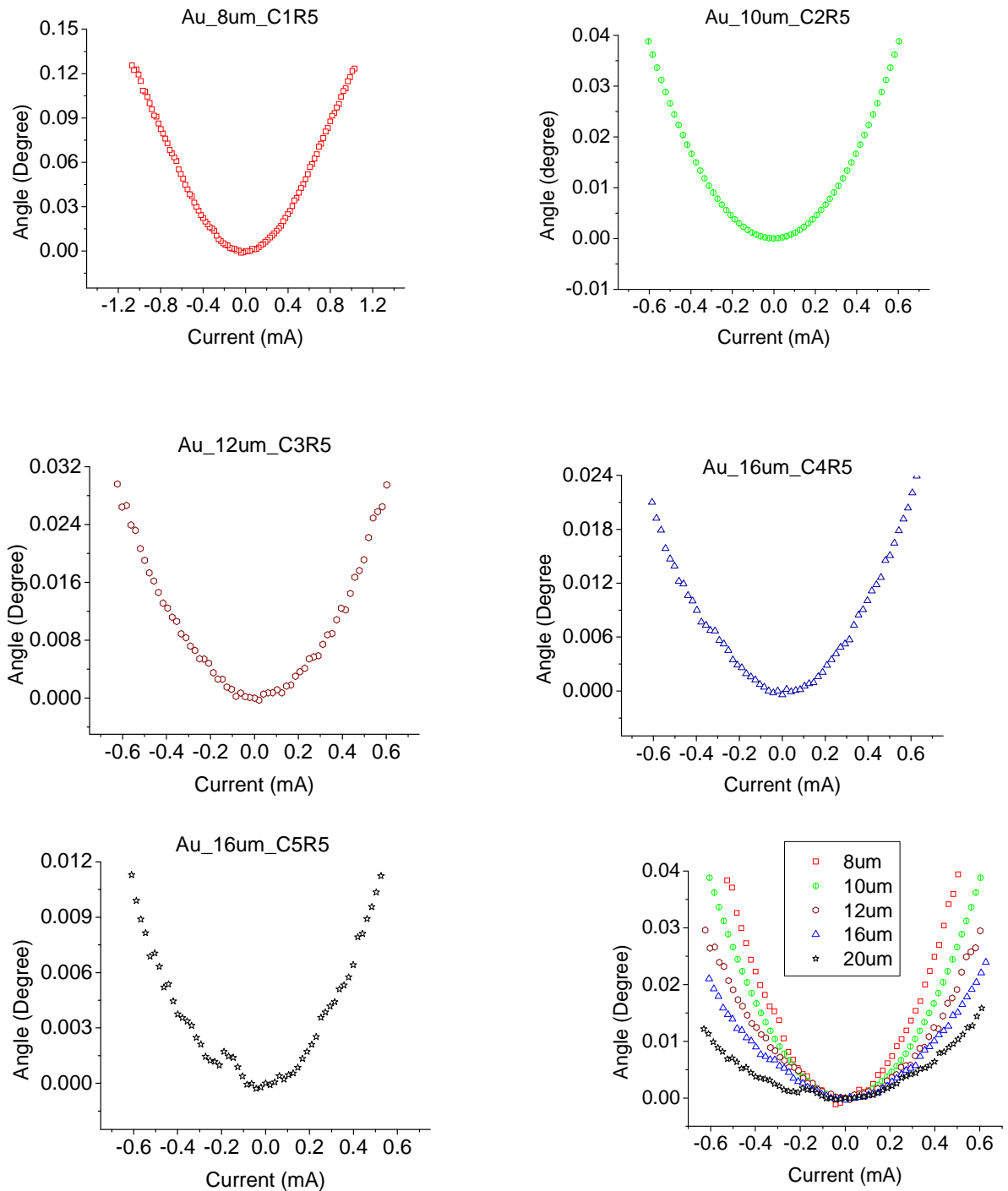
Fig. 5.10 Torsion angle as a function of Current for different beam width, b of free standing structure (Top Row→ Left: b=8µm, Right: b= 10µm; Middle Row→ Left: b=12µm, Right: b=16µm; Bottom Row→ Left: b=20µm, Right: combined plot of angles for all microstructures observed)

Figure 5.10 shows the measurement of angles as a function of current for micromirrors of beam widths 8, 10, 12 16 and 20µm. Parabolic curves show that the torque experienced by the free standing structures is in the same direction for both directions of current. It has been observed under optical microscope that the change in current direction doesn't change the torsion direction. The last of Figure 5.10 is the combined plot showing torsion angle of all the microstructures in the same scale. This shows that if the same current is passed to the microstructures of different beam widths, then the torsion produced in the structure of smallest beam width is the largest, and the torsion angle goes down as the beam width increases. The curves for 8, 12, 16 and 20µm wide beamed structure are the experimental data. They are following certain pattern, and the analysis of their curvatures can be helpful in predicting the curvature of such parabolic curves for microstructure of 150µm × 150µm, and with different beam widths. This method can be used to find torsion angle of any microstructure of this dimension but with different beam widths. After fitting these curves, we get the fitting equations. The coefficients of the quadric terms give the curvature of parabola. So, the coefficients of these quadric terms were taken, and plotted as a function of beam widths which are shown in the Fig. 5.11. The fit equation of this curve gave the relation of the coefficient (C) with the beam width (b). It was found to be: $C = 3.521 \ b^{-1.52}$, where b is in µm. The parabolic dependence of the torsion angle on the dc current that is passed to actuate the mirror allows us to write the torsion angle in degrees as $\theta = C \ I^2$. Using the above equation we can write $\theta = 3.521 \dfrac{I^2}{b^{1..52}}$, where I is in mA and b is in micrometers. This empirical relation predicts the torsion angle of micromirrors with dimensions of 150µm × 150µm but with different beam widths when current I is passed through them. Using this technique, the torque angles for the structure with 10µm beam width

has been predicted and plotted together with the experimental data as shown at the last of Fig.

5.10. This falls in the right position of the pattern for different structures.
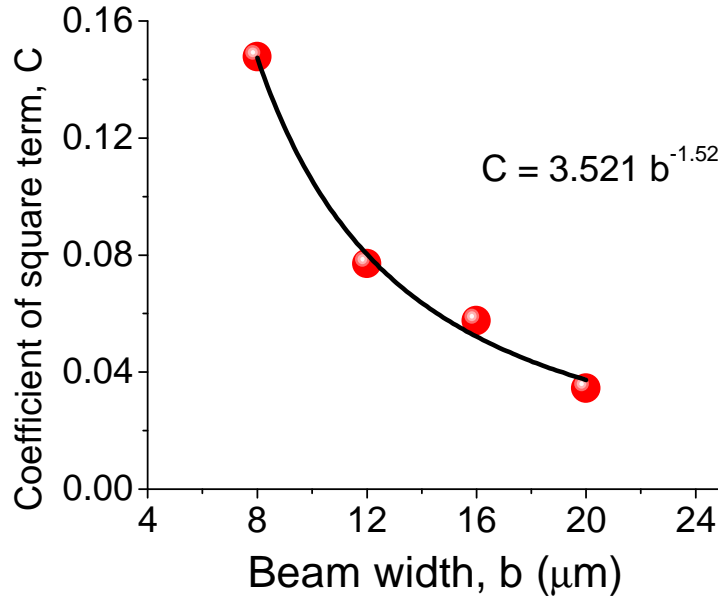
Fig. 5.11 Coefficients of quadratic terms as a function of beam width of micro structures

5.5. Torque estimation as a function of current

For rectangular torsion bar $K_\phi = \dfrac{k_1 G h^3 b}{L}$, where $k_1 = \dfrac{1}{3}(1 - \dfrac{192}{\pi^5}\dfrac{h}{b}\sum\limits_{n=1,3,5,}^{\infty}\dfrac{1}{n^5}\tanh\dfrac{n\pi b}{2h})$. In

case of narrow rectangular cross section b>>h so that this expression reduces

to $k_1 = \dfrac{1}{3}(1 - 0.63\dfrac{h}{b})$. For the experimental values of the beam widths and thicknesses, $h/b << 1$

and thus the coefficient k_1 is practically constant [Minhang Bao, 2005]. The torque produces

torsion in the torsion bars so that the mirrors actuate. Since torque is proportional to torsion

angle, and also it is proportional to acceleration, it can be said that the acceleration is

proportional to the torsion angle. Accelererometers have been developed based on this. So,

knowing torque of such micromechanical mirrors is important.

The torque $T = K_{\Phi} \cdot \Phi = 2 \times K_1 \times G \times a^3 \times b/L \times \Phi$ can be calculated for Si_3N_4 by using the value of shearing modulus $G = 1.27 \times 10^{11}\, N/m^2$, thickness of beams $a = 0.4\mu m$, beam widths $b = 8, 10, 12, 16$ and $20\mu m$, length of each beam $L = 175\mu m$, and using the values of the torsion angles measured for these microstructures. The factor 2 is introduced for two beam structures of the freestanding mirror. Since the torsion angles were measured as a function of current passed to actuate the structure, the torque can be expressed as a function of current as well. From the analysis of the coefficients C in the expression $\Phi = CI^2$ of the parabolic fits of the curves in Fig.5.11, we found that $C(b) = 3.521\, b^{-1.52}$, where b is the size of beam width in μm. This leads to the expression $T = (K_1 Gh^3 b/L)\,(3.52/b^{1.52})\, I^2$, resulting in a series of parabolic curves as shown in Fig. 5.12 with the magnitude of torque on the order of $10^{-14}\, Nm$.
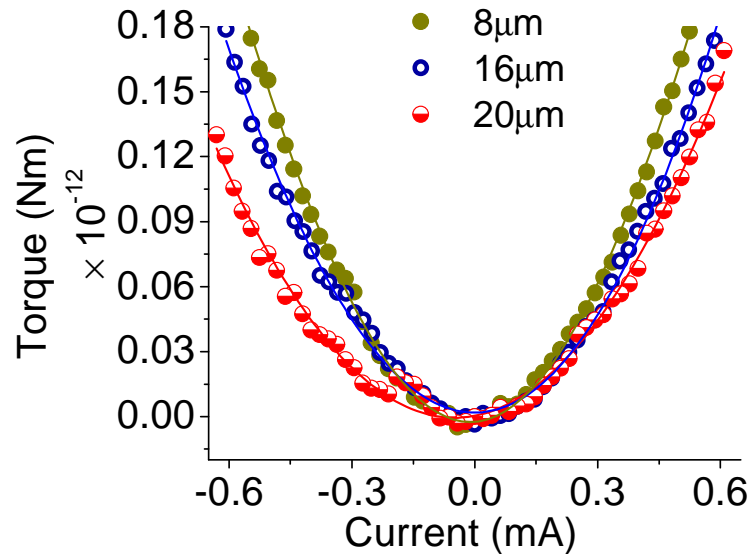
Fig. 5.12 Torque of micromechanical mirrors ($150\mu m \times 150\mu m$) as a function of actuating current.

For a given current passing through the freestanding structures of different beam widths, it would be interesting to know how the torque depends on the width of the beam. This will help to design suitable beam width of the structure depending on the need of the torque while passing

certain current. The curves shown in Fig. 5.12 indicate that the torque for a structure with a narrower beam is larger than for a structure with a wider beam (at the same current), as expected. The estimates above work well for all beam widths, except for the beams of less than 10µm wide, for which the torque calculated based on the measured values of torsion angles Φ, increases disproportionally faster compared to the structures with wider beams. In general, for constant I and for h<<b, we get T~1/ b $^{0.52}$.

5.6. Moment of inertia of microstructure as a function of beam width

For knowing the inertial resistance of the free standing micro structure to rotational acceleration, one can find the moment of inertia which, for the geometry of the micro structure with mirror plate and two supporting beams, is given by the expressions:

$$ J_{L_1} = \rho_{SiN} \frac{b^3 L_1 h}{12} + \rho_{SiN} \frac{h^3 b L_1}{12} $$

$$ J_{L_2} = \rho_{SiN} \frac{b^3 L_1 h}{12} + \rho_{SiN} \frac{h^3 b L_1}{12} \qquad (L_1 = L_2 \text{ for this design of microstructure}) $$

$$ J_{mirror} = \rho_{SiN} \frac{L^3 B h}{12} + \rho_{SiN} \frac{h^3 L B}{12} $$

Where J_{L1} = Moment of inertia for one beam with length L1, width b, thickness h;

J_{L2} = Moment of inertia for the other beam with length L2, width b, thickness h;

J_{mirror} = Moment of inertia for the mirror plate of length L and width B (in our case,

L = B) for Si_3N_4 with density of ρ_{SiN}.

For the structure being used, L1 = 175µm, L2 = 175µm, h = 0.4µm, L = 150µm, B = 150µm, and ρ_{Si3N4} = 3440 kg/m^3. Using these values the total moment of inertia of the actuating system J = J_{L1}+ J_{L2}+ J_{mirror} was calculated for five different sizes of b, viz. b = 8µm, 10µm, 12µm, 16µm and 20µm. Since $J_{L1} + J_{L2} \ll J_{mirror}$, the moment of inertia is only weakly

dependent on the beam widths, varying from 5.81×10^{-20} to 5.84×10^{-20} kg·m^2 for $b = 8\mu$m and $b = 20\mu$m respectively.

5.7 Electric Power dissipation in the mirror-beam structure

One of the reasons of actuation of free standing mirror beam structure while passing current through it could be due to electric heating that expands the structure fixed at both ends resulting its torsion. In this context, it is important to know the amount of heat dissipation in the structures of different beam widths. The resistances of the structures with Au deposition were measured which were found to be 20.048Ω, 17.568Ω, 14.721Ω, 11.163Ω, and 9.028Ω for the structures with beam widths of 8, 10, 12, 16, and 20μm respectively. The electric power dissipation, $P_n = I^2R_n$, calculated as function of current supplied, is shown in Fig. 5.13. The curves show that the power dissipation in the structures with narrower beam is greater than in the structures with wider beams. This correlates with the higher torsion angles in case of the structures with narrower beams while passing current. This correlation also serves as an additional indication of the role of thermoelectric effects in the actuation of these structures by electric current.
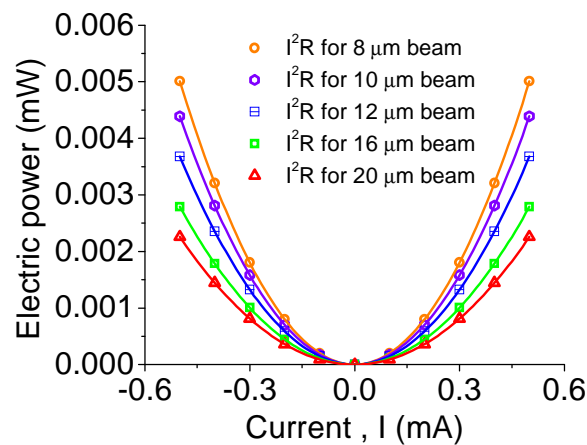
Fig. 5.13 Electric power as a function of current in the free standing mirror-beam structure

5.8   Resistance of Au layer on the microstructures as a function of beam width

Resistances of the microstructures were measured which seems decreasing with beam width b as shown in Fig. 5.14. Smaller resistance of wider beamed structures will dissipate smaller joule heating which might be one of the causes of smaller torsion angle of wider structure due to less expansion causing smaller twist of the structure.
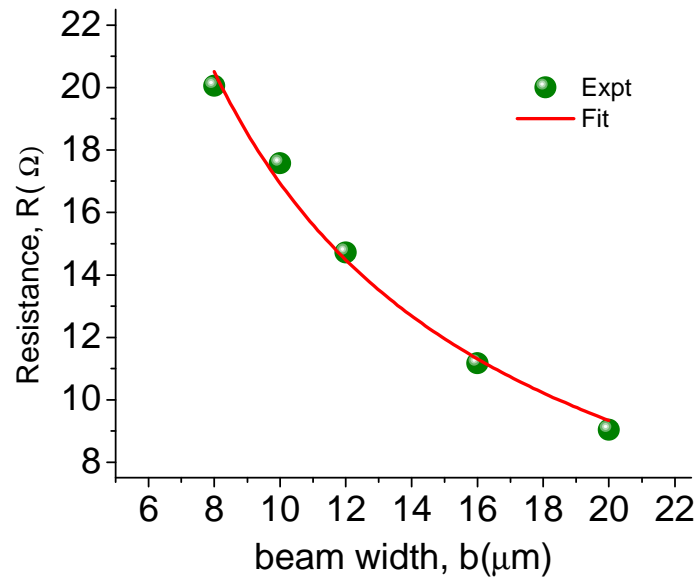
Fig. 5.14 Dependence of resistance on beam widths of free-standing structures

5.9. Torsion of freestanding microstructure in Gallium stands

One of the micro mirrors was detached from the Si wafer and was placed its two ends on Gallium at room temperature so that the microstructure stands freely, and the ends of the structure are free to move along their axes in case if the structure expands while passing current. DC current was passed starting from few micro amperes, and increasing until the structure showed some torsion. The mirror was observed under optical microscope. The structure showed clear torque when 7mA of current was passed through it. The actuation was similar to the case

when the beams of the mirror were fixed at both ends with Si wafer. When the current was passed, the microstructure would tort in one direction and when the current was turned off the structure would go back to its initial position. This was observed for repeated actuation by manually turning the current on and off.

The reason to check this qualitatively was to check if the torsion is seen when the two ends of the beam were free to move along their axes should there be any effect of expansion while passing current. It was assumed that liquid Gallium would not be able to hold the ends of the structure from moving along the axis if the structure and the beams expand. Despite this degree of freedom given to the micro structure, its tendency to show the torsion indicates that the possible expansion of the structure along the beam length due to joule heating is not the only reason, if it is suspected, for producing the torsion of the microstructure with Au coating on it. While passing current the expansion is not only linear. If we assume superficial expansion of the mirror plate, then the expansion of the mirror plate along the direction perpendicularto the beam length produces some elastic potential difference laterally which is easily released as a twist. The linear component of elongation is helpful in triggering the twist.

The observation was carried out by cooling a microstructure by touching the frame with liquid Nitrogen. When the current was passed before cooling, the twist was seen. The mirror was allowed to remain in excited state before cooling, and then while the current remained passing, the structure was cooled by touching the Si frame by liquid Nitrogen. Even after cooling, the structure didn't come back to its initial position, and it came to its initial position only after current was turned off. This adds confusion on the explanation of torsion due to heating only. However, the Joule heating might still be effective even though it was cooled by liquid nitrogen because of existing resistance, and may be the observation by naked eyes under optical

microscope cannot distinguish some change in the twist. So, there could be other reason responsible for torsion apart from joule heating. This needs further careful investigation.

5. 10   Discussion

Torsion was observed in micromechanical freestanding mirrors (preliminary samples or set A samples, with dimensions ~390 µm× 290 µm with beam width ~7µm) coated with Ni or Au or Ag when current was passed through them. It was observed and measured in another set of samples (set B samples) with the mirror size 150µm×150µm and with different beam widths (8, 10, 12, 16, 20µm), and was found that the torsion produced is bigger in the case of the samples with narrower beam widths. The torsion angles as a function of current were measured for these samples. Switching time, torque and moment of inertia were measured for the microstructures of set B samples, and they were found in the order of milli-second, 10^{-12} Nm and 10^{-20} kgm^2 respectively. The angle of torsion measured for Au sample (set A) when 38 mA of current was passed is about 26 degree. The structure with Au deposition survived until the current was 40 mA. Such a huge torsion angle is important for MEMS from the technological viewpoint. This torsion angle is much bigger than any torsion angle that could have been produced by any other known effects such as Wiedemann effect, transfer of momentum of spin, or heating effect alone [Li, 2005]. Since spin torque is supposed to be observed in hybrid wires, and such mechanical torques change sign with the electric current direction [Covalev et al., 2007], it is unlikely that the torsion we have observed is due to spin torque since the torque we observed is always in the same direction for both directions of the current. Another interesting feature in our observations is that a microstructure with deposition of only one metal, so far tested with nickel, gold and silver only, can actuate appreciably, and the angle of torsion is controllable by simply increasing or decreasing the current. The actuation of certain mirror is always in the same direction which

may be related to the asymmetric structural strength of the Si_3N_4 membrane. Once the structure is actuated it remains there stable until the current is turned off. In case of our mechanical system, there may be several sources of actuation. Contraction of Si_3N_4 due to electrostriction on applying the electric field E, and superficial expansion of metallic layer due to Joule heating on passing dc current may work together for producing effective strain which results the enhanced electromechanical performance as in hybrid actuation system [Su et al., 2004]. Since the metallic layer is constrained by Si_3N_4 layer, the nonequilibrium strain causes a deformation which finds its lowest energy after the freestanding system makes torsion by certain angle which seems dependent on the applied current quadratically. Since the electrostriction of Si_3N_4 is proportional to E^2, where E is the electric field applied to Si_3N_4, and the thermal strain on the top layer is also proportional to I^2, it is reasonable for the effective strain to be proportional to I^2, which seems the reason of why the measured torsion angles are proportional to the dc current passed through the structure. However, the applied electric field of 2 KV/m on 0.5mm long Si_3N_4 structure of electrostriction coefficient of 0.17×10^{-21} m^2/V^2 [Rattikorn et al., 2002] seems to produce a strain of 0.7×10^{-13} which may be too small to produce such a large torsion effect observed. Maxwell Stress compression may also be too small because of its small magnitude compared to the observed large torsion. Out of three effects known to produce a quadratic behavior: electrostriction, Joule heating and Maxwell Stress compression [Choi et al., 1992], the elimination or the negligible effect of electrostriction and Maxwell Stress compression leaves the third effect, the Joule heating which is mostly responsible for the actuation of such microstructures while passing current. Moreover, our observation of qualitatively similar current-induced torque in the gold and silver deposited micromirror structures makes it unclear whether and to what extent magnetic effects play a role in actuating the mirrors. However, torsion angles

can be increased easily by controlling the dc current. At this stage, the torsion angles that can be produced by passing current through micromechanical structures seem to have some potential for technological use, though the origin of such torsion is yet to be determined. Due to the high sensitivity of the photodiode as a detector, the optical measurement system we have developed may be used to measure even smaller torques, possibly the torque produced in heterostructure of magnetic and nonmagnetic materials as proposed by P. Fulde and S. Kettemann [Fulde et al., 1998]; Yu et al. [Yu et al., 2007] and Zolfagharkhani et al. [Zolfagharkhani et al., 2008].

5.11   Conclusions and future work

Nano and micro machines utilize torsion angles to operate. We have observed torsion in magnetic and non-magnetic micromirrors while passing current through the structure. Since the angle is easily controllable by dc current, such devices may be very useful. Experimentally accessible range of torsion can be used in information technology as optical switches.

To understand the cause of actuation in more detail, it will be helpful to study asymmetric mirrors, may be by cutting one side of the beams. Further understanding of torsion phenomena in these samples will be helpful for potential use of such micro structures in MEMS technology.

PART II

CHAPTER 6

SPINTRONICS: EVOLUTION AND PRESENT DIRECTION

6.1   Introduction

The term "spintronics" was coined by S.A.Wolf in 1996 for spin electronics. Its research relies on the results obtained in diverse areas of physics such as magnetism, semiconductor physics, superconductivity, optics and mesoscopic physics; and establishes new connections between its different subfields. It involves the study of active control and manipulation of spin degrees of freedom in solid-state systems (Zutic et. al., 2004). The control of spin is a control of either the population and the phase of the spin of an ensemble of particles, or a coherent spin manipulation of a single or a few-spin system. The research in this area tends to find an effective way to polarize a spin system, measure the time for which the system is able to remember its spin orientation, find a way to detect spin, and investigate the spin polarized transport in electronic materials. Study of spin transport properties can lead to the knowledge of spin polarization of a material. In this dissertation, Point Contact Andreev Reflection Spectroscopy has been used as a useful technique to study spin polarization of various materials with potential for the use in spintronic applications.

Electronic devices are traditionally based on the charge of an electron. Intel co-founder Gordon Moore (Moore, 1965) indicated that the number of transistors in a chip doubles every 24 months. In this situation, the size of transistors should be reduced to make small and portable electronic devices. Not only reducing the size, but also improving the performance of transistors is important. With the advancement of electronic technology, the desire and need to increase the data processing speed, information storing capacity, low power consumption, and miniaturization of electronic devices has inspired researchers to develop new technology with

such capabilities. Use of the spin properties of electrons would enable researchers achieve these goals. Adding spin degree of freedom would help to control current, based on the degree of spin orientation. The devices based on spin would be nonvolatile and faster in data processing. They consume less electric power and have increased integration densities compared with conventional semiconductor devices (Wolf et. al. 2001). It is envisioned that merging of electronics, photonics, and magnetic will lead to spin based multifunctional devices such as spin-FET (field effect transistor), spin-LED (Light emitting diode), spin-RTD (resonant tunneling device), optical switches operating at terra-hertz frequency, modulators, encoders, decoders, and quantum bits for quantum computation and communication (Wolf et. al. 2001).

6.2   Spintronic devices

6.2.1   Magnetoresistance

Anisotropic magnetoresistance in bulk ferromagnets such as Fe and Ni was observed first by Lord Kelvin (Thomson, 1857). He found that in presence of magnetic field the resistance of iron was different, and it was bigger if the current was flowing in the direction of the field and was smaller if the current was flowing perpendicular to the field. The difference in electrical resistivity was due to spin-orbit interaction. The magnetoresistance is defined as R_{ap}-R_p/R_p or R_{ap}-R_p/R_{ap}, where R_{ap} is the antiparallel state resistance and R_p is the parallel state resistance. The better known magnetoresistance was ~1%.

6.2.2   TMR

Concept of spin polarized transport became important to understand magnetoresistance. Mott (Mott 1936a, b) realized that at sufficiently low temperatures, where magnon scattering becomes vanishingly small, electrons of majority and minority spin, with magnetic moment parallel and antiparallel to the magnetization of a ferromagnet, respectively, do not mix in the

scattering processes (Zutic et. al., 2004). After series of tunneling experiments by different people (Kasuya and Yanase, 1968; Esaki et al., 1967) to understand the spin polarized transport, Jullier`e (1975) measured tunneling conductance and formulated a model for a change of conductance between the parallel (↑↑) and antiparallel (↑↓) magnetization in the two ferromagnetic regions F1 and F2, as shown in Fig. 6.1. The corresponding tunneling magnetoresistance (TMR) in an F/I/F magnetic tunnel junction (MTJ) is defined as

$$TMR = \frac{\Delta R}{R_{\uparrow\uparrow}} = \frac{R_{\uparrow\downarrow} - R_{\uparrow\uparrow}}{R_{\uparrow\uparrow}} = \frac{G_{\uparrow\uparrow} - G_{\uparrow\downarrow}}{G_{\uparrow\downarrow}},$$

where conductance G and resistance R=1/G are labeled by the relative orientations of the magnetizations in F1and F2. This model showed that the resistance of a device can be manipulated by the relative orientation of magnetization of F1 and F2.
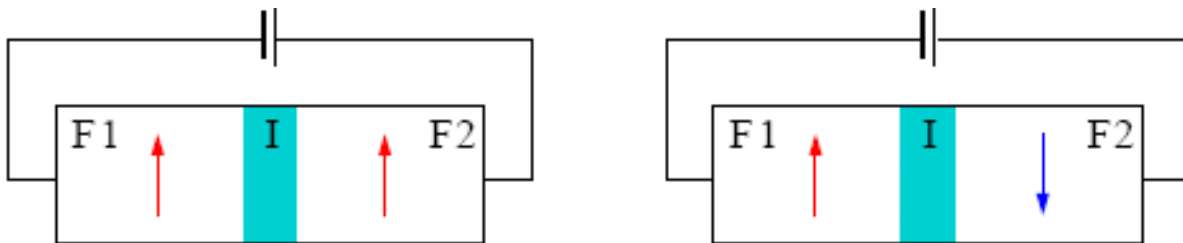
Fig. 6.1. Illustration of electron tunneling in F/I/F tunnel junctions: (a) parallel and (b) antiparallel orientations of magnetizations in ferromagnetic metals (arrows in ferromagnets represent the majority spin-subbands) (Zutic et. al. 2004).

6.2.3 GMR

Spin based electronics started after the discovery of giant magnetoresistive effect (GMR) in 1988. Albert Fert and Peter Grünberg made a sandwitch of a nonmetal between two ferromagnetic layers and observed that, in presence of small magnetic field (100 to 1000 Oe), the resistance of the system was smaller if the magnetic moments of the ferromagnetic layers were parallel, and it was larger in the case when the magnetic moments of the ferromagnetic layers were antiparallel. This was true for both the configurations of whether the current is in plane

(CIP) or the current is perpendicular to the plane (CPP). They called this property the GMR ("giant" for reflecting the magnitude of the effect more than ~10%). Multilayered structures of GMR can be used for non-volatile memory applications (Hartman (Ed.), 2000; Hirota et al., 2002; Parkin, 2002). Schematics of such multilayered structures are shown in Fig. 6.2. Many read heads for magnetic hard-disc drives are based on GMR. IBM launched the first commercial read heads based on GMR in 1997. This technology is being used in nearly all computers worldwide. It is also being used in some digital cameras and MP3 players. Though many spintronic applications are based on GMR effects, tunneling magneto resistance devices are potential candidates for several MRAM prototypes (Parkin et al., 1999; Tehrani et al., 2000) due to discovery of room temperature large TMR in them and researchers' renewed interest in them (Miyazaki and Tezuka, 1995; Moodera et al., 1995).
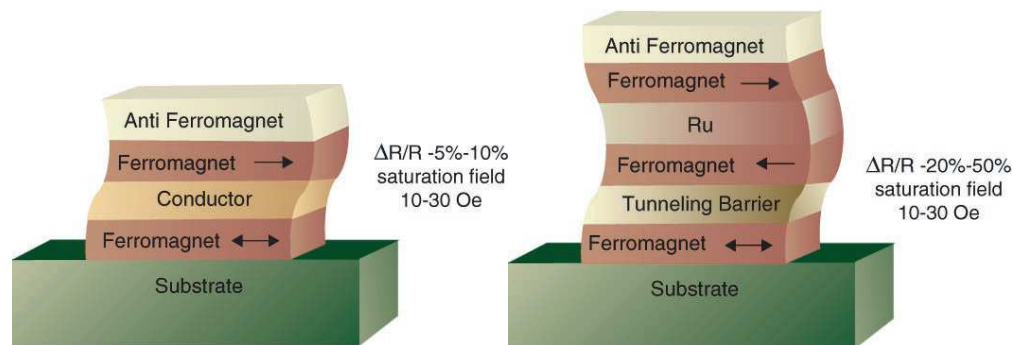
Fig. 6.2. GMR and TMR structures for spin dependent transport (a) spin valve, (b) magnetic tunnel junction (Wolf et al., 2001)

6.2.4 Magnetoresistive random access memory (MRAM)

Magnetoresistive random access memory (MRAM) has added features on semiconductor RAM chip. It stores information based on the direction of magnetization, and can readout the information based on magnetoresistance. MRAM can retain data even when the power is off. It has one thousand times faster write time than electrically erasable programmable read-only

memory (EEPROM) and flash memory, and has no wearouts with writing cycles and consumes less energy. Their data access timings are 10,000 times faster than that of hard drives (Wolf et al., 2001). Even though the GMR was discovered in the late 1980s and TMR was discovered in the early 1990s, it took several years for their improved performances for realizing in technology. Prototype of MRAM was announced in 2003, its first commercial product started to ship in 2006 (Engel et. al., 2005). Today 180- and 90-nm standalone MRAM products are finding more and more applications in various areas where their unique features of being nonvolatile fast and of unlimited endurances are vital: satellite applications, automotive data recorders, industrial controls, etc. Efforts are ongoing to scale MRAM technology to 65 nm for both standalone and embedded applications (Wolf et. al., 2010).
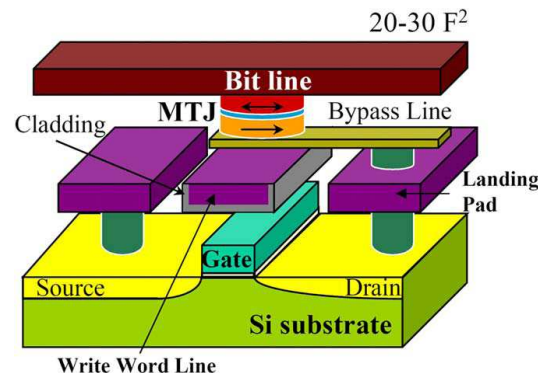
Fig. 6.3. Schematic drawing of MRAM (Wolf et al., 2010)

6.2.5   Spin transfer torque random access momory (STT-RAM)

New memory devices should have smaller and denser memory sizes with lower power consumption. However, conventional MRAM has a drawback of the need of increased switching current as the size is scaled down. To circumvent this problem, and with simpler architecture and manufacturing than conventional MRAM, a different memory called the spin transfer torque random access memory (STT-RAM) was proposed theoretically in 1996; and first demonstrated,

though the switching current density was high, in metallic spin valve thin film (Slonczewski et al., 1996; Pufall et al., 2003). Spin polarized current is applied vertically through the magnetic tunnel junction (MJT) element in STT-RAM. SONY Corporation demonstrated STT-RAM test chip in 2005 for the first time (Hosomi et al., 2005); and Hitachi and Tohoku University demonstrated a circuit design for 2 Mb- STT-RAM chip in 2007 (Kawahara et al., 2007). Recent report was even lower writing current on 50-nm perpendicular MTJ dots (Kishi et al., 2008) and 45-nm STT-RAM chips on CMOS (complementary metal-oxide-semiconductor) platform using in-plane MTJ films (Lin et al., 2009). The writing current scaling with the size of MTJ element is shown in Fig. 6.4.
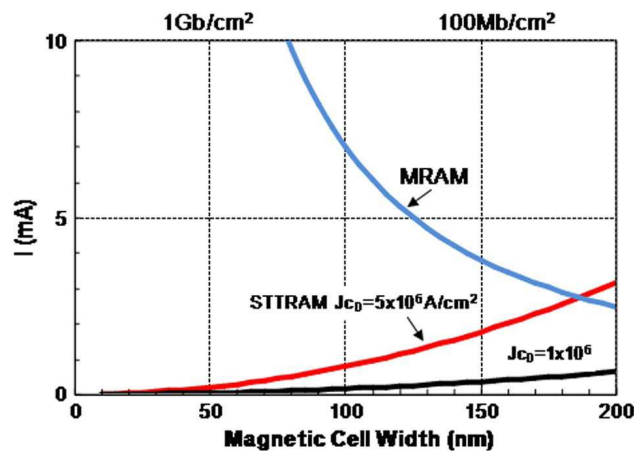
Fig. 6.4. MRAM and STT-RAM in terms of writing current scaling trend (Wolf et al., 2010)

Because of size challenge of SRAM, DRAM, and Flash beyond less than 45nm, and high power consumption of SRAM, need of refreshing of DRAM, and limited endurance and slow write speed of Flash memory, STT-RAM may also work as a replacement for storage class memory with all the major benefits (fast, nonvolatile, no wear-out mechanisms, unlimited endurance and scalability to sub-10-nm nodes). It is assumed that STT-RAM after incorporating in mobile applications can dramatically reduce power by up to 75%. The comparison of performance of different memory devices is shown in table 6.1.

Table 6.1. Comparison of performance of different memory devices (SRAM = DRAM = Flash (NOR) = parallel, Flash (NAND) = series, FeRAM = MRAM = magnetoresistive random access memory, PRAM = STT-RAM = spin transfer torque random access memory, (Wolf et al., 2010)

	SRAM	DRAM	Flash (NOR)	Flash (NAND)	FeRAM	MRAM	PRAM	STT-RAM
Non-volatile	No	No	Yes	Yes	Yes	Yes	Yes	Yes
Cell size (F^2)	50–120	6–10	10	5	15–34	16–40	6–12	6–20
Read time (ns)	1–100	30	10	50	20–80	3–20	20–50	2–20
Write / Erase time (ns)	1–100	50 / 50	1 µs / 10 ms	1 ms / 0.1 ms	50 / 50	3–20	50 / 120	2–20
Endurance	10^{16}	10^{16}	10^5	10^5	10^{12}	$>10^{15}$	10^{10}	$>10^{15}$
Write power	Low	Low	Very high	Very high	Low	High	Low	Low
Other power consumption	Current leakage	Refresh current	None	None	None	None	None	None
High voltage required	No	2 V	6–8 V	16–20 V	2–3 V	3 V	1.5–3 V	<1.5 V
	Existing products						*Prototype*	

6.2.6   Spin transistor

With semiconductor region in one side, and with the aim to integrate spin and charge transport within traditional devices such as junction and field-effect transistors, several spin transistors have been proposed. Spin transistors that contain metallic as well as insulating regions have been proposed (Datta and Das, 1990; Johnson, 1993; You and Bader, 2000; Bauer et al., 2003; Zvezdin et al., 2003). Also, single electron transistors have been proposed and investigated (Datta and Das, 1990; Ono et al., 1996; Barnaś and Fert, 1998; Korotkov and Safarov, 1999; Ciorga et al., 2002; Martinek et al., 2002).

Datta-Das spin field effect transistor (SFET) (Datta and Das, 1990) is a prototypic spintronic device, which has, as in field effect transistor (FET), a drain, a source, a narrow channel, and a gate for controlling the current as shown in Fig. 6.5. But the difference in SFET is the presence of ferromagnetic metals or semiconductors with parallel magnetic moments as

source and drain acting as the injector and detector of electron spins. Electrons are injected from the source with wave vector **k**. When the electrons pass ballistically through the narrow channel (made of GaAs/InAlAs in a plane normal to **n**) , their spins precess about the precession vector Ω because of the effective magnetic field produced in the direction Ω as shown in Fig. 6.5 due to the electrostatic potential of the gate, and due to the spin-orbit coupling in the substrate material. Only the spins which have the same direction as the spins at the drain are allowed to enter to the drain (ON), otherwise they are scattered away (OFF). By controlling the gate voltage, the electron spins can be controlled to be parallel or antiparallel or anything in between as compared to the spins at the drain. This results the control of the current. For an example, the current is large if the electron spin at the drain is pointing the initial direction as shown in top row, and it is small if the spin is pointing the opposite direction as shown in bottom row in Fig. 6.5.
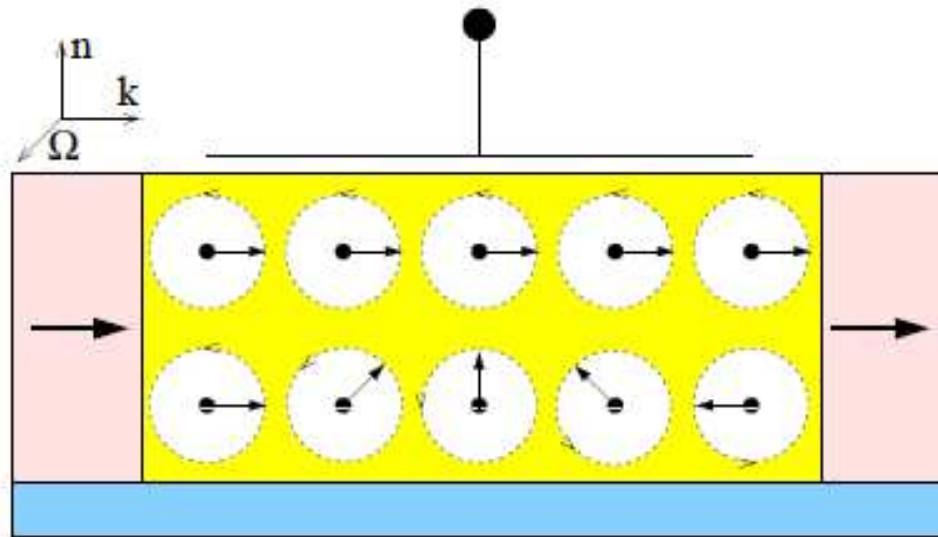
Fig. 6.5. Scheme of Datta-Das spin field effect transistor (SFET) (Zutic et al, 2004)

6.3 Creating non equilibrium spins

Non equilibrium spins at Fermi level are necessary in a material so that its spin polarization is high as needed for technological use of such materials for injecting spins and

getting spin polarized current. Such nonequilibrium can be created by different techniques such as transport, optical and resonance methods. Traditionally, electron spins can be oriented by transferring angular momenta of circularly polarized photons. However, electrical spin injection is more desirable for device applications. Magnetic electrode is connected to the sample as a source for spin injection. When current is passed, it drives the spin polarized electrons from the magnetic electrode to the sample so that nonequilibrium spins accumulate at the sample. Spin relaxation, which is the process of bringing the nonequilibrium spin population back to equilibrium, determines the rate of spin accumulation. Spin relaxation time is determined by spin-orbit coupling and momentum scattering, and it ranges from picosecond to microsecond. Spin detection is done by sensing the change in signal due to nonequilibrium spin.

6.4   Spin Injection

There are different ways of spin injection. They can be injected to nonmagnetic metal from ferromagnetic material at the interface (F/N junction). Its theory was first offered by Aronov (1976b). The theory was extended to F/N/F junctions. For efficient spin injection it is expected that the F and the N regions should have different band structure which would contribute to a significant contact resistance (Zwierzycki et al., 2003). In the interface between ferromagnetic material and semiconductor a space charge region such as depletion layer in p-n junction or Schottky contact is developed. Non-self-consistent analyses of a Schottky barrier spin injection were performed (Albrecht and Smith, 2002, 2003; Prins et al., 1995), while Osipov and Bratkovsky (2003) proposed an efficient spin injection method using a δ-doped Schottky contact.

6.5   Spin polarization

Knowledge of spin polarization in a material is important for its technological use. Development of highly spin polarized material, such as half metal is essential for successful

implementation of spintronics in technology. So, it is important to have the knowledge of the measurement of spin polarization. Next chapter will give emphasis on spin polarization, its measurement techniques, and special attention will be given to Andreev Reflection spectroscopy which is used for measuring spin polarization of various materials in this study.

CHAPTER 7

SPIN POLARIZATION MEASURING TECHNIQUES WITH EMPHASIS ON ANDREEV REFLECTION SPECTROSCOPY

7.1   Spin Polarization: Development and definitions

Not only the electrons, but also holes, nuclei and the excitations can show polarization. Electrons have intrinsic angular momentum called spin whose degree of alignment in a given direction gives their spin polarization which is defined in several ways depending on the regime of electron transport in a given material. Based on the density of states of majority and minority carriers at Fermi level, the spin polarization is defined as

$$P_N = \frac{N_\uparrow - N_\downarrow}{N_\uparrow + N_\downarrow},$$
(7.1)

where $N_\uparrow$ and $N_\downarrow$ are the electronic density of states (DOS) of majority and minority carriers at Fermi level. This "N"-definition, P_N, can be typically probed by spin-polarized photoemission technique. Its usefulness is limited by the fact that the transport phenomena usually are *not* defined by the DOS alone. This limitation is particularly true for materials which have both heavy *d*-electrons and light *s*-electrons at the Fermi level (e.g., Ni). While the DOS is mostly defined by the former, the electric transport is primarily due to the fast *s* electrons [Mazin, 1999]. In order to compare the calculations with the experimental data it is crucial to make sure that a proper definition of the DSP is used.   For instance, the tunneling spin polarization (P_T) determined by weighted average of DOS and tunneling matrix elements ($T_{\uparrow\downarrow}$) which are functions of the Fermi velocities as defined in equation 7.2 is not the same as P_N as defined by equation 7.1.

$$P_T = \frac{N_\uparrow(E_F)\left|T_\uparrow(E_F)\right|^2 - N_\downarrow(E_F)\left|T_\downarrow(E_F)\right|^2}{N_\uparrow(E_F)\left|T_\uparrow(E_F)\right|^2 + N_\downarrow(E_F)\left|T_\downarrow(E_F)\right|^2}$$
(7.2)

In terms of separate current densities $J_{\uparrow(\downarrow)}$ for spin up and spin down electrons, the DSP can be defined [Mazin, 1999] as DSP = $(J_{\uparrow}-J_{\downarrow})/(J_{\uparrow}+J_{\downarrow})$, where $J_{\uparrow(\downarrow)}$ is proportional to $NV^2_{\uparrow(\downarrow)}$ $\tau\uparrow(\downarrow)$ which on assuming the same relaxation time for both spins leads to a new "P_{Nv}^2" definition of spin polarization given by

$$P_{Nv^2} = \frac{\langle Nv^2\rangle_{\uparrow} - \langle Nv^2\rangle_{\downarrow}}{\langle Nv^2\rangle_{\uparrow} + \langle Nv^2\rangle_{\downarrow}} \qquad (7.3)$$

This new definition is for diffusive (or Maxwell) regime in which the electron mean free path (λ) is smaller than the ferromagnetic- superconductor contact size (d). Another definition for spin polarization comes from Sharvin derivation with the assumption that an electron going through the contact experiences the acceleration by the electric field so that its energy increases [Mazin, 1999]. This assumption leads to the expression that J is proportional to <Nv>, so that the third definition for spin polarization, for the case of ballistic (or Sharvin) transport in which the electron mean free path (λ) is bigger than the superconducting contact size, comes to be

$$P_{Nv} = \frac{\langle Nv\rangle_{\uparrow} - \langle Nv\rangle_{\downarrow}}{\langle Nv\rangle_{\uparrow} + \langle Nv\rangle_{\downarrow}} \qquad (7.4)$$

Half-metallic magnets do not have any electrons at the Fermi level in one of the two spin channels so that they have 100% spin polarization. For regular magnetic metal, which has Fermi surfaces in both spin channels, it is not obvious *a priori* how to define the degree of spin polarization. However, the estimate of the transport regime by Zeeman Formula

$$\sigma_{\uparrow(\downarrow)} = 1/3e^2 N_{(\uparrow\downarrow)} v^2_{F(\uparrow\downarrow)}\tau \qquad (7.5)$$

and Wexler's formula [Wexler, 1966],

$$R_c \approx 4\rho L/3\pi d^2 + \rho/2d \qquad (7.6)$$

gives the idea of experimental conditions of transport, which can be compared with the theoretical calculations based on the definitions of spin polarization.

7.2 Spin polarization measurement techniques

There are different techniques capable of measuring spin polarization of a material. Every technique has some strengths and weaknesses. These are explained briefly here.

7.2.1 Photoemission Spectroscopy

Spin polarized photoemission spectroscopy has capability of measuring spin polarization directly, but this method can measure the spin polarization of electrons emitted only from 5-20 Å of surface of the ferromagnet, and hence it is surface sensitive [Johnson, 1995]. This technique lacks the necessary energy resolution (1 meV) [Feder, 1985]. This technique is based on Einstein's photoelectric effect. The modification is the ejection of spin polarized electrons from initial state below the Fermi level of magnetic materials to final state (the vacuum level), and their detection by polarimeters. This allows the analysis of the spin polarization and other electronic structure of solids of interest based on conservation of momentum and energy of ejected photoelectrons.

7.2.2 Spin polarized tunneling (SPT) spectroscopy

Tunneling experiment was developed by Meservey and Tedrow in 1970 in which they showed that the quasi particle energy states in thin superconducting Al films are split in a high magnetic field by the interaction of the field with the quasi particle spin magnetic moments [Meservey et al., 1970]. Later, they used such a polarized tunnel current to investigate the polarization of the current carriers in ferromagnetic nickel [Tedrow et al., 1971], and it was later extended to measure the spin polarization of Fe, Co, Ni and Gd thin ferromagnetic films [Tedrow et al., 1973]. These SPT experiments showed that the conduction electrons in ferromagnetic metals are spin polarized and that the spin is conserved in the tunneling process. These pioneering experiments are the fundamental basis for the MR effect in MTJs, as well as many other spin polarized phenomena. This technique gave the spin polarization values of the

ferromagnetic thin films more or less in agreement with the corresponding values measured by photoemission spectroscopy, as shown in table 7.1.

Table 7.1 Comparison of percent polarization P measured in thin ferromagnetic films by Photoemission spectroscopy and spin polarized tunneling [Tedrow et al., 1973]

Magnetic thin film materials	Photoemission (%)	Tunneling (%)
Fe	+ 54	+ 44
Co	+ 21	+ 34
Ni	+ 15	+ 11
Gd	+ 5.7	+ 4.3

Magnetoresistance on trilayer junctions of FM-Insulator-FM was measured first by Julliere in 1975 [Julliere, 1975] with the interpretation that the tunneling current depends on the relative orientation of magnetization of the electrodes. This model suggests the TMR to be given by

$$TMR = \frac{R_{AP} - R_P}{R_P} = \frac{\Delta R}{R_P} = \frac{2P_1 P_2}{1 - P_1 P_2},$$

(7.7)

Where P1 and P2 are the spin polarizations of two ferromagnetic electrodes as measured by SPT spectroscopy.

Towards late 1980s, the notion that spin polarized current can be obtained by the use of one of magnetic film electrodes in tunnel junctions changed, and the concept of spin-filtering effect was introduced. In this effect, magnetic semiconductors such as EuO, EuS, and EuSe as tunnel barriers display different barrier heights for two spin directions due to exchange splitting, and hence allow high spin polarized current through them [Moodera et al., 1988; Hao et al., 1990; Moodera et al., 1993; Santos and Moodera, 2004].

7.2.3 Positron Spectroscopy

Radioactive positron sources such as ^{22}Na, ^{64}Cu, ^{58}CO are used to inject positrons into solids where they annihilate with their anti particle electrons (e$^-$) with the emission of γ-rays, which yield detailed information regarding both the electron density and electron momenta in the region from which the positron annihilates [Siegel, 1980]. Positron (e$^+$) has spin ½ and it carries magnetic moment equal to that of an electron. This property can be utilized to image the electronic structure of magnetic materials [Berko, 1983]. Positrons emitted from a radio-isotope like Na-22 [Zwart et al., 1985] are partially spin-polarized [Rabou, 1983], a relativistic consequence of non-conservation of parity in the beta-decay process. Switching the magnetization direction of a magnetic material allows one to extract its spin-resolved electronic structure, as the positron annihilates preferentially with an electron of opposite spin direction.

7.2.4 Point Contact Andreev Reflection Spectroscopy

Spin polarization of a metal that requires no magnetic field and places no special constraint on sample; thin films, single crystals and metallic foils can be measured by point contact between the sample and a superconductor (SC) [Soulen et al., 1998] as shown in schematic drawing of the set up shown in Fig.7.1. This experimental technique developed by Soulen et. al. in 1998 in point contact geometry [Soulen et al., 1998] and by Upadhyay et al. in 1998 in lithographically fabricated ballistic nanocontacts [Upadhyay et al., 1998] is based on well known Andreev reflection which is a process of converting normal current to supercurrent at a metallic interface [Andreev, 1964]. Three years earlier in 1995, de Jong and Beenakker had shown that the transport properties of Ferromagnet-superconductor (FS) junctions are qualitatively different from the non-ferromagnetic case, because the Andreev reflection is modified by the exchange interaction in the ferromagnet [de Jong, 1995].
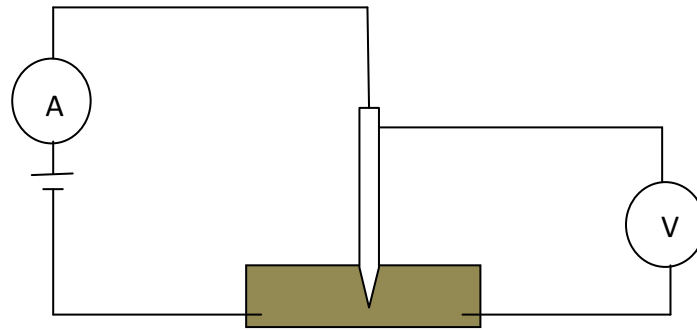
Fig. 7.1. Schematics of point contact set up to obtain conductance curves (After Soulen et al., 1998).

In an interface between a normal metal (non-magnetic) (N) and a superconductor (S) , an electron from N forms a Cooper pair taking another electron of opposite spin from opposite spin band at Fermi level of N, and as the Cooper pair travels through the superconductor within its BCS gap Δ, a hole is reflected to the N in the direction opposite to the incident electron. This process is called Andreev reflection which is also called retro-reflection, and it is illustrated in Fig. 7.2. Andreev reflection is always allowed at the interface of N and S. Momentum is conserved in this process, and such reflection has time reversal symmetry.
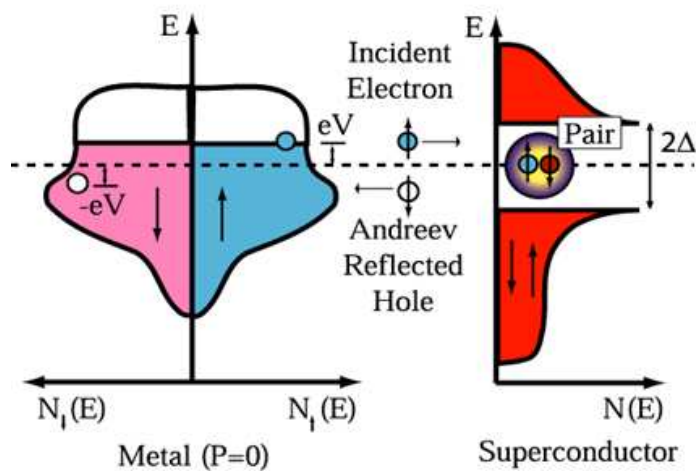
Fig. 7.2. Schematic of the energy diagram for supercurrent conversion by unhindered Andreev reflection at the NS interface. The solid and open circles are for representing electrons and holes respectively (Soulen et al., 1998).

But the situation is no longer true at the interface of magnetic metal and a superconductor. The Andreev reflection is limited by a minority spin population. In half metals which do not have minority spin states at Fermi level, a hole is not reflected and Cooper pair cannot be formed so that the Andreev reflection and hence the conductance is supressed for the electrons with energy less than superconducting BCS gap. Such situation was emphasized first by de Jong and Beenakker in 1995 [de Jong, 1995]. The schematics of supression of Andreev reflection is shown in Fig. 7.3.
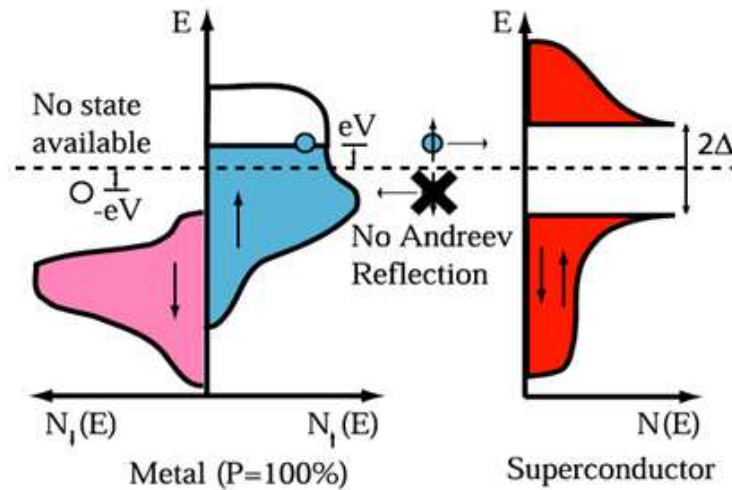
Fig.7.3. Schematic of the energy diagram for suppression of Andreev reflection at the ferromagnetic superconductor (FS) interface. The solid and open circles are for representing electrons and holes respectively (Soulen et al., 1998).

As the Cooper pair moves into the superconductor in N-S contact, the charge conservation at the interface requires the reflection of a hole. This doubles the charge flow (2e) at the interface which inhances the conductance to double compared to the normal state (i.e. at bias much larger than the superconducting gap). If we represent the conductance when the Andreev reflection is not taking place at N-N situation as G_n, and the conductance due to unpolarized current due to Andreev reflection at the N-S interface as $\dfrac{dI_{unpol}}{dV}$, then due to the

double charge flow during Andreev reflection, the normalized conductance for zero bias

(eV<<Δ) and K_BT<<Δ for no barrier scattering at the interface (Z = 0) can be taken as 2, i.e.

$$\frac{1}{G_n}\frac{dI_{unpol}}{dV} = 2 \qquad (7.8)$$

Since, no polarized current flows in this situation, the normalized conduction for polarized

current can be taken as zero, i.e. $\qquad \frac{1}{G_n}\frac{dI_{pol}}{dV} = 0 \qquad (7.9)$

When a spin polarized current flows in an interface of N-S, the total current (I) is the sum of the

unpolarized (I_{unpol}) and polarized (I_{pol}) currents, i.e.

$$I = I_{unpol} + I_{pol} \qquad (7.10)$$

This allows to write an expression for the normalized conductance($\frac{1}{G_n}\frac{dI}{dV}$) that is dependent on

V, T, P_c and Z, as shown in equation (7.11).

$$\frac{1}{G_n}\frac{dI}{dV} = (1-P_C)\frac{1}{G_n}\frac{dI_{unpol}}{dV} + P_C\frac{1}{G_n}\frac{dI_{pol}}{dV} \qquad (7.11)$$

From equations 7.8, 7.9, and 7.11, one can write the normalized conductance in terms of spin

polarization P_c at T→0, eV→0 (low bias) and for clean interface (Z=0) as,

$$\frac{1}{G_n}\frac{dI}{dV} = 2(1-P_C) \qquad (7.12)$$

This is highly simplified expression for ideally clean interface at zero bias and at T→0.

However, the reality would be different due to interfacial scattering, and finite temperature. In

such situation, the spin polarization can be extracted by numerically fitting the conductance data

over the entire voltage range with modified form of BTK model. The original and modified BTK

models will be discussed in th efollowing sections.

7.3 BTK Theory

G.E. Blonder, M. Tinkham, and T.M. Klapwijk (BTK) proposed a theory for the I-V curves of normal-superconducting (N-S) microconstriction contacts [Blonder et al., 1982]. This model is a unified treatment to understand classic (high-barrier) tunnel junctions, metallic (no-barrier) junctions and transitional (small-barrier) junctions, and is based on generalized Andreev reflection model. This model considers ballistic transport, includes a barrier of arbitrary strength at the N-S interface, and gives detailed insight into the conversion of normal current to super-current at the interface. In this theory, the reflection and transmission probabilities at the interface are found by solving the Bogolubov-de Gennes equation for electrons incident on the N/S interface.

At temperature higher than 0 K, all incident electrons may not form Cooper pairs. The unpaired electrons known as quasi-particles can have energy of an electron either greater than the average energy of Cooper pair (electron-like state, $|e\rangle$) or less than the average energy of Cooper pair (hole-like state, $|h\rangle$). Such quasi-particles can be described by using Bogolibov-de Gennes equation

$$i\hbar \frac{d\psi}{dt} = \begin{pmatrix} H & \Delta \\ \Delta & -H \end{pmatrix} \psi,$$
(7.13)

Where the Hamiltonian

$$H = \frac{-\hbar^2}{2m} \frac{d^2}{dx^2} - E_F + V(x),$$
(7.14)

And the wave function of the quasi-particle

$$\psi(x,t) = f(x,t)|e\rangle + g(x,t)|h\rangle, \, or \, \psi(x,t) = \begin{pmatrix} f(x,t) \\ g(x,t) \end{pmatrix}$$
(7.15)

Where $f(x,t)$ and $g(x,t)$ are probability of finding the quasi-particles in states an electron-like and hole-like states $|e\rangle$ and $|h\rangle$ respectively. In electron-like state the quasi-particles obey Schrodinger equation, and in hole-like state they obey time reversed Schrodinger equation. Electronlike excitations cannot be made inside the Fermi sphere, since the states there are fully occupied in the ground state, and the hole excitations are possible only outside the Fermi sphere [Blonder et al., 1982].

The scattering at the interface due to different reasons such as oxide layer in a point contact or the localized disorder in the neck of a short microbridge, or the intentional oxide barrier in tunnel junction is modeled by a repulsive potential Hδ(x) located at the interface. A dimensionless barrier strength $Z = K_FH / 2E_F = H / \hbar v_F$, where K_F and v_F are the Fermi wave vector and Fermi velocity respectively, is assigned to simplify the reflection and transmission probabilities A (Andreev reflection probability), B (the normal reflection probability), C (electron-like transmission probability) and D (hole-like transmission probability) at the interface. These probabilities are also the function of energy E which is written for convenience in terms of dimensionless parameter, $\varepsilon = \sqrt{\dfrac{E^2}{E^2 - \Delta^2}}$.

Table 7.2. The Andreev reflection coefficient A, the ordinary reflection coefficient B, the transmission coefficient without branch crossing (electron-like) C, and the transmission coefficient with branch crossing (hole-like) D.

	A	B	C	D
E<Δ	$\dfrac{\varepsilon^2 - 1}{\varepsilon^2 - (1 + 2Z^2)^2}$	$\dfrac{4Z^2(1 + Z^2)}{(1 + 2Z^2)^2 - \varepsilon^2}$	0	0
E>Δ	$\dfrac{\varepsilon^2 - 1}{(\varepsilon + 1 + 2Z^2)^2}$	$\dfrac{4Z^2(1 + Z^2)}{(\varepsilon + 1 + 2Z^2)^2}$	$\dfrac{(\varepsilon + 1)(1 + Z^2)}{(\varepsilon + 1 + 2Z^2)^2}$	$\dfrac{2(\varepsilon - 1)Z^2}{(\varepsilon + 1 + 2Z^2)^2}$

Transmission probability (C+D) can be calculated if A and B are known by using the fact that the total probability is 1, i.e. A+B+C+D = 1. The probability of Andreev reflection goes down as the value of Z increases (Fig. 7.4 (a)), where as the normal reflection plays a dominating role in the total reflection coefficient (Fig. 7.4 (b)). Andreev reflection is completely suppressed in low energy regime when the value of barrier strength Z goes very high which represents the tunneling transport regime. An incident electron with E<Δ (sub gap energy) cannot enter the superconductor as quasi-particle, i.e., the total reflection probability, A+B =1. An electron with E>Δ does not Andreev reflect so that the total transmission probability, C+D is 1- (A+B). If we set Δ → 0, i.e. $\varepsilon \to 1$, one can find the total transmission probability (C+D) to be $\dfrac{1}{1+Z^2}$, which is the standard transmission of a δ-function barrier [Griffiths, 1995].
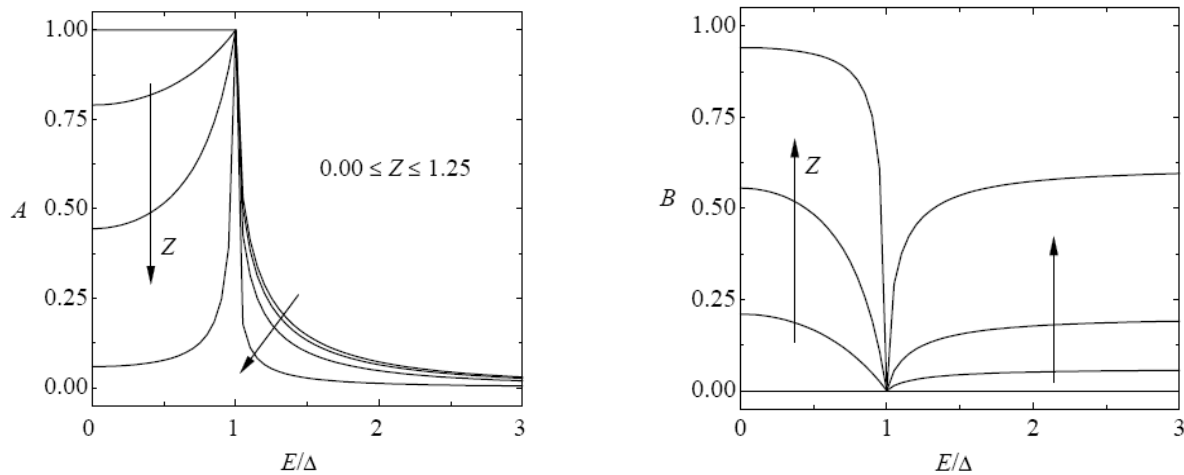
Fig. 7.4. Probalility for (a) Andreev reflection, and (b) normal reflection as a function of particle energy for values of $Z = 0.00, 0.25, 0.50$, and 1.25. The direction of arrows indicate increasing trend of Z [Kant, 2005].

For a given bias voltage, the current in a normal metal (N) or a superconductor (SC) making the interface can be found by using the reflection and transmission coefficients A and B. Let an electron is incident from N-side (say on the left). There will be current flowing to the N-side from the interface because of Andreev reflection, and also there will be current flowing to the SC-side (say on the right). The current flowing to the right for an electron with an energy in $[E, E + dE]$ is given by

$$eSv(E)\rho(E)f(E)dE; \qquad\qquad\qquad\qquad (7.16)$$

where e is the charge of the electron, S the area of the N/S interface, $v(E)$ the electron velocity, $\rho(E)$ the density of states and $f(E)$ the Fermi distribution function. The expression $\rho(E)f(E)dE$ is the density of electrons with an energy in $[E, E + dE]$. Because of the Andreev reflected part $A(E)$ of incident electrons as holes, an additional current flows to the right which is given by

$$eSv(E)\rho(E)A(E)f(E)dE, \qquad\qquad\qquad\qquad (7.17)$$

The current flowing to the left due to the normal reflection of part $B(E)$ of the incident electrons is given by

$$eSv(E)\rho(E)B(E)f(E)dE, \qquad\qquad\qquad\qquad (7.18)$$

Due to the particles originated and incident with probability X from the S-side, the current that flows to the left can be written as

$$eAv(E)\rho(E)X(E)f(E)dE, \qquad\qquad\qquad\qquad (7.19)$$

where X=1+A-B so that the total current is zero in absence of an externally applied bias voltage. Non-equilibrium particle distributions will be generated when a bias voltage is applied. It raises the energy of the normal metal by eV with respect to the superconductor. In this case, the distribution function of the electrons coming from S-side is f(E), and that for incoming electrons from N-side have the distribution f(E-eV). Thus, for obtaining the current for a given bias

voltage, we should replace $f(E)$ in expressions (7.16-7.18) by $f(E - eV)$. Consequently, the current resulting from electrons incident from the N-side is given by

$$eS \int v(E)\rho(E)[1 + A(E) - B(E)]f(E - eV)dE, \tag{7.20}$$

and the current resulting from particles incident from the S-side is given by

$$eS \int v(E)\rho(E)[1 + A(E) - B(E)]f(E)dE, \tag{7.21}$$

where we have used that $X = 1 + A - B$. The total current becomes

$$I(V) = eS \int v(E)\rho(E)[1 + A(E) - B(E)][f(E - eV) - f(E)]dE \tag{7.22}$$

The function $f(E - eV) - f(E)$ is nonzero only in a region of size eV in the vicinity of the Fermi level. Since $eV \approx \Delta << E_F$, the electron velocity v and the density of states ρ of the normal metal at Fermi level can be considered as constants and can be taken outside of the integral sign, giving

$$I(V) = eSv\rho \int [1 + A(E) - B(E)][f(E - eV) - f(E)]dE \tag{7.23}$$

The conductance $G_{NS} = dI/dV$ then becomes

$$G_{NS} = -e^2 Sv\rho \int [1 + A(E) - B(E)]f'(E - eV)dE, \tag{7.24}$$

where f' is the derivative of the Fermi distribution function. The function $-f'(E)$ is zero everywhere except near $E = 0$ where it has a pulse-shape similar to a delta-function with a width proportional to kBT. When both sides of the interface are normal metal ($\Delta = 0$), equation (7.24)

reduces to
$$G_{NN} = \frac{e^2 Sv\rho}{1 + Z^2} \tag{7.25}$$

since $A = 0$ and $1 - B = 1/(1 + Z^2)$. The conductance in the superconducting state normalized by the conductance in the normal state is the main result of the BTK theory given by

$$\frac{G_{NS}}{G_{NN}} = -(1 + Z^2) \int [1 + A(E) - B(E)]f'(E - eV)dE \tag{7.26}$$

7.4   Modified BTK Theory and other developments

BTK theory is unclear in interpretation of the barrier strength, Z. Proximity effect is not considered in this theory, and it has not incorporated spin polarization, P. These limitations of BTK theory needed modifications, and after 19 years of their work, Strijkers et. al. [Strijkers et al., 2001] came up with a model that extended BTK theory to include spin polarization and proximity effects. This allowed to reliably interpret experimentally observed data in both cases of magnetic superconducting (Nb/Ni, Co, Fe), and nonmagnetic superconducting (Nb/Cu) contacts [Strijkers et al., 2001].   Mazin et al. contributed more by considering for the F/S interface that the Andreev reflection probability is not zero, rather the Andreev reflected hole as a spatially decaying evanescent wave with finite probability but carrying no net current [Mazin et al., 2001]. This model was able to explain the interfacial conductance curves as a function of voltage not only for ballistic transport but also it was able to calculate the same for diffusive case.
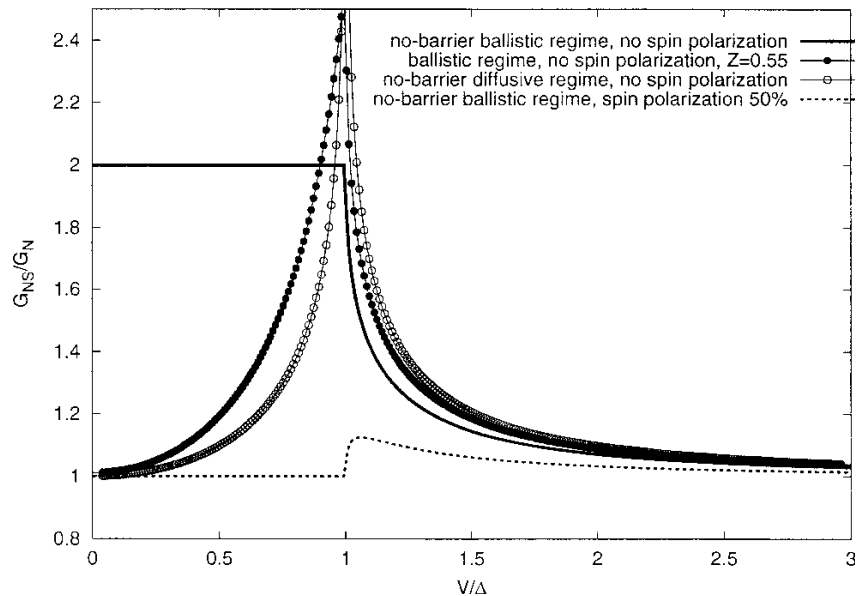
Fig. 7.5. Andreev conductance in different regimes [Mazin et al., 2001].

In this paper they have argued that they have addressed the issues like different number of conduction channels (CC) for different spins, finite interface resistance, band structure effects, effect of an evanescent Andreev hole on quasiparticle current in half-metallic CC, and diffusive transport in the ferromagnet. They concluded that while it is difficult to separate the suppressive effects of diffusive transport on the conductance from the effect of a high Z value in a ballistic contact, it is possible to distinguish the effect of spin polarization from the two, as shown in Figure 7.5.

Many of the experimental works [Ji et al., 2001; Nadgorny et al., 2001] utilized either the model of Strijkers et al. [Strijkers et al., 2001] or Mazin et al. [Mazin et al., 2001]. In a comparison of these models regarding interpretation of the experimental data for determining spin polarization, Ji et al. [Ji et al., 2001] concludes that both models can be used to extract spin polarization from experimental results for a variety of ferromagnetic materials including half-metallic CrO_2 within the difference in P values of less than 2%. However, by introducing an evanescent wave in the minority band Mazin et al. [Mazin et al., 2001] removed the conjecture of Strijkers et al. [Strijkers et al., 2001] that Andreev reflection amplitude must be set to zero in the case of half-metal, which resulted in a more accurate determination of P by about 2% - 4% [Nadgorny, 2011].

Auth et al. considered that the transport at the interface may not be only elastic (ballistic or diffusive) [Auth et al., 2003]. Working with thin films of double perovskite Sr_2FeMoO_6 and bulk material of the Heusler compound $Co_2Cr_{0.6}Fe_{0.4}Al$, which are ferromagnetic samples with a predicted half metallic behavior and comparably low conductivity, they included inelastic process in their analysis and concluded that the thermal effect can have significant effect in data

evaluation, such as smaller values of transport spin polarization. They remained inconclusive about the effect of ballistic and diffusive transport on transport spin polarization.

Measuring accurate value of spin polarization has been a debate and matter of research for a long time. For consistent data analysis to avoid misinterpretation of data, Woods et al. considered the relationship between ballistic and diffusive transport, the effect of different transport regimes on spin polarization measurements, and the importance of unambiguous identification of the type of transport regime [Woods et al., 2004]. They found that the spin polarization in the case of diffusive transport is only about 3% lower than in the case of ballistic transport, and the barrier strength Z larger by~0.5-0.6. They found that the value of P_C is system dependent on Z, presumably due to spin-flip scattering at the interface. However, the exact type of this dependence is hard to determine with any statistical certainty.

Xia et al. [Xia et al., 2002] indicated the possibility of some interaction between the ferromagnet and superconductor not included in the BTK model such as the Zeeman splitting of the superconducting densities of states caused by the stray magnetic fields of the ferromagnet. They also pointed out that the reduction in transparency of the F/S interface not only depends on the Fermi velocity mismatch, but also on the mismatch of the wave-function character at the Fermi energy.

After the introduction of barrier scattering Z at the N/S interface by BTK, and after its extension for F/S interface by others [Soulen et al., 1998; Mazin et al., 2001; Strijkers et al., 2001], the spin polarization of ferromagnetic materials were measured by several researchers, and it was found that the P was systematically suppressed with decreasing interface transparency which means increasing barrier strength Z [Ji et al., 2001; Strijkers et al., 2001]. Intrinsic value of spin polarization would be found from Z dependence of P by setting Z = 0 for clean interface.

However, the physical mechanism of dependence of P on Z was not clear at this point. Kant et al. [Kant et al., 2002] incorporated spinflip scattering in the interface region of the contact, and identified Z^2 as an effective scattering parameter, and explained the decay of P exponentially with Z^2. On the other hand, as we have shown in Chapter 10 that the extracted values of P and Z for a given set of experimental data depend on the fitting parameters such as temperature, spreading resistance or the superconducting gap. This observation, which will be explained in detail in §8.5 of Chapter 10, indicates that different Z can be related to the changes in the fitting procedure. However, such P-Z dependence gives similar intrinsic value of P corresponding to Z = 0 as given by using the P-Z dependence of data for multiple contacts as described above.
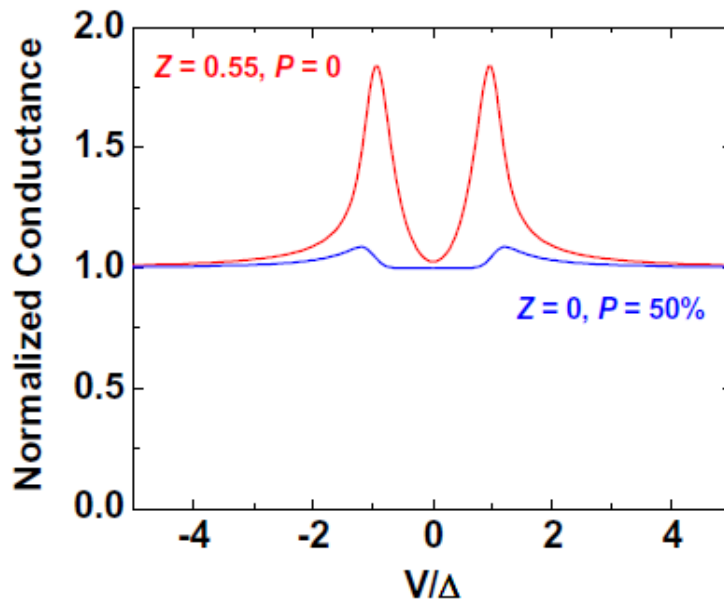
Fig. 7.6. Extended BTK theoretical normalized conductance curves at 1.5K and superconducting gap of 1.5meV (calculated with the modified BTK theory of Mazin et al.)

For a given sample, the intrinsic value, and hence the most accurate value of P is found for Z = 0. However, P will be overestimated if it is found based on zero bias conductance when Z

is not zero. For example, the zero bias conductance for $Z = 0$ and $P = 0.50$ is almost same as for the case of $Z = 0.55$ and $P = 0$ as shown in the theoretically calculated conductance curves for these cases as shown in Fig.7.6. So, the P value is found by fitting the conductance curve for the entire range below and above the superconducting gap.

In case of Andreev reflection experiments of ferromagnetic semiconductors, the spin polarization measurements are limited by high resistivity at low temperature, presence of Schottky barrier, and high velocity mismatch at the superconductor-semiconductor interface. Using heavily doped magnetic semiconductor (Ga,Mn)As having metallic type conductivity , hence narrow Schottky barrier and small Fermi velocity mismatch at the interface, spin polarization was extracted [Barnes et al., 1978; Panguluri et al., 2005] using reduced superconducting gap and higher effective temperature. Though the uncertainty in the P values was high, they found that the carrier concentration can be increased by doping heavily. This reduced the Schottky barrier so that its role in uncertainty in spin polarization was reduced.

CHAPTER 8

THEORETICALLY PREDICTED CURVES GENERATION AND FITTING OF DATA

8.1   Effect of Z on normalized conductance curves

Modified BTK model of Mazin et al. [Mazin et al., 2001] incorporates barrier strength Z as explained earlier. For different values of Z in this model, the normalized conductance obtained for superconducting gap of Nb, Δ= 1.5 meV at 4.2 K and 1.5K are shown in Fig. 8.1 [Mazin et al., 2001]. For Z = 0 at low bias, when all incident electrons undergo Andreev reflection so that P = 0, the normalized conductance is 2. As Z increases, increasing number of electrons suffer normal reflection so that only rest of the electrons undergo suppressed Andreev reflection which is the cause of local minimum of conductance at zero bias. The conductance is maximum at the edge of superconducting gap Δ, and those peaks are sharper as Z increases. Also, these peaks are more pronounced at lower temperature, and get smeared at higher temperature as shown in lower and upper panels respectively of Fig. 8.1.
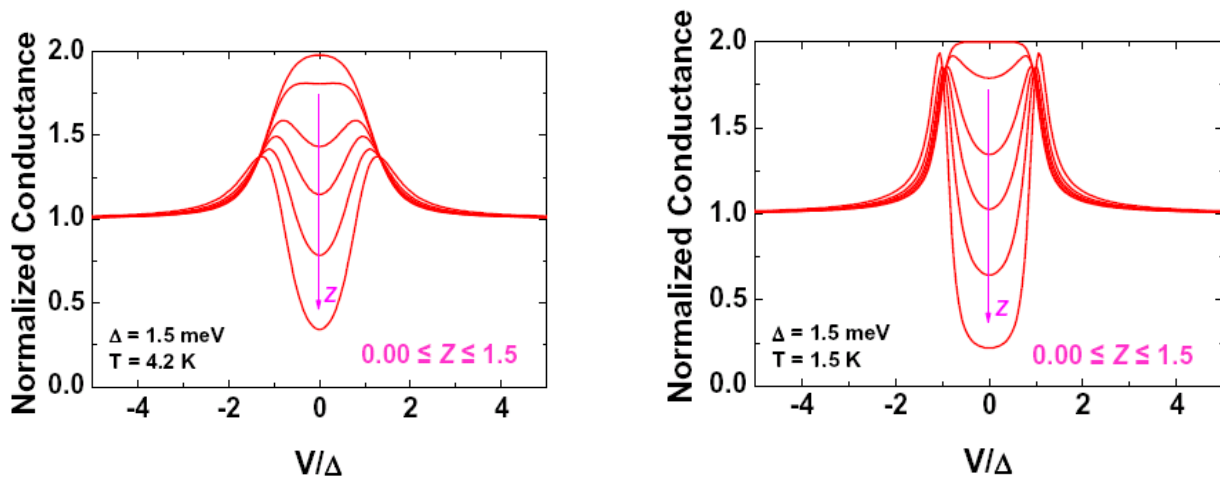
Fig 8.1. The Normalized conductance of an N/SC contact calculated with the mBTK theory (P=0) with Z= 0.00, 0.20, 0.40, 0.55, 0.80 and 1.5, for T = 4.2 K (Left Panel) and 1.5K (Right Panel). The arrows indicate the trend with increasing Z [Mazin et al., 2001].

The normalized conductance curves generated with P = 0, Δ =1.55 meV at T =1.2K for different values of Z, as shown in the legend, are shown in Fig. 8.2. It also shows that the conductance at low bias is suppressed for larger Z, where as the maximum conductance peaks at the edge of the gap energy are sharper for such larger Z. The case of ideal interface (Z = 0) at P = 0 shows conductance of 2.
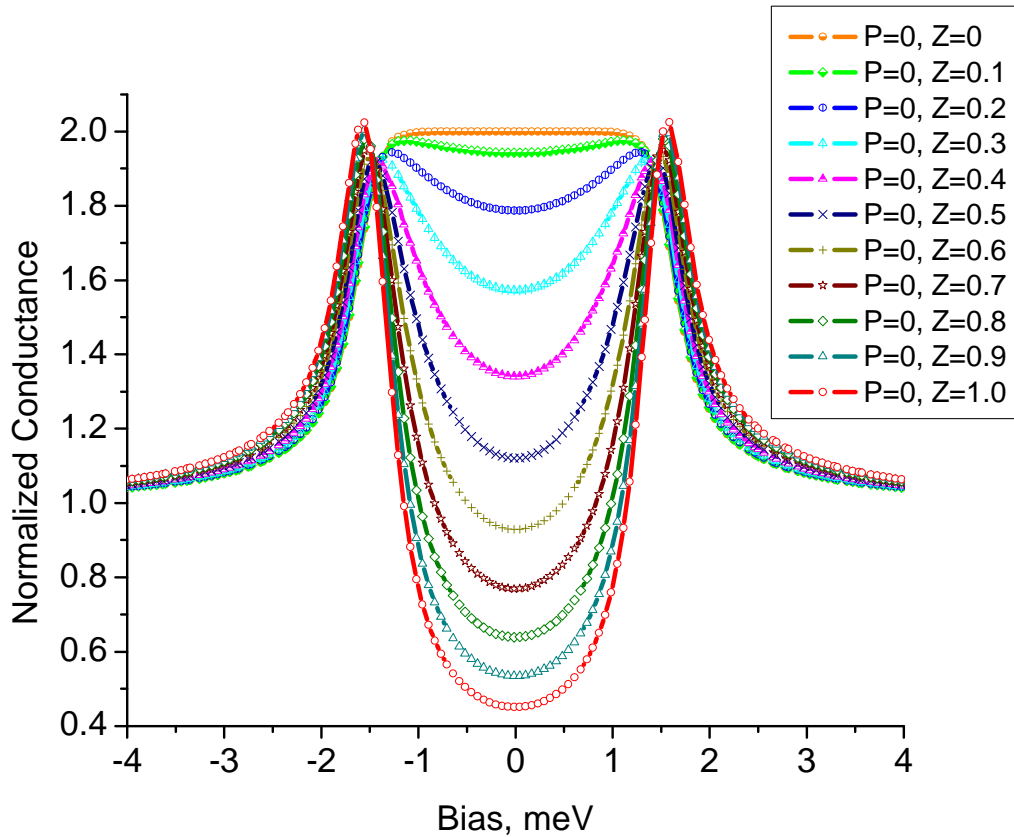
Fig. 8.2. Normalized conductance curves at T = 1.2K for P=0 with Δ =1.5 meV for different values of Z

8.2 Effect of P on normalized conductance curves for clean interface (Z=0)

If the SC/FM interface is ideal, i.e. the barrier strength is "zero", then the conductance curves for materials with different P values will be as shown in Fig. 8.3.The conductance is higher for lower P values, and it is equal to 2 for P=0, and the zero bias conductance decreases for higher P. However, we clearly notice enhanced zero bias conductance up to P ≈ 40+ % , and

it gets suppressed from around P≈50 - %, and the normalized conductance reaches to 0 for P=100% as shown in Fig. 8.3. The conductance at low bias lower than ~Δ seems to be constant for every value of P in this case when Z = 0. This nature of the conductance curves, however, changes in most of the experimental conditions when Z is no longer "zero" due to the presence of barrier scattering at the contact interface of the superconductor and the sample under study.
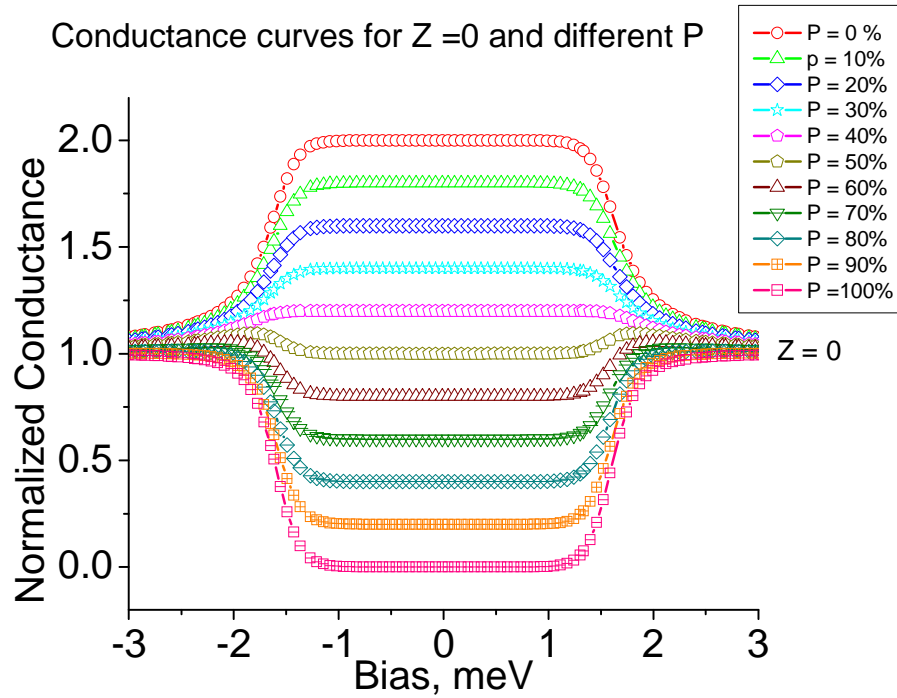
Fig. 8.3. Normalized conductance curves predicted by mBTK model for ideal interface (Z =0) and for different P values. BCS gap used to generate these curves is Δ = 1.5meV.

8.3   Effect on normalized conductance curves due to change in Z and P

Figure 8.4 shows, for an example, the conductance curves generated for different values of (Z,P) such as (0,0), (0.1,0.1), (0.2.0.2),(0.3,0.3),(0.4,0.4),(0.5,0.5),(0.6,0.6), (0.7,0.7), (0.8,0.8), (0.9,0.9) and (1,1). Even though, these are generated curves from model, and might be the situation for different sample systems, it is reasonable to expect lower values of P as the values of Z go up for different contact situations for a particular sample. While doing experiments, though the (Z,P) values are system dependent, mostly encountered values of Z

range from 0.2 to 0.6, and P values range from 0.6 to 0.3 for non half metallic materials. For any

particular system, intrinsic P value is found from plotting Z versus P, and extrapolating the curve

for $Z = 0$.
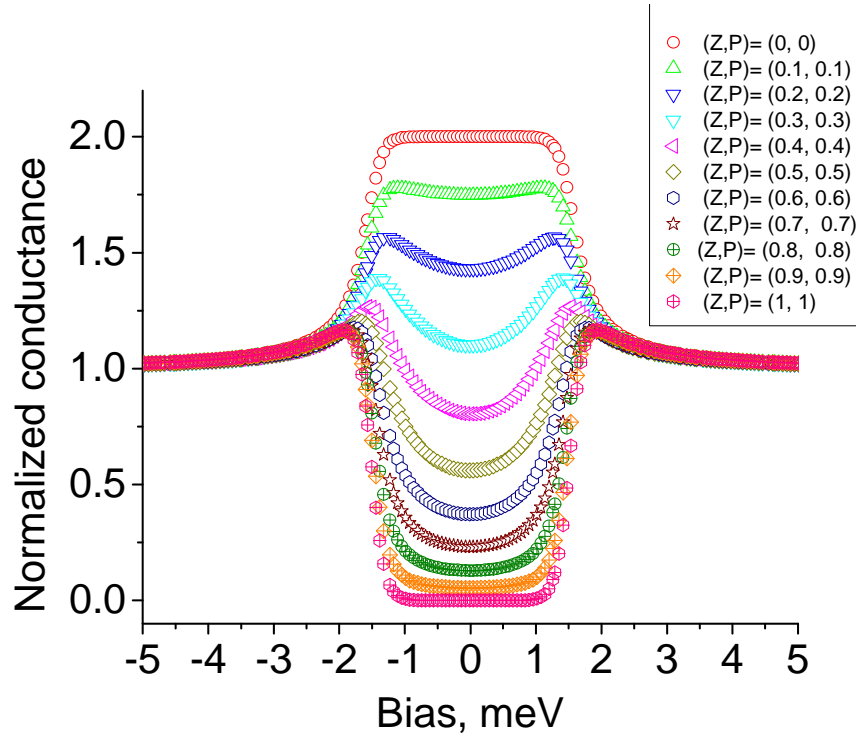
Fig. 8.4. Normalized conductance curves generated theoretically by using mBTK model for different values of Z and P at T=1.2K and for Δ=1.55 meV.

8.4   Effect of elevated temperature in fitting conductance curves by mBTK model

Temperature is another fitting parameter. Even though the data are taken at certain

temperature like 1.2K or 1.5K, sometimes one encounters a problem in fitting the data exactly at

the same temperature. It could be due to thermal broadening. However, use of slightly higher

temperature allows exact fitting of the conductance curves, especially at the maximal region of

conductance corresponding to the edge of superconducting gap Δ. So, it is important to have the

knowledge of how this elevated T as fitting parameter changes the conductance curves. For this

purpose, theoretical curves are generated using mBTK model for fixed Δ =1.55 meV and for

different values of temperature ranging from 1.2K to 4K as shown in Fig. 8.5. The experimental

data have tendency to fit around the conductance peaks around Δ at higher temperatures. This could be due to the fact that it is difficult to see very sharp peaks in experimental data. Generally, the conductance peaks in this region (at around 1.5 meV) are sharper if the curves are generated at lower temperature, and they become less sharp , i.e. more and more smooth curves if the data are generated using slightly higher temperatures as shown in Fig.8.5. We can clearly see the decreasing conductance peak at Δ≈1.5 meV even for the temperature increase of 0.1K. Initially, the curve at 1.2K was generated for P=0. The other curves were generated by changing temperature at fixed Δ of 1.55 meV. Knowing how the shape of conductance curve changes with temperature as a fitting parameter helps for fitting a given set of experimental data.
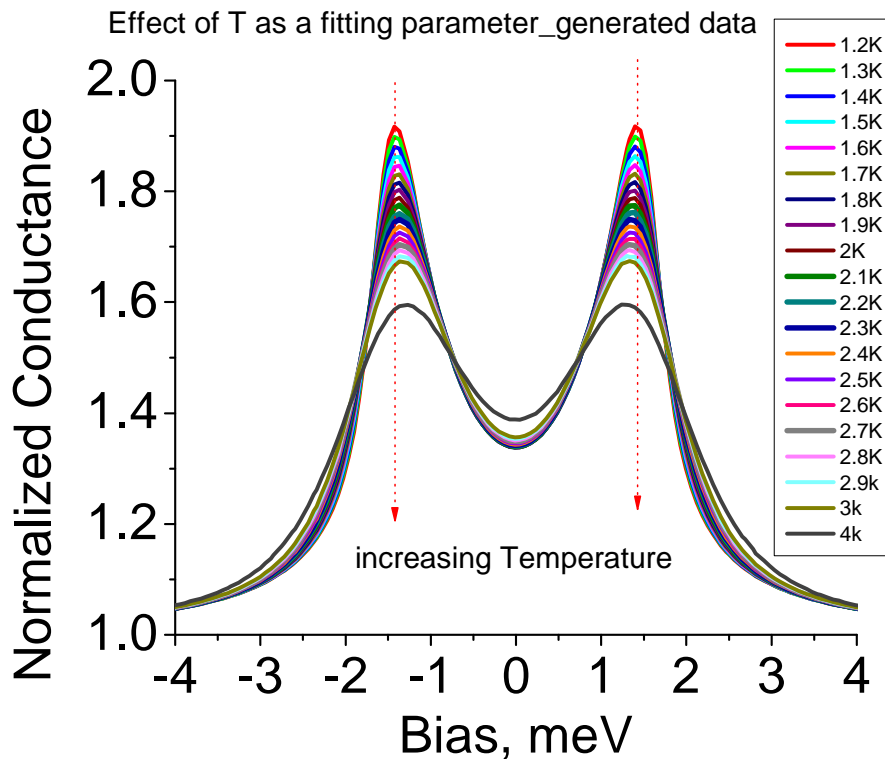
Fig. 8.5. Effect of elevated temperature in fitting conductance curves with P=0: the shape of the conductance curves changes with reduced conductance maxima at the edge of Δ, but P = 0 doesn't change.

8.5 Uniqueness of fitting

The parameters Z and P are extracted from fitting of the experimental data. Knowing how uniquely these quantities represent the fitting of a given set of data is important. In order to test this, a nice set of conductance data obtained for MnBi (sample: u1MnBiX103010) was fitted by the modified BTK model by changing different parameters in different possible ways. Different parameters involved as input parameters in the fitting are the temperature (T) at which the data are collected, superconducting gap Δ_{Nb} =1.5 meV, initializing value of Z for fitting, initializing value of P for fitting, spreading resistance of the sample (R_s), the number of data points being used for fitting, and the slope correction which was taken to be zero in all cases. The fitting was initially done for 1.4K with some initializing values of Z and P, and with the spreading resistance R_s=2Ω. Figure 8.6 (a) shows such a fitting.
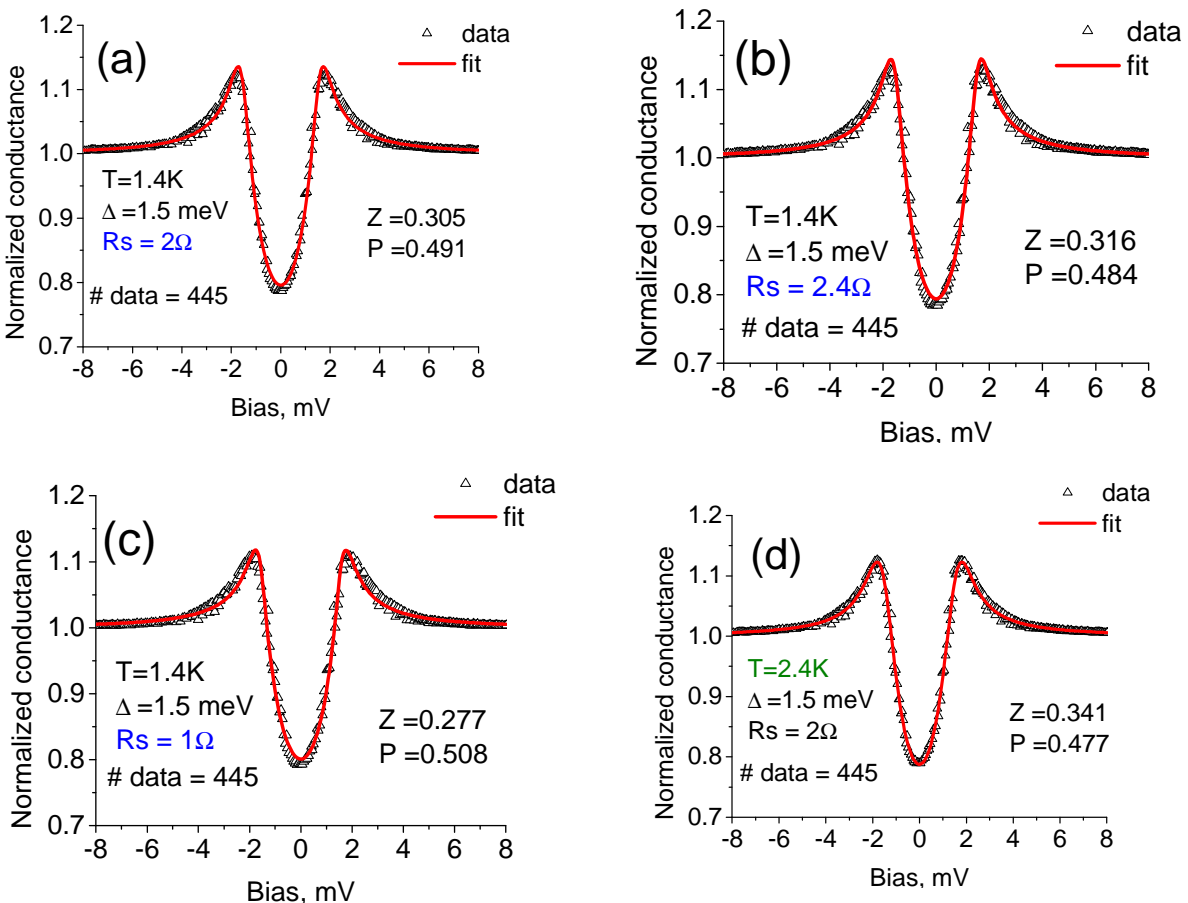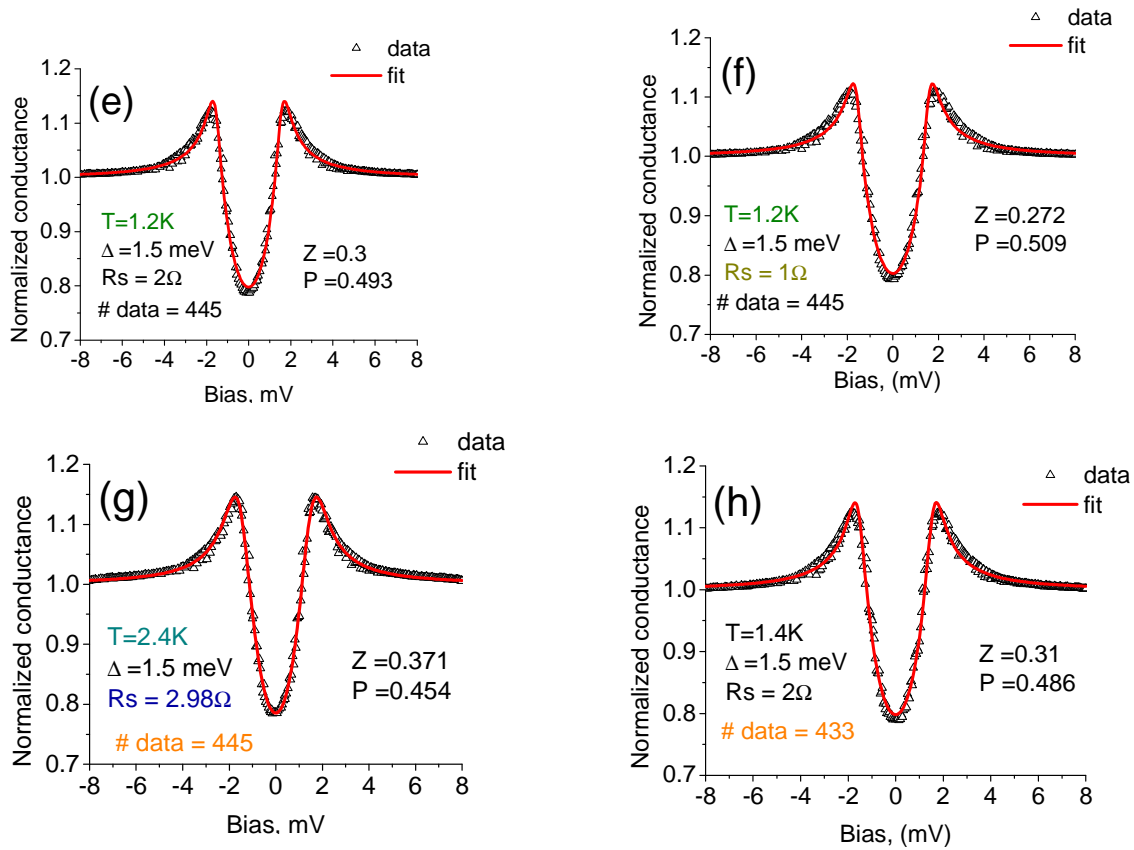
Fig. 8.6. Fitting of the same set of experimental data with different fitting input parameters giving different values of Z and P : (a), (b), (c) showing effect of spreading resistance; (d), (e) showing effect of temperature; (f), (g) effect of temperature and spreading resistance; (h) effect of number of data points

The input fitting parameters and extracted values of Z and P are shown in every fitting plot in Fig. 8.6. Even though the real physical situation is represented by Fig (a), other possibilities of fitting as shown in Fig (b) through (h) have been explored. Fig (b) and (c) show the effect on extracted values of Z and P when the values of spreading resistance are taken slightly different but still retaining reasonably well fitted curve. Fig. (d) and (e) show the reasonable fitting with slightly different values of T. Fig. (f) and (g) show the fittings with different T and Rs, and Fig. (h) shows the fitting with different number of data points taken in the same set of data. All of these curves look reasonably good fits despite the use of slightly different values of input parameters which lead to different values of extracted Z and P. Figure 8.7 (a) shows how P depends on Z in general and for different cases viz., change in R_s, change in

T, change in T and Rs, and change in data points while fitting the same set of data. This indicates that the variation of T and R_s both at a time can have larger spread in Z and P, where as the different numbers of data points considered while doing fitting has also some effect in Z and P, but with minimum spread in these values. The spread in P in this fitting is within ±3% from the mean value of P= 48. However, the intrinsic value of P is different.
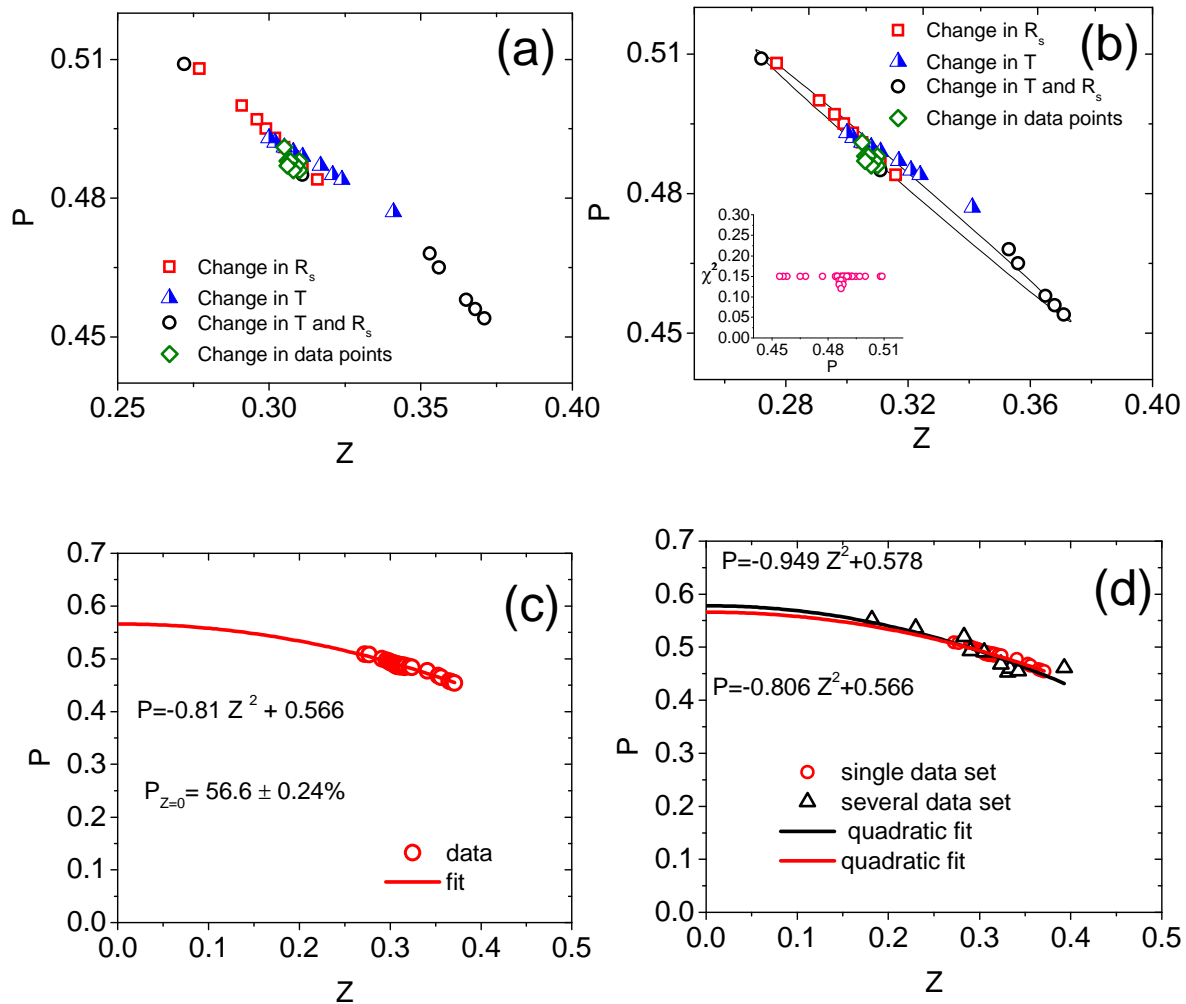
Fig. 8.7. Dependence of P on Z on different possible fittings of the same data set (a) showing the effect of different fitting parameters, (b) the loop in the P-Z plane indicates the constant error bar as shown by χ^2 versus P plot shown in the inset, (c) quadratic fit of the P-Z data extracted from fitting of a single data set, (d) comparison of P-Z data extracted from fitting a single data set to that of the extracted values from fitting of various data sets for the same sample.

While fitting this set of conductance data the fitting error bars were found almost constant as shown in the inset of Fig 8.7 (b). This is represented by the loop in Z-P data in this plot. Quadratic fit of the Z dependence of P in Fig. 8.7(c) gives the value of P corresponding to Z=0 as 56.6% which is within error bars of intrinsic value of P (= 57.8±1.6)% for clean interface (Z=0) as determined from the fittings of several sets of conductance data taken for various contacts for the same sample. This is shown by comparing the quadratic fits for these cases in Fig. 8.7 (d). Interesting observation here is that the Z dependence of P obtained by fitting a single set of conductance data for various input parameters close to exact experimental physical parameters gives the same P for clean interface as determined by fitting several sets of conductance data. Also, one thing noteworthy here is that the interfacial scattering barrier denoted by Z does not represent to the physically scattering barrier, but it also arises due to fitting of the conductance data. In conclusion, the fitting gives Z dependence of P. In this sense, the fitting is not unique. However, the intrinsic value of P seems unique within the error bars.

CHAPTER 9

DETAILS OF EXPERIMENTAL TECHNIQUES

9.1   Preperation of samples

The samples used for measuring spin polarization are either single crystals or thin films deposited mostly on Si wafers and sometimes on glass wafers. MnSi, LSMO, $BaFe_2As_2$, and Ni were single crystals, where as the other samples such as MnBi, Pt, PdNi, InN were thin film samples deposited mostly by e-beam evaporation and by magnetron sputtering. Thin films of MnBi and Pt were deposited in Nebraska Center for Materials and Nanoscience by Prof. Dave Sellmyer's group. PdNi samples were deposited by Prof. Norman Birge's group in Michigan State University, and the work in InN was done in collaboration with the group of Dr. Gavin Lawes at Wayne State University. MnSi single crystals were provided by Dr. Fabrizio Carbone in Ecole Polytechnique Fédérale de Lausanne (EPFL), Switzerland.

9.1.1   Evaporation techniques (thermal, e-beam, magnetron sputtering)

Thin film samples were deposited by using e-beam evaporation technique and magnetron sputtering technique. In these systems the pressure was reduced to about 1.3×10^{-6} Torr, and the thickness of the sample was monitored by crystal monitor.

9.1.2   Polishing the sample

In case of single crystal like MnSi, the crystal was polished by mechanical polishing method by using several grits starting from coarse to fine. Alumina gel was used for final finishing. This technique helped to make the surface shining almost free of any scratches.

9.1.3   Tip preparation for point contact

Superconducting Nb tips were prepared by electrochemical etching of 99.99% pure Nb wire of diameter 0.25mm. Volume ratio of HNO_3 : HF : CH_3COOH = 5 : 4 : 1 was taken as

etchant for Nb. DC voltage of 8V was supplied between the positive Nb electrode and negative Carbon rod electrode both dipped into the etchant taken in a plastic container. Nb tip was dipped such that the current flowing initially would be about 800mA for getting pointed tips. The etching would complete once the current drops to zero. The etching would take place predominantly on the surface of etchant. The etched tips were rinsed with deionized water carefully so that the tips would not get damaged, and such tips were stored apex up on a foam pad in a box in a desiccator after confirming good quality of the tips by observing under optical microscope. Such tips would require dipping into HF for about 40 sec before mounting into the probe for point contact experiment so that any Oxide layer or any other dirt would be removed leaving behind clean and pure Nb tip for point contact with the sample being used. The electrochemical etching gives the radius of curvature of the tip less than 100nm [Faiz, 2009].

In some experiments, Sn tips were used. Such tips were fabricated by mechanically polishing tin wires. Careful polishing with lapping papers would give fine tips usable for making point contacts. In case of the use of superconducting sample such as Barium Iron Arsenide [$BaFe_2As_2$], we used normal metal tips made of Au wires. Since Au wires are soft, the tips were made by cutting the wire at an angle of about 45 degree so that the very tip of the wire is sharp and pointed.

9.2   Characterization techniques

X-ray Diffraction was used for structural analysis. Constructive interference of the reflected rays from different lattice planes gives the peak intensity in the X-ray spectrum. X-ray diffraction analysis is based on the well known Bragg's law $2d\sin\theta = n\lambda$, where θ is Bragg's angle and λ is the wavelength of X-ray, and d is the lattice spacing. Crystallelographic structures are known by knowing the location of the peaks and their intensities.

Elemental composition was studied by Energy Dispersive X-ray (EDX) spectroscopy which is a technique in which a X-ray emitted from an element when it is bombarded with electron beam is detected. The X-ray energy is characteristic of the element from which it is emitted. This technique is used in conjunction with scanning electron microscopy (SEM) which was also used for electron beam lithography on MnSi sample to make nano contact of Niobium. This will be discussed in detail later.

Transport properties such as dc resistivity measurement at low temperature were done by using quantum design Physical Property Measurement System (PPMS). This device can be used to perform a variety of experiments that require precise thermal control. It can be used to execute magnetic, electro-transport, or thermo-electric measurements, or with some modification it can be used to AC measurements, heat capacity or Ultra-Low field. This has the capability of operating from 1.9K to 400K with the temperature accuracy of 0.01K. PPMS can be equipped with 1-T, 7-T, 9-T, 14-T or 16-T longitudinal magnet, or a 7-T transverse magnet. PPMS MultiVu software application is the interface software used to operate the Model 6000 PPMS Controller. This device has slew rate from 0.01K/min up to 12 K/min with temperature stability $\leq 0.2\%$ for T ≤ 10K, and $\leq .02\%$ for T>10K. This instrument was used even to obtain temperature dependence and field dependence of conductance curves in point contact measurements such as for point contact measurements of MnSi single crystal. In such case, the tip was driven by squiggle piezo motor. This will be covered more while discussing MnSi in different chapter later.

Magnetic characterizations of the samples were done by using quantum design's Magnetic Property Measurement System (MPMS) also known as Superconducting Quantum Interference Device (SQUID). It consists of temperature control unit, and provides a compensated superconducting magnet capable of producing a very uniform magnetic field (B) up

to ± 5.5 T over the entire sample. M-H loops and M-T data were obtained using this instrument. With the use of liquid helium, this device works in the temperature range of 2K to 400K with temperature accuracy of 0.01K, and the magnetic field resolution of 1G for B > 5KG and 0.1G for B < 5KG.

Atomic force microscopy was used to study surface topography of samples such as Pt when surface roughness played important role in the magnetism of these thin films. This will be discussed later while discussing magnetism in Pt thin films. Neutron scattering was used to cross-check the surface magnetism of Pt thin films. This technique is the most reliable one to measure small magnetic moment present on a sample.

Point contact geometry was used to obtain conductance curves (dI/dV vs V) which were used to extract spin polarization of various materials. The point contact geometry was implemented first by Soulen [Soulen et al., 1998] and Upadhay [Upadhay et al., 1998], and later it has been used by several researchers such as Nadgorny [Nadgorny et al., 2000], Kant [Kant et al., 2005], etc. A superconducting tip is allowed to touch the sample of interest at low temperature, and conductance curves are obtained. In case of a superconducting sample, a normal metallic tip such as Au can be used instead. The tip can be approached in several ways: manually driving, piezo driving, and by lithography technique. Superconducting tip is mounted on the tip holder in such a way that the tip is right above the sample. Manual driving facility has a shaft with pitch of screw of 100μm so that the contact resistances can be controlled by fine movement of the tip. The schematics of the point contact arrangement, experimental set up and the probe head are shown on the left panal, middle panel and right panel respectively in Fig. 9.1.

Standard lock-in technique was used to acquire conductance data. For bias voltage V, let the current be I(V). Then corresponding to the bias voltage (V+dV), the current will be I

$$(V + dV) = I(V) + \frac{dI}{dV} dV + ...,$$ where the ac modulation voltage $dV = v \sin \omega t$ is superimposed to dc bias voltage which was supplied by Agilent DC Power Supply Dual Output E3620A. So the above expression becomes, $I(V + v \sin \omega t) = I(V) + \frac{dI}{dV} v \sin \omega t$. Due to small modulation voltage, there is small ac signal with amplitude equal to the conductance. This amplitude in the current signal is measured by lock-in.

Lock-in is sensitive to the signals at reference frequency only. The lock-in amplifier multiplies the current signal with the ac modulation voltage v sinωt. This product is passed through a low pass filter to average out all components in the current signal with a frequency different from ω. If a signal has the frequency ω but is not in phase with the ac modulation voltage, the lock-in averages out such signals too.
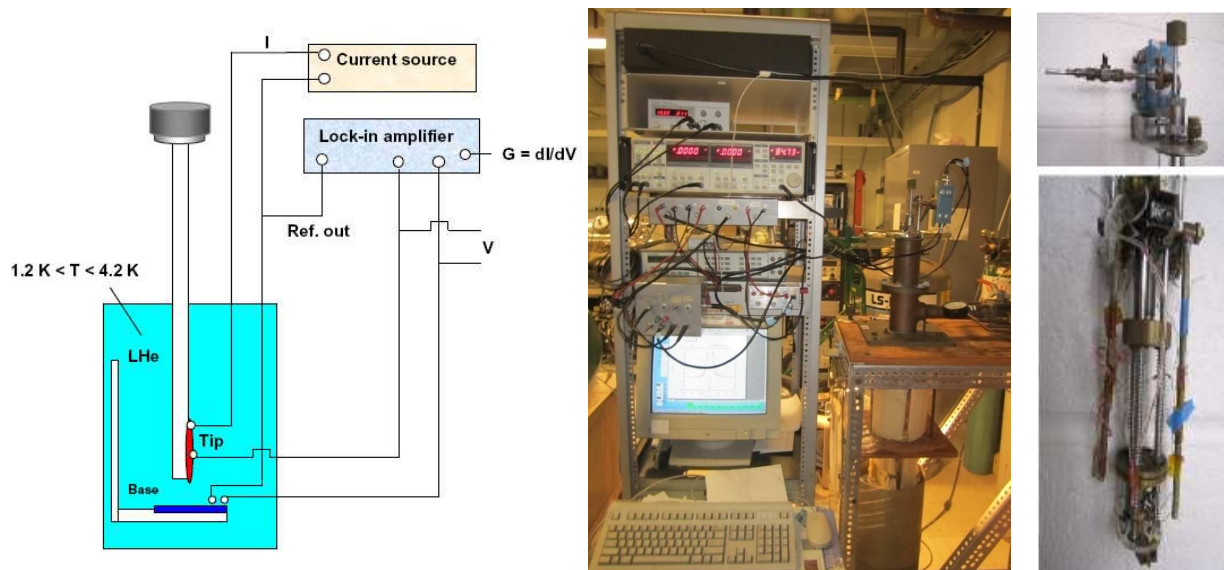
Fig. 9.1. Left panel: Schematics of the point contact arrangement, Middle panel: experimental set up, right panel: probe

CHAPTER 10

POINT CONTACT ANDREEV REFLECTION IN Cu AND La$_{0.7}$Sr$_{0.3}$MnO$_3$

10.1 Conductance curves for Copper

Point contact Andreev Reflection Spectroscopy (PCAR) was used to observe conductance curves for copper using electrochemically etched Nb tip. The motivation to see how conductance curves look for this superconducting/normal metal interface has two folds. Firstly, it gives chance to compare our observation with the observations found in literature; and secondly it helps to show, as expected, that the spins of the electrons in normal metal (Cu here) are not polarized. At the same time, these observations would be helpful to establish that our experimental set up is ready for reliable measurements of spin polarization of different other spin polarized materials to be discussed later.

10.1.1 Conductance curves of Nb/Cu by Soulen et al.

It is found in literature that people have done experiments to find conductance curves for Copper using Niobium as superconducting tip for the point contact. Soulen et. al. [Soulen et al., 1998] published the conductance curve taken for the configuration of mechanically polished Niobium tip pressed into copper foil in liquid helium at 1.6K. Figure 10.1 shows their observation of I-V curve as well as corresponding normalized conductance curve. As the bias voltage between the superconducting tip (Nb) and the normal metal (Cu) is less than the superconducting gap (1.5mV for Nb), a supercurrent flows through the configuration due to the flow of cooper pair during which an electron at Fermi surface of normal metal takes another electron with opposite spin state which results retroreflection of a hole which behaves as parallel channel for the flow of current, hence enhancing the flow of current from normal to supper current. When the super current flows, there is 0.2 mA of excess current than in the normal state

at low voltage bias, and the normalized conductance is twice that at normal state [Soulen et al., 1998] as shown in Fig. 10.1.
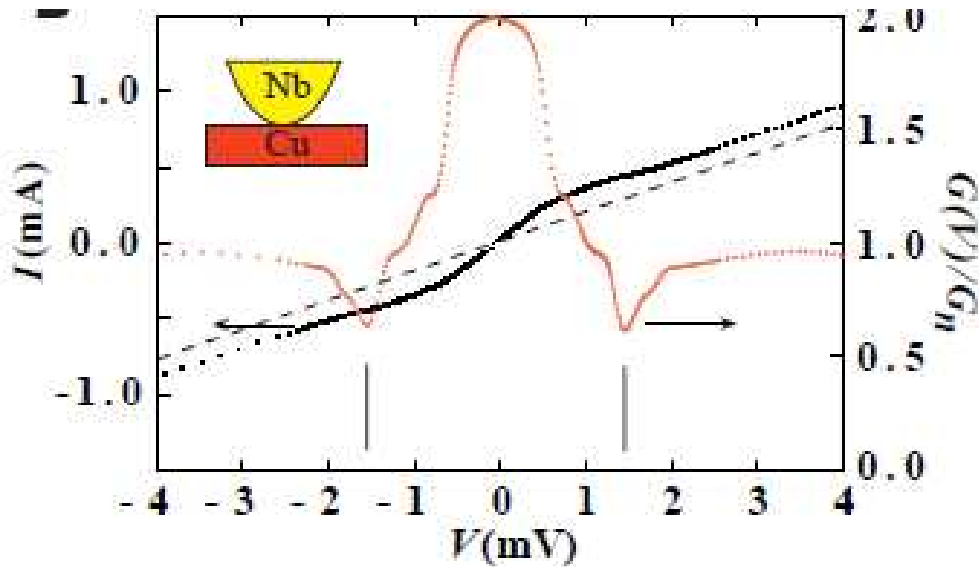
Fig.10.1 Normalized conductance curve and the I-V curve at 1.6 K for copper foil when superconducting Nb tip is pressed against it [Soulen et al., 1998]

The mechanism how super current flows is shown in the schematic diagram in Fig.10.2. In this model, a spin up electron at Fermi level of the metal (Cu) is considered to form a cooper pair with a spin down electron at the same Fermi level of the normal metal. The cooper pair travels through superconductor (Nb tip). Momentum of the electrons is conserved by the reflection of a hole at the interface between the normal metal and the superconductor. The hole that provides a parallel channel for the flow of current is responsible for the enhanced conductance in N/S configuration. Zero value of spin polarization of a normal metal in N/S configuration shows unhindered Andreev reflection due to sufficiently available inter-spin electrons for the cooper pair formation.

It has been seen in the literature that the conductance curves for Nb/Cu configuration has been observed by many scientists. Interesting enough, it is found that the conductance curves observed by different people look slightly different in their shape, still preserving the spin polarization value to be zero. What different shapes of conductance are reported in literature, and what factors are responsible for such variation is important to know. Before presenting my measurements for conductance of similar system, it seems important to review on what people have observed.

10.1.2 Conductance curves of Nb/Cu by Miyoshi et al.

Another literature [Miyoshi et al., 2005] has reported the field dependence of conductance curves for Nb/Cu system as shown in Fig. 10.2. They have shown the conductance curves for the magnetic field parallel to the superconducting Nb tip (upper panel), and for the magnetic field perpendicular to the superconducting tip (lower panel) as shown in Fig. 10.2, both taken at 4.2K. Our aim here is not to focus in the field dependence, but it is relevant to consider the conductance curve obtained for the case of zero magnetic field. We can see the conductance curves for zero magnetic field in the upper and lower panels of Fig. 10. 2. If the field is zero, we don't need to consider the field parallel or perpendicular to the tip; it means the tip position is same, and it is just like taking two sets of data may be for different contacts between the superconducting tip and the normal metal, Cu in this case. It is desirable to have similar conductance curves in these two cases, however the curves look entirely different indicating the possibility of different conductance curves for different contacts which are presumably characterized by different interfacial conditions.
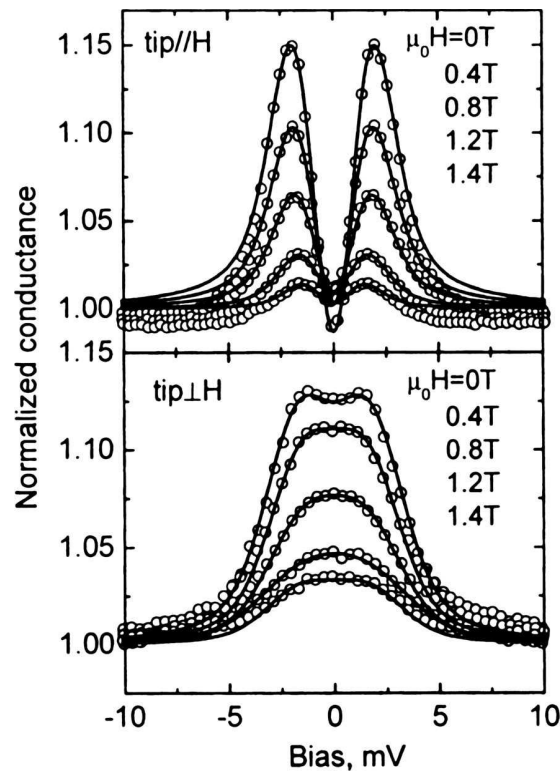
Fig. 10.2. Conductance curves for Nb/Cu film when the magnetic field is parallel (top panal) and when the field is perpendicular (bottom panal) to the Nb tip. Notice different shapes of conductance curves for zero field in these two graphs.

10.1.3 Conductance curves of Nb/Cu by Gavin Burnell

Gavin Burnell, University of Leeds reports I-V curve and conductance curve for Nb/Cu configuration as shown in Fig. 10.3 Conductance at lower bias is similar to the data shown in Fig.10.1 in the sense of its enhancement, however the shape of characteristic curve has some differences. Interfacial barrier, scattering and possibly other factors play important role for the shape of conductance curves. Lack of universality in conductance curves is a matter of concern for everybody working in this area. This difference arises not only in the observations between different investigators but also in different observations by the same investigator. Difficulty in maintaining the identical situations for different observations, especially for different contacts is an arduous challenge, and it leads to slightly different types of conductance curves.
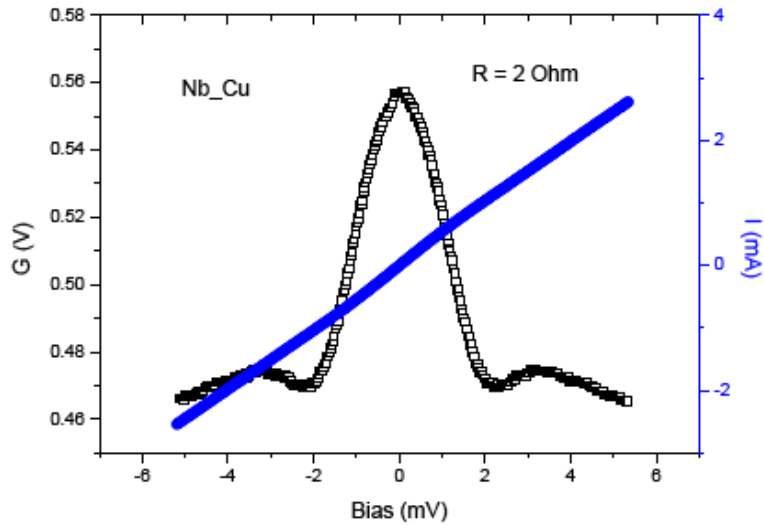
Fig.10.3. Conductance curve for Nb/Cu [Burnell, University of Leeds]

10.1.4 Conductance curves of Nb/Cu by Blonder et al.

G. E. Blonder and M. Tinkham [Blonder et al., 1983] have given theoretical conductance curve for Nb/Cu configuration as shown in Fig. 10.4. Dotted line shows the conductance for the ideal case (T = 0K, Z = 0: pure metallic, and equal Fermi velocities in Cu and Nb). When Fermi velocity ratio r is 1.414, the conductance curve takes the position shown by solid line. However, the case of r = 1.414 can be mimicked for r =1 (same Fermi velocity) by taking the scattering barrier potential Z = 0.175. This shows that the scattering due to velocity mismatch can be incorporated in the barrier scattering potential Z which is mainly responsible for different shapes of the conductance curves.
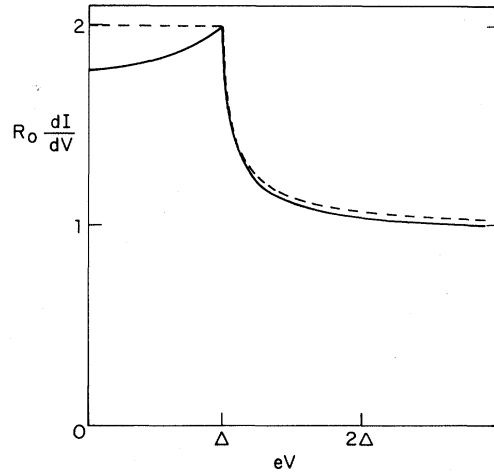
Fig. 10.4. Conductance curve for Nb/Cu configuration

10.1.5 Conductance curves for Pb/Cu by Chalsani et al.

Chalsani [Chalsani et al., 2007] has given dV/dI curve, shown in Fig. 10.5, as a function of voltage across the junction of nanocontact device for Cu-Pb configuration. The curves shown are taken at 4.2K, one with the application of magnetic field of 2000 Oe and the other in absence of magnetic field. Showing the presence of low energy clear phonon spectra of Pb in Cu-Pb and Co-Pb configurations [Chalsani et al., 2007], they have concluded that the electron transport is in ballistic regime, l>d, where l is the electron mean free path and d the size of the contact.

(a)   (b)
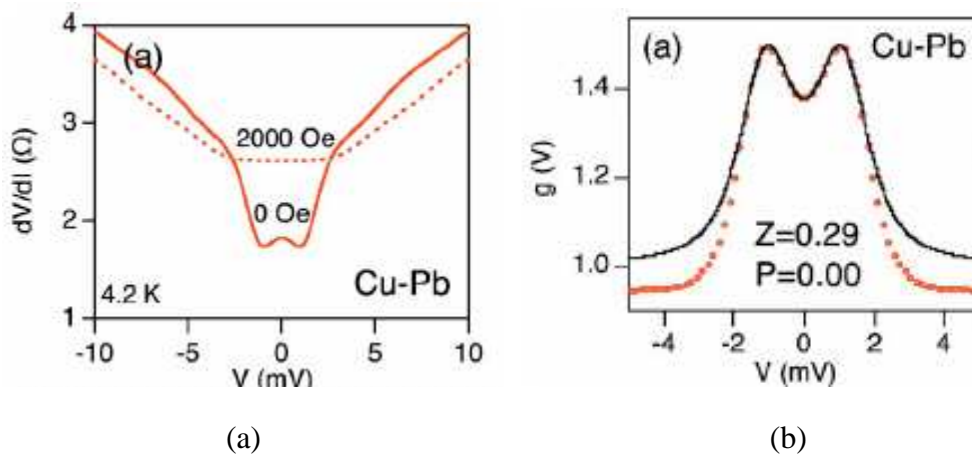
Fig. 10.5. For Cu-Pb configuration, (a) dV/dI curve at 4.2 K; (b) normalized conductance curve (open circles: experimental data, and solid line: 3D BTK fit)

Figure 10.5 (b) shows the normalized conductance curves taken for Cu-Pb system at 4.2 K. At this temperature, lead behaves as superconductor so that the spin polarization of Cu can be extracted from the fit, and it has been shown in the figure to be 0 with the interfacial barrier scattering Z = 0.29. In this fit, Chalsani et al. have considered that there is no Fermi energy mismatch, i.e E_{fN} = E_{fS}, where these energies are given by $E_{fS} = \hbar^2 k_{fs}^2 / 2m$ and $E_{fN} = \hbar^2 k_{fN}^2 / 2m$. This assumption corresponds to the temperature T = 0.79 K and the exchange energy J = 0. The fitting shows good agreement for /V/ < 2mV. The discrepancy between data and theory at higher bias in Cu-Pb system arises from nonequilibrium effects where the injection of nonequilibrium quasiparticles into the lead gradually reduces the gap and suppressed the extra overall conductance arising from Andreev reflection [Chalsani et al., 2007].

10.1.6 Our observation of conductance curves for Nb/Cu

Point contact exhibits a seemingly endless variety of I-V curve shapes [Blonder et al., 1983]. The shapes of differential conductance change accordingly. The excess current over the normal current can be found from the I-V curves whereas the fitting of conductance curves yields some fitting parameters, especially physically significant parameter: the spin polarization of a material. In this regard, we have taken several measurements of conductance curves for different copper samples with electrochemically etched Nb tip for the point contact. For different pressures of the contact (i.e. different contacts leading to different resistance), and for different samples, the conductance curves were obtained. To be consistent with the observation for Nb/Cu configurations as discussed in reference [Blonder et al., 1983], the Nb tip was electrochemically etched in HNO_3: HF: Acetic Acid = 5:4:1 by volume, and a copper single crystal was also etched in the similar solution for short time. The Nb tips produced were similar to the one shown in reference [Blonder et al., 1983]. Similar to their observations [Blonder et al., 1983], Nb tips were

observed before and after several contacts were made with Cu sample and were found as shown in Fig.10.6.
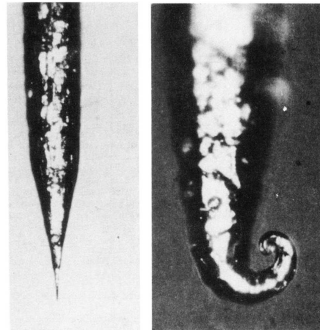
Fig.10. 6. electrochemically etched Nb tip before (first) and after (second) the point contacts were made with Cu sample [Blonder et al., 1983]

Conductance curves were observed using standard Lock-in technique. The data were fitted with modified BTK model. Fitted conductance curves were found, and different fitting parameters were extracted which are presented ahead.

Fig. 10.7 shows the I-V curve taken for Nb/Cu configuration. Nonlinear region of the curve is responsible for the feature of its differential conductance. This region corresponds to the flow of super current below superconducting gap. Above the superconducting gap, the I-V curve is linear which corresponds to the constant base line of the conductance curve.
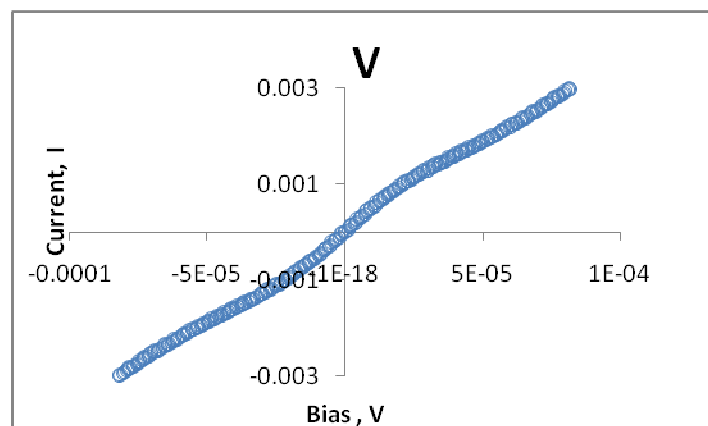
Fig. 10. 7. I-V curve for the point contact Nb/Cu configuration

Etched Niobium tip was used to make point contact against Copper slab which was made by cutting a bigger Cu slab, and by cleaning it with acetone. Normalized conductance data as shown in Fig.10.8 was fitted with modified BTK model. The fitting was done for superconducting gap of Niobium as 1.5 meV. Even though the data was taken at 1.36K, the best fitting was possible for the temperature of 3.1K. Thermal broadening might have been the cause for the need of higher temperature as fitting parameter for the best fit of the data. The barrier scattering potential was found to be Z = 0.677. The fitting not only yields the conductance curve, it also allows to extract the spin polarization of the sample that is used to make point contact with the superconducting tip. The extracted value of spin polarization for copper was found to be P = 0 as expected for normal metal.
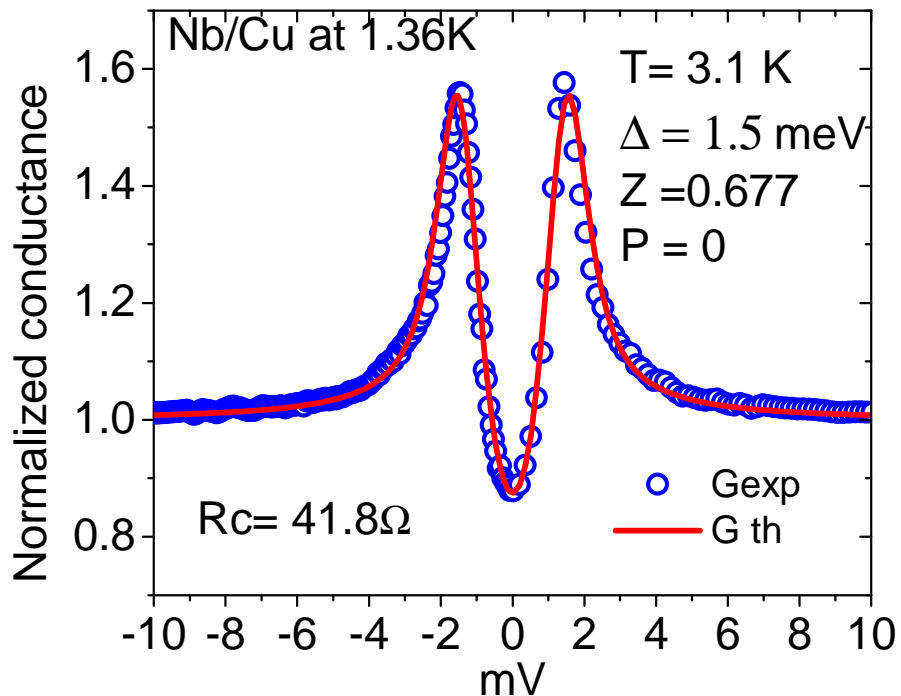
Fig. 10.8. Normalized conductance curve for Nb/Cu slab configuration

Purity of sample is essential factor for reliable data. Copper single crystal was taken after it was etched with the acid solution same as the one used for Nb etching. The single crystal was dipped into the acid solution for short time to remove any oxide layer on the surface. As used for the previous case, Nb tip was used after dipping into HF for a while. The data was taken for conductance curve which was fitted with the same fitting program (noresist) as in the previous case. Fitting was done separately for the data for the positive and negative bias voltages. The fitting was possible even in this case at slightly elevated temperature of $T = 1.9K$ which was not much higher than the actual temperature of He while taking data. The Ruthenium thermometer was used to measure the temperature of He while being pumped, and at the time of taking data the temperature was 1.2K. As in the previous case the need of higher temperature might be due to thermal heating while making the contact and on passing current through the junction. The superconducting gap of Nb was used 1.55 meV. The interfacial barrier scattering which plays important role in the shape of the conductance curve was found to be $Z = 0.78$, and the spin polarization of Cu was extracted to be 0. Slight change of the value of Z was observed in different observations. This is inevitable in point contact experiment due to the difficulty to maintain identical contacts. However, small changes in the values of T and Z in the fitting don't change the value of P for Cu. As anticipated, the value of the spin polarization was found zero in several observations for Cu in the configuration being used. Several conductance curves were taken for different contacts, and also with Sn as superconducting tip. The fitting parameters with correspondingly extracted values of Z and P in these observations are given in Fig.10.9.
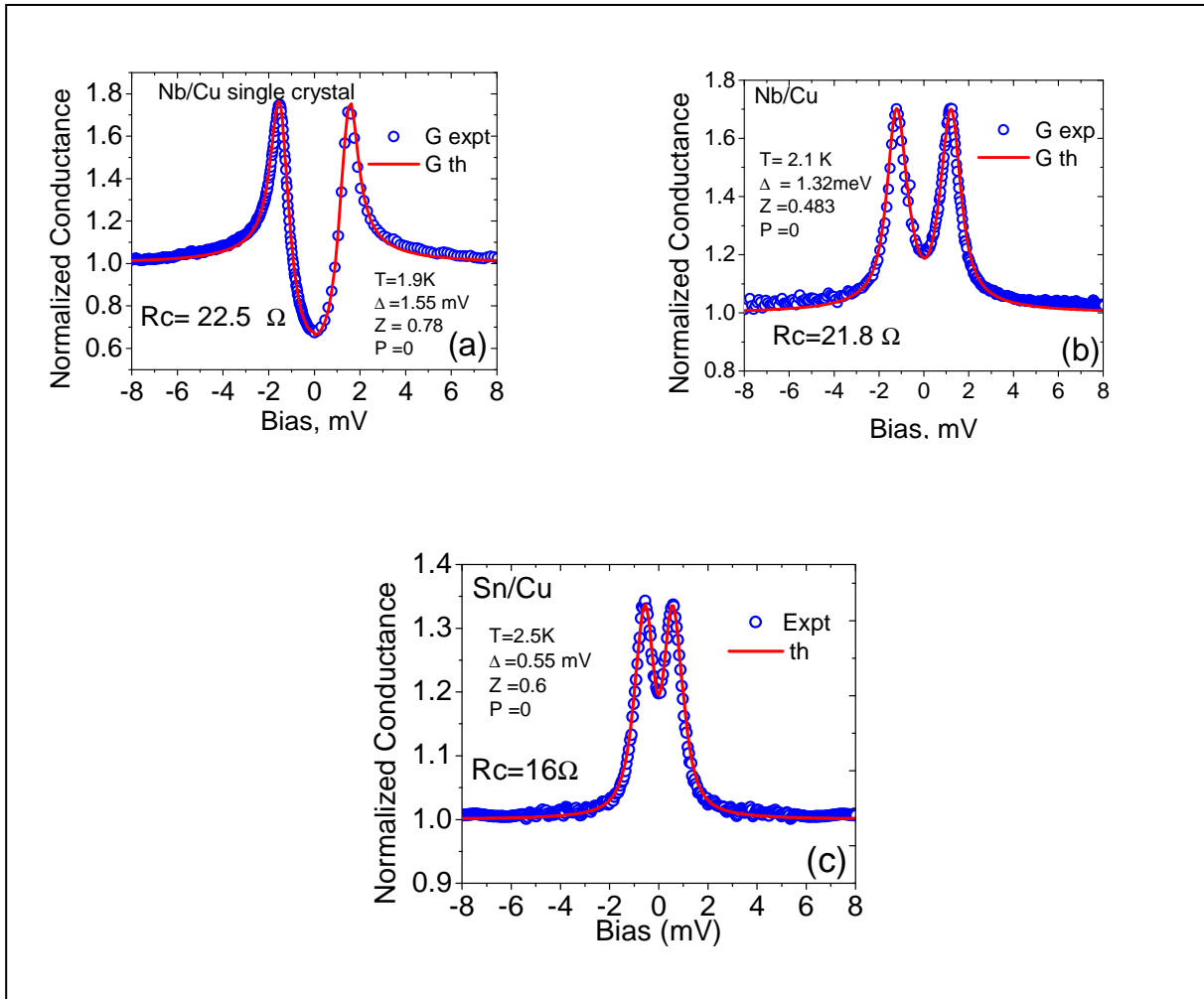
Fig. 10.9. Conductance curves corresponding to different contact resistances for Nb/Cu [(a) and (b)]; and for Sn/Cu [(c)].

As a test of the PCAR set up for its reliability, the measurements were done in other standard LSMO sample. The data obtained are discussed in the following sections.

10.2 PCAR of LSMO ($La_{0.7}Sr_{0.3}MnO_3$)

Conventional half metals in which the density of electrons in the minority bands at Fermi level is zero, and the density of electrons is only in the majority bands at Fermi level are supposed to have almost 100% spin polarization. Possible application of such materials in spintronic applications such as non-volatile logic and memory and spin transistors has attracted the attention of scientists to study such materials. Due to colossal magneto resistance, manganese perovskites, $La_{1-x}A_xMnO_3$ (A = Ca, Ba, or Sr), which are also called CMR Oxides have attracted interests of researchers. However, different reported experimental values of spin polarization of optimally doped $La_{0.7}Sr_{0.3}MnO_3$ (LSMO) have put it in controversy [Nadgorny, 2007]. The reported values [Park et al., 1998; Lu et al., 1996; Sun et al., 1997; Worlege et al., 2000] of spin polarization (35%-100%) was found to vary according to the measurement technique, the use of the definition of spin polarization, and the type of sample such as single crystal or epitaxial films or irradiated films [Nadgorny, 2007]. As reliability test of the PCAR system, and a test of reproducibility of spin polarization, optimally doped $La_{0.7}Sr_{0.3}MnO_3$ (LSMO) sample was used to measure spin polarization. The conductance curves obtained for two different contacts of Nb as superconducting tip to the LSMO single crystal are shown in Fig. 10.10. These data were taken at 1.2K, and the fitting was done with superconducting gap of Nb as 1.5 meV. The extracted values of spin polarization was 58.4% which agrees with the reported value of P=58% for the LSMO single crystal with Sn as superconducting tip [Nadgorny, 2007]. Unlike conventional half metals, experimental results [Nadgorny et al., 2001] have indicated that LSMO has minority spin states at Fermi level, but still mimics the behavior of a true half-metal in transport experiments, hence the material can be called a *transport* half-metal [Nadgorny et al., 2001].
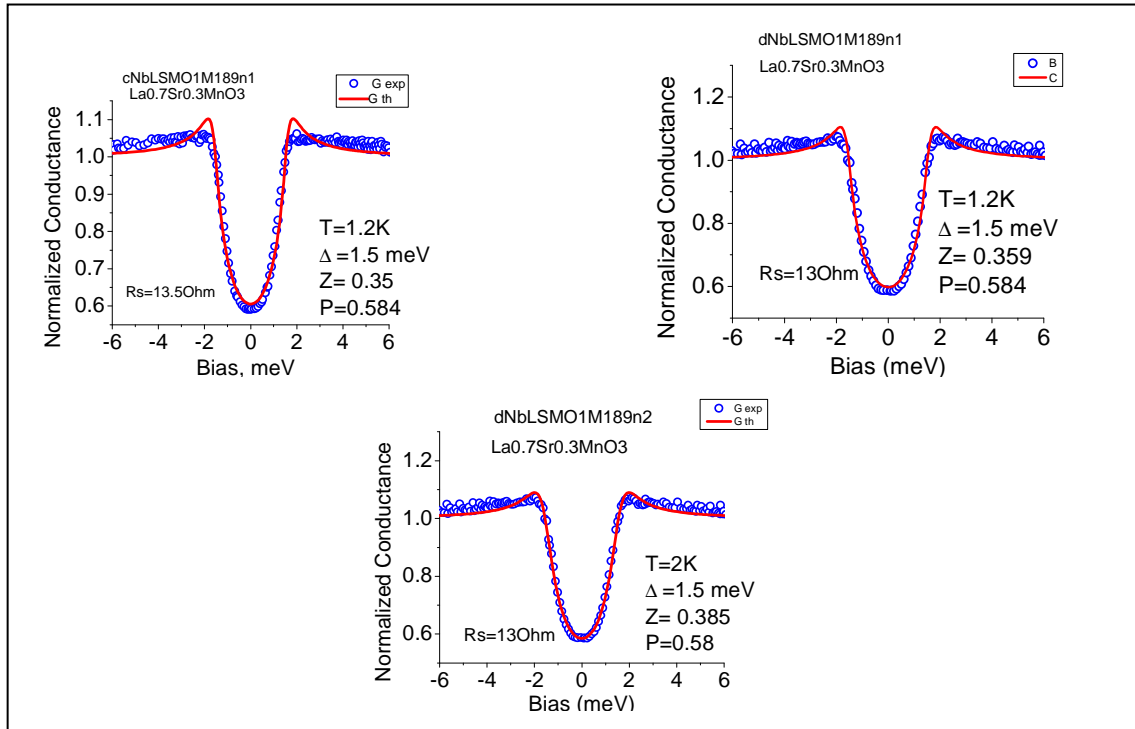
Fig.10.10. Normalized conductance curves for Nb/ LSMO interface showing the spin polarization of 58%.

The temperature dependent conductance curves for $La_{0.7}Sr_{0.3}MnO_3$ are different, however, its spin polarization is reported to be independent of temperature. Rather it was reported to be dependent on the residual resistivity of the samples indicating that the defect level in the sample plays important role to control P value [Nadgorny, 2007].

In conclusion, PCAR measurements of Cu sample gave the value of spin polarization to be 0 as reported by other people. The conductance curve can have various shapes dependent on the contact. Spin polarization value for $La_{0.7}Sr_{0.3}MnO_3$ sample was reproducible and agreed with the reported value of 58% for single crystal. Hence, the point contact measurement set up works fine with the capability of measuring the spin polarization values of different samples with high precision.

CHAPTER 11

POINT CONTACT ANDREEV REFLECTION STUDIES OF ITINERANT MAGNET MnSi SINGLE CRYSTALS

11.1 Introduction

Manganesesilicide has drawn attention of researchers for a long time due to its varieties of magnetic and electrical properties (Williams et al., 1966, Shinoda et al., 1966, Wernick et al., 1971). Its crystal structure is generated by the cubic B20 structure (Borèn et al., 1933, van der Marel et al., 1998). The unit cell contains 4 Mn atoms at crystallographycally equivalent positions, with the basic structural element as an equilateral triangle of three Mn atoms. Each Mn atom connects three triangles sharing the corners, with the triangles at four different orientations along the body diagonal of the cubic unit cell (Carbone et al., 2006). Figure 11.1 shows two views of B20 crystal structure of MnSi. It is traditionally considered weakly itinerant ferromagnet (Moriya et. al., 1973; Taillefer et al., 1986), i.e. the spin polarization is modeled as a relative shift of bands of delocalized Bloch states for the two spin directions (Carbone et al., 2006). There are several evidences of why MnSi in the induced ferromagnetic (paramagnetic) state can be classified as a weak itinerant ferromagnet (Ishikawa et. al., 1977). MnSi undergoes magnetic phase transition when magnetic field is applied below critical temperature. Neutron small angle diffraction study revealed that in zero magnetic field MnSi has the helical spin structure below $29.5 \pm 0.5K$ with the long period of 180Å propagating along the [111] direction (Ishikawa et al., 1976). When a magnetic field is applied greater than 0.6T the crystal is saturated with spontaneous magnetic moment of $0.4\mu_B$ per Mn atom, which is substantially smaller than the effective moment of $1.4\mu_B$ evaluated from the Curie-weiss relation in paramagnetic region as reported by Ishikawa et al., 1976, and that of $2.2 \mu_B$ per Mn in the

paramagnetic phase as reported by Wernick et al., 1972. This difference is considered as a signature of the itinerant nature of magnetism (Stishov et al., 2008).
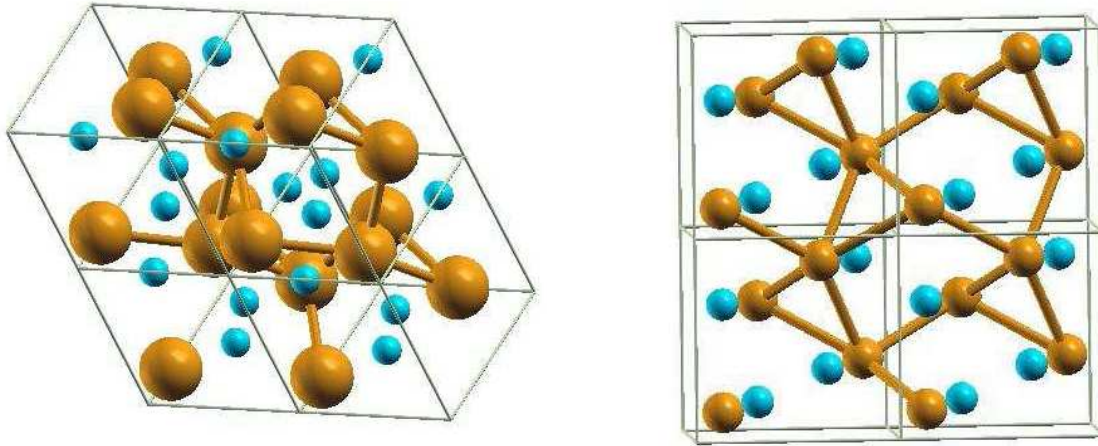
Fig. 11.1 Two views of the B20 crystal structure of MnSi, showing four cells. The larger atoms are Mn and are connected by sticks; the smaller spheres are Si atoms. Left: a view along the (111) direction. Right: view nearly along the (100) axis (Jeong et al., 2008)

Magnetic phase diagram of MnSi is shown in Fig. 11. 2. It shows that the spin structure at zero external field is helical. If magnetic field of about 1 KG is applied, the moments tilt toward the applied magnetic field and hence form conical structure. The cone becomes smaller in angle as the magnetic field is increased. When H is 6.5 KG, the moments are aligned in the direction of the external field, with the crystal reaching the saturation magnetic moment of 0.4 μ_B, and hence MnSi becomes induced ferromagnetic, which is shown in the phase diagram by solid line. The broken line indicates a boundary where the magnetic moment induced in the field direction decreases distinctly (Ishikawa et al., 1977). Three energy scales govern the magnetic properties of MnSi. Exchange interaction, the strongest energy scale, between the spins keeps them on plane ordering. Weaker than exchange interaction is Dzyaloshinskii Moriya spin-orbit interaction ($H = \mathbf{D} \cdot (\mathbf{S}_i \times \mathbf{S}_j)$) which is responsible for the chirality of the spin structure i.e., helical

structure, and the axis of the helix is kept in (111) direction by even weaker exchange-crystal anisotropic interaction in MnSi crystals.
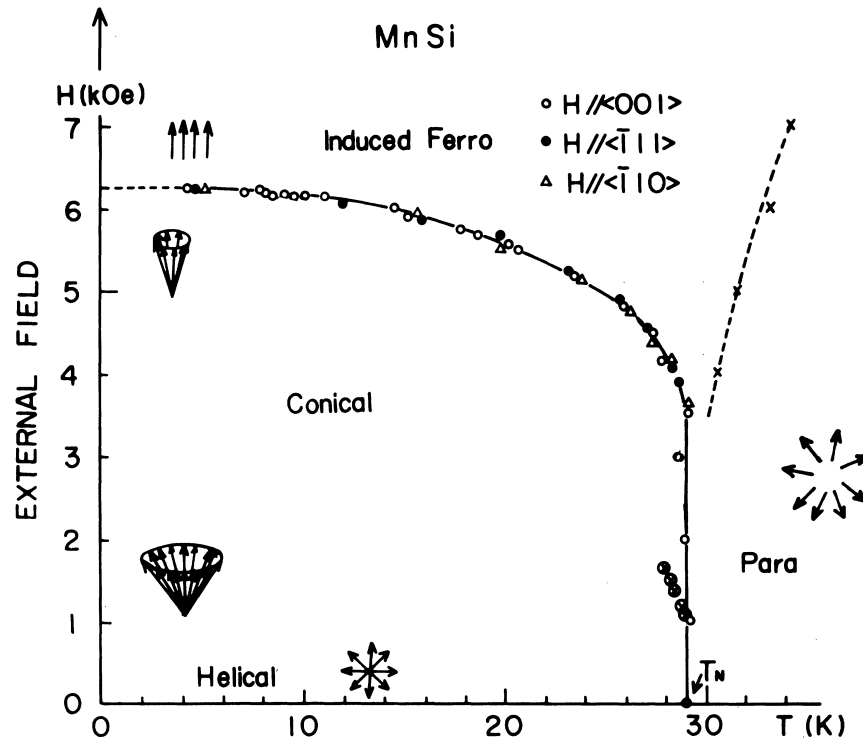
Fig. 11.2 Magnetic phase diagram of MnSi (Ishikawa et al., 1977)

MnSi might be an ideal playground to study the properties of itinerant magnets in general, which are one of the less understood and yet more interesting materials (Carbone, 2007). In this context, we are motivated in exploring another property i.e., spin polarization of MnSi which has not been done by any one so far. Spin polarization is well defined in conventional ferromagnets and has been measured by different techniques such as positron scattering, Tedro-Meservy, tunneling spectroscopy, photoemission spectroscopy and point contact Andreev reflection spectroscopy. However, this property has not been investigated in case of MnSi, with very unusual magnetic properties, exhibiting various magnetic structures from helical to conical

to induced ferromagnetic phase. So, in this research we wanted to study transport properties of MnSi, and to detect any possible changes in spin polarization as MnSi undergoes various magnetic transition.

11.2 Magnetization and AC susceptibilities measurememnts of MnSi

Magnetization and susceptibility measurements were done by SQUID, and they were taken by using MnSi single crystal grown by floating zone technique. Susceptibility measurement, as shown in Fig.11.3 (a), shows that the susceptibility suddenly increases at 30 K showing that the magnetic ordering begins at this temperature. When the magnetic field of 1 KG is applied the susceptibility even goes higher at this temperature indicating that the helical phase changes to conical phase. When the increasing magnetic field reaches to about 6.5 KG, we can see that the susceptibility curve shows different behavior showing the transition from conical phase to induced ferromagnetic phase.

Magnetization measurement (Fig. 11.3 (b)) shows that the magnetization is saturated at 6.5 KG and the saturation magnetization is ~0.4 Bohr magneton/ Mn at low temperature (5K). Susceptibility and magnetization measurements are consistent to each other and also consistent to the literature.

(a)   (b)
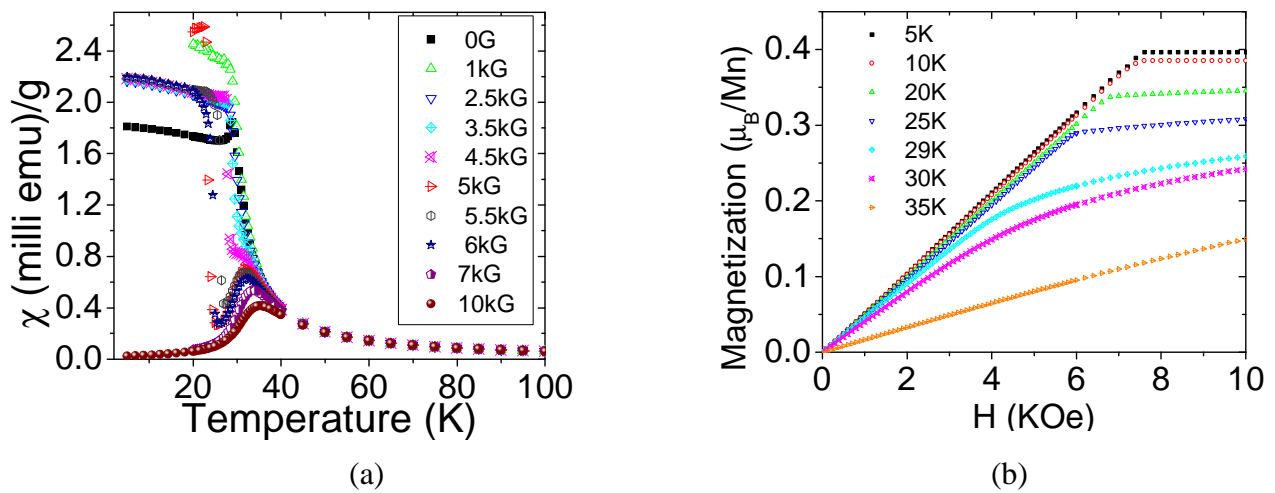
Fig. 11.3 Left: AC susceptibility, Right: magnetization measurements for MnSi single crystal

11.3   Resistivity measurements of MnSi single crystal

Resistivity measurement also shows the phase transition at ~30 K as shown in Fig. 11.4.
T^2 dependence of resistivity below Tc shows that the transport is governed by the spin
fluctuation. Resistivity at 2K was 5 μΩcm showing that the MnSi single crystal we used was a
good conductor.
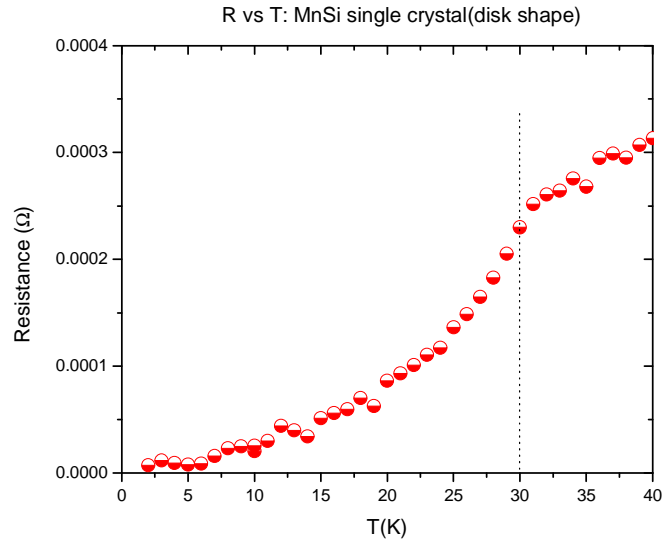
Fig. 11.4. Resistivity of MnSi single crystal as a function of temperature

11.4   PCAR measurements of spin polarization of MnSi

Presence of magnetic moment and low resistivity showed that the crystal being used for
magnetic and transport measurements was good for spin polarization measurements. We used
Andreev reflection spectroscopy to measure spin polarization. Andreev reflection is a process of
converting normal current to super current at the junction of a metal and a super conductor. In a
normal metal in which the spin polarization is zero, there are spin-up and spin-down bands at the
Fermi level. A spin up electron takes a spin down electron at the Fermi level to form a Cooper
pair which travels through superconductor if the applied energy is less than superconducting gap.
This process enhances the current. In case of highly spin polarized materials like half metals in

which P = 100%, a spin up electron does not get spin down electron in the Fermi level so that cooper pair cannot be formed. This results in suppression of current.

Spin polarization is given by the formula,

$$P_C = \frac{< N_\uparrow(E_F)v^n_{F\uparrow} > - < N_\downarrow(E_F)v^n_{F\downarrow} >}{< N_\uparrow(E_F)v^n_{F\uparrow} > + < N_\downarrow(E_F)v^n_{F\downarrow} >}$$

$$= \frac{I_\uparrow - I_\downarrow}{I_\uparrow + I_\downarrow}$$

We pass current through the junction between a superconducting tip and a metal, MnSi in this case; and measure voltage and conductance. The conductance curves obtained are fitted using modified BTK model.

11.4.1 Point contact by approaching the superconducting tip by squiggle

MnSi single crystal was polished mechanically to get the best possible shining surface free of any scratches. It was mounted in a probe and was mounted into PPMS. For our experiment, we used electrochemically etched Niobium tips whose small protrusions at the tip have size of couple of micrometer. Such a tip is mounted in a tip holder as shown schematically in Fig. 11.5 (a). The tip holder is driven by squiggle piezoelectric motor as shown in Fig 11.5 (b).

(a)   (b)
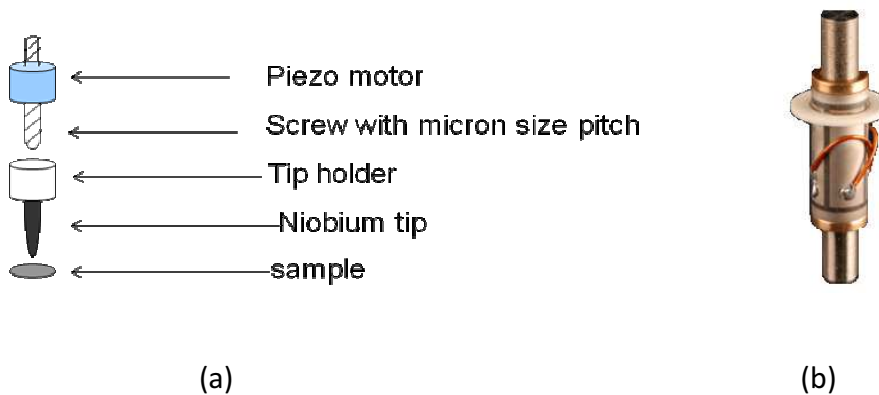
Fig. 11.5 Superconducting tip holder (a) schematic, (b) Squiggle motor

Conductance curves were fitted and the spin polarization was extracted from the fitting parameters. Several conductance curves were fitted for the data taken for different point contacts at 2K. The average value of spin polarization was found to be 44±4%. The spin polarization was extracted from the conductance curves taken even at 1.2 K, and it was found to be 47.8% which is within the error bar of the average value. An example of such conductance curves is given in Fig. 11.6 as representative of several curves taken and fitted for the extraction of spin polarization. The interfacial scattering barriers which are extracted by fitting the curves and are denoted by Z are shown in individual plots.
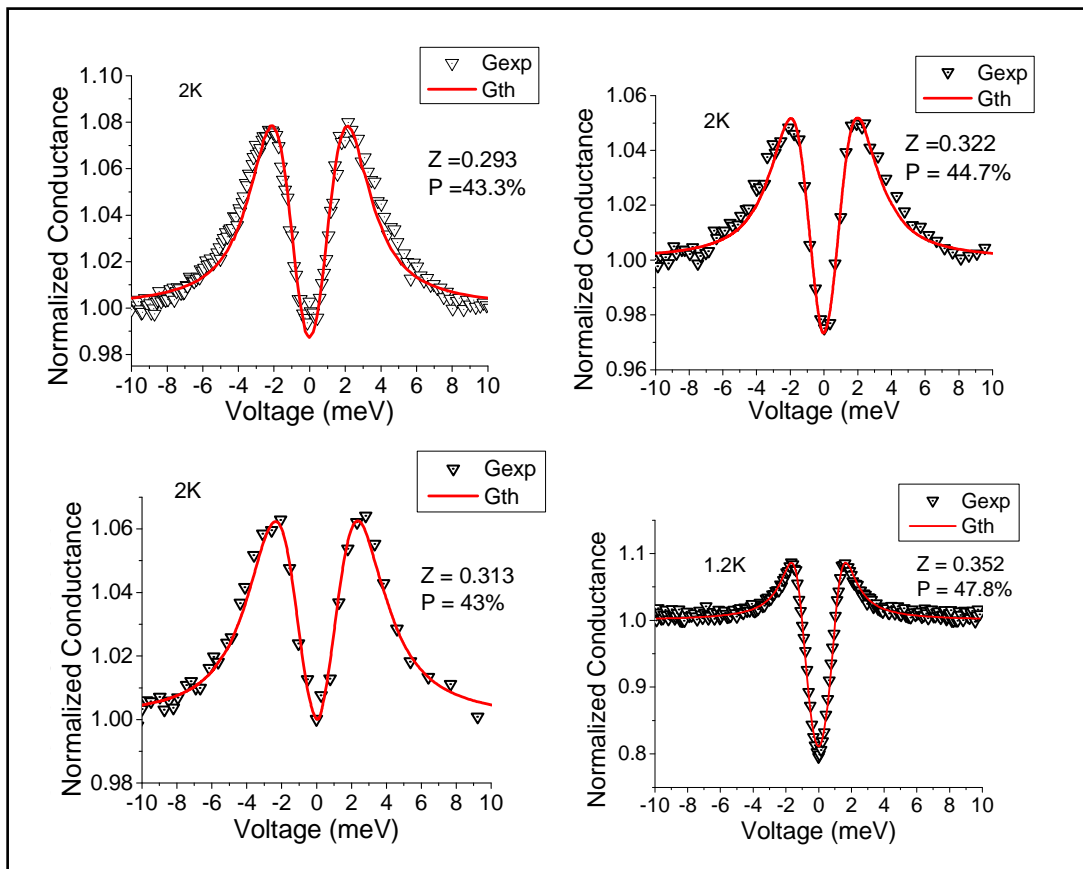
Fig. 11.6 Normalized conductance curves obtained for MnSi single crystal with Nb superconducting tip

11.4.1.1 Magnetic field dependence conductance curves of MnSi

We wanted to detect any possible change of spin polarization with the magnetic field as MnSi underwent magnetic phase transition. We saw some change in P at different magnetic fields. Fig 11.7 shows the field dependence conductance curves taken at 2K. These spectra show that the amplitude of the conductance curves decreases with higher external magnetic field.
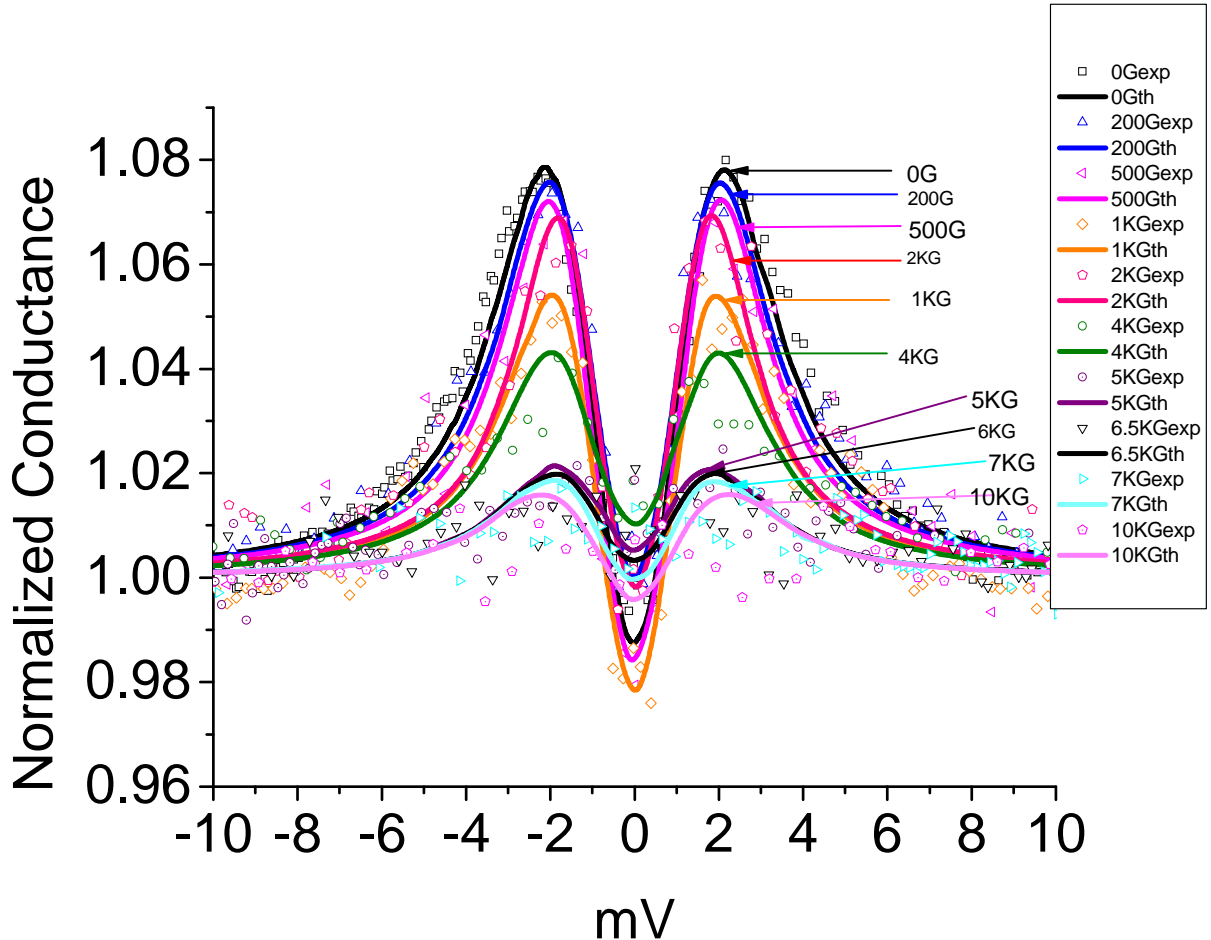
Fig. 11.7 Magnetic field dependence normalized conductance curves for MnSi single crystal

However, we found in literature (Miyoshi et al., 2005) that people have obtained conductance curves of Nb/Cu point contact system at different applied magnetic fields. They have shown the change in conductance with the applied magnetic field as shown in Fig. 11.8. The top graph shows the change when magnetic field is parallel to Nb tip, and the bottom graph

shows the change when the magnetic field is perpendicular to the Nb tip. We also observed similar type of change of conductance curves in Nb/MnSi system when H is parallel to the Nb tip. So, at this point it is hard to differentiate the contribution of Nb and MnSi. This needs further investigation.
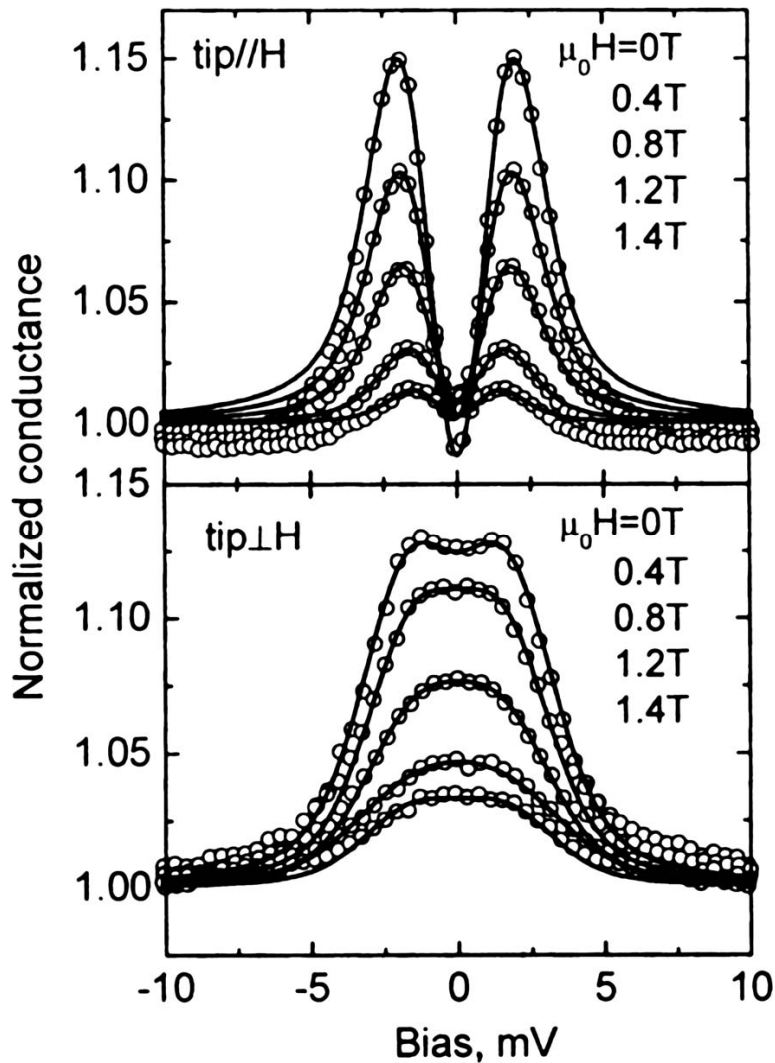
Fig. 11.8 Magnetic field dependence of conductance curves for Nb/ Cu system, Top: when Nb tip is parallel to the applied magnetic field, Bottom: when Nb tip is perpendicular to the applied magnetic field (Miyoshi et al., 2005).

Finally, in conclusion, we have studied spin polarization in MnSi single crystals characterized by Tc of 29.5 K with saturation magnetic moment of $0.4\mu_B$/Mn at 5K and a residual resistivity of $5\mu\Omega$cm. And, the average spin polarization of MnSi single crystal as measured by PCAR technique by driving the superconducting tip by squiggle motor was found to be 44 ± 4% in zero magnetic field. With increasing magnetic field, when the maganese monosilicide single crystal undergoes magnetic phase transition, the spin polarization is found to be higher as the transition is from helical to conical to induced ferromagnetic. Figure 11.9 shows how P is found to change with H. It is seen that the increase is not monotonic, rather the spin polarization saturates beyond the magnetic phase transition to the induced ferromagnetic phase when the applied magnetic field is about 6.5KG. This is consistent with what one expects as the magnetic moments are aligned in the direction of applied field.
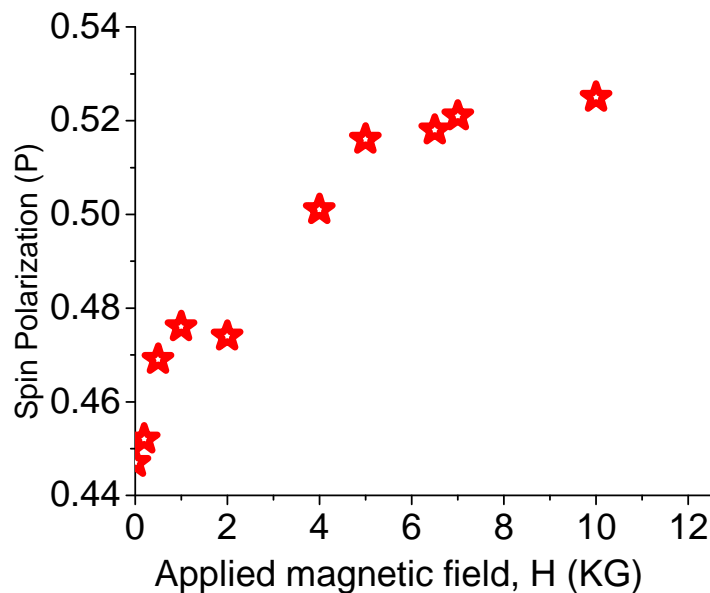
Fig. 11.9 Magnetic field dependence of spin polarization of MnSi as it goes under magnetic phase transition.

11.4.1.2   Approaching the superconducting tip manually

Conductance curves were also obtained by driving the superconducting tip manually to bring it in point contact with MnSi. This arrangement gives more flexibility in control of the contact resistance. Conductance curves were obtained for different contact resistances. In this arrangement, the facility of pumping liquid Helium allows to lower the temperature below 2K which was the minimum limit that could be achieved while using PPMS for point contact experiments by as discussed in section 11.4.1. With this arrangement, the data were taken at 1.5K , and the mBTK fittings were done with cuperconducting gap value of Nb as 1.5 meV. The fitting parameters and the extracted values of P and interfacial barrier scattering Z are shown in the corresponding plots shown in Fig. 11.10.
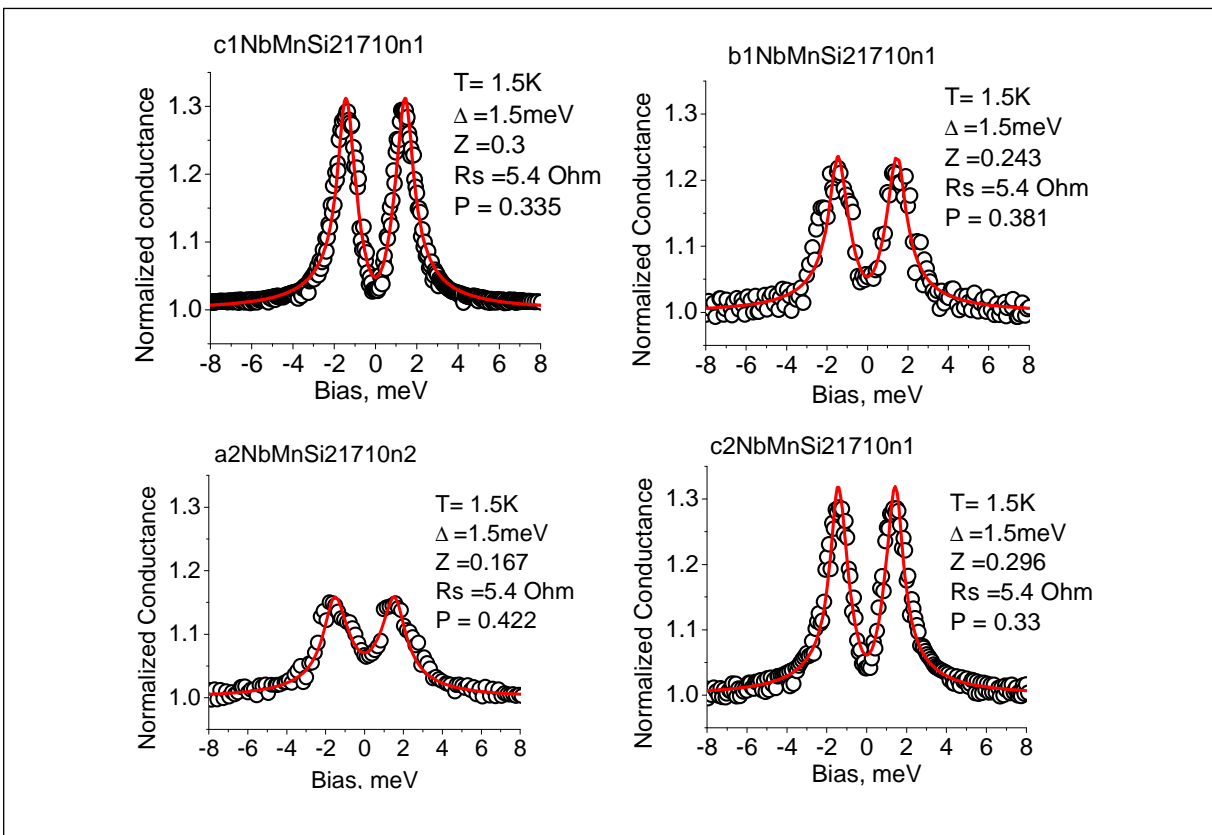
Fig. 11.10 Normalized conductance curves for Nb/MnSi interface while the superconducting tips were driven manually

It was observed that the P values have quadratic dependence on Z values. So, the intrinsic value of P, which corresponds to Z = 0, was found from the extrapolation of P (Z) curve as shown in Fig.11.11. This gives the intrinsic value of P to be 45.2% which is within the error bars in previous measurements by squiggle technique. This confirms the reliability of the spin polarization values of MnSi single crystal.
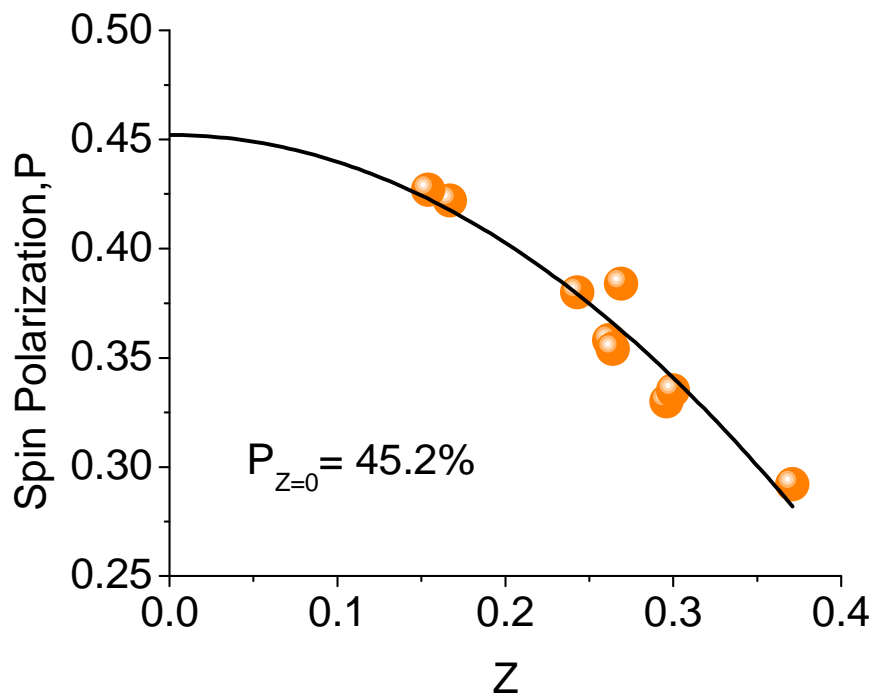
Fig. 11.11 Dependence of P on interfacial barrier scattering

11.4.1.3   **Conductance of the interface between Nb thin film sputtered on MnSi after**

               e-beam lithography on PMMA

In the previous measurements by squiggle and manual techniques to approach the Nb tip, it was not easy to get clean field-dependent and temperature-dependent data. Thinking that the situation can be improved if Nb contacts are made on MnSi by e-beam lithography and depositing Nb, one more technique was implemented to get conductance curves of Nb/MnSi interface. Interestingly, new features such as zero-bias conductance with amplitude greater than 2 and conductance oscillations outside superconducting gap have been observed which may be due to the formation of triplet Cooper pairs at the interface of Nb and MnSi in the geometry being used. This is discussed hence forth.

11.4.1.3.1   **E-beam lithography on MnSi surface and Nb deposition**

On the surface of polished MnSi single crystal, PMMA 950A4 was spin coated. It was baked for 15 minutes at 180°C. E-beam lithography was done on the surface of PMMA to open two square holes each of 1μm×1μm, and 10μm apart as shown in Fig. 11.12, which is the optical image taken after the lithography was developed.
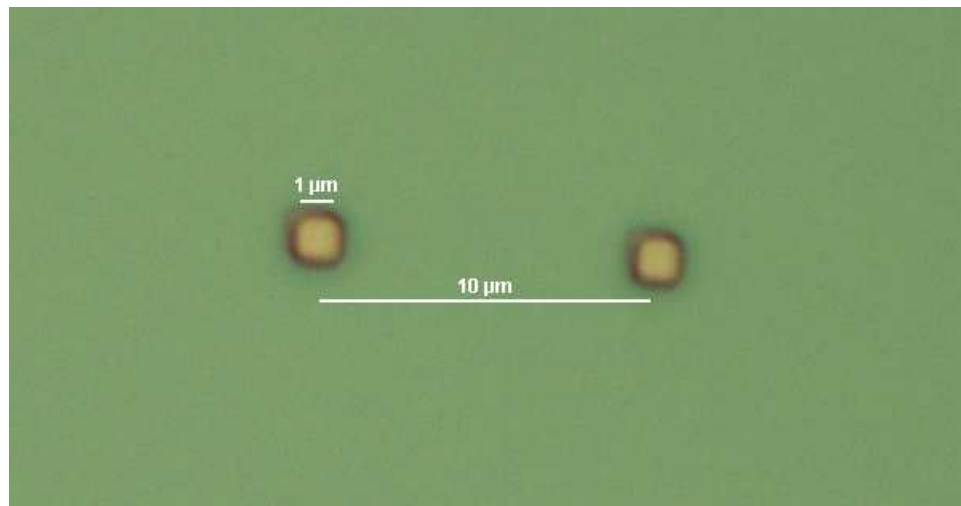
Fig.11.12. Optical image of the openings on PMMA after the lithography was developed

With appropriate masking, Nb was deposited by sputtering on and within the area of PMMA so that Nb would come in contact with MnSi surface only through the opened holes shown in Fig. 11.12. The Nb film sputtered at the chamber pressure of 1.4×10^{-7} Torr showed superconducting transition temperature T_c of 5.5K as shown in Fig. 11.13.
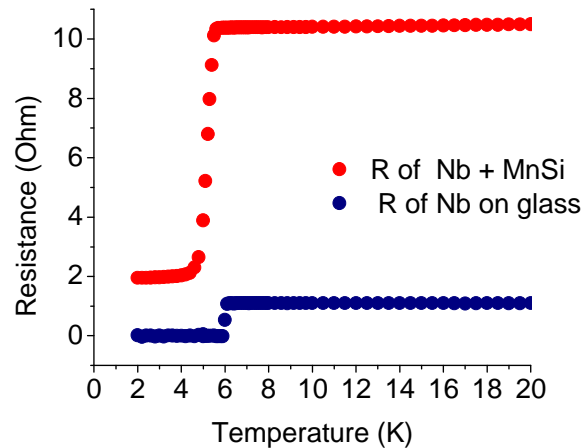
Fig. 11.13 Superconducting transition temperature of Nb thin film (Red: includes Nb and MnSi; Navy: Nb on glass)

11.4.1.3.2   Magnetic field dependent and temperature dependent conductance curves

Silver paste contacts were made on Nb film and MnSi. Magnetic field dependence at 2K with field perpendicular and parallel to the sample surface, and temperature dependence conductance curves in both cases were obtained which are catalogued below:

a.1) Field dependence of conductance curves with magnetic field parallel to the Sample surface (B∥Surface) at 2K

This configuration of sample with the magnetic field parallel to the sample surface was achieved after some data were taken in the perpendicular configuration at 2K. The purpose of mentioning the sample configuration-sequence is to discuss about the topography change observed on the sample surface. This will be discussed in the next section. Figure 11.14 shows

the magnetic field dependence normalized conductance curves for the Nb-MnSi interface. Surprisingly, the conductance curves are different in this lithographically defined interface of Nb and MnSi compared to the conductance curves obtained for manually obtained point contacts as discussed earlier. The amplitude of zero-bias conductance was highest when no external magnetic field was applied. It kept on decreasing as the magnetic field was increased. However, the amplitude was still more than 2 until the applied magnetic field was more than ~ 25KG. The amplitude of zero bias conductance decreases faster for the magnetic field more than ~30KG. There exists a small zero bias conductance at ~35KG. However, it disappeared completely at around 38KG. This may be due to the destruction of superconductivity of Nb due to the applied magnetic field.
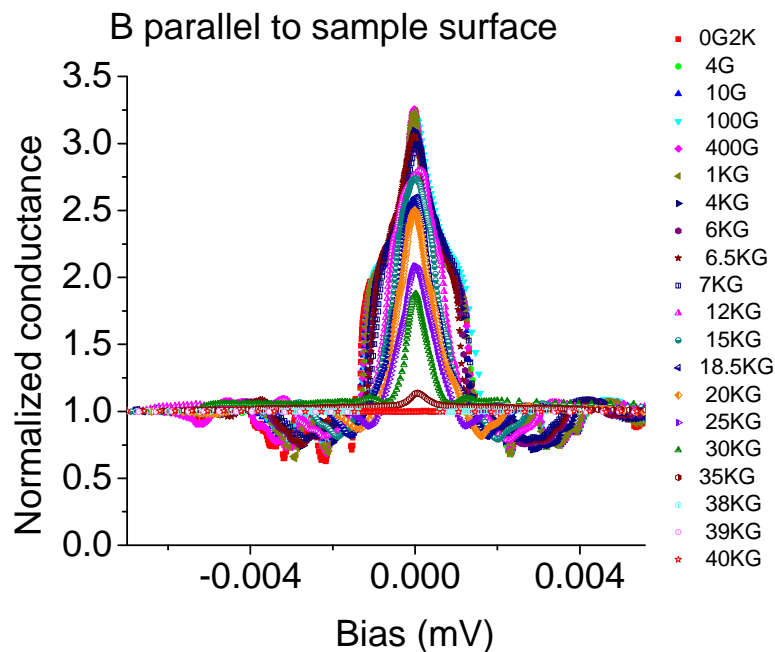
Fig. 11.14. Normalized conductance curves at different magnetic fields parallel to the sample surface at 2K for Nb/ MnSi interface defined by e-beam lithography

For the purpose of clarity, the normalized conductance curves presented in Fig 11.14 are plotted again in Fig. 11.15 after the curves are shifted separating consecutive curves by 0.4. This

allows one to see clearly how the curve features are changing from no applied field (top curves) to high applied field of 40KG (bottom curves).
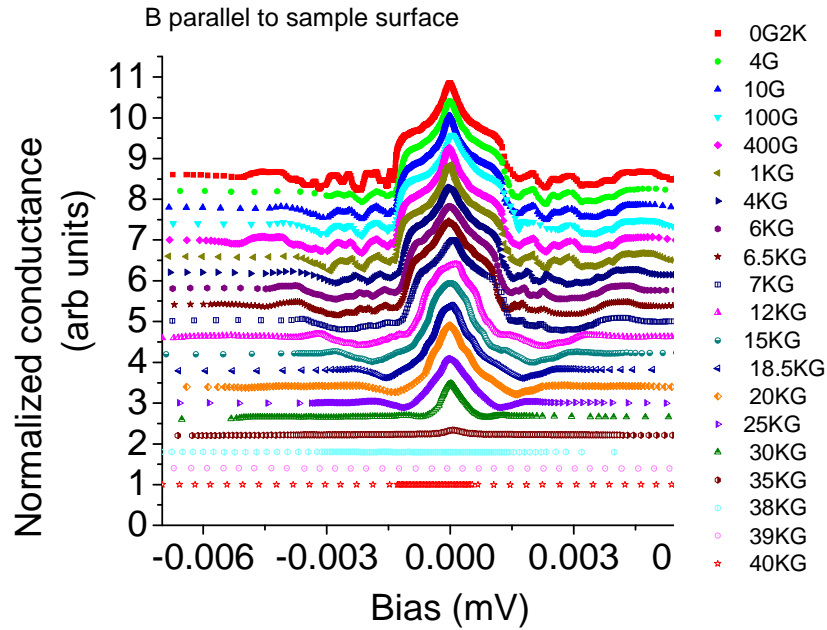
Fig. 11.15. Normalized conductance curves with shift in y-axis for clarity for Nb/MnSi interface defined by lithography and when it is in parallel configuration.

Interestingly, the other unusual feature of these conductance curves is the presence of conductance oscillations outside superconducting gap. These oscillations decay as we go farther from the superconducting gap edge. With the increasing magnetic field the amplitudes of these oscillations decrease, and disappear after H = 6.5KG is applied. Below this magnetic field, the oscillations in different conductance curves obtained at different magnetic fields are in phase to each other (Fig. 11.15). These oscillations disappear when the applied magnetic field is more than 6.5KG [Fig. 11.16]. As we know that MnSi undergoes magnetic phase transition from conical to induced ferromagnetic phase at 6.5KG, it is found that the conductance oscillations do not appear in the ferromagnetic phase.
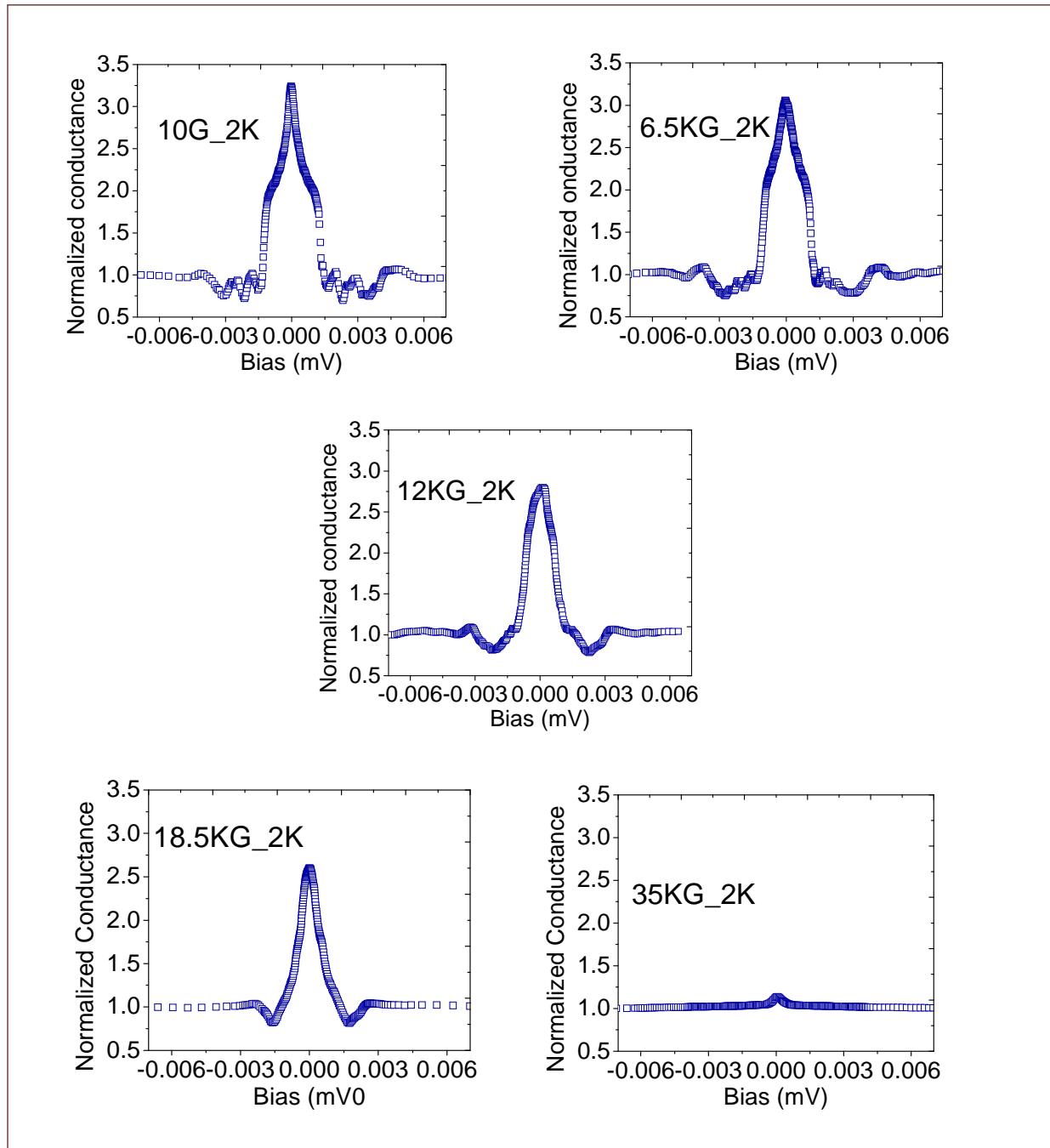
Fig. 11.16. Magnetic field dependence of zero bias conductance, and conductance oscillations outside superconducting gap of Nb in contact with MnSi with its surface in parallel to the applied magnetic field

Figure 11.17 (a) shows the dependence of normalized zero bias amplitude on the applied magnetic field. The amplitude is more than 2 for the magnetic field less than about 26KG. Beyond this magnetic field, the amplitude goes down as the field goes up and finally levels down to 1 when the field is 38KG and more. The amplitude ratio of the first and the second peaks was almost equal to 1 for all conductance curves.

(a)   (b)
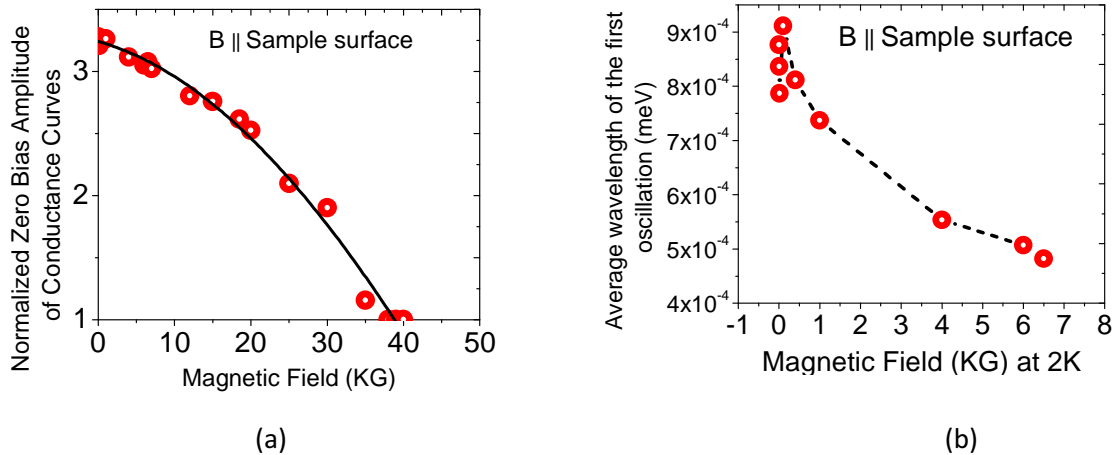
Fig. 11.17   Effect of magnetic field (a) on normalized zero bias conductance, and (b) on wavelength of the first oscillation of conductance curve outside superconducting gap of Nb that is in contact with MnSi

a2) Temperature dependence of conductance curves with magnetic field, B = 0 in parallel

   configuration at 2K

The amplitude and the shape of conductance curves changed with the change in temperature well below T_c of Nb (This Nb film had T_c of 5.5K) indicating that the effect is due to the changes in properties of MnSi. Figure 11.18 (a) shows as collected conductance curves of Nb/MnSi interface at 2K when no external field was applied.   The same set of data after normalization is shown on the right panel. It shows that the zero bias conductance at 2K is about 3.5, and this amplitude decreases with increasing temperature. Figure 11.18 (c) shows the normalized data with a consecutive shift of 0.4 in Y-axis for the purpose of clarity and comparison.
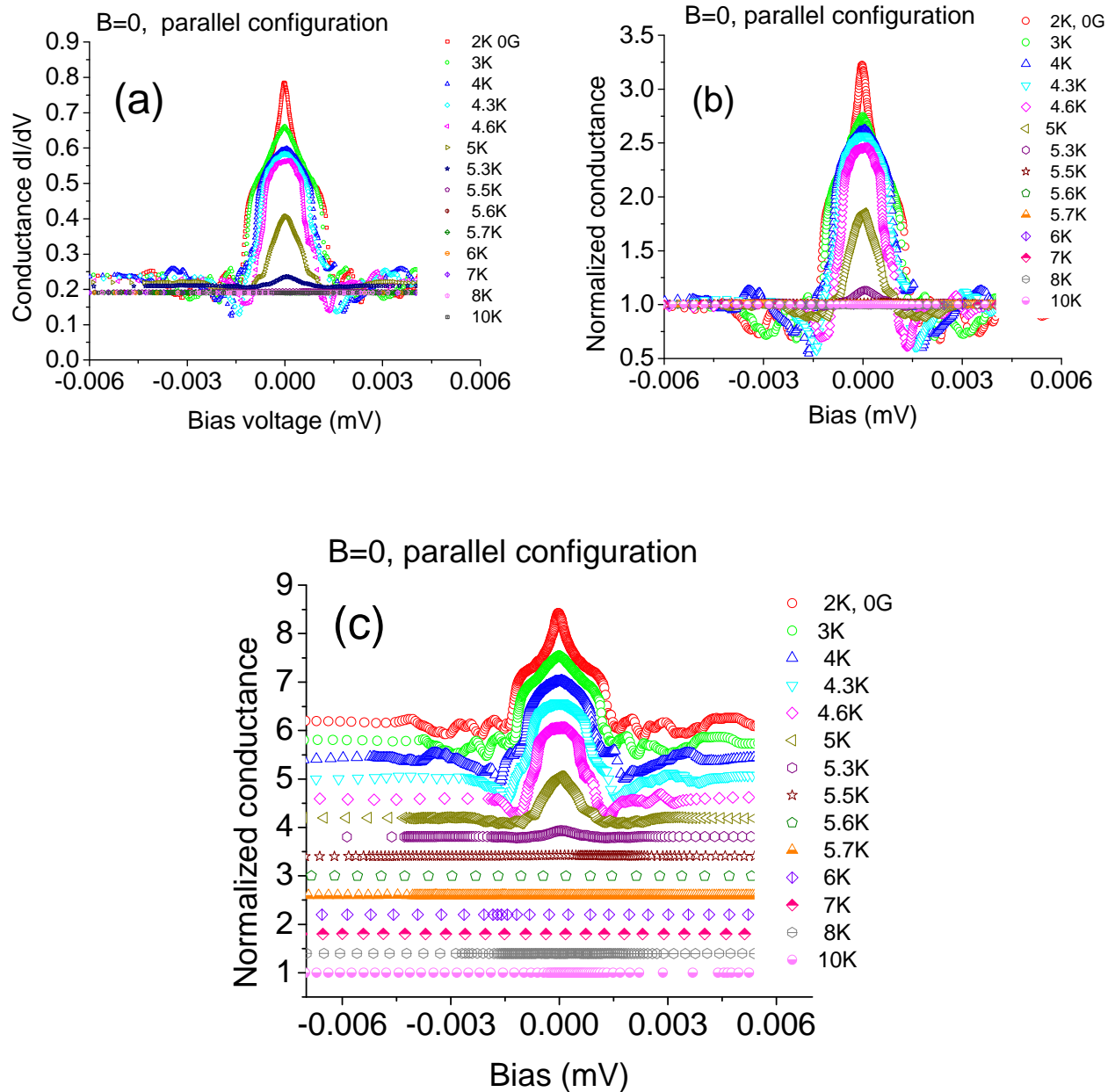
Fig. 11.18 conductance curves for Nb/MnSi interface at different temperatures in absence of magnetic field: (a) as collected, (b) normalized, and (c) normalized and shifted for clarity

The conductance oscillations are present in this case also. In order to show these oscillations more prominently, some of the conductance curves are shown in Fig. 11.19. The amplitudes of oscillations decrease with temperature, and they disappear at 4K and higher temperatures. Zero bias normalized conductance amplitude also keeps on decreasing with temperature, and disappears at 5.5K as shown in the last plot in Fig. 11.19.
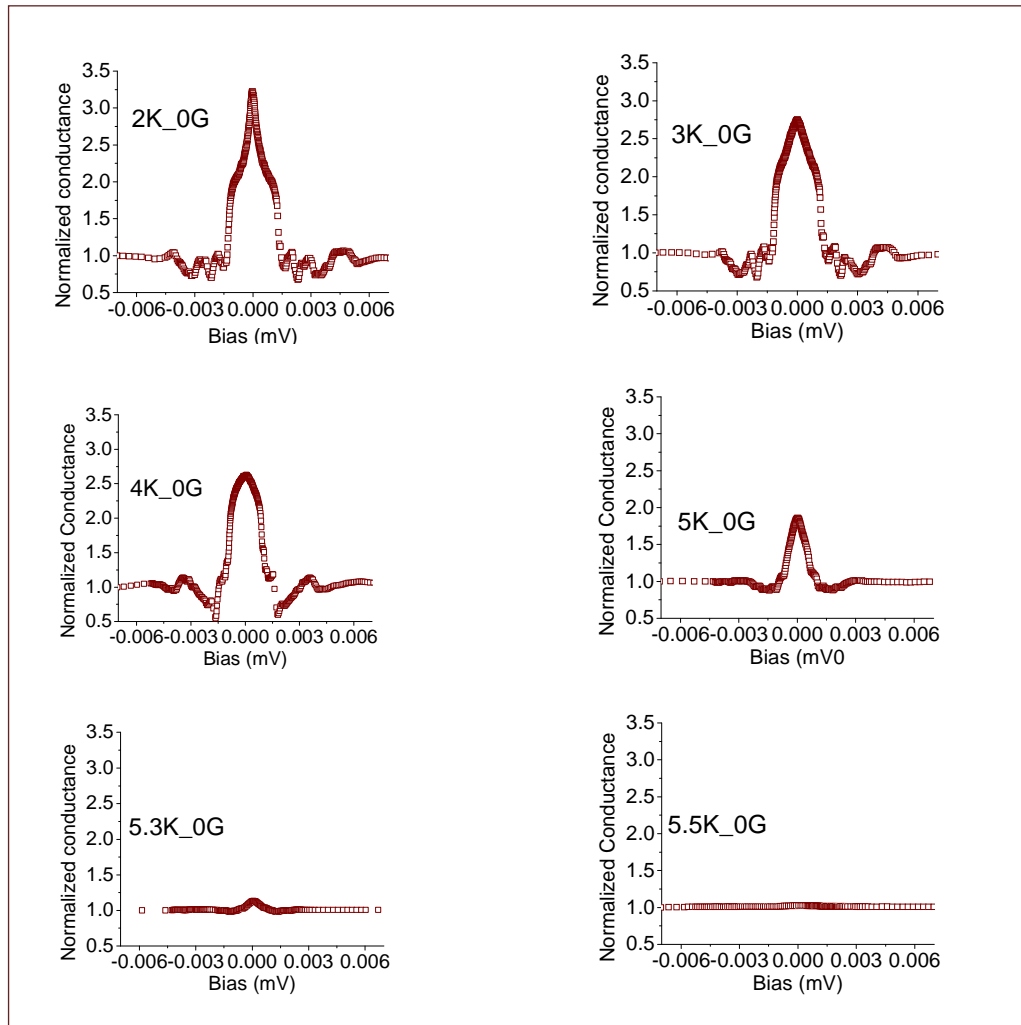
Fig. 11.19. Temperature dependence of conductance curves of Nb/MnSi point contact interface at no external magnetic field applied

The dependence of normalized zero bias amplitude with temperature as observed in the experimental data are shown in Fig. 11.20. It is observed that the conductance amplitudes decrease faster after 4.6K to 5.5K, and then the normalized amplitude just levels to 1 as shown in Fig. 11.20. The wavelength of oscillations is in decreasing tendency with the increasing temperature.
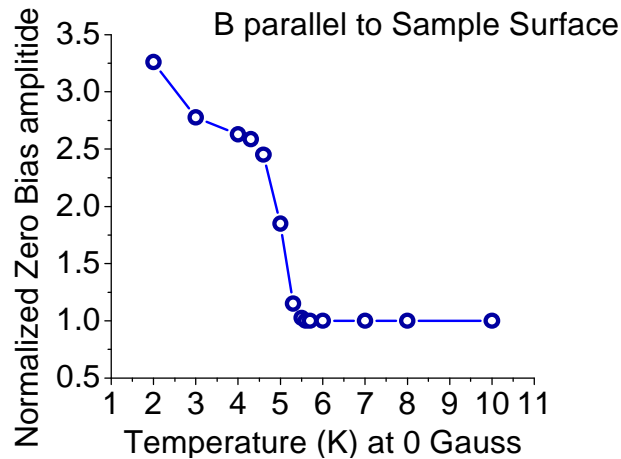
Fig. 11.20 Dependence of normalized zero-bias amplitude on temperature for Nb/MnSi interface in parallel configuration.

After taking field dependence and temperature dependence conductance curves in parallel configuration the sample was taken out from PPMS. The surface of Nb looked different. So, it was observed under optical microscope, and very interesting patterns developed were found on the surface. These patterns shown in Fig. 11.21 were imaged with optical microscope. These patterns were not developed when the sample was kept perpendicular to the magnetic field. They were developed only when the magnetic field was applied parallel to the Nb thin film surface.
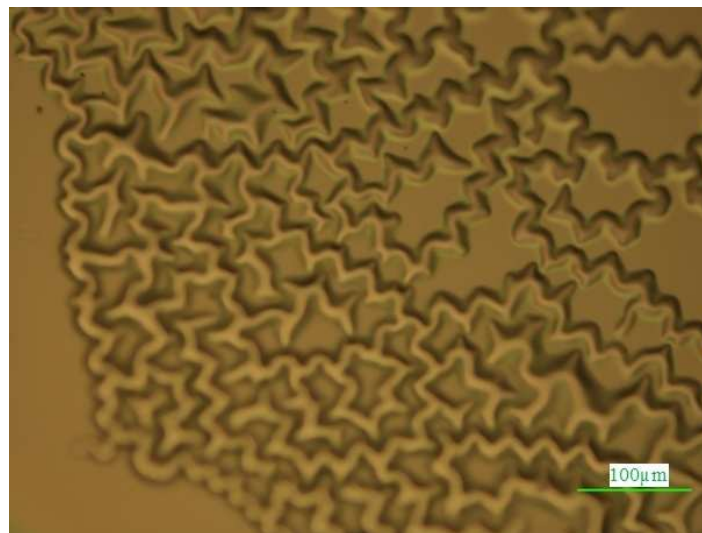
Fig. 11.21. New surface topography developed on Nb film sputtered on PMMA spin coated on MnSi. This was developed when the magnetic field was applied parallel to the sample surface.

b1) Field dependence of conductance curves with magnetic field perpendicular to the Sample surface (B ⊥ Surface) at 2K

The sample was mounted again into PPMS with its orientation restored in previous configuration, i.e. the sample was kept such that Nb deposited surface would be perpendicular to applied magnetic field. The data obtained in this configuration are given in Fig. 11.22. These conductance curves were almost similar to those in parallel configuration, but with smaller zero bias amplitude compared to the parallel configuration.
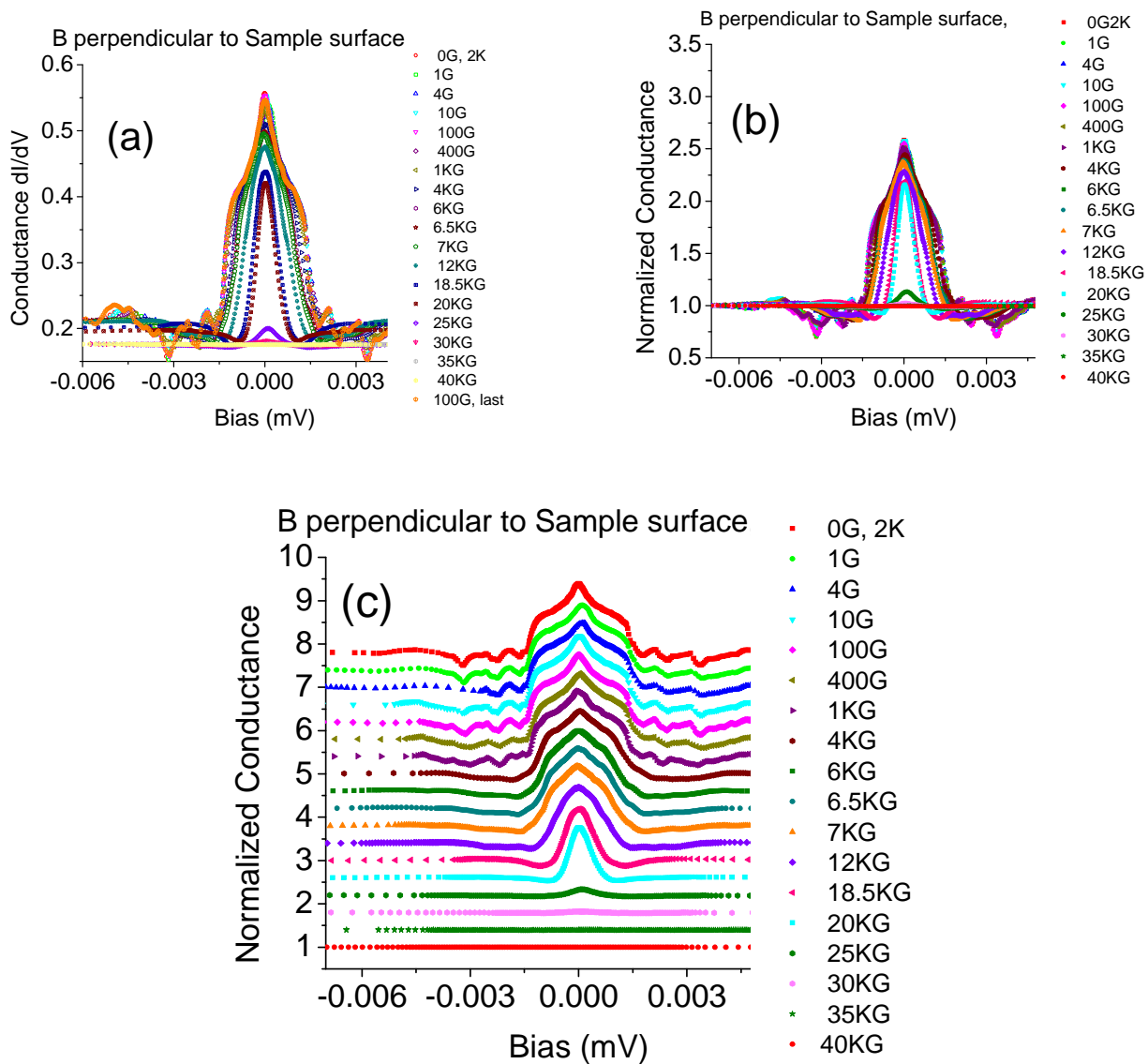
Fig 11.22. Field dependence of conductance with the field perpendicular to the sample surface

Conductance oscillations outside superconducting gap edge were observed for applied fields less than 4KG. The shapes of these curves were similar for the magnetic fields within 0G to 4KG, and then within 4KG to 20KG. From 20KG to about 35 KG the shapes were similar to each other. The zero bias amplitude disappeared at 35KG and beyond as shown in Fig. 11.23.
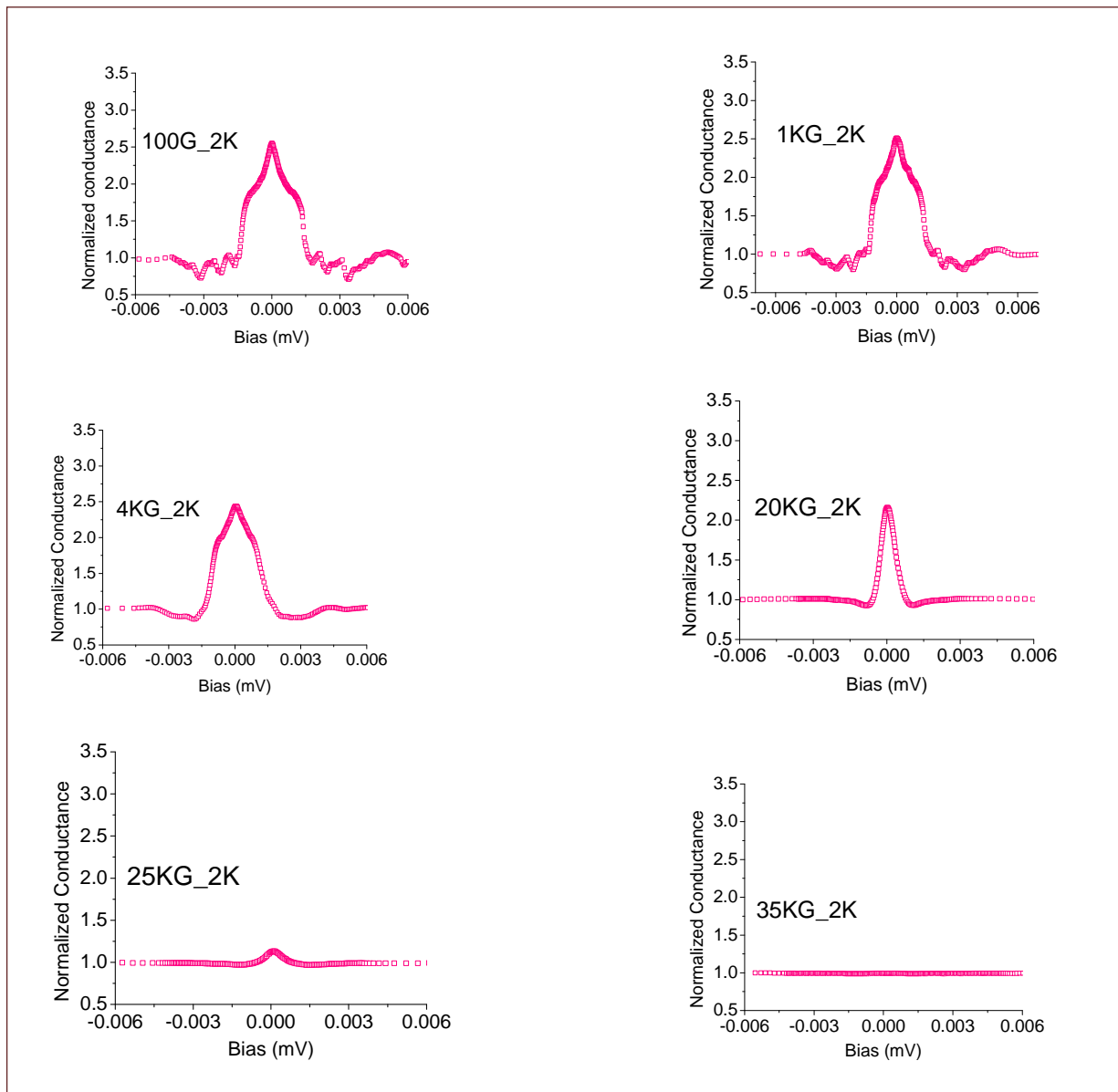
Fig. 11.23. Conductance curves for Nb/MnSi interface to show the disappearance of conductance oscillations outside superconducting gap when higher magnetic fields are applied

The zero bias amplitude decreases with magnetic field as shown in Fig. 11.24 (a). This pattern looks similar to the case of field dependence in parallel configuration. The conductance feature collapses at about 30 KG. The wavelengths of conductance oscillations seen around superconducting gap increase initially after magnetic field is applied from zero to about 10G, and then decreases for the higher magnetic fields. As shown in Fig. 11.24 (b). This pattern is also similar to the case of parallel configuration. The amplitudes of the first and second oscillations are almost equal.
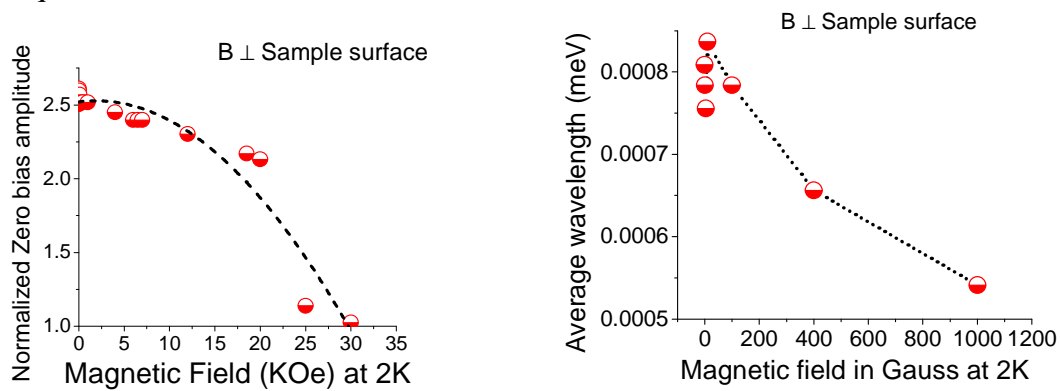
Fig 11.24 Effect of applied magnetic field on (a) normalized zero bias amplitude, (b) average wavelength of the conductance oscillations when the field is perpendicular to Nb/MnSi surface

The conductance curves before applying magnetic field was compared with the one taken after the applied magnetic field was set to zero. Their coincidence as shown in Fig. 11.25 indicates that there is no temperature dependent hysteresis in the conductance curves.
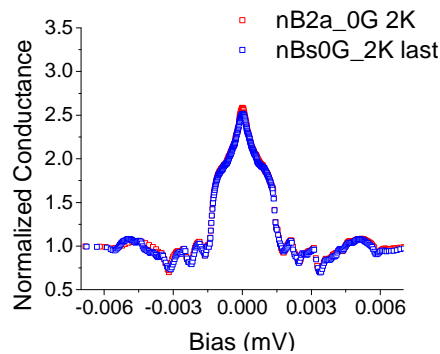
Fig 11.25. Normalized conductance curves before applying magnetic field, and after setting the applied magnetic fields to zero.

b2) Temperature dependence of conductance in perpendicular configuration

In the same configuration as in (b1), the conductance curves were obtained as function of temperature at zero magnetic field. Figure 11.26 (a) shows the data as collected, (b) shows the normalized data, and (c) shows the same data after shifted for clarity. These data have also similar conductance features with conductance oscillations.
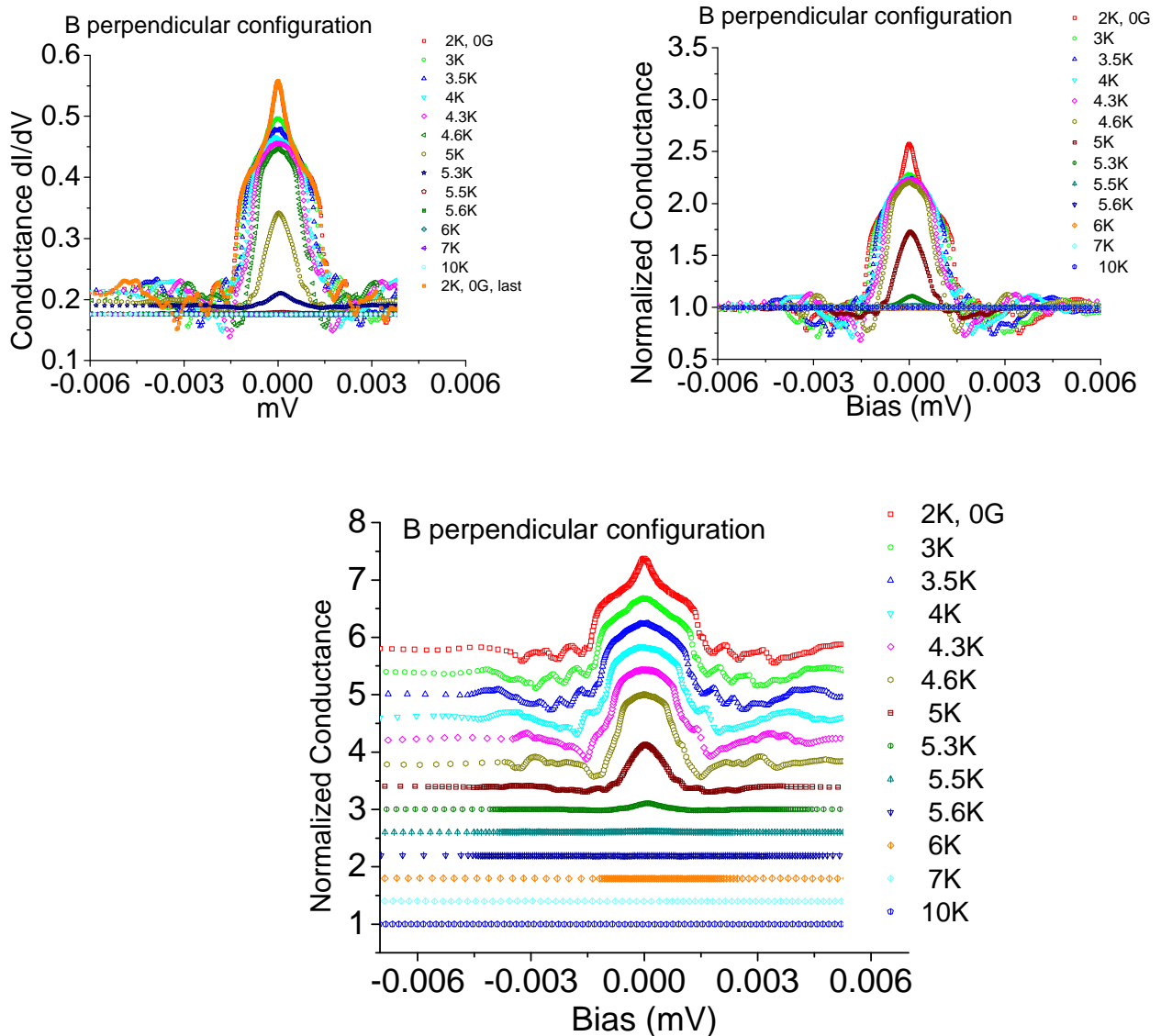
Fig. 11.26 Temperature dependence of conductance in perpendicular configuration (a) as collected conductance curves, (b) normalized conductance curves, and (c) normalized conductance curves with a shift

Figure 11.27 shows the conductance curves at different temperatures sowing the presence of conductance oscillations at lower temperatures lower than 4K. The oscillation features disappear at around 4K. The shape of conductance curve changes for 5K, and with its amplitude vanishing at 5.5K.
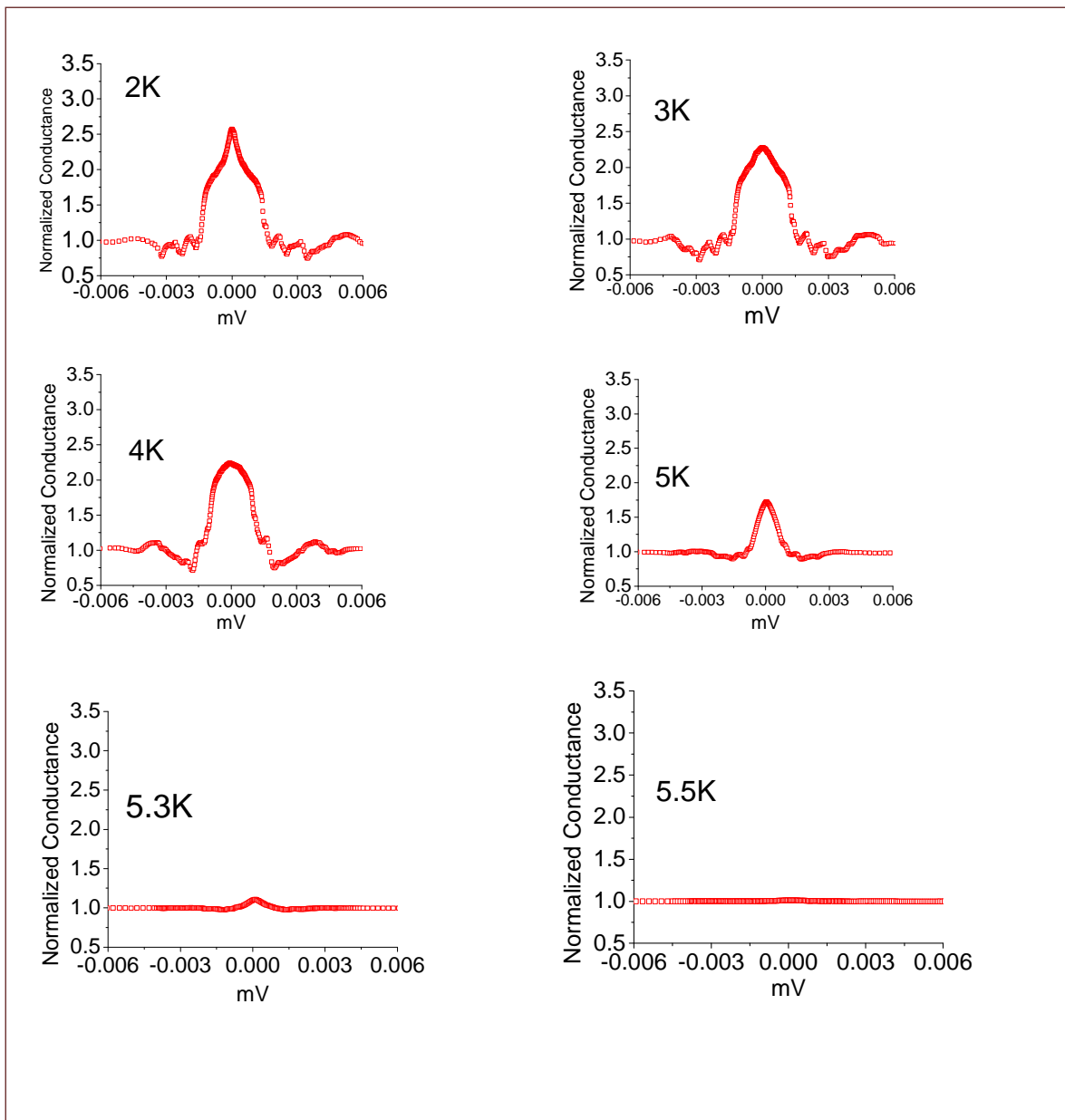
Fig. 11.27 Normalized conductance curves for Nb/MnSi interface showing the dependence on temperature

With the increase in temperature, the zero bias amplitude was found to decrease, but the pattern of this change was different than due to the effect of magnetic field. As shown in Fig. 11.28 (a), the amplitude decreases slowly at first when temperature is increased from 2K to about 4K, and it decreases abruptly from 4K to about 5.5K. The pattern of change of zero bias amplitude with temperature is similar in both parallel and perpendicular cases. The wave length of conductance oscillations seems slightly decreased at higher temperatures as shown in Fig. 11.28 (b).
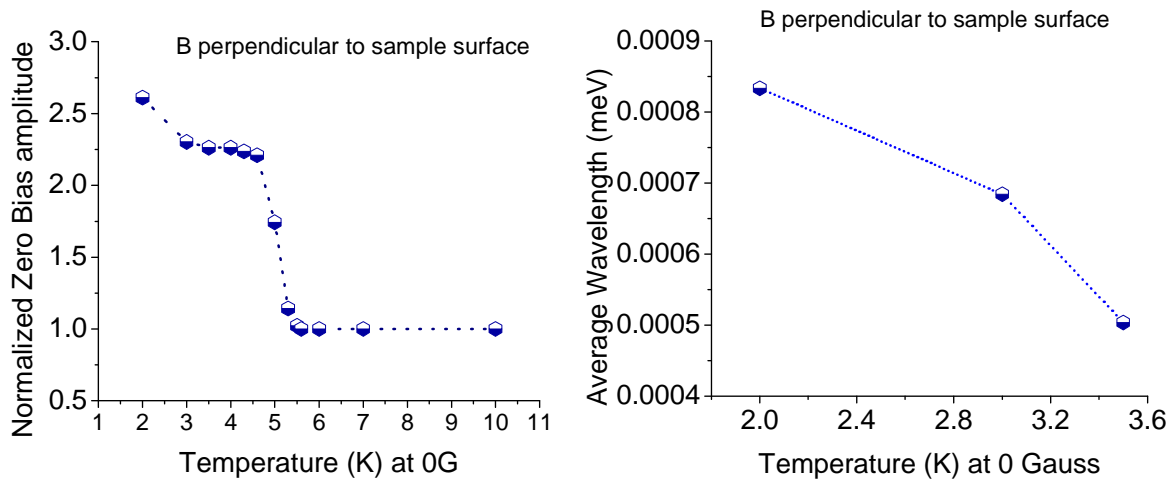
Fig. 11.28. Effect of temperature on (a) normalized zero bias amplitude, and (b) the average wavelength of conductance oscillations around superconducting gap for Nb/MnSi interface

After taking data for increasing temperatures, the data was taken for 2K at last. This data coincides with the data taken at 2K initially before increasing temperature. This shows that there is no hysteresis in conductance curves caused by the temperature cycle. The data at 2K before and after temperature cycle are shown in Fig. 11.29. This also indicates that the change is really due to the temperature change in the temperature dependence complete set of conductance data. The average amplitude seems slightly increased when the temperature is increased.
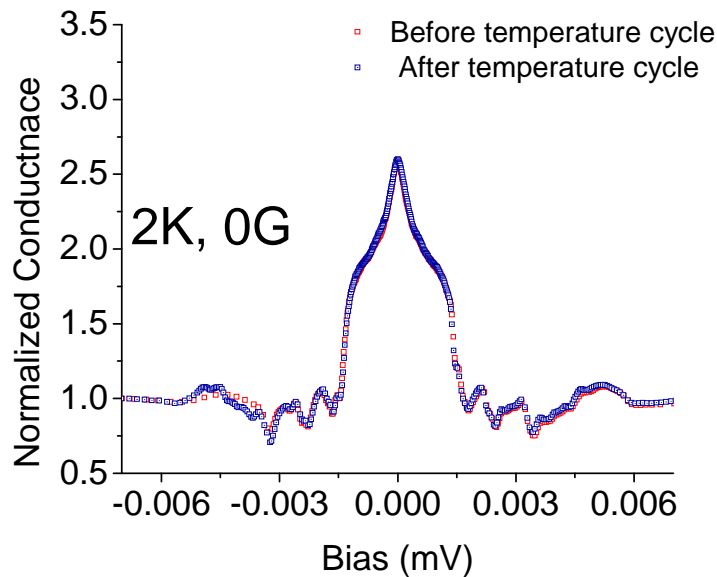
Fig. 11.29. Normalized conductance curves at 2K before and after temperature cycle in Nb/MnSi.

11.4.1.4 Discussion and conclusions

The spin polarization of MnSi single crystal was measured at 2K by point contact Andreev reflection technique driving the superconducting tip by a piezo motor in PPMS, and it was found to be 44±4%. It was measured at 1.5K by driving the tip manually, and the intrinsic value of P at 1.5K was found to be 45.2%. Since MnSi undergoes magnetic phase transition from helical to conical to induced ferromagnetic phase, it would be interesting to know how the spin polarization changes in these phases. For this purpose, the spin polarization of MnSi single crystal was measured as a function of applied magnetic field. It was found that the spin polarization increases with the applied magnetic field, and finally saturates once it reaches to the ferromagnetic phase. In another approach, the superconducting tip contact was established by e-beam lithography on PMMA on top of MnSi surface, and depositing Nb on top of it so that Nb would touch MnSi only through 1μm ×1μm two holes. The conductance curves in this case were found unconventional and interesting because of their large zero bias amplitude and conductance

oscillations outside the superconducting gap edge. These conductance curves obtained in parallel and perpendicular cases as magnetic field dependent and temperature dependent curves were analyzed.

To understand the interesting features of these curves, we consider the following model for FS interface. Bulk itinerant magnet MnSi is connected to a BCS superconductor Nb of finite thickness d. Niobium, being a standard BCS superconductor, has Cooper pairs which are made of electrons with opposite spins so that the total spin is 0, and hence the superconductivity is singlet. However, as Nb comes in contact with a ferromagnet with inhomogeneous magnetization such as helical or conical magnetic structure of MnSi in the present case, spin-triplet Cooper pairs are generated [Bergeret et al., 2005; Fominov et al., 2007]. Probably all three types of triplet Cooper pairs: 1 heterospin ↑↓+↓↑ and 2 equal-spin: ↑↑, ↓↓ are generated, but for us most interesting are equal spin ones since only for those pairs Andreev reflection couples electron and hole in the same spin subband, i.e. will not be suppressed by spin polarization, as seen by the enhanced Andreev reflection in our data. These triplet pairs can then penetrate into superconductor side and coexist with singlet pairs. They penetrate into the ferromagnet also but with shorter coherence length. For the transport between superconductor and a ferromagnet, the Andreev reflection is suppressed due to electron-like or hole-like quasiparticle not getting particle of opposite spin at Fermi level in different spin subband, and hence the scattering is very sensitive to a spin polarization. However, for equal spin triplet pairs (total spin =1), Andreev reflection is not suppressed at all by spin polarization of the ferromagnet because one spin can take the other spin from the same spin subband, i.e. Andreev reflection conserves spin subbands. Hence, at low magnetic field less than 6.5KG when the spin structure in MnSi is in helical or in conical phase Andreev reflection at the FS interface is the dominant scattering process. As a

result, the following sequence of reflections is possible: electron-like excitation is injected into S across the FS interface, it crosses over S film and reflects from its free surface as an electron by the normal reflection process, then it arrives FS interface again and is reflected as a hole-like excitation (with the same spin). Created hole crosses S film as well and is then converted to an electron at the SF interface. As a result, electron-like state reappears but with the phase shift due to momentum difference between electrons and holes in a superconductor. At energy E above the superconducting gap Δ, the momentum mismatch is

$$k_e - k_h = \frac{2\sqrt{E^2 - \Delta^2}}{\hbar v_F}$$

Since each electron and hole cross S film two times, the phase shift is

$\varphi = 2d(k_e - k_h) = \frac{4\sqrt{E^2 - \Delta^2}}{\hbar v_F}$. The condition $\varphi = 2\pi n$ provides energy levels, which for $E >> \Delta$

can be approximated by simple formula

$$E_n = \left[\Delta^2 + \left(\frac{\pi \, \hbar v_F n}{2d}\right)^2\right]^{1/2}$$

This is slightly modified realization of classical Tomash effect [Tomash, 1966] which should result in oscillations of conductance at energies above the superconducting gap. At bias V $>>\Delta$, oscillation have period $\delta V = \pi \, \hbar v_F / 2d$.

Above 6.5KG of applied magnetic field, the conical structure in MnSi disappears, and hence the triplet Cooper pairs disappear. Consequently, the conductance oscillations outside the superconducting gap should disappear which is seen in our experimental data.

The enhanced zero bias conductance peak (ZBCP) exceeding the standard Andreev factor-of-two can be qualitatively explained from the present model of triplet superconductivity

in Nb/MnSi. Generated triplet pairs are so-called odd-frequency pairs, with more complex spectral properties. It was shown theoretically that quite generally [Bergeret et al., Tanaka et al., Eschrig et al., 2003] odd- frequency pairing leads to a strong peak in the density of states at low energy, which in turn, should provide ZBCP. This peak should be suppressed on applying external magnetic field, which it does beyond 30KG and 38KG in parallel and perpendicular configurations respectively. However, its existence in fields over 6.5KG may be due to additional mechanism of zero bias conductance peak formation.

CHAPTER 12

STUDY OF ANDREEV REFLECTION SPIN POLARIZATION AND MAGNETIZATION OF Pd$_{1-x}$Ni$_x$ ALLOYS WITH DIFFERENT Ni CONCENTRATION

12.1   Introduction

Magnetocrystalline anisotropy observed in PdNi (Trupti et.al., 2009) makes this alloy an interesting system. Filled 4d orbital ([Kr]4d^{10} 5s^0 configuration) fcc element Pd is nonmagnetic which is isoelectronic to the magnetic 3d element Ni so that it is reasonable to expect 4d elements to be almost magnetic (Moruzzi et. al., 1989). Be it isolated Ni impurities with local moment of 1µ$_B$ (Loram et. al., 1985), or Ni atoms in clusters of three or more to have local moments (Chouteau et. al., 1976; Cheung et. al. 1981), magnetic 3d impurities induce large host polarizations (Oswald et.al., 1986) leading to the appearance of magnetism by the creation of giant moments in PdNi alloys at atmospheric pressure as well as under pressure (Beille et.al., 1975). The critical concentration of Ni in Pd matrix for the onset of ferromagnetism is 2% (Aldred et.al., 1970) for the bulk and 6.3% in Pd/Ni nano-alloys (Nunomura et.al., 1998).

Bulk Palladium on the other hand is itself an interesting material in terms of its magnetism. Expansion of fcc lattice by 5% (Fritsche et. al.;1987; Chen et.al.,1989; Alexandre et.al, 2006) or thin films of Pd with hcp crystal structure (Alexandre et. al., 2006) show induced moment whereas Palladium rests on the edge of magnetism with the density of states at the Fermi energy just below the Stoner criterion (N_{loc} (E_F) $I > 1$, where I is the exchange integral and N_{loc} ($EF)$ is the local density of states at the Fermi energy) for ferromagnetism (Alexandre et. al., 2006). Magnetic moments have been predicted for coaxial Palledaium nanowires (Stewart et.al., 2006) and at (100) facets of polyhedron structure of the clean gas-evaporated Pd fine particles with an average radius between 60 Å and 144 Å with maximum magnetization of 1.4±0.05 emu/g at 5K for a sample with 80 Å average radius (Shinohara et. al, 2003).

In a ferromagnetic superconducting system PdNi shows long range proximity effects. It is a weak ferromagnet (Fulde et. al., 1964; Larkin et. al., 1965). Change in Ni concentration in PdNi helps to control exchange energy and hence coherence length which is inversely proportional to the exchange energy (Kontos, et al., 2001; Ryazanov et. al., 2001). Long range character of Josephson current in samples with PdNi represents evidence for its spin triplet nature (Keizer et al., 2006; Khaire et. al., arXiv: 0912.0205).

Energy as a function of density of states shows that the 3d bands of electron in Ni splits into different energy levels for up spin and down spin electrons as shown in Fig. 12.1. This develops ferromagnetism in Ni, and so PdNi is an example of strong magnetic susceptibility enhancement of nearly ferromagnetic Pd by Ni impurities (Lederer et. al., 1968). Because of split bands, spin polarization is expected. So, in our research, we are interested to find the correlations between the spin polarization and the magnetization of the sample. For this purpose, PdNi thin films with different Ni concentrations were prepared by magnetron sputtering of Pd target with Ni inserts into it. Magnetization as a function of external applied magnetic field at 10K, and magnetization as a function of temperature in presence of 10 Oe magnetic field were measured by quantum design SQUID (Superconducting Quantum Interference Design) magnetometer. The conductance curves for these samples were measured at 1.5K by using Point Contact Andreev Reflection (PCAR) technique and the Spin polarization values were extracted by fitting the data with modified BTK model. Measurement of conductance curves and extraction of spin polarization of Pd in bulk helps to understand how the surface of Pd bulk behaves magnetically, and it also provides the ground to compare the spin polarization of PdNi alloy with Pd, and to understand the exotic role of Ni in the alloy for its spin polarization. The detailed data of such measurements are presented in the following sections.
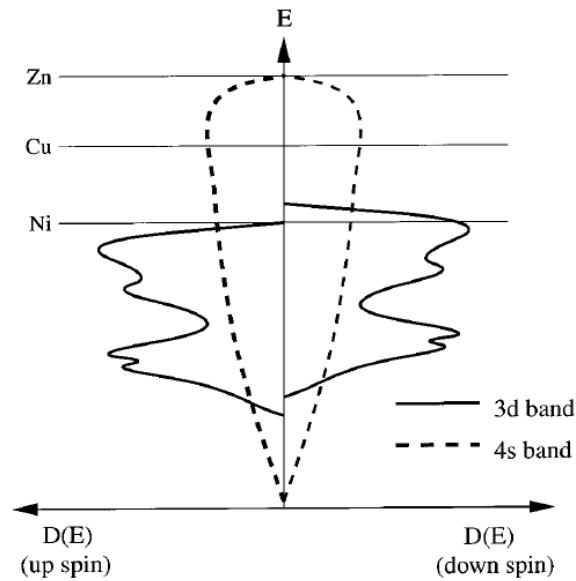
Fig. 12.1 Energy levels as function of electron density of states (Nicola Spaldin, ferromagnetism in metals, Cambridge University press)

12.2   The case of $Pd_{1-x}Ni_x$ sample with Ni 12%   ($Pd_{0.88}Ni_{0.12}$)

12.2.1 Magnetization and Curie Temperature measurements of $Pd_{0.88}Ni_{0.12}$ sample

The magnetization of PdNi thin film with Ni concentration of 12%, as measured by EDAX, was measured by SQUID. The sample was ferromagnetic which is indicated by nice M-H loop shown in Fig. 12.2 (a). It shows that the saturation magnetization of such sample is 112 emu/cm^3.
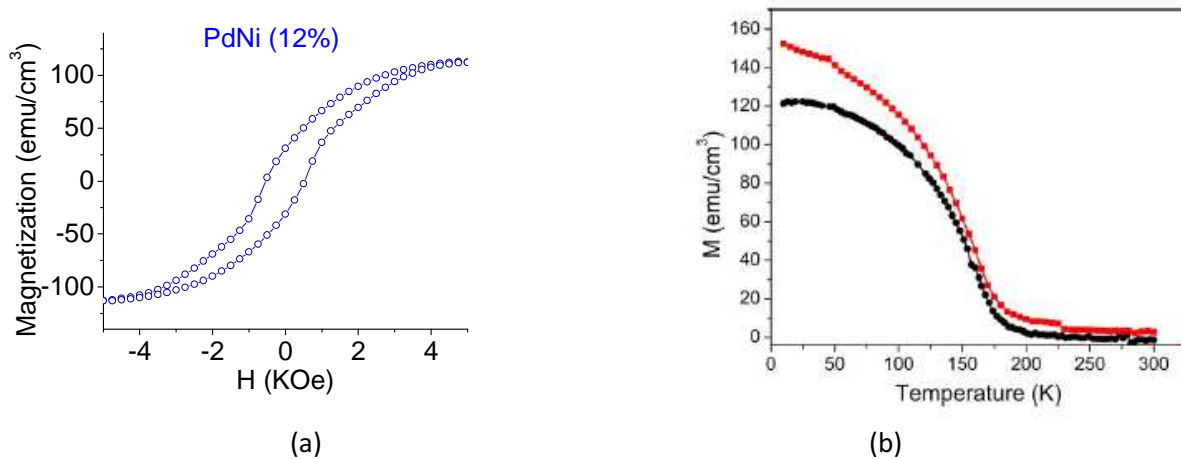
Fig. 12.2. Measurement of (a) magnetization; and (b) Curie Temperature of of $Pd_{0.88}Ni_{0.12}$ sample (Khaire et. al., 2009).

Fig. 12.2 (b) shows how magnetization varies with temperature. The Curie temperature of PdNi with 12% Ni concentration is found to be 175K. The purpose of finding magnetization and Curie temperature is to find any possible correlation between them and with the spin polarization of the sample.

12.2.2 Spin Polarization measurements of $Pd_{1-x}Ni_x$ sample with Ni 12% ($Pd_{0.88}Ni_{0.12}$)

Point Contact Andreev Reflection Spectroscopy (PCAR) was used to obtain several sets of conductance curves corresponding to different contact resistances. Some of such representative normalized conductance curves are shown in Fig.12.3. Electrochemically etched Nb tips were used as superconducting tips. The fitting of such curves was done by using modified BTK model to extract spin polarization values. The experiment was done at 1.2K. Fig. 12.3 (a) is one set of normalized conductance curve whose fitting parameters are T = 2K, cuperconducting gap Δ=1.5meV, interfacial scattering barrier Z = 0.15 with spin polarization P = 49%. Similarly Fig. 12.3 (b) shows conductance curve with the fitting parameters of T = 2K, Δ =

1.5meV for Nb, Z = 0.136 with P = 49%. The fitting was done in slightly elevated temperature of

2K. However, the use of exact experimental temperature of 1.2K can still fit the data with sharp

peaks near the superconducting gap, but still giving the other fitting parameters almost same and

giving the same spin polarization values as shown in Fig. 12.3 (c) and (d) which correspond to

the data(a) and (b) respectively.
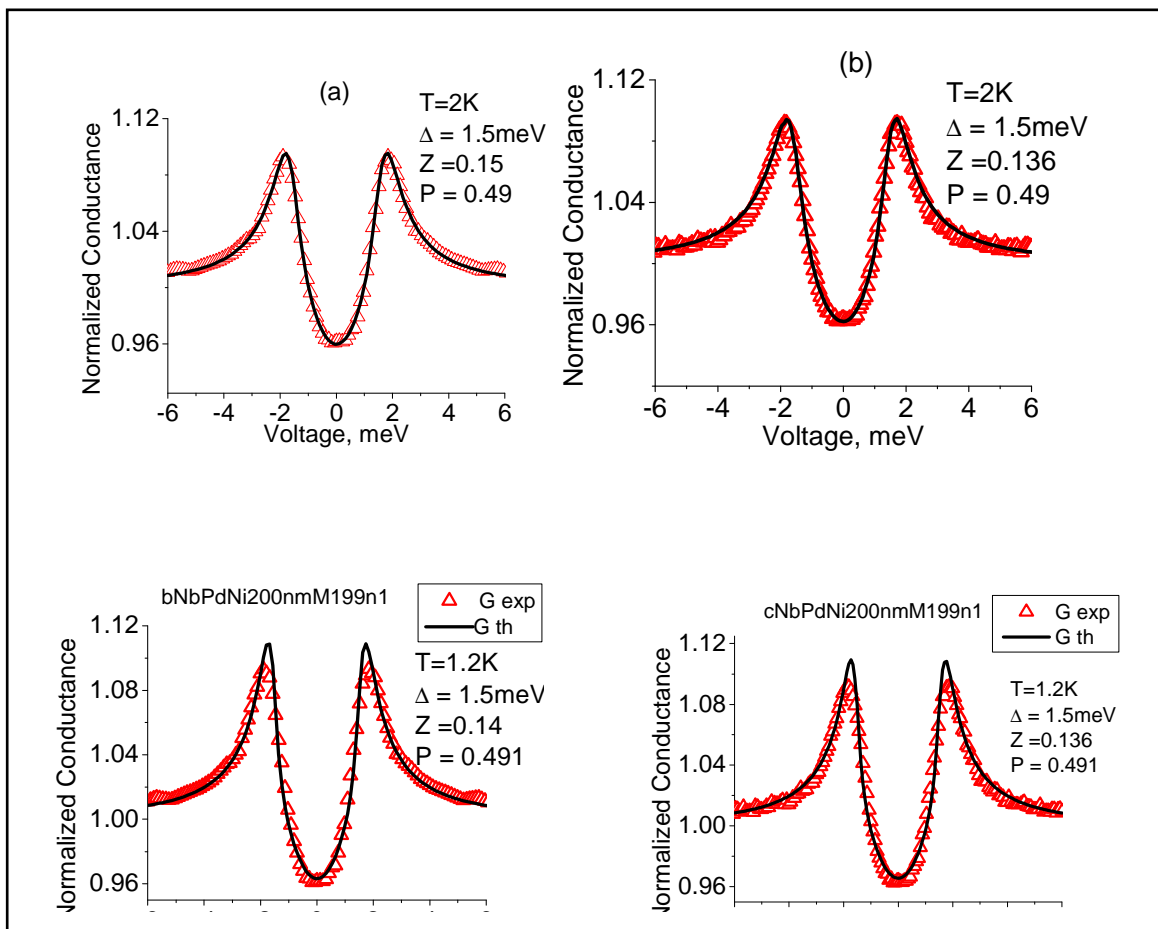
Fig. 12.3. Normalized Conductance curves for PdNi sample with Ni 12%

In order to find the intrinsic value of spin polarization, i.e spin polarization independent

of interfacial barrier scattering Z, a plot of P as a function of Z is plotted as shown in Fig. 12.4.

For this sample, P was almost independent of Z, and the intrinsic value of spin polarization is found to be 48.8%.
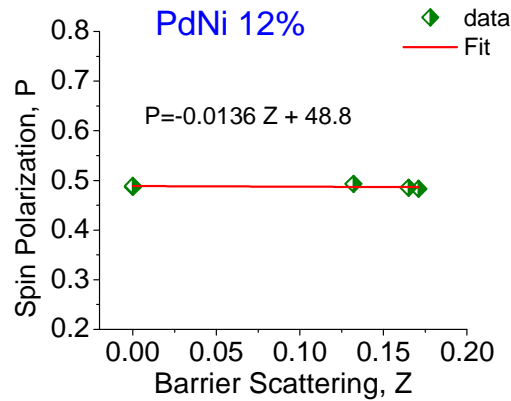
Fig. 12.4. Spin polarization as a function of interfacial barrier scattering for PdNi with Ni 12% sample

12.3 The case of $Pd_{1-x}Ni_x$ sample with Ni 6% ($Pd_{0.94}Ni_{0.06}$)

12.3.1 Magnetization and Curie Temperature measurements of $Pd_{0.94}Ni_{0.06}$ sample

As shown in Fig. 12.5 (a), the saturation magnetization of PdNi with Ni 6% sample was found to be 55 emu/cm^3 at 10K; and the Curie temperature was found to be 95K at 10 Oe field as shown in Fig 12.5 (b). The presence of lower concentration of Ni has shown lower Ms and lower Tc.
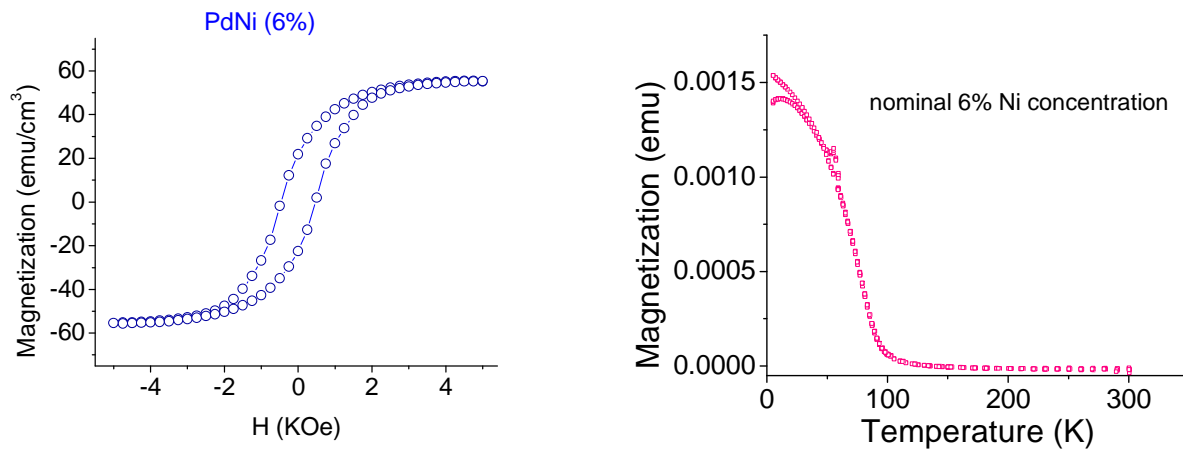
Fig. 12.5. Measurement of (a) magnetization; (b) Curie temperature of PdNi with Ni 6% sample

12.3.2 Spin Polarization measurements of $Pd_{1-x}Ni_x$ sample with Ni 6% ($Pd_{0.94}Ni_{0.06}$)

Insert of Ni rods was reduced reduced in Pd target during magnetron sputtering to reduce the percentage of Ni than before. Fig.12.6 shows four different conductance curves taken for different contact resistances. Temperature used as one of the fitting parameters is same as the experimental temperature of 1.5K. Supreconducting gap of Nb is 1.5meV which has given reasonable fittings with Z ranging from about 0.3 to 0.65. The spin polarization values are shown in these figures separately.
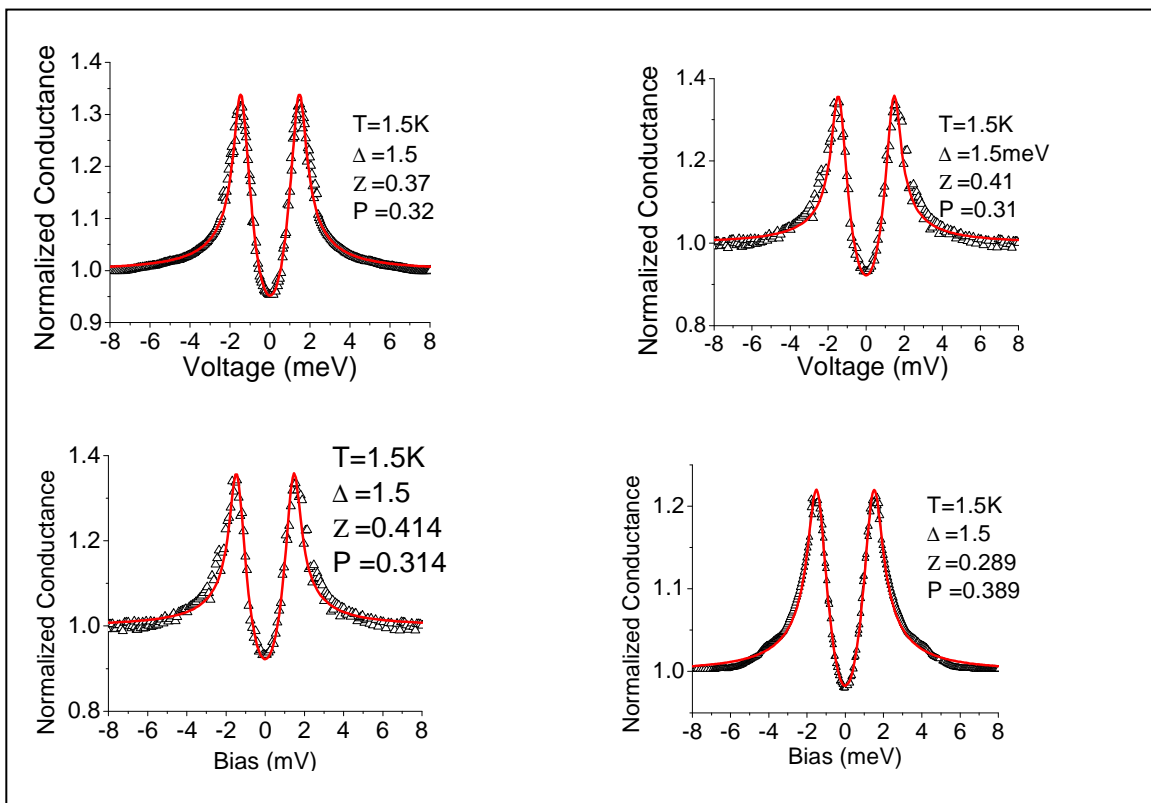
Fig.12.6. Conductance curves for PdNi sample with Ni 6%

Since, the polarization, P is found dependent on the barrier scattering Z; intrinsic values of spin polarization corresponding to probable clean interface is found by interpolation of P-Z graph as shown in Fig. 12.7. This gave the value of P as 37.5%.
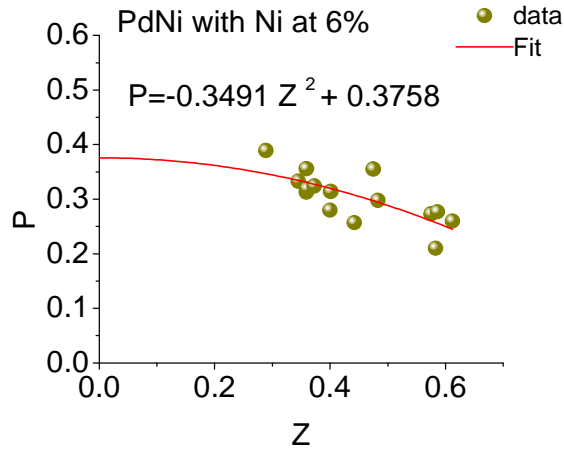
Fig. 12.7. Spin polarization as a function of interfacial barrier scattering for PdNi with Ni 6% sample

12.4   The case of $Pd_{1-x}Ni_x$ sample with Ni 3% ($Pd_{0.97}Ni_{0.03}$)

PdNi sample with 3% Ni concentration gave saturation magnetization of 12.6 emu/cm3 at 10K, and it gave Curie temperature of 40K at 10 Oe magnetic field as shown in Fig. 12.8 (a) and (b) respectively.
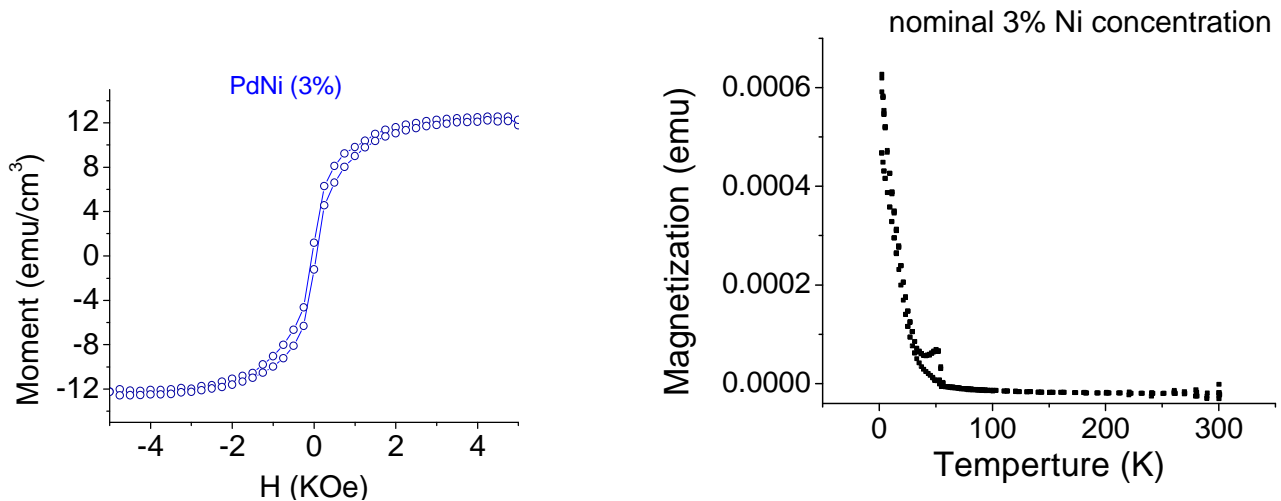
Fig. 12.8. Measurement of (a) magnetization; (b) Curie temperature of PdNi with Ni 3% sample

Conductance curves were obtained as usual using Nb tips as superconducting tips. Several such conductance curves were obtained. Some of representative curves are shown in Fig. 12.9. For consistency, these conductance curves were taken at the same temperature as it was done for samples with different concentrations. The fitting parameters as shown in corresponding plots are T=1.5K, Δ for Nb= 1.5 meV. Barrier scattering seems high even in these samples with typical values ranging from 0.4 to 0.6 showing the spin polarization values dependent on the barrier strength.
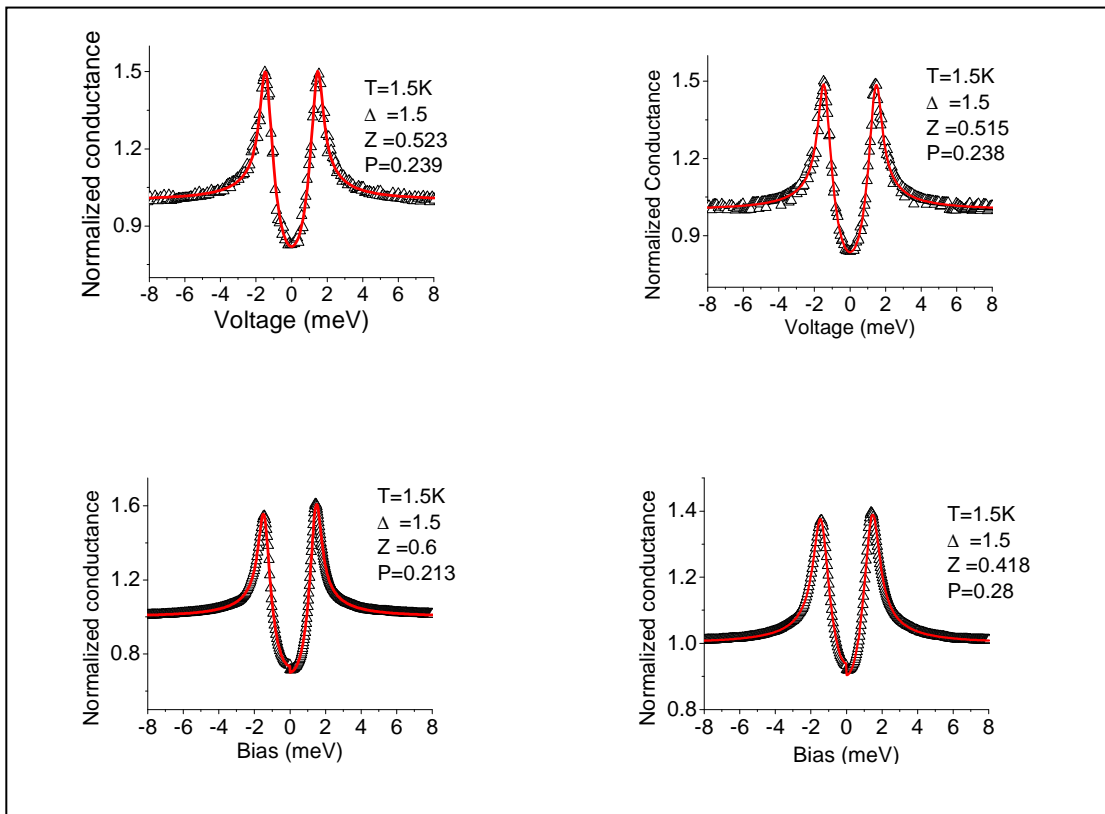
Fig. 12.9. Normalized conductance curves for Nb/PdNi with 3% Ni samples

The P vs Z plot for 3% Ni sample of PdNi is shown in Fig. 12.10. Interpolation of the quadratic fit of the data shows the intrinsic value of spin polarization of this sample to be 32.9% which is less than for 6% Ni sample. With lower concentration of Ni, it has been seen that the

values of saturation magnetization, Curie temperature and spin polarization go lower. This trend has been seen in the samples sputtered in the same lot under identical growth conditions of the samples.
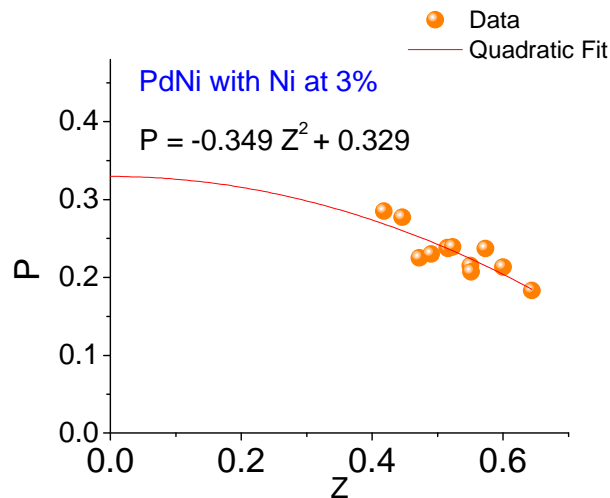
Fig.12.10 Spin polarization as a function of interfacial barrier scattering for PdNi with Ni 3% sample

12.5   The case of $Pd_{1-x}Ni_x$ sample with Ni 2% ($Pd_{0.98}Ni_{0.02}$)

Separate batch of PdNi samples were sputtered reducing insert of Ni rods in Pd target so as to get 2%Ni in PdNi thin films. However, the rate of deposition was maintained different while depositing the same thickness of PdNi thin films. While characterizing the films, different saturation magnetizations were found in these samples. Curie temperatures were also found different. This indicated that magnetization and Curie temperature depend on the growth conditions of the sample. This helps to anticipate that the spin polarization might also depend on the growh conditions. The exact measurements for this sample are discussed in this section.

12.5.1 The case of $Pd_{1-x}Ni_x$ sample with Ni ~2% (sample 1A)

Figure 12.11 (a) shows that the saturation magnetization for this sample is 1.43 emu/cm^3; and (b) shows the Curie temperature of this sample to be 8.43K. The M-H loop shows that PdNi

with Ni about 2% is still ferromagnetic. However, the saturation magnetization is low as expected. Correspondingly, the Curie temperature is also low.
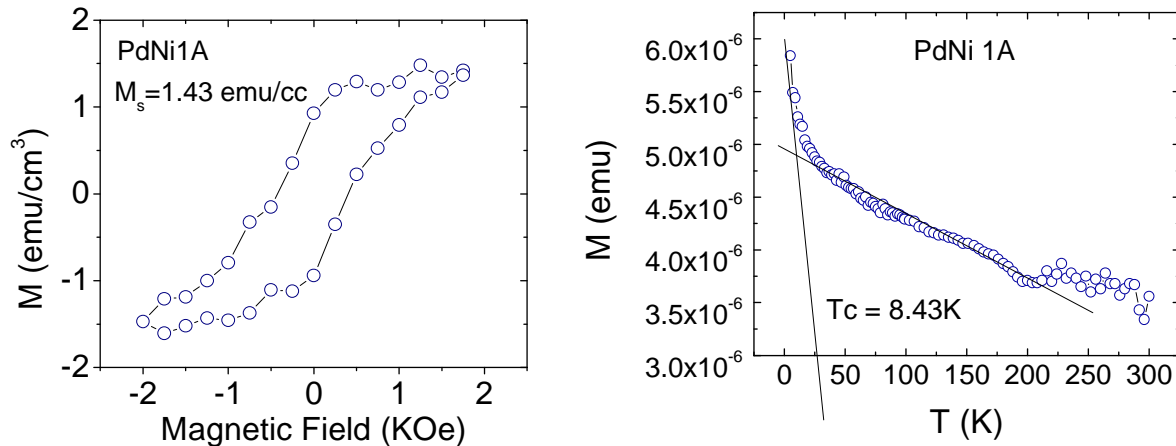
Fig. 12.11 Measurement of (a) magnetization; (b) Curie temperature of PdNi with Ni 2% sample 1A

The motivation was to see the transition of spin polarization, if any, in PdNi samples with low magnetization values. For that, PCAR spectra were obtained at 1.5K, and the fittings were done by the same BTK model as was used for other samples with higher Ni concentrations. The conductance curves look conventional. Fig. 12.12 shows four different conductance curves taken for different interfacial contact resistances.The fittings were possible for T = 1.5K, Δ = 1.5 for Nb. Barrier scattering values were different for different contacts. These values were typically in the range of 0.0 to 0.7.
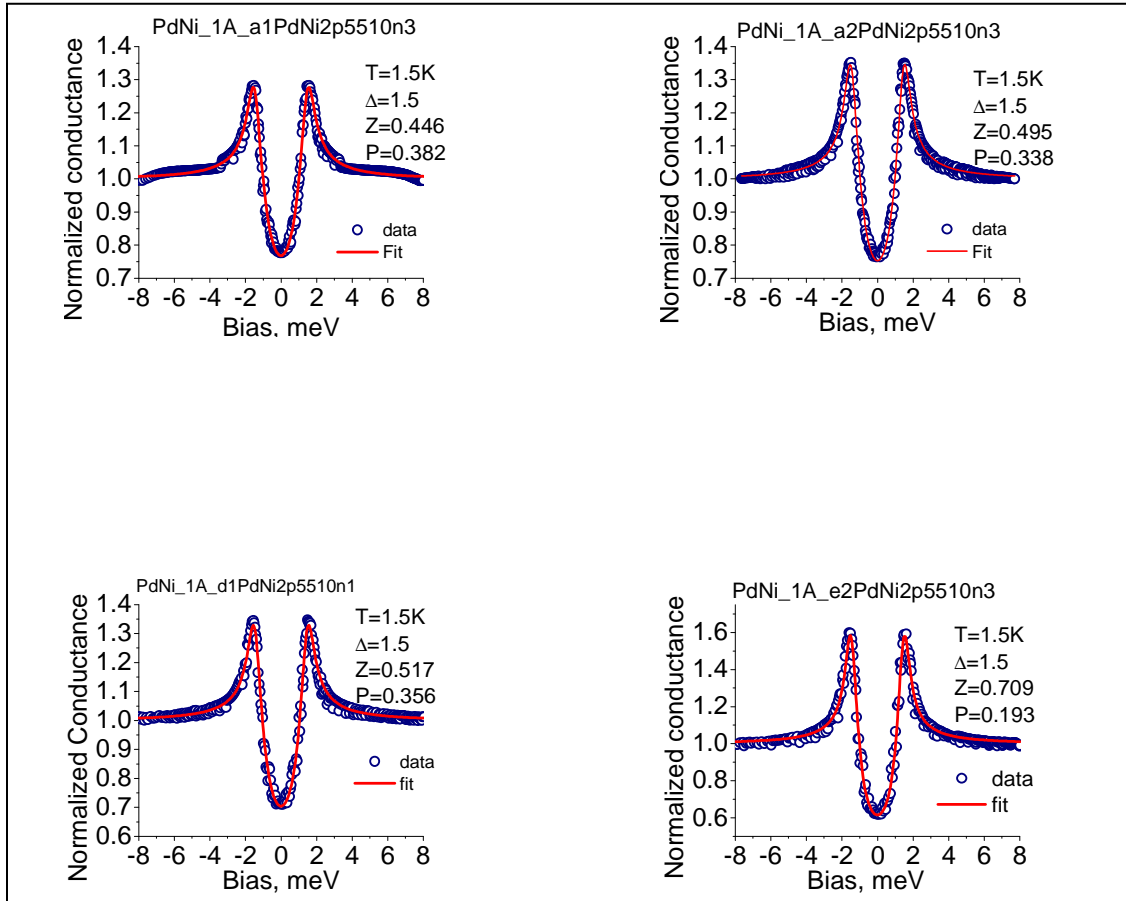
Fig. 12.12. Normalized conductance curves for Nb/PdNi with 2% Ni sample (1A)

As shown in Fig. 12.12, the spin polarization values were different for different conductance curves. It was found that P values were Z dependent as they were found for previous samples. Z values, which cannot be controlled as we desire, depends on the scattering situation of electrons at the interface. Making several contacts and getting conductance curves gives a chance of arbitrary change of Z values. Some lucky chances give smaller Z which we generally prefer to be more confident of the intrinsic values of the samples. In this sample, some of the lower Z and corresponding P values confirm that the quadratic fit is reliable enough to get intrinsic value of spin polarization accurately. Z dependence of P for this sample is shown in Fig. 12.13, from which the intrinsic spin polarization of PdNi with 2% Ni is found to be 40.23%. Interesting enough, the value of P is higher for this sample than for 3%Ni sample of PdNi.

Different growth condition might be responsible for this change, or there may be overshooting of P for PdNi samples with concentration close to critical concentration. This is not clear at this pont. More samples of PdNi with concentration of Ni ~2% were measured to get better idea.
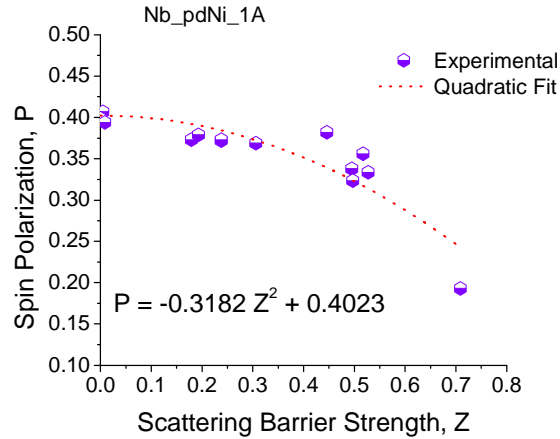
Fig. 12.13 Spin polarization as a function of interfacial barrier scattering for PdNi with Ni 2% sample 1A

12.5.2 The case of $Pd_{1-x}Ni_x$ sample with Ni ~2% (sample 2A)

Saturation magnetization and Curie temperature for this sample were found to be 2.23 emu/cm^3 and 41.8K as shown in Fig. 12.14 (a) and (b) respectively.
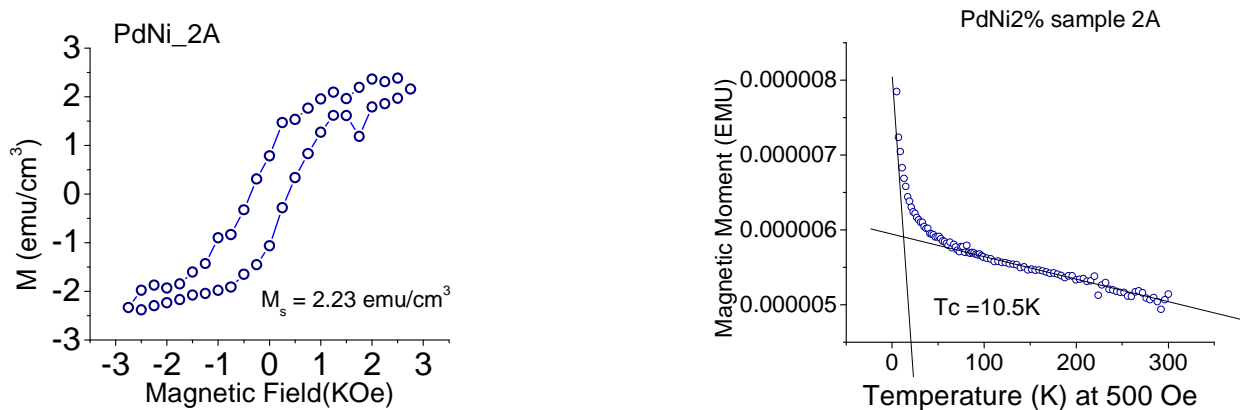
Fig. 12.14 Measurement of (a) magnetization; (b) Curie temperature of PdNi with Ni 2% sample 2A

The conductance curves obtained for this sample are conventional, and their fitting is done at 1.5K, the experimental temperature. They fit for $\Delta_{Nb} = 1.5$ meV giving typical values of Z from 0.3 to 0.5, and the P values dependent on Z. Figure 12.15 shows some of representative conductance curves for this sample.
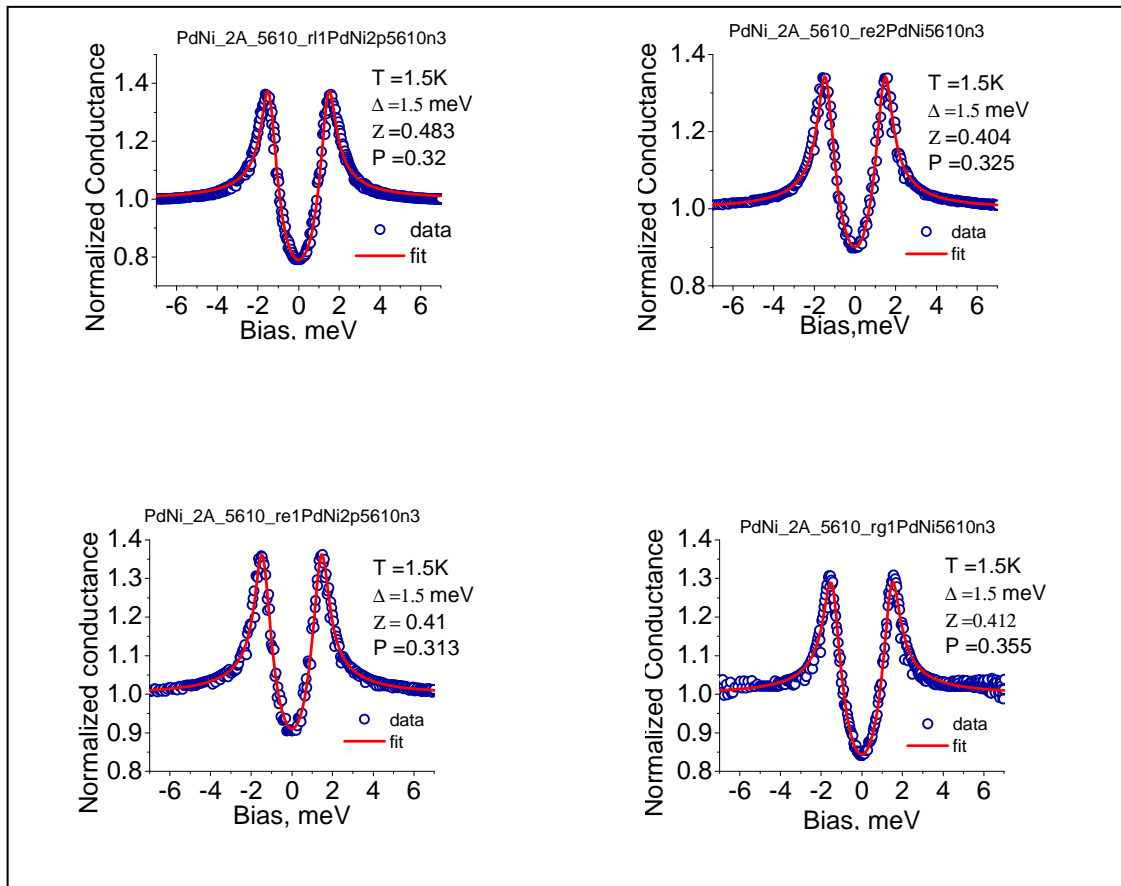
Fig. 12.15 Normalized conductance curves for Nb/PdNi with 2% Ni sample (2A)

Interpolation of Z dependence curve gives the intrinsic value of P for this sample to be 41.8% as shown in Fig. 12.16. The difference in P is due to different saturation magnetization compared to the previous sample which will be compared in detail later.
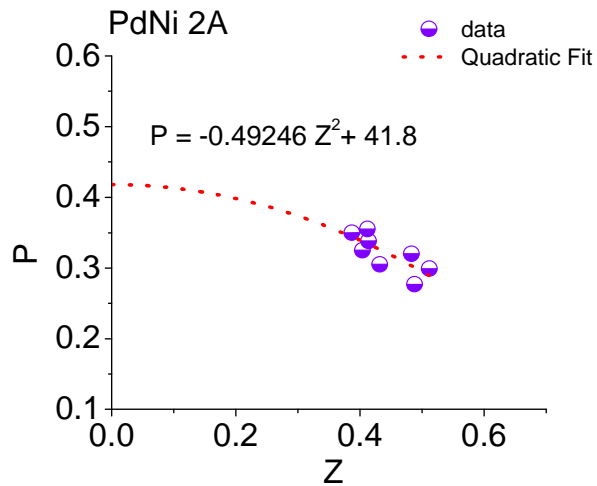
Fig. 12.16. Spin polarization as a function of interfacial barrier scattering for PdNi with Ni 2% sample 2A

12.5.3 The case of $Pd_{1-x}Ni_x$ sample with Ni ~2% (sample 3A)

Saturation Magnetization for this sample was measured to be 6.05emu/cm^3, and the Curie temperature was measured to be 16.6K as shown in Fig. 12.17.
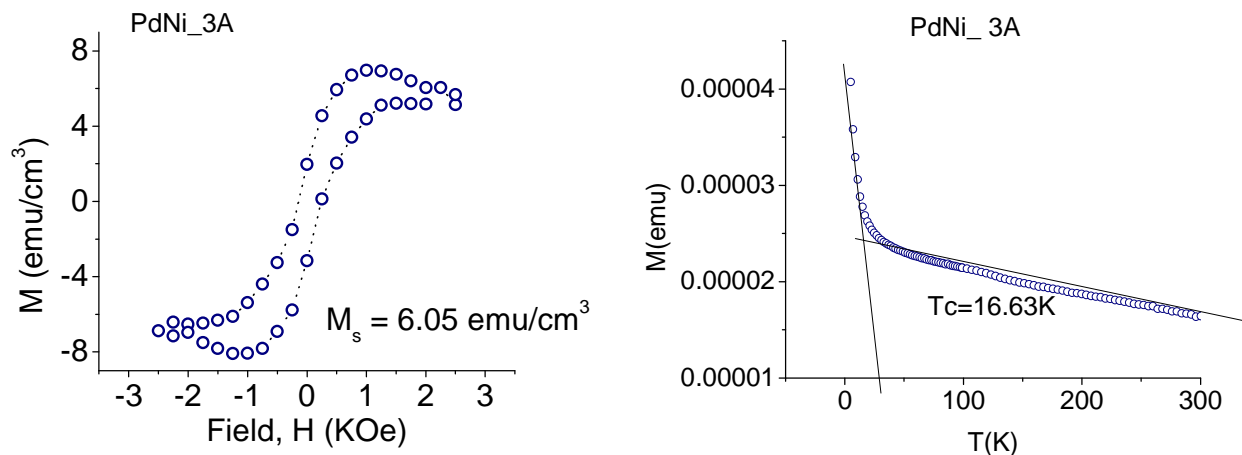
Fig.12.17. Measurement of (a) magnetization; (b) Curie temperature of PdNi with Ni 2% sample 3A

Fitting of conductance curves was done at T = 1.5K, Δ = 1.5meV. For this sample also, a range of barrier scattering values were obtaiened as shown in some of the representative curves shown in Fig. 12.18.
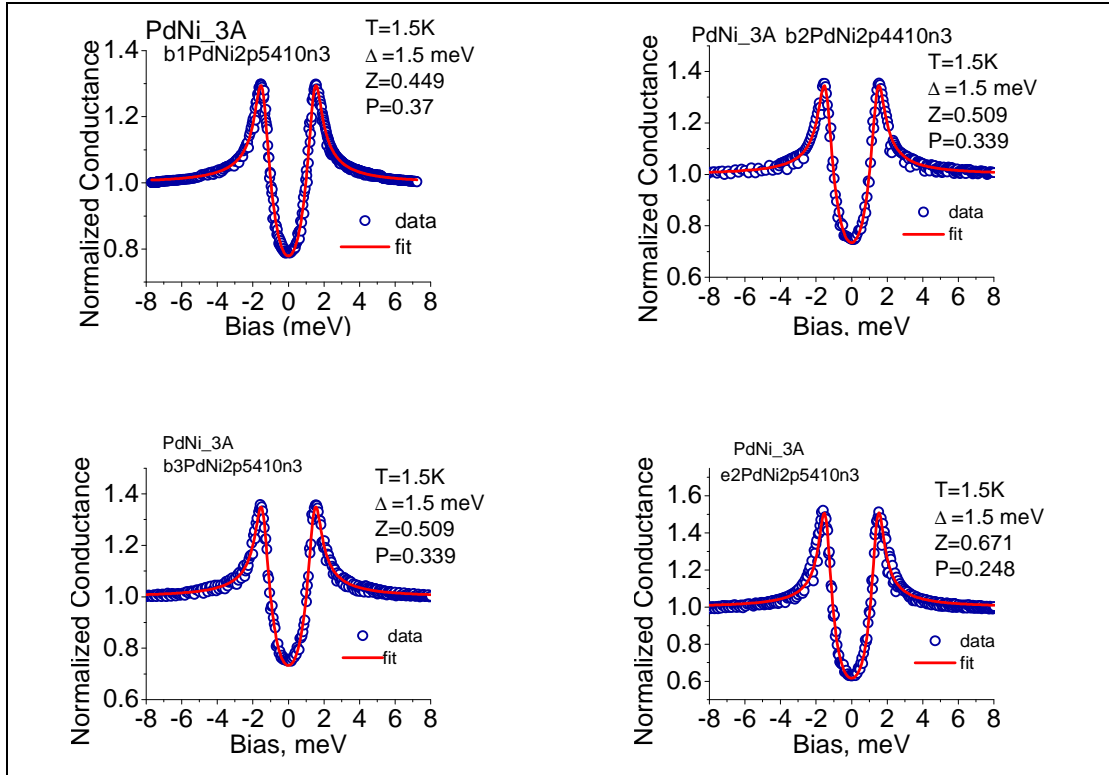
Fig. 12.18. Normalized conductance curves for Nb/PdNi with 2% Ni sample (3A)

Quadratic fit of Z-dependance curve gave the intrinsic value of P to be 47.7% as shown in Fig. 12.19. Even though the magnetization is low, P value came high for this sample showing some inconsistency in the correlation of P with saturation magnetization which will be discussed later.
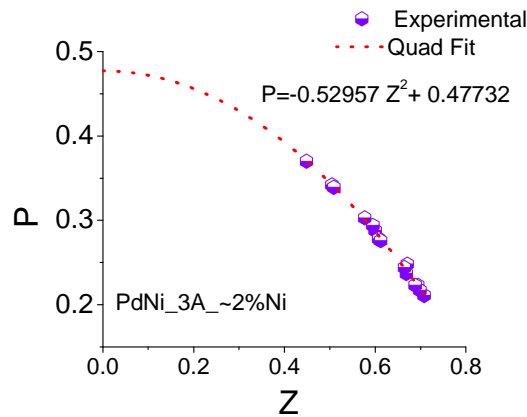
Fig. 12.19. Spin polarization as a function of interfacial barrier scattering for PdNi with Ni 2% sample 3A

12.6   The case of pure Pd

Fcc structure of bulk Pd presents a high paramagnetic susceptibility value (Litran et. al., 2006) close to fulfilling Stoner Criterion of magnetism. The electron spin fluctuations in a strong paramagnet are known to renormalize the quasiparticle energy which affects the electron spin fluctuation coupling constant so that the phase relationship of electron and back scattered hole changes controlling the quantum interference in normal metal (Aprili et. al., NATO Science series, Springer). In paramagnetic regime, the S/N structure is described in dirty limit by Usadel equations (Aprili et. al., NATO Science series, Springer):

$$\frac{\hbar D_N}{2}\frac{\partial \theta}{\partial x^2}+i(1+\lambda_{sf})ESin\theta+2\Gamma_{AG}Sin\theta-Cos\theta+\Delta_N Cos\theta=0,$$

$$\Delta_N=2\pi T\lambda_N\sum_{\omega}Sin\theta,$$

where θ, the pairing angle contains all the information about equilibrium properties.
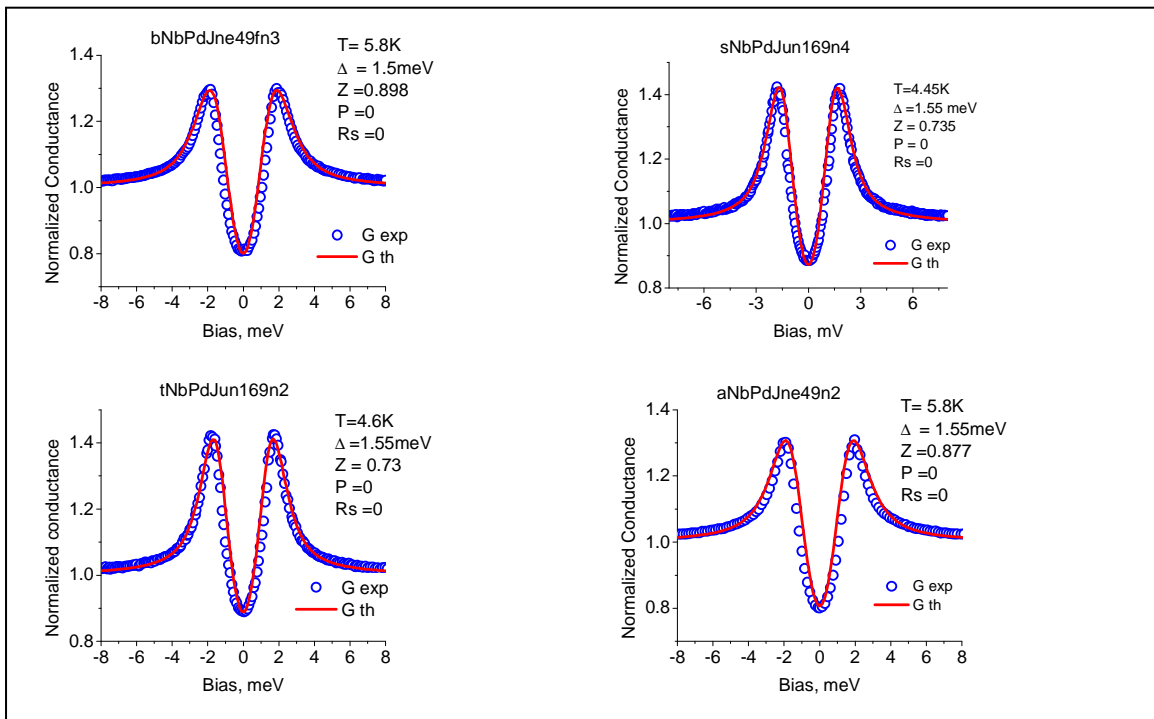
Fig. 12.20 Normalized conductance curves for polished Pd slab

For larger spin fluctuations that occur in paramagnetic Pd, $\sum Sin\theta$ is smaller so that T goes higher. It may be the cause of the need of higher temperature to fit data for Pd slab. In case of ferromagnetic PdNi, exchange field acts like spin dependent potential which doesn't act like the spin fluctuations that renormalize the energy of the quasiparticles. This may be related to high Z in Pd and low Z in case of PdNi as discussed earlier. The normalized conductance curves for Pd are shown in Fig. 12.20.

Figure 12.21 shows that the spin polarization of Pd is zero for different values of scattering barrier potential which arise while changing the tip pressure on the Pd surface to have different contacts, and hence different contact resistances. In both cases of PdNi with Ni 12% sample and Pd slab, the spin polarization is Z independent.
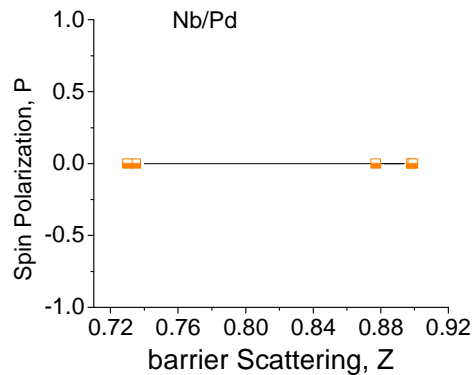
Fig. 12.21. Dependance of spin polarization P on the barrier strength Z for Pd sample

12.7   Combined results and discussions for different concentration of Ni in PdNi

We can summarize all the results so far for PdNi samples with different Ni concentrations. Table 12.1 shows the experimental values of Curie temperature, saturation magnetization and spin polarization for these samples. Samples 1A,2A and 3A correspond to nearly 2%Ni concentration samples deposited with different rate during magnetron sputtering.

Table 12.1. Curie temperature, saturation magnetization and Spin polarization of $Pd_{1-x}Ni_x$

sample	Tc(K)	Ms (emu/cc)	P%
1A	8.43	1.43	40.23
2A	10.5	2.23	41.8
3A	16.63	6.05	47.7
3%	40	12.6	32.9
6%	95	55	37.5
12%	175	112	48.8

Curie temperature of PdNi samples was found proportional to the saturation magnetization in the observed range of saturation magnetization from 1.4 to 112 emu/cm^3. This was found consistent in the samples of different batch. Figure 12.22 shows the linear relation. This indicates that controlling the magnetization, it is possible to control Curie temperature of PdNi alloy.
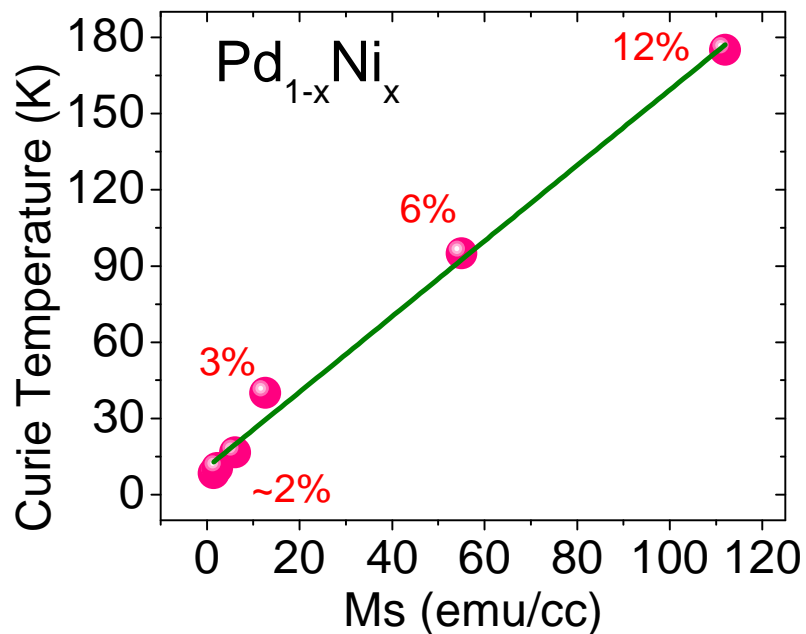
Fig. 12.22 Curie temperature of PdNi samples as a function of saturation magnetization controlled by controlling the concentration of Ni

Spin polarization values of PdNi samples was found proportional to Curie temperature for the samples of the same batch indicating the dependency on growth condition. However, when all data is considered together for samples of different batches, it is seen that P is in higher profile in the samples with lower Curie temperature corresponding to Ni concentration of about 2% as shown in Fig.12.23. At Tc of about 40K, P value was found lowest and it was found increased at higher Curie temperature to 112K, our largest observed value of Tc for 12% Ni concentration sample. From the overall trend, it is difficult to find the generalized correlation between the spin polarization and Curie temperature of PdNi samples.
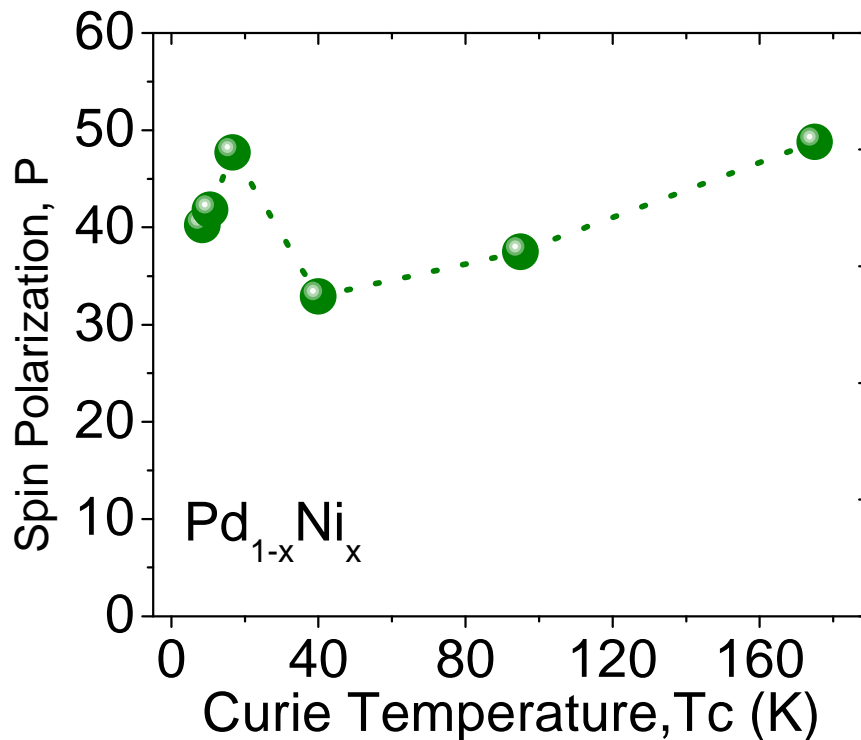
Fig. 12.23. Spin Polarization as a function of Curie temperature of PdNi sample with different Ni concentration

Finding the correlation between the spin polarization and saturation magnetization was main objective of this project. With the measurements with two different batches of samples, it is observed that P values are proportional to Ms for the same batch of samples (Fig. 12.24). The linearity of Ms dependence of P is seen for concentration range of Ni from 3% to 12%. This is also observed at around 2% Ni concentration for the samples with different magnetization. However, naturally slightly different growth condition of different batches of samples might be responsible for the the nonlinearity for the overall samples from 2% to 12% Ni concentration. It is unlikely that this linearity holds true for higher concentration because the value of P is already close to the value of P for Ni. So, P values reach to saturation beyond certain concentration, probably 12% Ni as observed in these experiments.
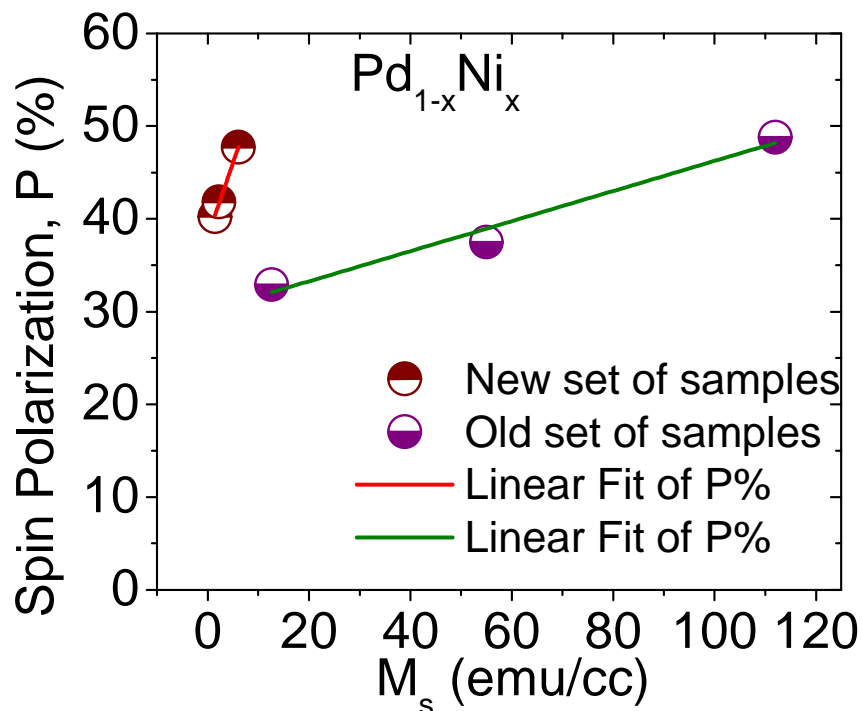
Fig. 12.24. Spin Polarization as a function of saturation magnetization of PdNi samples with different Ni concentrations

12.8   Spin polarization of PdNi (sample 1A with Tc = 8.4K) at 4.2K and 1.42K

For the sample with low Tc, it is worth knowing how much the value of P is at temperature closer to Tc and at lower temperature than Tc, such as 1.5K. Within the constraint of available instrument, i.e. He dewer we used, it was possible to measure P only at 4.2K which is the temperature of liquid Helium if it is not pumped in the dewer. Conductance curves were obtained at 4.2K. Some of such curves plotted after fitting was done are shown in Fig. 12.25.
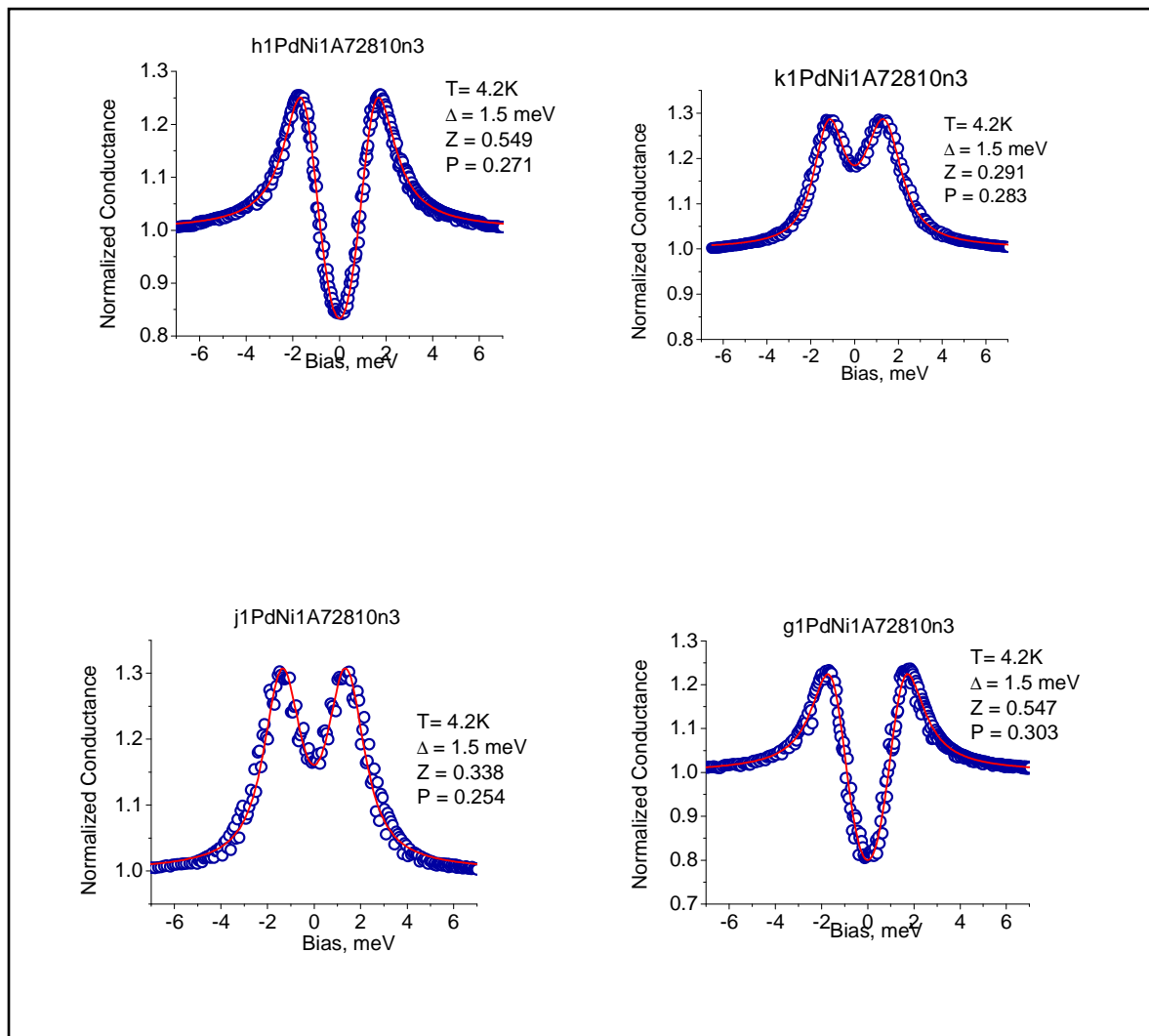
Fig. 12.25. Normalized conductance curves for Nb/PdNi with 2% Ni sample (1A) at 4.2K

Several such conductance curves were taken for different contacts which means different contact resistances. The shape and amplitude of conductance curves are dependent on Z as shown by example of such curves in Fig. 12.25. The Z- dependence of P at 4.2Kis found to be almost uninfluenced by Z as shown in Fig. 12.26. The intrinsic value of P at 4.2K is found to be 27.9% which will be compared to the P value of the same sample at lower temperature.
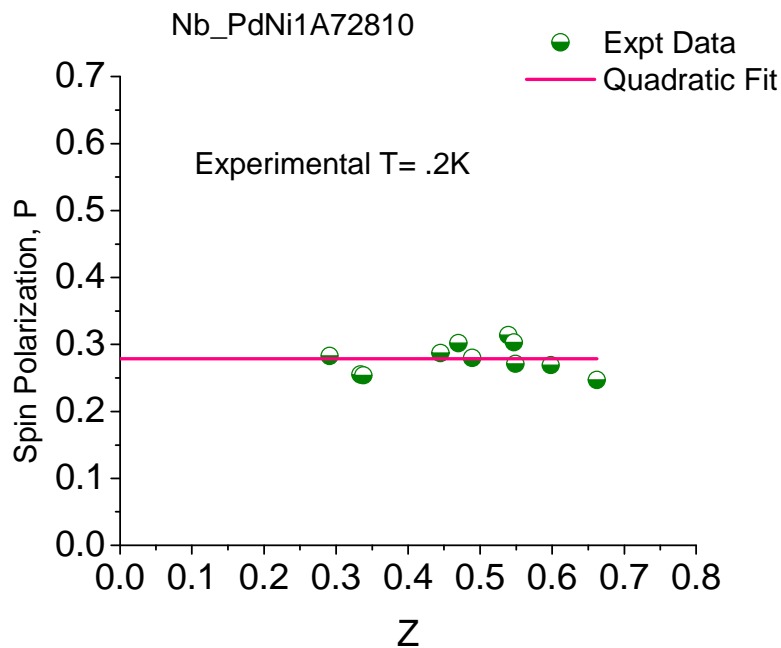
Fig. 12.26. Spin polarization as a function of interfacial barrier scattering for PdNi with Ni 2% sample 1A, at 4.2K

Though the spin polarization of this sample was measured already at 1.5K, it would be more relevant to measure it again for the same tip, and same contact in the present set up in order to compare them. So, the conductance curves were obtained in the same set up lowering the temperature by pumping Helium in the cryo dewer. The data were taken at 1.42K, and the examples of such fit curves are shown in Fig. 12.27.
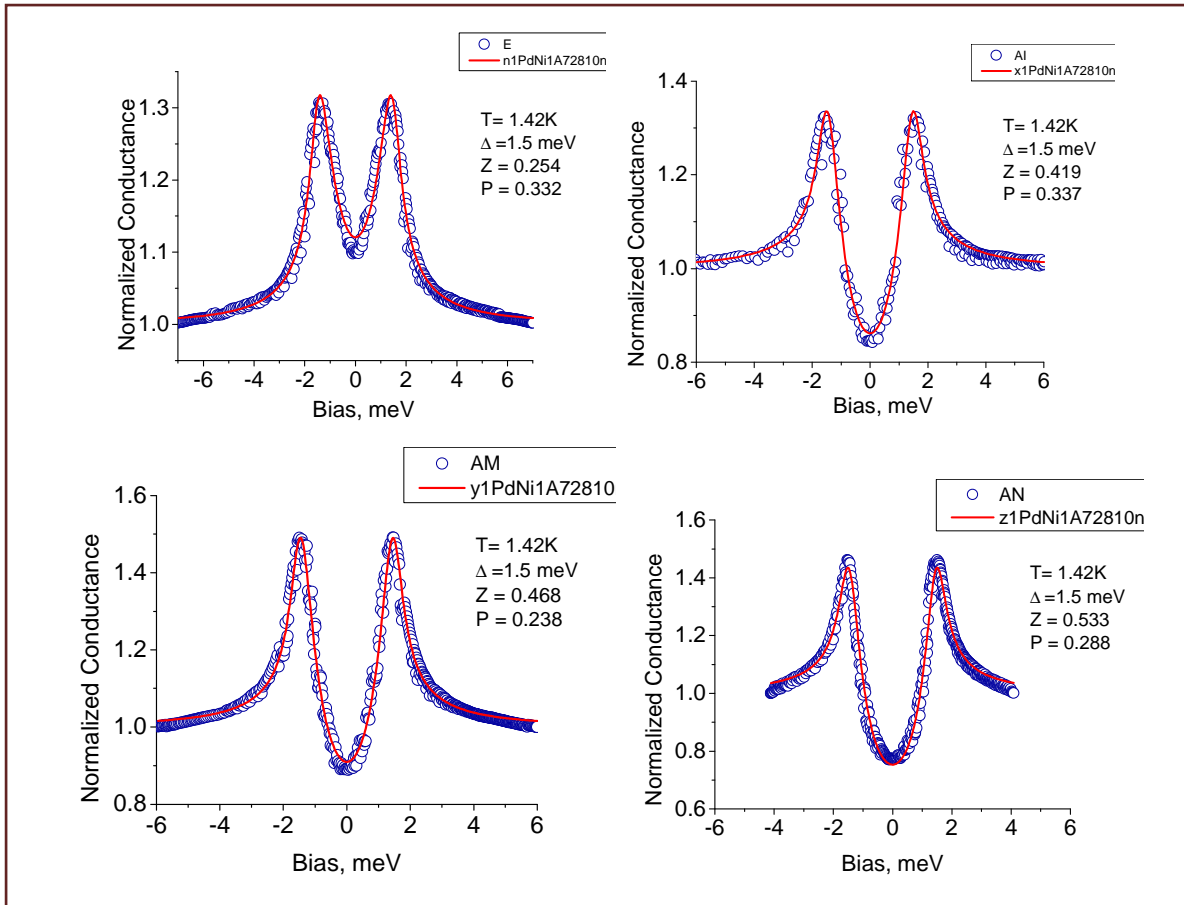
Fig. 12.27. Normalized conductance curves for PdNi with Ni 2% sample (1A), at 1.42K

Fitting was done for more than a dozen of conductance curves, and P was found to be Z dependent as before for this and for other samples. P at 1.42 K for clean interface (Z=0) was found to be 37.23% as shown in Fig. 12.28. It is clearly observed that the spin polarization at 4.2K (P = 27.9%) is lower than the spin polarization at 1.42K (37.23%) by 8.3%. The lower value of P at higher temperature is due to lower magnetization of the sample at higher temperature. We may expect no spin polarization above Tc, but due to technical difficulty, it was not possible to obtain conductance at higher temperature than 4.2K in the system we used.

For this particular sample, the spin polarization was measured before also as shown in Fig 12.12 at 1.5K, and it was found to be 40.2%. Present value at 1.42K is 37.23% which is close within +/-3%, which is reasonable in such measurements. This provides a concrete example of reproducibility of the P values.

PdNi 2% _sample 1A 72810

$T=1.42K$

$P=-0.4196\ Z^2+0.3723$
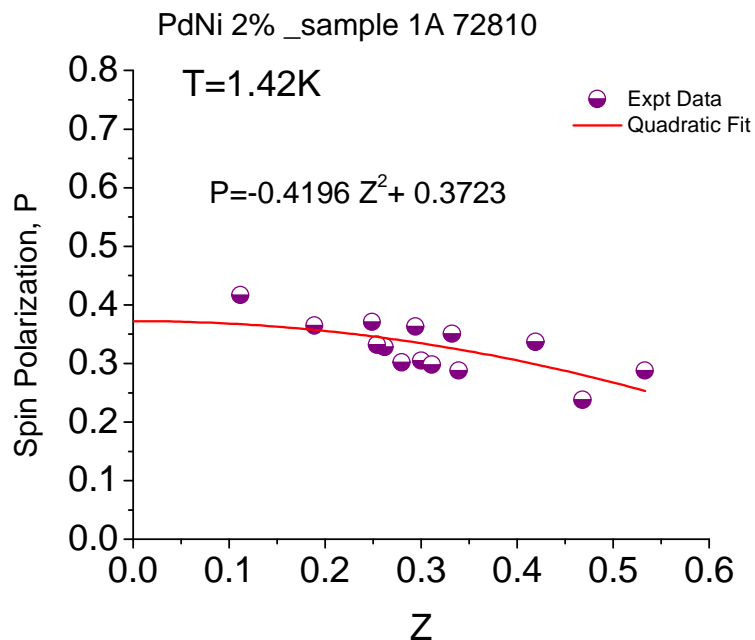
Fig.12.28 Spin polarization as a function of interfacial barrier scattering for PdNi with Ni 2% sample 1A, at 1.42K

12.9   Conclusion

Curie temperature, saturatioin magnetization and spin polarization were measured for six different thin film samples of PdNi with different Ni concentrations. Curie temperatures of the samples were found to be proportional to their saturation magnetization. Spin polarization was found to be proportional to the saturation magnetization and the Curie temperature as well but this proportional trend was true only for the samples sputtered at the same batch, otherwise the proportionality had different slope for the samples sputtered at different batches. This is possible

due to the fact that spin polarization values may be surface sensitive, and the surfaces of the films fabricated at different batches might have different topological and termination properties. This needs further study to understand the trend of the data. The spin polarization values ranged from about 33% to 49% in PdNi samples with the highest value for the sample with 12% Ni concentration, the largest concentration of Ni in our study.

CHAPTER 13

MAGNETISM AND SUPERCONDUCTIVITY IN COBALT DOPED IRON PNICTIDE $BaFe_2As_2$

13.1   Introduction

After the first discovery of superconductivity in Hg with transition temperature T_c of 4.2K in 1911 by H. Kamerlingh [Onnes, 1911], scientists were intrigued to find materials with higher transition temperature for the purpose of practical application of such materials. Among pure metal, the highest T_c of 9.2K was found in Nb [Meissner et al., 1930]. Next possibility remained to investigate the alloys, and the highest T_c of 23K was found in Nb_3Ge in 1972 [Gavaler, 1973]. After 14 years, a dramatic breakthrough was the report by Bednorz and Muller of T_c of 35K in copper based alloy $La_{2-x}Ba_xCuO_4$ for x = 0.15 [Bednorz et al., 1986]. Frenetic search for other materials gave the T_c of 92K in $YBa_2Cu_3O_{7-\delta}$ (δ = 0.1) in 1987 [Wu et al., 1987], 110K in $Bi_2Sr_{3-x}Ca_xCu_2O_{8+\delta}$ (x≤1) in 1988 [Maeda et al., 1988], 125K in $Tl_2Ba_2Ca_2Cu_3O_{10}$ in 1988 [Hook et al., 1991]. Although cuprate superconductors (LaBaCuO) have transition temperature above boiling point of Nitrogen, they exhibit a very short coherence length, very high anisotropy, and are brittle which hinder large scale applications [Wen, 2008]. This forced the superconductivity community to discover non-cuprate superconductors with high T_c.

In 2008, Hosono from Tykyo institute of technology reported superconductivity in $LaO_{1-x}F_x$ FeAs (x = 0.05-0.12) which is F-doped in parent material LaOFeAs (known as "1111" structure) with T_c of 26K [Kamihara et al., 2008]. Soon, Such other materials were reported to show superconductivity with T_c of 43K in $SmO_{0.85}F_{0.15}FeAs$ [Chen et al., 2008], 50K in $NdO_{0.85}F_{0.15}FeAs$ [Chen et. al., arXiv:cond- mat/0803.3790], 50K in $PrO_{0.85}F_{0.15}FeAs$ [Ren et. al., 2008] . These materials with layered structure in c-axis are referred to as quaternary oxypnictides and have the general formula LnOMPn where Ln = La, Ce, Pr, Nd, Sm, Eu, and

Gd etc.; M = Mn, Fe, Co, and Ni, etc, Pn = P, and As, etc. As being in the nitrogen group, these compounds are the compounds of Nitrogen group material and are called "pnictides". Fig. 1 shows the layered crystal structure of 1111 FeAs material where FeAs layers are separated by spacer layers of LaO. Fluorine dopants are introduced in LaO layers as shown, and the tansport measurements show that F-dopped materials have electron-like charge carriers with low density. This is because the Fluorine replaces Oxygen donating electrons to the FeAs layer. Later it was found that iron based superconductivity is possible in hole-dopped (substituting trivalent La by divalent Sr and without F doping) system [Wen et al., 2008]. In these materials, either by changing pressure or by doping on 1111 parent materials, it was possible to achieve T_c beyond 50K. However, the search for simpler class of materials with the hope of possibly increasingly higher T_c continued, and superconductivity in $BaFe_2As_2$ parent compound , the 122 structure, without LaO spacer layers was found to be superconducting with comparable T_c to compounds with the 1111 strucuture. Co dopping in $BaFe_2As_2$ has shown T_c up to 22K, and the Co doping system gives robust superconductivity in FeAs layer as compared to cuprate superconductors in which the doping on the Cu sites destroys the superconductivity. With this historical development of why $BaFe_2As_2$ compounds are being developed and considered for potential high T_c superconducting materials, this study will focus on other magnetic and superconducting properties of $BaFe_2As_2$. It is important to recall that the conventional superconductors can be explained by BCS theory, while high Tc materials cannot be explained by this.

(a)   (b)
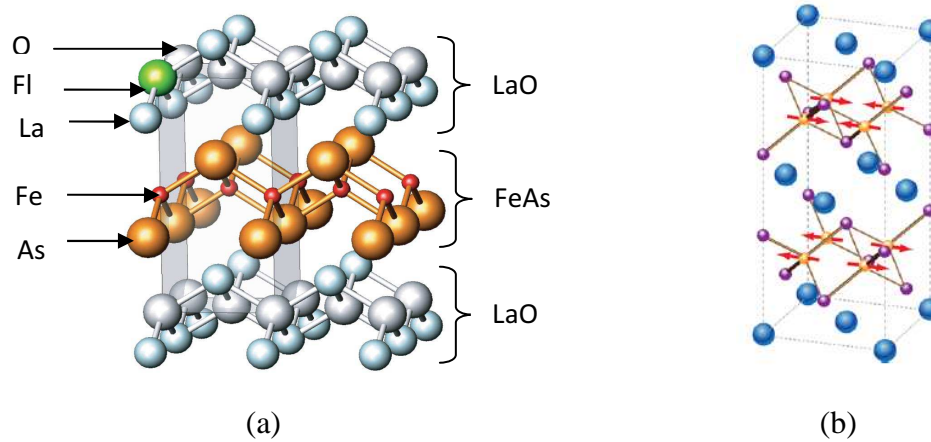
Fig. 13.1. Crystal structure of Iron Pnictides (a) 1111 FeAs material [Takahashi et al., 2008], (b) 122 FeAs material [Goldman., arXiv:0807.1525v$_2$]. Iron moments (shown by red arrows) form stripped antiferromagnetic pattern in the parent compound of both materials.

13.2   Structural and magnetic transitions in BaFe$_2$As$_2$

BaFe$_2$As$_2$ compounds show different structural and magnetic transitions compared to LaOFeAs type of compounds. Unlike separate structural and magnetic transitions in 1111-type materials, the first order simultaneous structural and magnetic transition has been observed by neutron diffraction studies in 122 type materials [Huang et al., 2008]. The magnetic transition in BaFe$_2$As$_2$ occurs at the same temperature where the structural transition from tetragonal to orthorhombic symmetry occurs. Fig. 2 shows the dependency of resistivity of BaFe$_2$As$_2$ with temperature, and it shows the anomaly of resistivity at 142K which is due to the first order structural transition which is indicated by the hysteresis in neutron diffraction intensity at diffraction angle $2\theta = 95.8^{\circ}$ as shown by the inset in Fig. 2. In terms of the magnetic structures, antiferromagnetic transition occurs at the same temperature as the structural transition, and the antiferromagnetic alignment and magnetic moment are both along the longer a-axis in the FeAs plane. The first order structural and magnetic transition indicates strong coupling between the structural and magnetic order parameters.
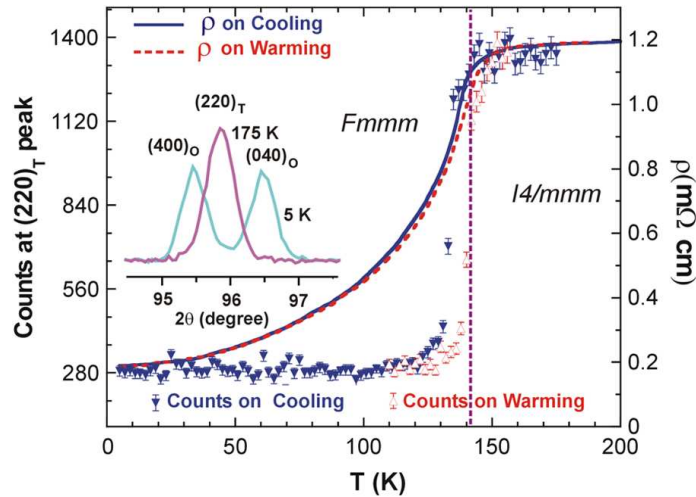
Fig. 13.2. Resistivity while cooling and warming of BaFe$_2$As$_2$, and showing structural transition at T$_s$ = 142K. Inset shows the splitting of neutron diffraction peak below T$_s$ indicating magnetic transition [Huang et al., 2008].

13.3   Effect of Co doping in BaFe$_2$As$_2$

Co (or Ni) doping which is the electron doping in BaFe$_2$As$_2$ replaces Fe atom in FeAs layer producing superconductivity [Sefat et al., 2008]. Even though higher T$_c$ of 38K was found by hole doping (replacing some of Ba+ by K+) with the doping of Potassium [Rotter et al., 2008] in BaFe$_2$As$_2$, Co doping is more advantageous due to directly added carriers in FeAs layers, and it being easier to handle than alkali metals despite its lower T$_c$ = 22K [Sefat et al., 2008]. Temperature dependent resistivity in the ab- plane of parent and its Co-doped compound as measured by Quantum Design PPMS is shown in Fig. 3(a). Both BaFe$_2$As$_2$ and BaFe$_{1.8}$Co$_{0.2}$As$_2$ show metallic behavior with the parent compound showing its resistivity at 300K and 2K to be 5.9 mΩcm and 5 mΩcm respectively. However, the resistivity for BaFe$_{1.8}$Co$_{0.2}$As$_2$ is much smaller than BaFe$_2$As$_2$ as shown in the inset of Fig. 3(a). The resistivity of BaFe$_{1.8}$Co$_{0.2}$As$_2$ drops suddenly as the temperature is lowered down below 22K showing onset of superconductivity at 22K at 0T of magnetic field, and it shifts to lower temperatures with the magnetic field as shown for 8T of magnetic field in Fig. 3(a). The transition width of

$BaFe_{1.8}Co_{0.2}As_2$ is $\Delta T = 0.6K$ in absence of magnetic field, and it becomes wider ($\Delta T = 1.3K$ for

8T) when magnetic field is applied indicating that $BaFe_{1.8}Co_{0.2}As_2$ is type II superconductor.

Fig. 3(b) shows how Hall coefficient of $BaFe_{2-x}Co_xAs_2$ depends on temperature for various

Cobalt concentration (x = 0.08, 0.16, 0.20, and 0.60). For x = 0.08 and 0.16, the Hall coefficient

shows big slope corresponding to the anomaly in resistivity. Strong temperature dependence is

observed above the superconducting temperature for the Co concentration of x = 0.2 which,

being consistent with the fact that the Hall coefficient for the SDW state of a sample shows

strong temperature dependence above SDW transition temperature, indicates that this

concentration of Co gives spin density wave state of the sample and indicates strong magnetic

fluctuation. At higher concentration of x = 0.6 of Co, Hall coefficient seems independent of

temperature as expected in the Fermi-liquid state. Hence, the dependence and evolution of Hall

coefficient with Co concentration indicates that the system evolves from SDW state to the Fermi

Liquid state.

(a)   (b)
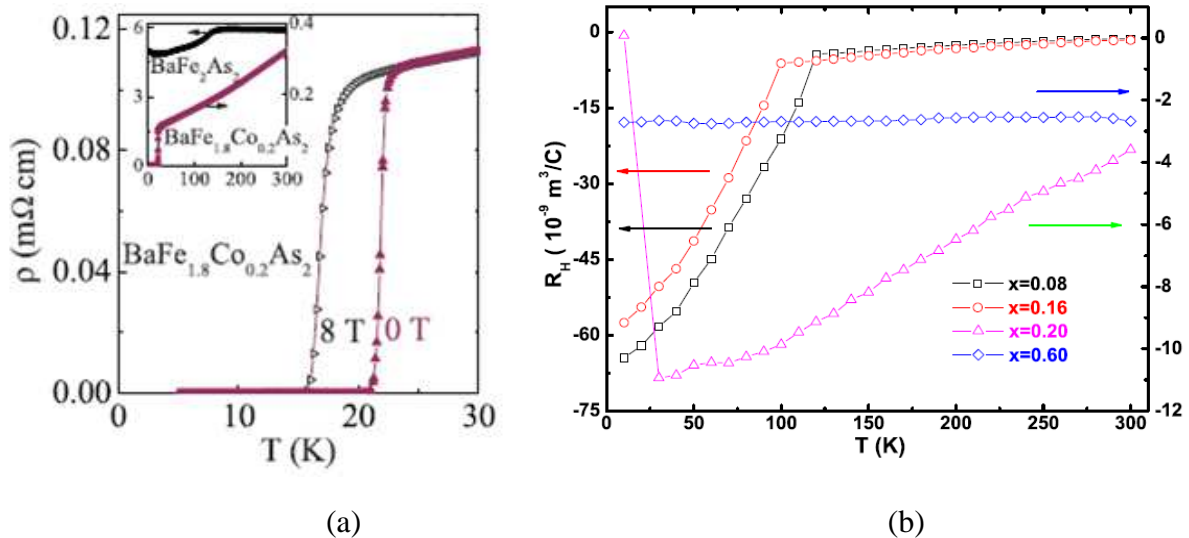
Fig.13.3. Temperature dependent (a) [Sefat et al., 2008] resistivity of $BaFe_{1.8}Co_{0.2}As_2$ at 0T and 8T magnetic fields with inset showing the comparison between the parent $BaFe_2As_2$ and Co doped daughter compound $BaFe_{1.8}Co_{0.2}As_2$, (b) [Wang et al., 2009] Hall coefficient of $BaFe_{2-x}Co_x As_2$ (x = 0.08, 0.16, 0.2, 0.6).

13.4   Effect in superconductivity of $BaFe_2As_2$ due to Co concentration

Field cooled (FC) and zero field cooled (ZFC) susceptibility show sharp superconductivity transition as shown in Fig. 4. These set of data show the data for temperature range of 2K to 30 K at fixed magnetic field of 5 Oe. Calculation of superconducting volume fraction shows that it reaches 100% at 2K for the $BaFe_{2-x}Co_xAs_2$ sample with x = 0.17, 0.18 and 0.25, and 80% for the sample with x = 0.20 indicating bulk superconductivity in these samples.
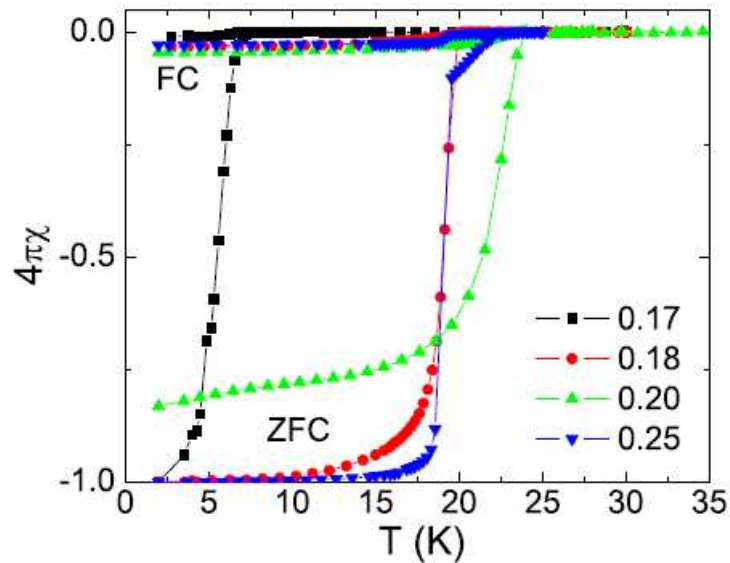
Fig.13. 4. Temperature dependent susceptibility for $BaFe_{2-x}Co_xAs_2$ (x = 0.17, 0.17, 0.2, 0.25) [Wang et al., 2009].

13.5   Similarities and differences of Cuprate and Pnictide superconductors

To understand the pnictide superconductors, people have tried to see the similarities and differences between superconducting mechanisms in cuprate superconductors and pnictide superconductors. The parent compounds of cuprates are Mott insulators whereas the parent compounds of pnictides are computed to be semi metals [Singh et al., 2008]. The pnictides are found to be more isotropic in a magnetic field [Ni et al., 2008] , which may facilitate technological application due to more effective pinning of quantized magnetic vortices [Norman, 2008]. Figure 5 shows the topographic images of cleaved surface of optimally doped single

crystal of $BaFe_{1.8}Co_{0.2}As_2$ at 6.15K in zero magnetic field, and taken by cryogenic scanning tunneling microscope (STM) [Yin et al., 2009]. Alternate rows of complex stripelike structures are seen on the image. Interatomic spacing from the Fourier Transform was found to be 3.96Å.

(a)   (b)   (c)
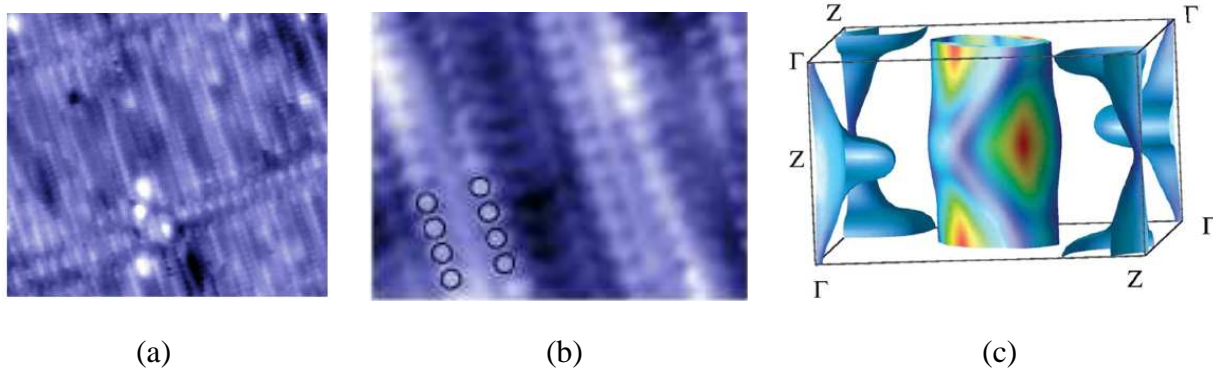
Fig.13.5. (a) Topographic image of the cleaved surface of $BaFe_{1.8}Co_{0.2}As_2$, (b) Zoom in within the image (a). The circles denote the position of stripe structures. The interatomic spacing is 3.96 Å [Yin et al., 2009]. (c) Local density approximation (LDA) Fermi Surface of $BaFe_{1.8}Co_{0.2}As_2$ (light blue is the low band velocity) [Sefat et al., 2008].

Co is more strongly hybridized with As than Fe. Fig. 5(c) shows the calculated Fermi surface of the virtual crystal without magnetism. Effect of Co doping on the structure of the Fermi Surface at the virtual crystal level is similar to the effect of electron doping on the Ba site [Sefat et al., 2008]. Possibility of two band superconductivity arises due to depleted Co contribution within E_F, and the same Co contribution as E_F starting from 0.2 eV above E_F. Strong interband scattering would lead to the assumption of an s-symmetry superconducting state [Sefat et al., 2008].

13.6   Pinning of vertex lattice in $BaFe_{2-x}Co_xAs_2$

Electron pairing, the fundamental property of superconductivity is characterized by the superconducting energy gap Δ of the material in the electronic density of states (DOS). Yin (Yin et. al., 2009) found the range of superconducting gap by taking a series of conductance data of $BaFe_{1.8}Co_{0.2}As_2$ from 4.5 to 8 meV, and the average of large pool of data was found to be

6.25meV at temperature of 6.25K and zero magnetic field [Yin et. al., 2009]. Muon spin rotation (µSR) technique allows to investigate the local magnetic field distribution on a microscopic scale and to directly access the corresponding volume fractions [Weidinger et al., 1989]. In this technique, muons are implanted into the bullk of the sample. The muons thermalize in short time scale of about 10^{-12}sec without any noticeable loss in their initial spin polarization. Analogously as in cuprate superconductors, these muons are likely bound to the negatively charged O or As ions which allows to probe certain volume of interest in the sample. Positive muon decays into two neutrinos and a positron which is emitted along the direction of the muon spin at the time of decay. Time resolved detection of the decay positron emission rate gives the time evolution of the spin polarization P(t) of the muon ensemble. Fig. 6(a) shows the result of a vortex–lattice pinning experiment. µSR lineshape data taken after the crystal cooled in presence of transverse field of 0.1 T to 5K during which vortex lattices are developed shows two peaks centered around 0.095T and 0.1T. The first peak corresponds to the background muons that miss the sample, and the second peak corresponds to the muons that stop in the sample where the vortex lattice forms below T_c that is strongly pinned by defects such that the magnetization density cannot follow the change of the external magnetic field. Splitting between the position of the background and vortex lattice signals with large amplitude indicates that the crystals $BaFe_{2-x}Co_xAs_2$ (x = 0.2, 0.25) are bulk superconductors. By fitting the ZF-µSR time resolved spectra at different representative temperatures of optimally doped $BaFe_{1.8}Co_{0.2}As_2$ single crystal by using relaxation function [Weidinger et al., 1989] the relaxation rate λ were extracted which depend on temperature as shown in Fig. 6(b). It suddenly increases below T_c = 25K which reveals the existence of weak magnetic correlations that set in right below T_c, and shows that the superconductivity-induced change in the spin dynamics.

(a)   (b)
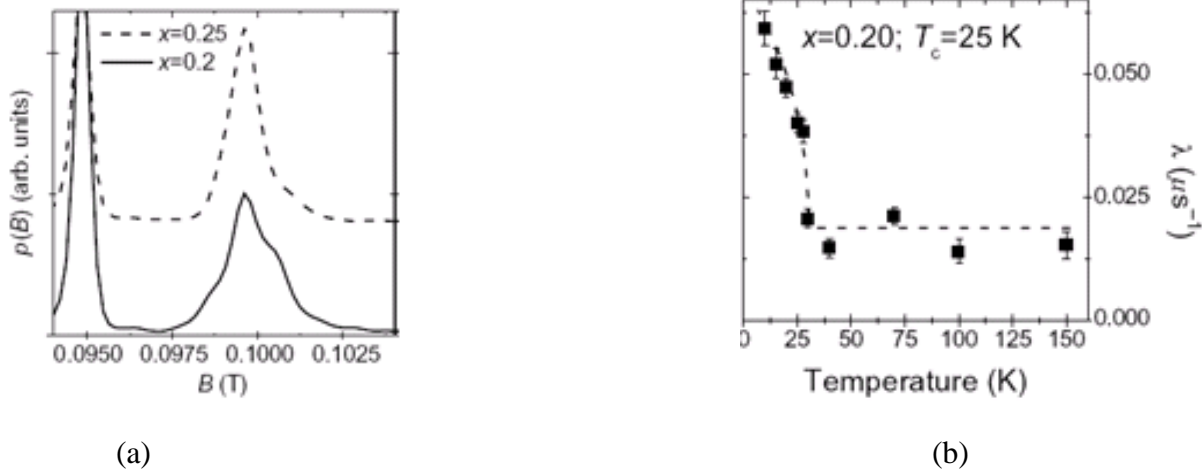
Fig. 13.6 (a) Transverse field cooling- μSR data on BaFe$_{2-x}$Co$_x$As$_2$ (x = 0.2 and 0.25) showing pinning of the vortex lattice, (b) temperature dependence of relaxation rate [Weidinger et al., 1989].

13.7. The phase diagram of BaFe$_{2-x}$Co$_x$As$_2$

A complete phase diagram of electronic evolution defined by the anomaly in resistivity (T$_s$) and the superconductivity (T$_c$) transition by resistivity and susceptibility respectively, as shown in Fig. 7 shows that the spin density wave (SDW) state is suppressed (reduction of SDW transition temperature) with Co doping, and Fermi liquid state develops. In the Co doping range of 0.15≤x≤0.20, SDW state and superconductivity coexist in BaFe$_{2-x}$Co$_x$As$_2$ system. Further increase in Co doping shows the temperature independent Hall coefficient, and Curie-Weiss-like behavior supporting the emergence of Fermi-liquid state. T-linear behavior in susceptibility is expected in superconducting samples, and it is observed up to 700K in BaFe$_{2-x}$Co$_x$As$_2$ system for x>0.2 showing strong magnetic fluctuation above SDW ordering, and T^2 behavior in susceptibility is observed in the overdoped sample [Wang et al., 2009]. This indicates that the strong magnetic fluctuation could be important for superconducting mechanism in iron based 122 systems.
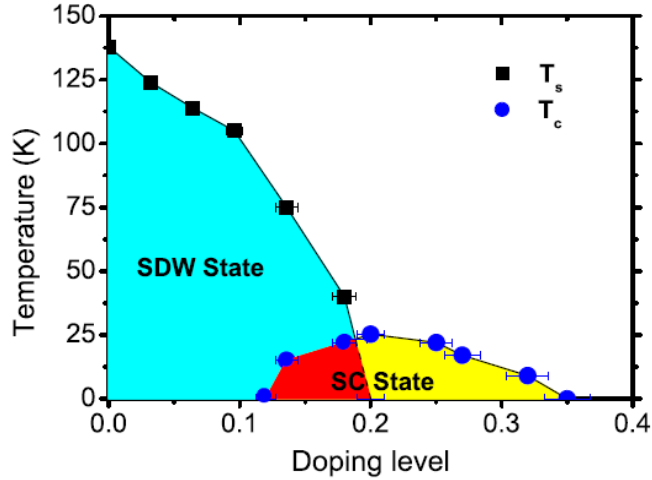
Fig.13. 7. The phase diagram of $BaFe_{2-x}Co_xAs_2$ within the range $0 \leq x \leq 0.40$. Both T_s and T_c are determined by resistivity [Wang et al., 2009].

13.8 Temperature dependent and magnetic field dependent conductance, and indication of pseudogap in $BaFe_{1.8}Co_{0.1}As_2$

Understanding the superconductivity in iron based superconductors is a growing interest, and Point Contact Andreev Reflection (PCAR) spectroscopy was used [Panguluri et al., unpublished] to obtain temperature spectra of conductance curves for $BaFe_{1.8}Co_{0.1}As_2$ at zero magnetic field as shown in Fig. 8(a) so that superconducting gap can be extracted from these conductance curves. Interestingly, besides regular BCS superconducting gap, different wider gap appeared below superconducting transition temperature at around 12 meV, and it was called pseudogap. It was possible to suppress this gap by applying magnetic field ~14 KG perpendicular to the ab-plane whereas the BCS gap is not suppressed even at 7T. Fig. 8(b) shows the magnetic field spectra at 12K for $BaFe_{1.8}Co_{0.1}As_2$. The magnetic field to suppress the BCS gap at 2K is 4T and at 7K is 2T (not shown here), showing the need of lower magnetic field to suppress the pseudogap at higher temperature. From this, it is possible to speculate that the pseudogap could arise from antiferromagnetic fluctuations emanating locally in this system.
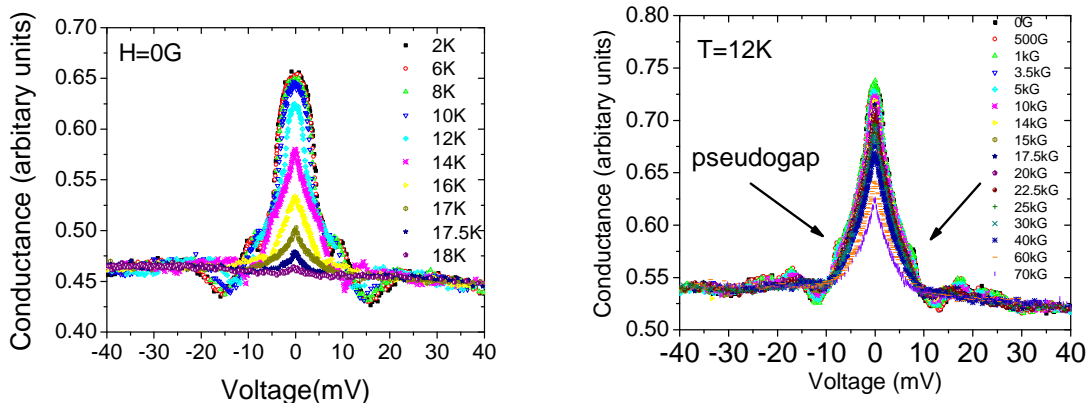
Fig. 13.8. (a) Temperature dependent conductance curves for a Au/ $BaCo_{0.1}Fe_{1.8}As_2$ with a contact resistance $\sim 7\Omega$ in zero magnetic field, b) Field dependent conductance curves for the same contact at 12K, and showing the pseudogap suppression by magnetic field perpendicular to ab-plane for the same contact.

13.9   Conclusions

To sum up, this study has attempted to summarize the historical development of superconductivity showing the trend on how Co doped 122 iron pnictides came into play. The transport, magnetic, and superconductive properties of $BaFe_{2-x}Co_xAs_2$ superconductors have been discussed. With Co doping, magnetic order is destroyed and superconductivity is induced. The evolution from SDW state to Fermi-liquid state, and their coexistence at x = 0.17 is shown by the phase diagram. Evidence of pseudogap below superconducting transition temperature, and its suppression with magnetic field, was found by Point Contact Andreev Reflection (PCAR) technique. In the pursuit of higher T_c superconductors, there can be different routes such as finding materials with new structures, or fabricating materials with layered structure of FeAs. However, exact reason of pairing mechanism for superconductivity in such materials is still a question of research.

CHAPTER 14

MAGNETISM AND SPIN POLARIZATION OF PLATINUM THIN FILMS

14.1 Introduction

Transition metal platinum with atomic number 78 has partially filled 5d shell with electronic configuration [Xe] $4f^{14} 5d^9 6s^1$ and a spin triplet ground state. In the bulk, Pt does not show magnetic ordering. However, literature shows that its magnetic properties have been studied in its different forms. Makoto [Sasaki et al., 1998] have reported that the samples of Pt nano-particles in the form of cluster, and samples of Pt nano wires in the form of nano-rods exhibit magnetism with magnetic moments of 1.54 μ_B per Pt and 0.131 μ_B per Pt respectively. They found different temperature dependence of magnetization of Pt nano particles and nano rods which they think is possible due to the anisotropic morphology of Pt nano-wires for the electron-spin ordering.

Ferromagnetism in Pt nanowires has been predicted theoretically by Delin et al. [Delin et al., 2004]. Their calculation showed that the magnetic moment of one dimensional equally spaced Pt chain in equilibrium bond length of 2.48 Å is 0.6 μ_B per atom and it increases if the bond length is stretched. The magnetism they observed was Hund's rule magnetism. They also predicted that more majority bands cross the Fermi level than do minority bands, resulting in a partial spin polarization of the transmitted electron current. Magnetic anisotropy of spontaneously magnetized nanosystem such as an adatom, a cluster or a nanowire is a crucial parameter because it helps to reduce the magnitude of thermal (superparamagnetic) fluctuations, and such anisotropy are theoretically predicted in monatomic free and deposited Pt nano wires by Smogunov et al. [Smogunov et al., 2008]. Orbital magnetization and the spin orbit coupling is the cause of such anisotropy whose maximal value should correspond to minimal atomic caging

such as adatom and linear atomic chain; and in the case of Pt chain, the anisotropy persists after weak adsorption on an inert substrate or surface step [Smogunov et al., 2008]. The magnetic profiles for the scalar and fully relativistic calculations are found to be different for Pt. Scalar relativistic calculation predicts that Pt is magnetic only for stretched wires, whereas the fully relativistic calculation predicts it to be magnetic in the range of bond lengths ~2.2 to 3.2 Å [Delin et al., 2003].

Detailed study of Pt clusters is found in Kumar et al. [Kumar et al., 2008]. They have reported that Pt clusters have small magnetic moments which tend to decrease with an oscillatory behavior as the cluster size increases which they explain considering ferromagnetic and antiferromagnetic couplings between the spins in some cases. Even the large octahedral clusters differ from bulk surface due to large dispersion and the presence of low coordination sites, such as edges and vertices, and such nearly planar as well as other open structures in the small size range give Pt particles with different structures and properties [Kumar et al., 2008]. Such behavior will be helpful in explaining the origin of magnetism in Pt thin films we observed.

Magnetism of 3d, 4d and 5d transition metals in their monolayer thin films on noble metal (001) substrates such as Ag (001) and Au (001)) was studied by Blügel [Blügel., 1992]. He predicted ferromagnetism of 5d transition metal monolayers for the first time. For Ir on Ag (001) and Au (001) substrate the magnetic moments of 0.9 μ_B were predicted theoretically. In some cases, the magnetism is found dependent on the substrate material. For an instance, Os was predicted magnetic on Ag (001) substrate but nonmagnetic on Au (001) substrate. Pd and Pt monolayers, which are in 4d and 5d series, are nonmagnetic [Blügel., 1992; Blügel., 1995] since the d-d hybridization between monolayers and substrate destroys the magnetic moment

[Redinger et al., 1995]. The hybridization between the d-orbitals and the sp electrons of the noble metal substrate is the controlling parameter of magnetism in such monolayers [Blügel., 1992].

After three years of studying the magnetism of monolayer, magnetism of 4d and 5d transition metal bilayers on noble elements Ag (001) substrate was studied by Blügel [Blügel., 1995] by *ab initio* calculations. It was reported that bilayer of Pt showed ferromagnetism as shown by Rh, Pd, and Ir, but compared to monolayers of Ir, Os on Ag (001), the moments are strongly reduced to less than $0.35\mu_B$ indicating that the magnetic moment is dependent on the thickness of the film and also indicating the possible effects of island growth and cluster formation in magnetic properties [Blügel., 1995]. In case of 3d metal films, Ferromagnetic monolayers Fe, Co, and Ni remain ferromagnetic upon deposition of additional layers, whereas V, Cr, and Mn monolayers show an in-plane antiferromagnetic order which, except V which becomes non magnetic, transforms after additional layer deposition to antiferromagnetic order normal to the surface [Blügel., 1995]. The sudden collapse of the magnetic moments of the bilayers was explained with the onset of the d-d hybridization due to the existence of the second transition-metal layer. The presence of weak magnetism in Pt bilayers is the onset of bulk effect, and it is driven by the expansion of the Pt lattice constants due to the Ag substrate [Blügel., 1995]. However, these studies were done for the Ag and Au (001) substrates only and possible magnetism for thicker films (several layers), and in other substrates such as Si is unknown in this study. Our study will try to address such issues.

Magnetism of 4d (Mo, Tc, Ru, Rh, Pd) and 5d (Re, Os, Ir) transition-metal over layers on Ag (111) was studied by Redinger et al. [Redinger et al., 1995]. Their *ab initio* calculations showed that Ru, Rh, and Ir have nonvanishing magnetic moments. Similar study on Ag (100) and Au (100) substrates were done [Blügel., 1992, Zhu et al., 1991, Eriksson et al.,1991, Blügel

et al., 1992, Wu et al., 1992], and the same trend in magnetic moment was found with the magnetic moments of the (111) oriented monolayers being smaller due to the increase of the coordination number in the monolayer film [Redinger et al., 1995]. These results show that the magnetism of monolayers of 4d and 5d transition metals depends on substrate orientation and local atomic coordination.

Thinking that the magnetism might have complicated effects due to intermixing of 4d and 5d transition metals with metal substrates like Ag and Au, Yang et al. [Yang et al., 2010] used oxide substrate such as MgO (001) to predict magnetism by *ab initio* calculations in ultrathin Pt monolayer films formed on them. They found a high density of states (DOS) peak of $N(E_F)$ = 4.42 states/eV/(1×1) at the Fermi energy E_F , and using the Stoner exchange integral, I = 0.295 eV [Sigalas et al., 1994], they found that the Stoner criterion for ferromagnetism, $N(E_F)$ I ≥ 1 is satisfied leading to the ferromagnetism of Pt monolayer on MgO(001) with magnetic moment of $0.89\mu_B$ [Yang et al., 2010] which is larger than the values of $0.23\mu_B$/atom and $0.33\mu_B$ /atom for the surface and the interface Pt atoms of magnetic Pt bilayers on Ag(001) [Blügel., 1995]. This magnetic moment on MgO (001) was close to the magnetic moment of calculated value ($0.8\mu_B$) of freestanding Pt monolayer which indicates that the unusual magnetism in 1-ML Pt/MgO(001) is related to the appearance of ferromagnetism in a freestanding Pt monolayer.

From these discussions we can summarize that the magnetic moments of lower dimensional Pt such as adatoms, nanorods, bilayers on noble metal substrates like Ag (001) and Au (001), and monolayer on oxide substrate such as MgO (001), and even freestanding monolayers are possible. However, it is not seen in the literature about the magnetism of several layers of Pt thin films. In our case, we studied the magnetism of Pt thin films ranging from 10nm to 100nm, and its dependence on the thickness of the film and the surface roughness of the films.

Magnetizations were measured using SQUID, and also they were cross-checked for some samples by using neutron scattering. Also, the transport spin polarization of Pt thin films was studied. Intrinsic values of transport spin polarization of 40.2% to 52.6% were measured for different Pt samples. This is a strong support for the existence of magnetism in Pt thin films. This will be discussed in the sections ahead.

The structural study of Pt thin films is reported by Lim et.al. [Lim et al., 2004]. They report that the sputtered Pt thin films usually show a highly (111) textured growth behavior with (111) direction perpendicular to the substrate surface, and the in plane orientation is random. The properties and structure of Pt films such as stress, grain size, degree of texturing, surface roughness, and defect concentration are influenced by the growth conditions. These factors influence the performance of functional thin films in various ways [Lim et al., 2004].

14.2   Platinum thin film fabrication

In order to study the magnetism in Pt thin films, and to study transport spin polarization in those films, several samples of different thickness were deposited by using Pt target of 99.99% purity. Platinum thin films of thickness 10, 12.7, 21.2, 25.55, 30, 33.3, 55.5, 65.18, 74, and 100nm were used for the study. 10nm and 30 nm thick films were prepared by e-beam deposition, and the rest of the films were deposited by magnetron sputtering. The deposition conditions were kept the same within experimental limitations.

14.2.1 Measurement of Film thickness

Film thickness was estimated by the crystal monitor during deposition. To cross check and confirm, the thickness of the films were measures by XRR method also. The thicknesses expected from the crystal monitor method were less reliable, so the thicknesses from the XRR

method were considered the final and exact values. Some of the fits of the data by XRR method are shown in Fig. 14.1.
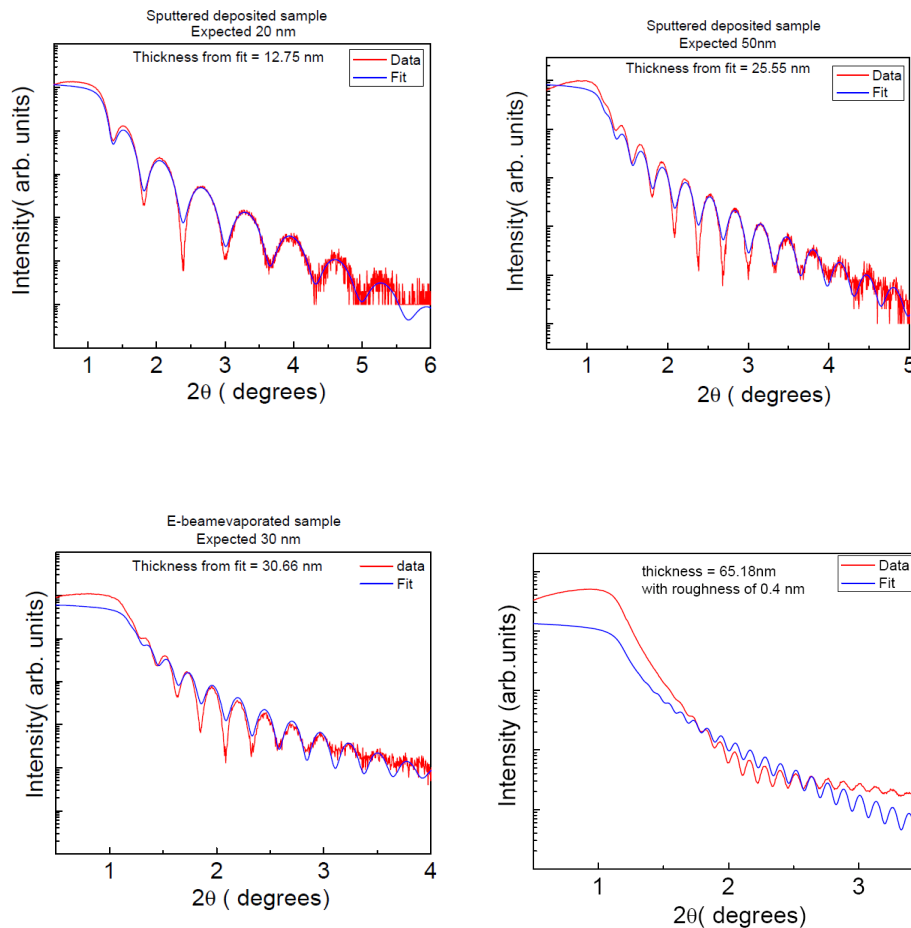
Fig.14.1. Some representative curves of measurements of Pt film thickness by XRR method: Top left panel, Pt thickness = 12.75nm, Top right panel, Pt thickness = 25.55nm, Bottom left panel, Pt thickness = 30 nm, Bottom right panel, Pt thickness = 65.16nm

14.3   Magnetization measurements of various Pt thin films

The magnetization of all thin films of Pt were measured by superconducting quantum interference device (SQUID) in both parallel and perpendicular configurations, i.e. when the plane of the sample is parallel to the magnetic field and when it is perpendicular to the magnetizing field in the SQUID respectively. Several pieces of the same sample were stacked so as to increase the signal of magnetization, which were later normalized with the volume of Pt

films used to get the magnetization in emu/cm^3. For every sample, the magnetization was measured at 300K and at 5K from -0.5T to +0.5T of magnetizing field. The M-H loops for different samples at 10K and 300K for H parallel to the sample plane and H perpendicular to the sample plane are given in Fig. 14.2 (a-j).
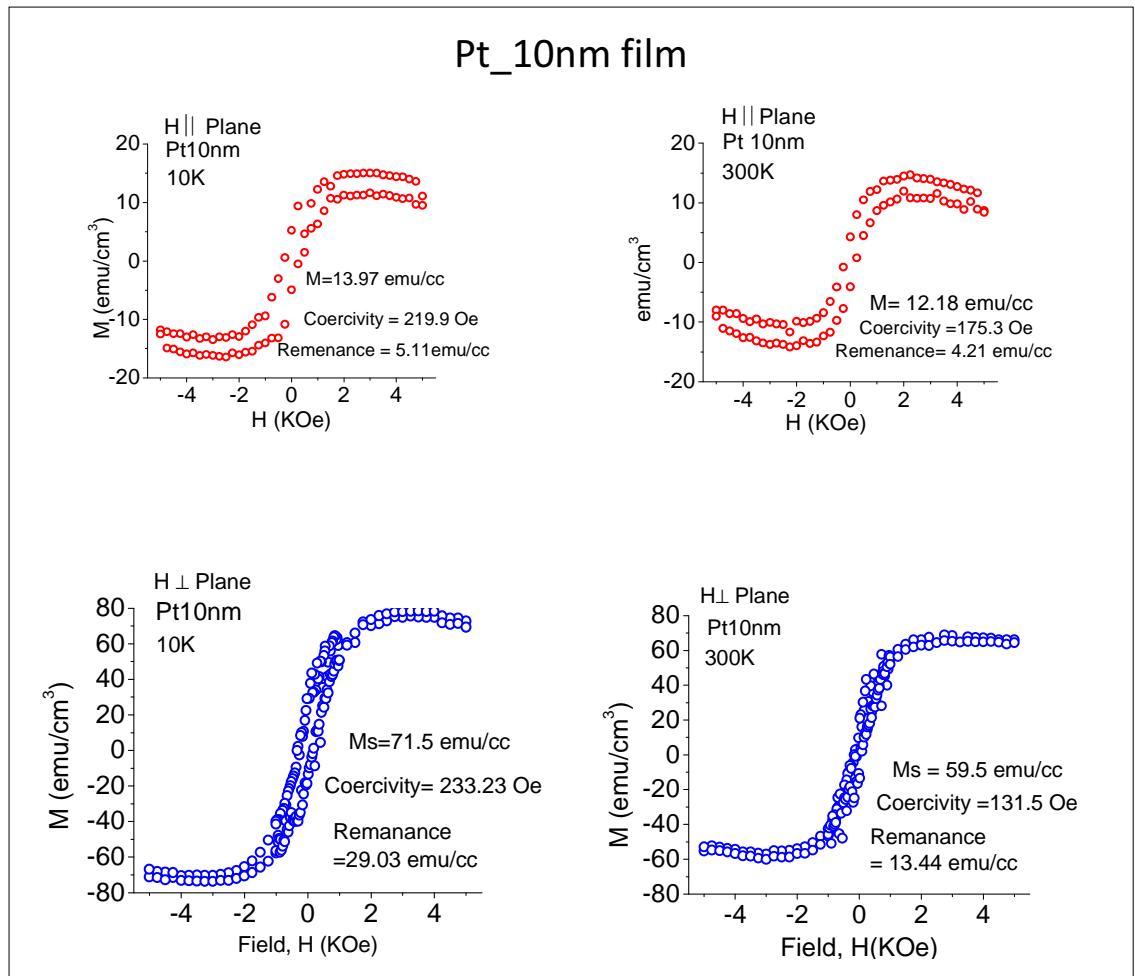
Fig. 14.2. (a) Magnetization measurements of Pt films 10nm in thickness in H parallel to sample plane (top two panels in red colour), and in H perpendicular to the sample plane (bottom two panels in blue colour).
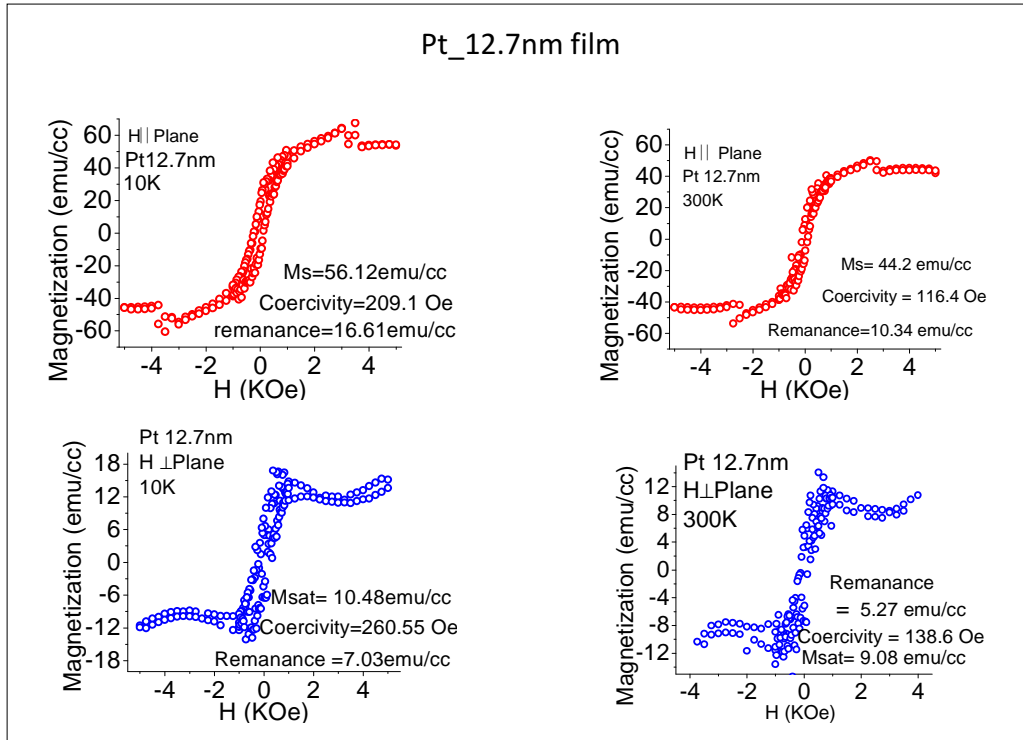
Fig. 14.2. (b) Magnetization measurements of Pt films 12.7nm in thickness in H parallel to sample plane (top two panels in red colour), and in H perpendicular to the sample plane (bottom two panels in blue colour).
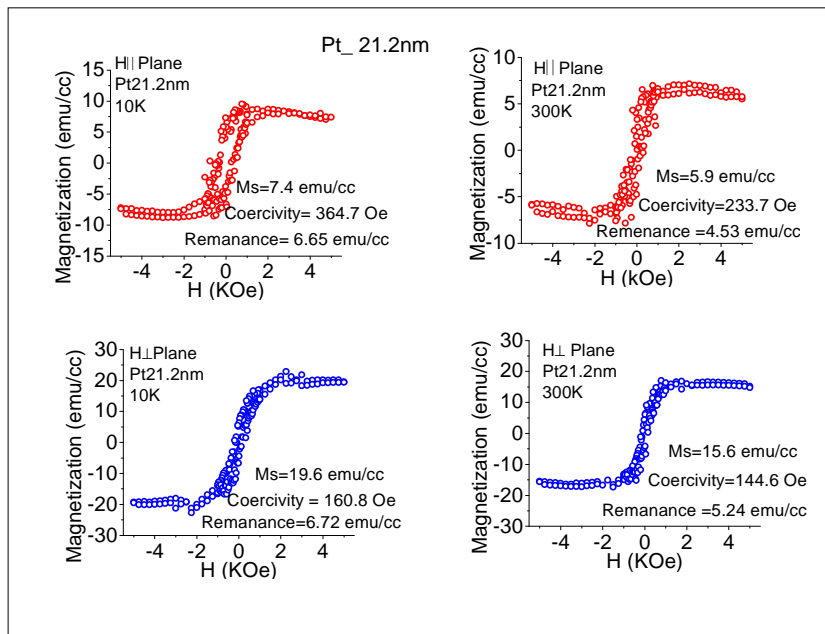
Fig. 14.2. (c) Magnetization measurements of Pt films 21.2nm in thickness in H parallel to sample plane (top two panels in red colour), and in H perpendicular to the sample plane (bottom two panels in blue colour).
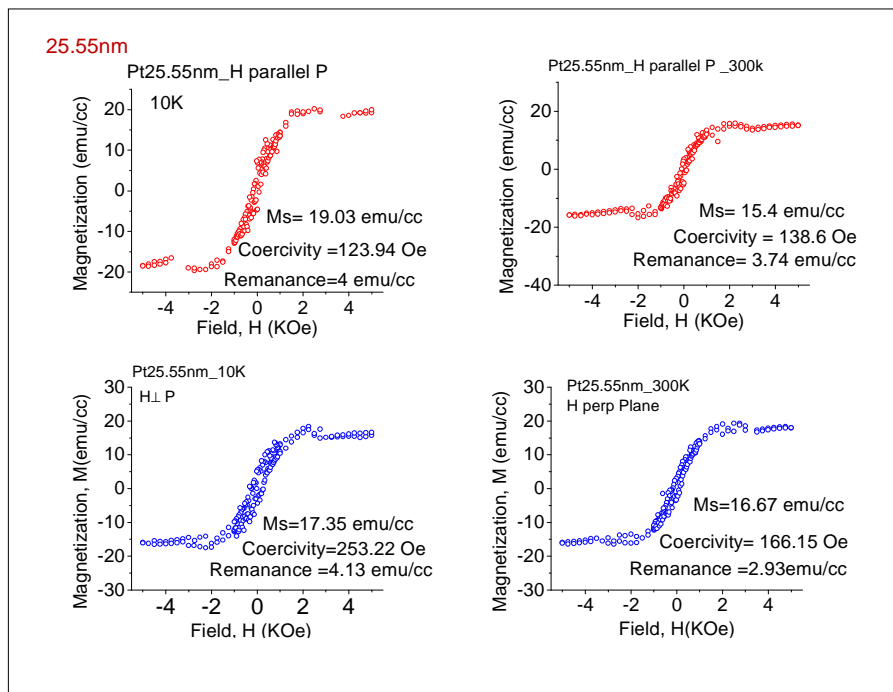
Fig. 14.2. (d) Magnetization measurements of Pt films 25.55nm in thickness in H parallel to sample plane (top two panels in red colour), and in H perpendicular to the sample plane (bottom two panels in blue colour).
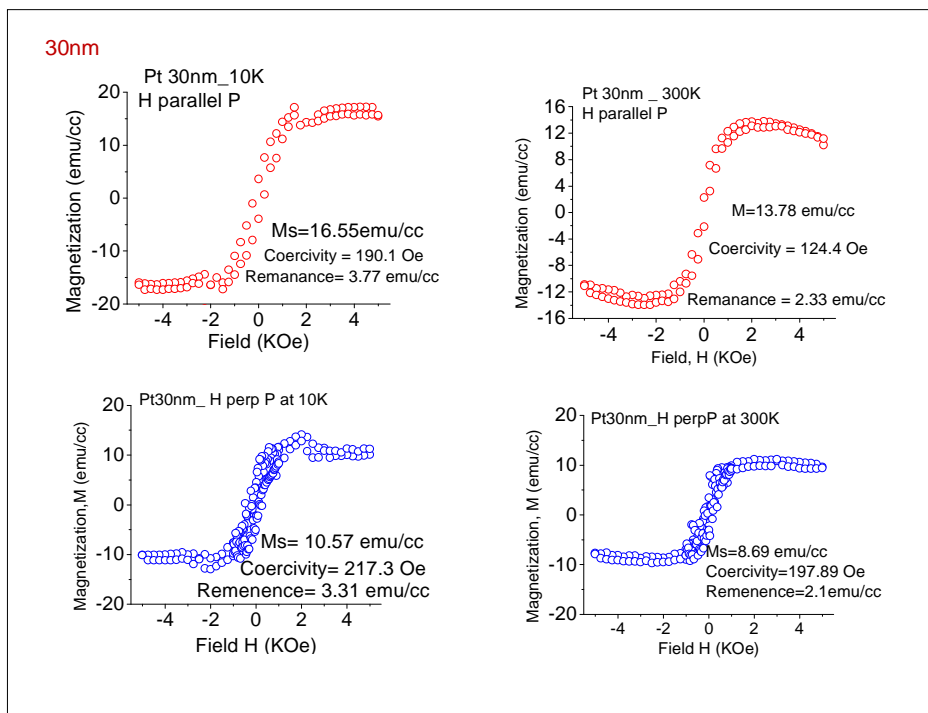
Fig. 14.2. (e) Magnetization measurements of Pt films 30nm in thickness in H parallel to sample plane (top two panels in red colour), and in H perpendicular to the sample plane (bottom two panels in blue colour).
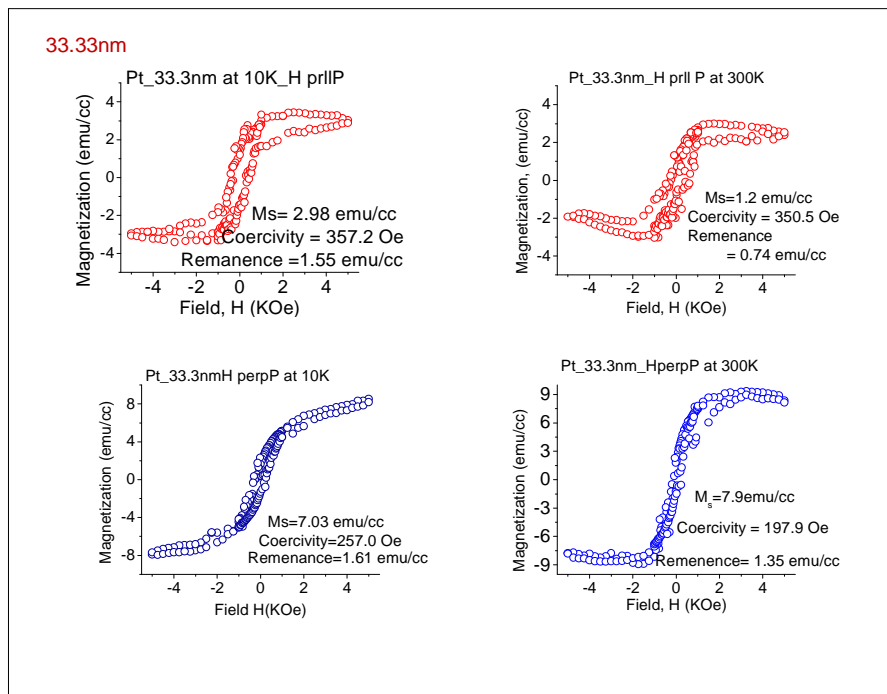
Fig. 14.2. (f) Magnetization measurements of Pt films 33.33nm in thickness in H parallel to sample plane (top two panels in red colour), and in H perpendicular to the sample plane (bottom two panels in blue colour).
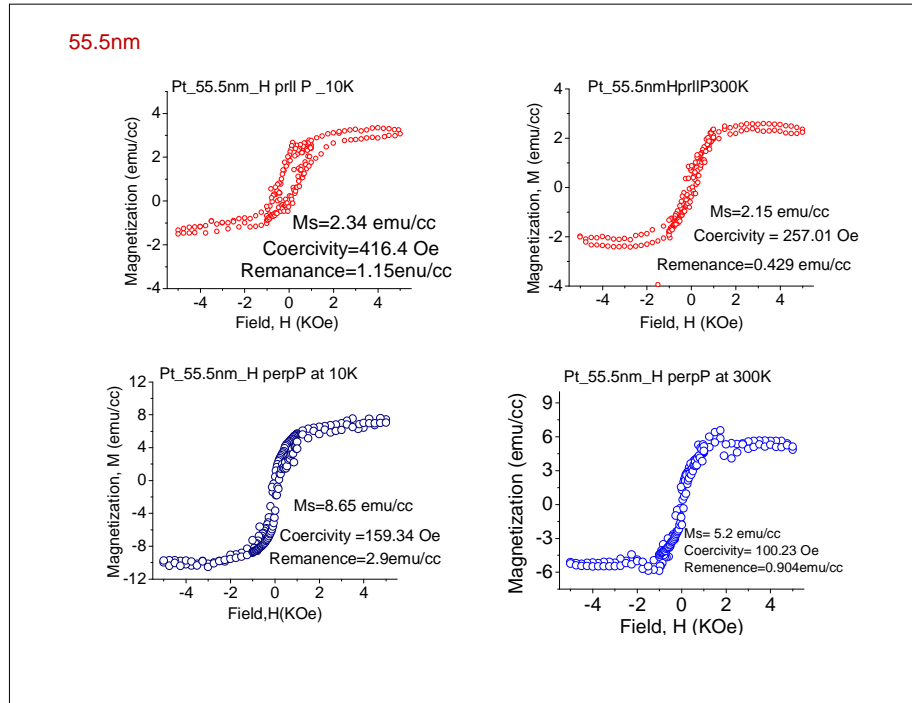
Fig. 14.2. (g) Magnetization measurements of Pt films 55.5nm in thickness in H parallel to sample plane (top two panels in red colour), and in H perpendicular to the sample plane (bottom two panels in blue colour).
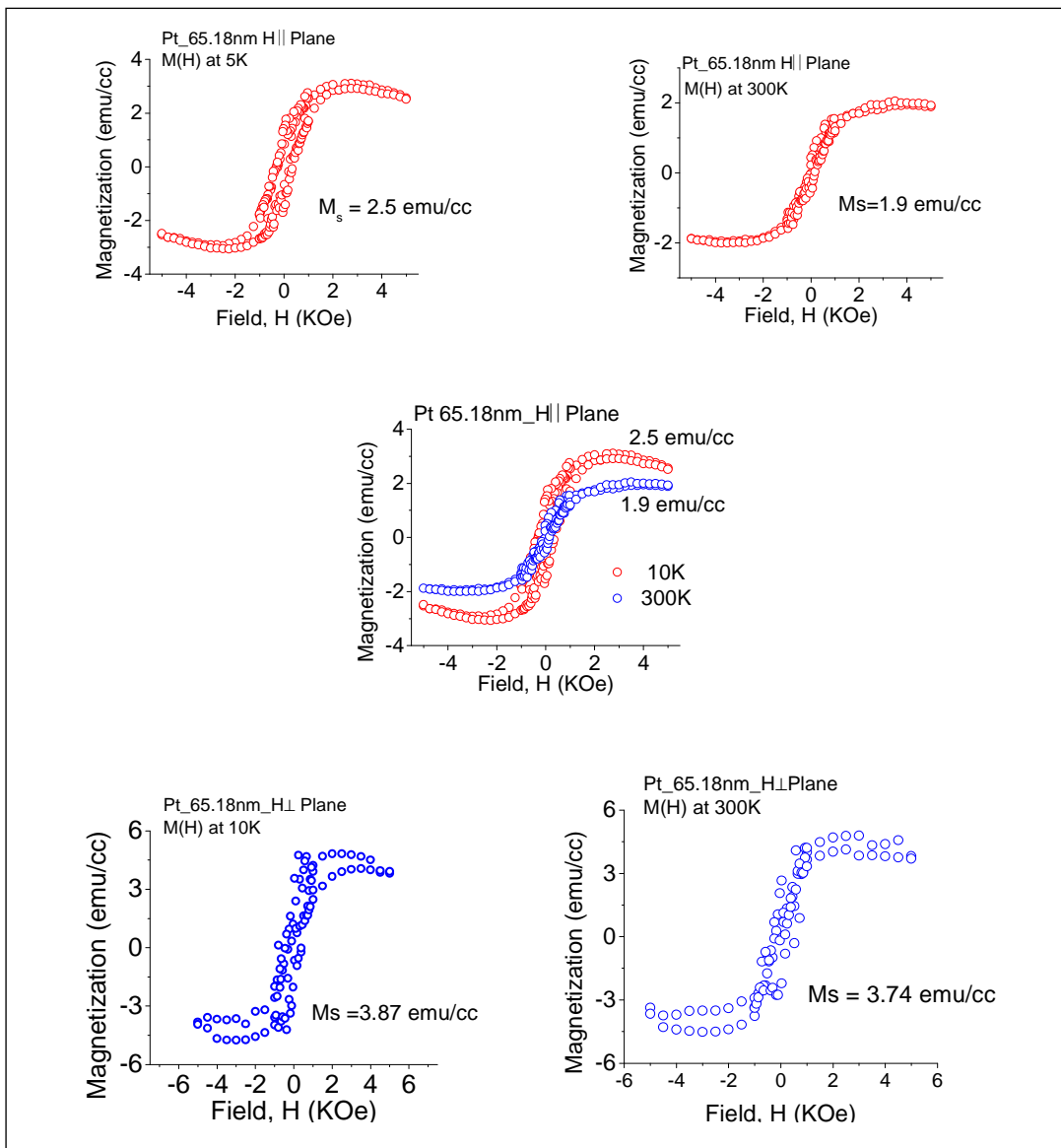
Fig. 14.2. (h) Magnetization measurements of Pt films 65.18nm in thickness in H parallel to sample plane (top two panels in red colour), the middle panel shows these data together, and the data in H perpendicular to the sample plane (bottom two panels in blue colour).
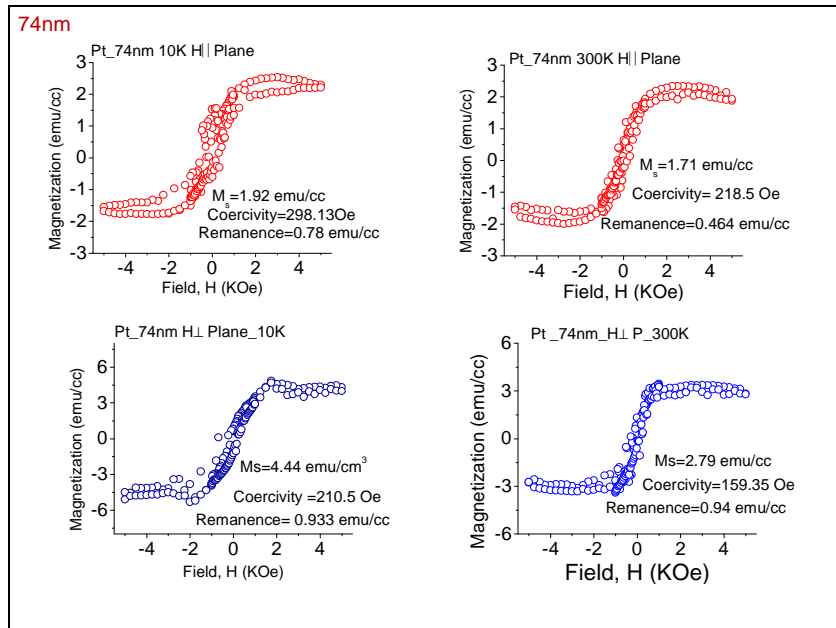
Fig. 14.2. (i) Magnetization measurements of Pt films 74nm in thickness in H parallel to sample plane (top two panels in red colour), and in H perpendicular to the sample plane (bottom two panels in blue colour).
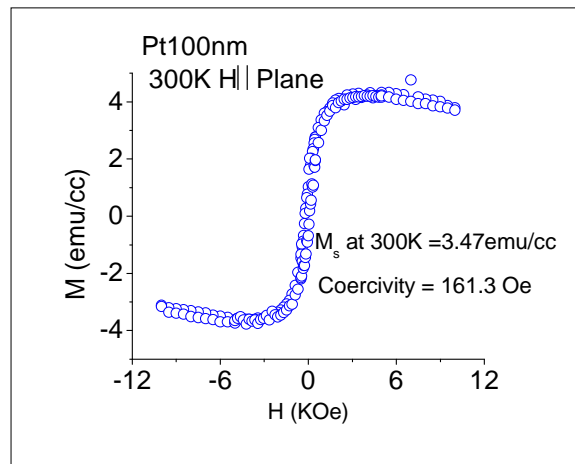
Fig. 14.2. (j) Magnetization measurements of Pt films 100nm in thickness in H parallel to sample plane (top two panels in red colour), and in H perpendicular to the sample plane (bottom two panels in blue colour).

14.3.1 Magnetization measurement by Neutron Scattering

Neutron scattering is reliable technique to measure magnetic moments on the surface. This technique was applied to the Pt thin film sample of 65.18nm. The fitting of the data as shown in Fig. 14.3 reveals the magnetic moment of about3 emu/cc consistent with the SQUID measurements of the same sample as discussed before. This confirms the existence of ferromagnetism on the surface of Pt thin films.
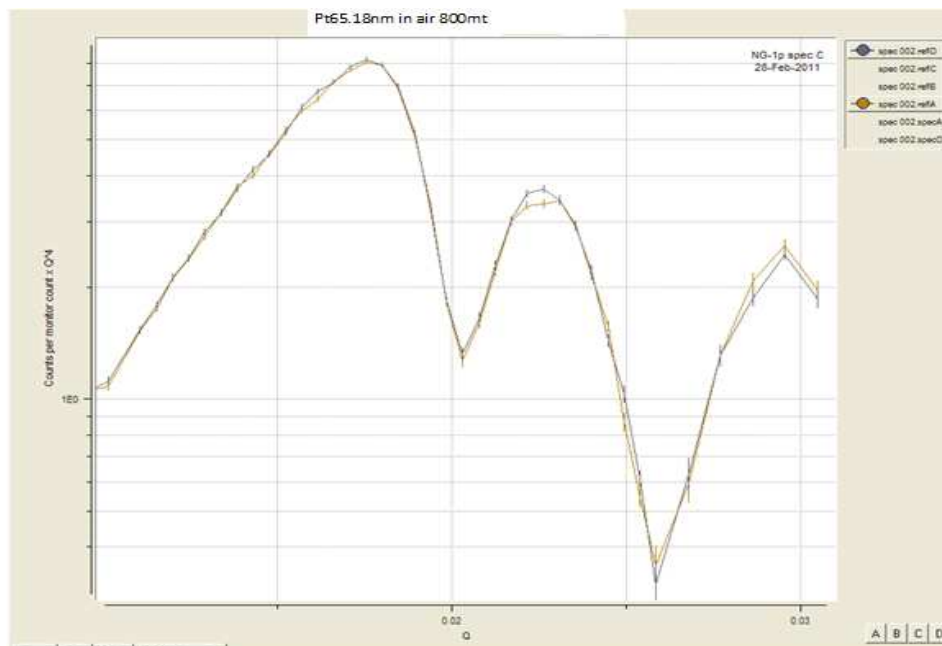
Fig. 14.3. Measurement of magnetism by neutron scattering

14.3.2 Magnetism of Pt rough surface from the first principle study

The possibility of magnetism of Pt (111) textured rough surface has been studied by the first principles. This study on different topological features on the surface of Pt (111) that are frequently observed in fcc metal surfaces shows that the ideal Pt surface as well as single layered thick surfaces are not magnetic, but the 3D islands in the shape of pyramid as shown in Fig. 14.4 have a net moment of $1.1\mu_B$. This demonstrates the importance of the local coordination and the roughness in the epitaxial films.
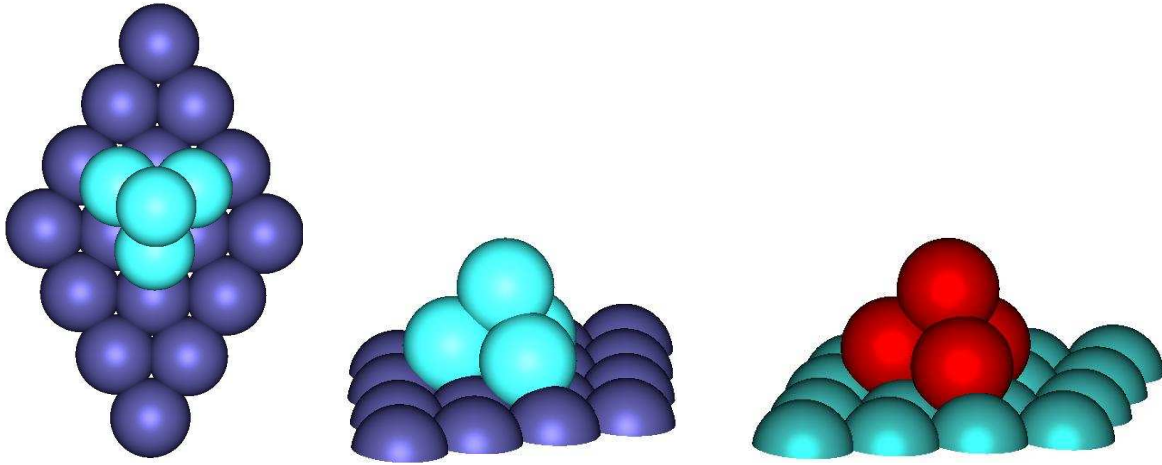
Figure 14.4. Atomic structure of the 4-atom Pt pyramid on Pt(111) surface.

The 3D islands can be viewed as supported cluster. This structure exhibits a local magnetic moment. The reason for the existence of the local moments is related to the charge transfer from the sharp pyramid vertex to the inner Pt sites making density of states at the Fermi level higher due to narrowing of the d-state peak as shown in Fig. 14.5. Stoner criterion is satisfied in this case and magnetic solution becomes stable.
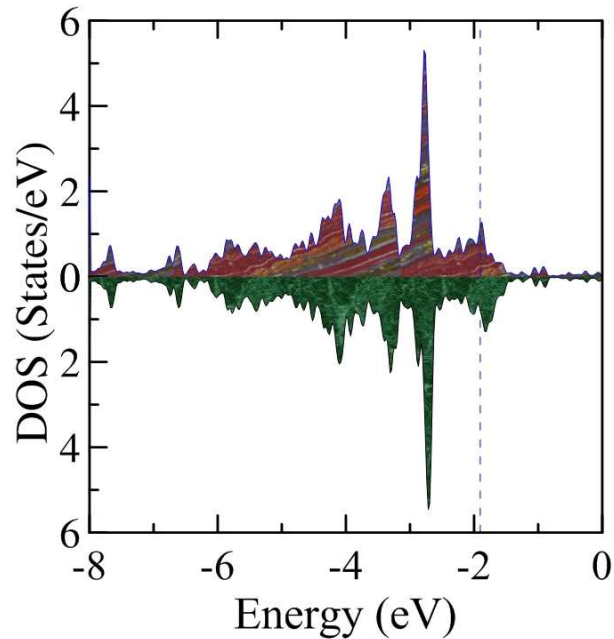
Fig. 14.5. Local densities of d-states of Pt at the vertex site of the pyramid.

The isosurface of charge density of Pt pyramid on Pt (111) surface as shown in Fig. 14.6 Shows that the largest charge density is at the 4 top Pt sites, but non-negligible contribution to total magnetization comes also from inner sites of Pt film.
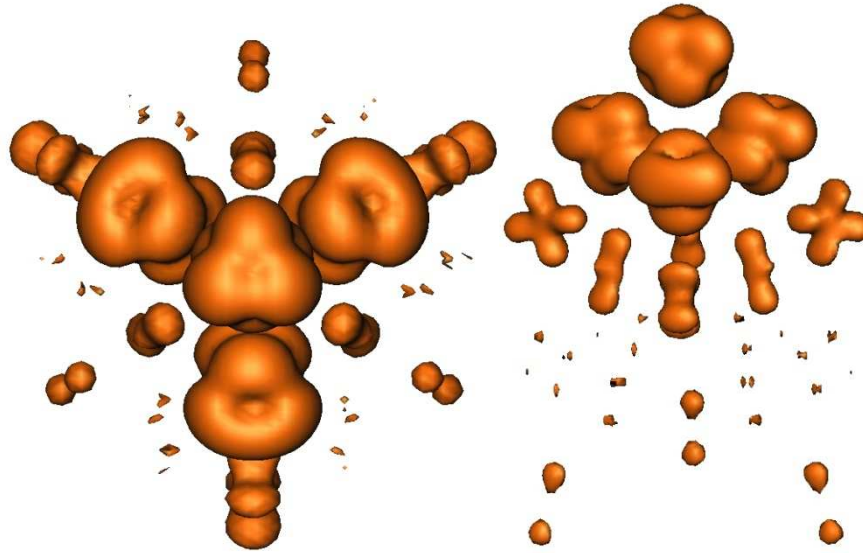
Fig. 14.6. Isosurface of charge density of Pt pyramid on Pt (111) surface

14.4   Roughness study by AFM

Roughness of Pt surface of all samples was measured by Atomic Force Microscope (AFM), and the data was analyzed by the image processing software XEI of Park Systems. Average roughness was recorded at different clean regions of the images, and their average was taken to find the final average roughness of each sample. Wenzel roughness or surface area ratio was measured for all samples. It is defined [XEI Software manual, Version 1.7.6] as 100(%) × (Geometric Area – Surface Area) / (Geometric Area). Figure 14.7 shows the AFM images of most of the samples studied.

Pt12.7nm film, Roughness=0.17nm
110111Topography005

Pt 55.5 nm film_Roughness=0.4425nm
110214Topography007 copy1
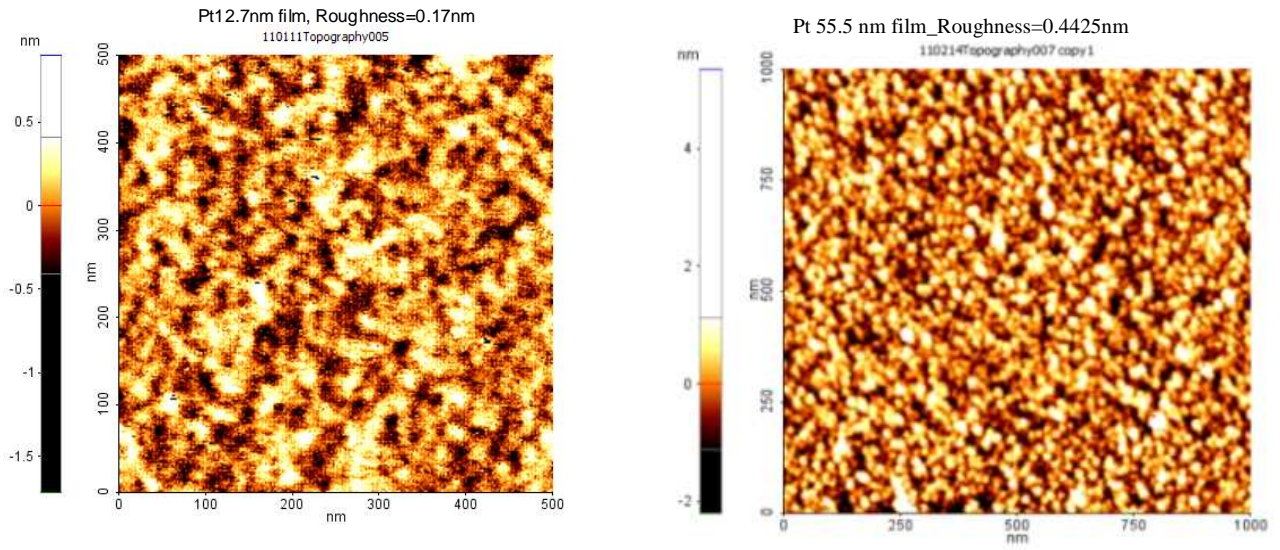
3D view of Pt 65.18nm film, Roughness = 0.5387nm
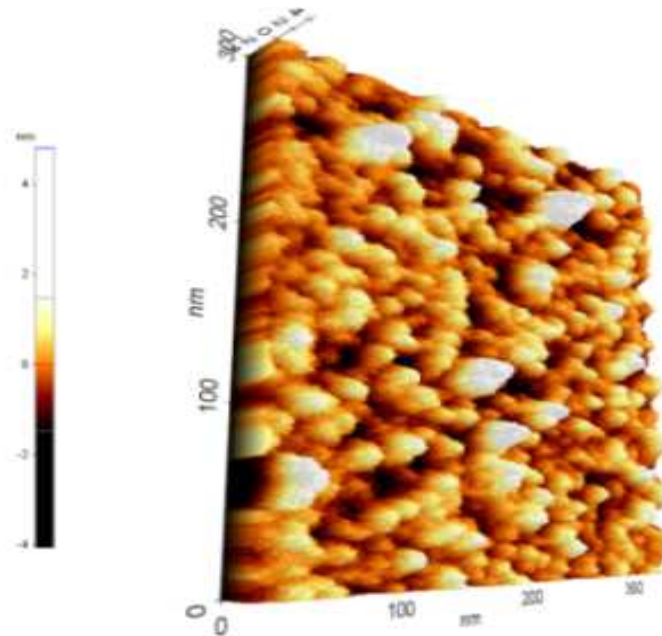
Fig. 14.7. AFM images of typical topography of Pt surfaces of different samples

The average roughness measured in nm as a function of thickness of the samples is shown in Fig.14.8 (a). It shows that the surface roughness has increased for the increasing thickness up to 65.18nm, and beyond this thickness, the surface roughness seems decreasing again up to the thickness of 100nm. Possibly small differences in sample fabrications conditions are responsible for such roughness variations.

(a)   (b)
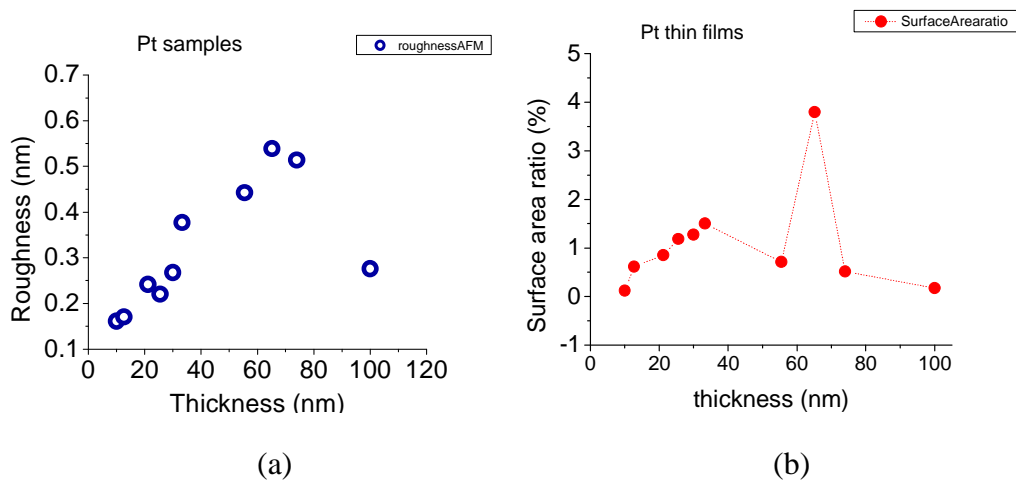
Fig. 14.8. Roughness of Pt thin film surfaces (a) roughness average of Pt thin film surface as a function of thickness of Pt deposition, (b) Wenzel ratio as a function of thin film thickness

The surface area ratio, also called Wenzel ratio, as a function of film thickness for these samples is shown in fig 14.8 (b). Even though it is not clear what parameters exactly control the surface roughness of the films, it is found that the film of thickness 65.18nm has the maximum surface area ratio among all other samples studied. It would be interesting to find whether the magnetism observed in Pt thin films is dependent on the surface roughness or not. This will be discussed shortly in the next section.

14.5   Correlation of magnetism with thickness

Magnetic moment in unit area of film surface of Pt samples of different thickness seems nearly independent of their thicknesses. Figure 14.9 shows the experimental data of M×d, where

M is the magnetization in emu/cm^3 and d is the thickness of the sample in cm. Figure 14.9(a) shows the magnetization data taken at 10K and 300K for the configuration when magnetizing field was parallel to the sample surface, and Fig. 14.9(b) shows the same data together with the magnetization data in the configuration when magnetic field is perpendicular to the sample surface. These plots show that the surface magnetism is independent of the film thickness and indicate that the magnetism observed in Pt thin films is not volume magnetism, rather it is developed on the surface with almost constant surface magnetization. The parallel and perpendicular cases show similar values of magnetization within experimental limitations, and these data indicate that Pt thin films are not anisotropic in terms of their magnetizations.

(a)   (b)
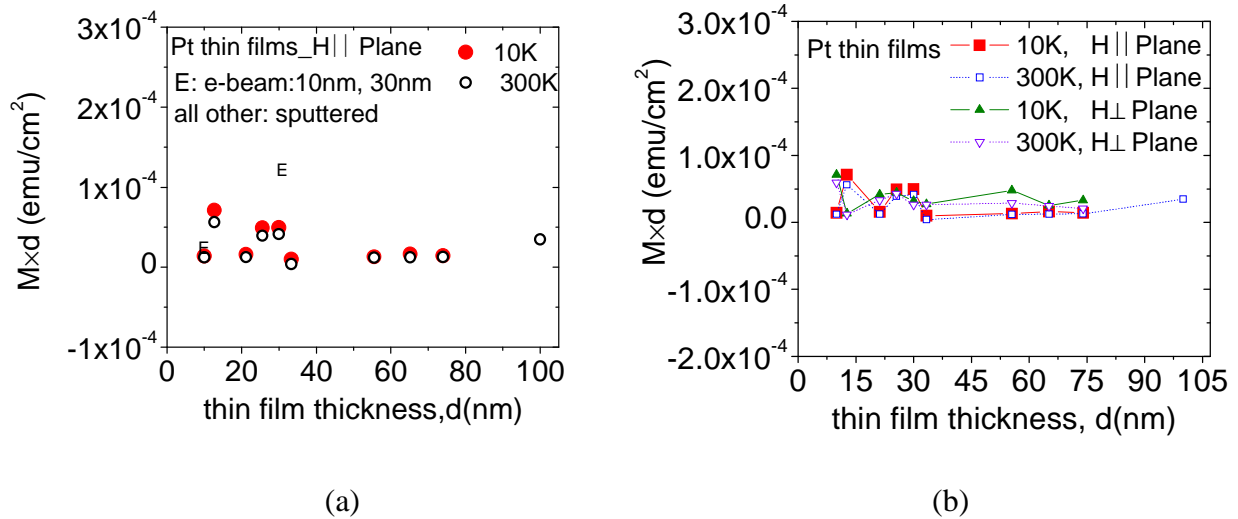
Fig.14.9. Surface magnetization of Pt samples as function of their thickness, (a) when the field is parallel to the sample surface, and (b) when the field is perpendicular to the sample surface as compared to the parallel case

14.6   Correlation of magnetism with roughness

Figure 14.10(a) shows the surface magnetization as a function of Wenzel roughness (surface area ratio). It also shows that the surface magnetization is more or less independent of Wenzel roughness. Such roughness independence was found, as shown in Fig. 14.10(b), even

when simply the roughness average was considered. It is possible that the presence of roughness itself, not its extent, on the Pt thin film surface is the cause of existence of magnetism in such films.

(a)   (b)
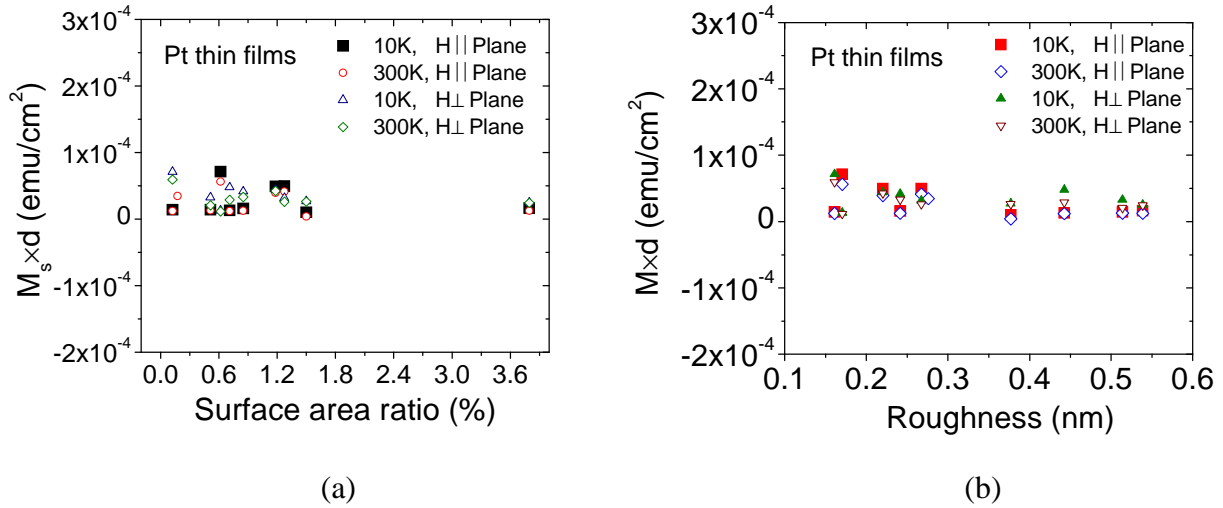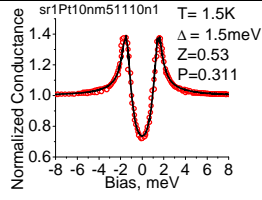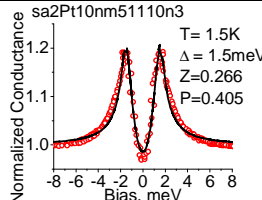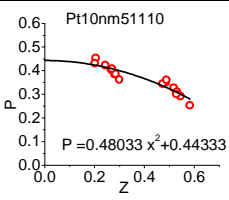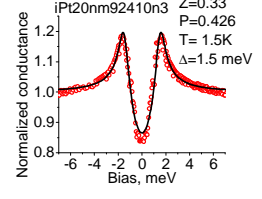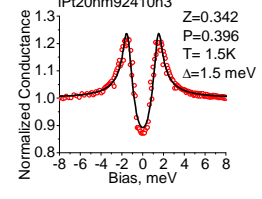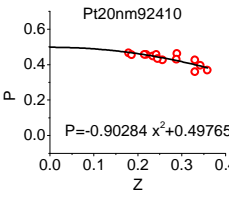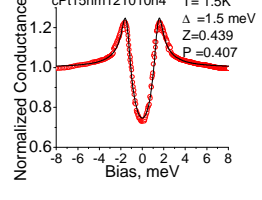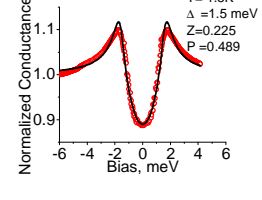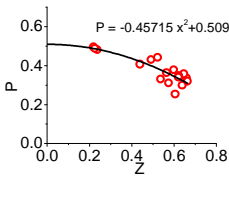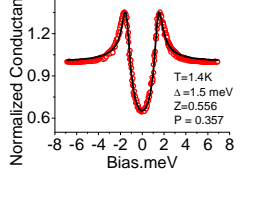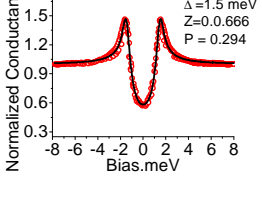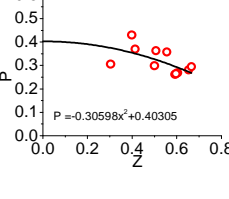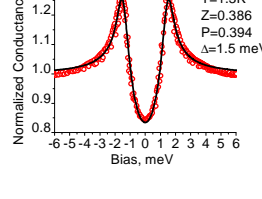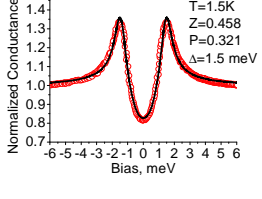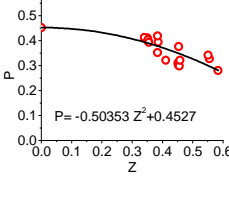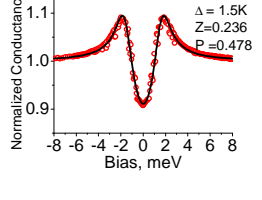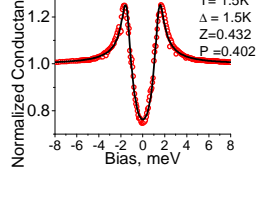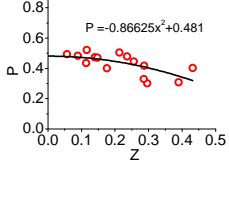
Fig. 14.10. Surface magnetization M×d (emu/cm^2) as a function of surface area ratio.

14.7   Spin polarization measurements for different Pt samples

Point contact Andreev reflection (PCAR) technique was used to measure the values of spin polarization of Pt samples with various thicknesses ranging from 10nm to 100nm. All data were obtained by using electrochemically etched Nb tips. Fitting of the conductance data were done by using modified BTK model. Conductance curves for several contact resistance were obtained for each Pt sample, and the Z dependence of P was found in each case. Two of conductance curves as representative curves for each Pt sample, and the Z dependence of P for each sample are tabulated in table 14.1. The intrinsic value of P which corresponds to Z=0 for each sample is extracted from P-Z curves. The data were taken at 1.5K and the superconducting gap of Nb, Δ =1.5 meV was used for fitting the data. The fitting parameters for individual conductance are shown along with the corresponding plots shown in table 14.1.

Table 14.1. Normalized conductance curves for various Pt thin films, Z dependence of P and intrinsic values of P measured by point contact technique.

Sample/ thickness	Representative Conductance curve 1	Representative Conductance curve 2	Z dependence of p	Intrinsic value of P for Z=0
Pt10nm				44.3%
Pt12.7nm				49.8%
Pt21.2nm				50.99%
Pt25.55nm				40.2%
Pt30nm				45.3%
Pt65.18 nm				48.1%

| Pt100nm | | | | 52.6% |
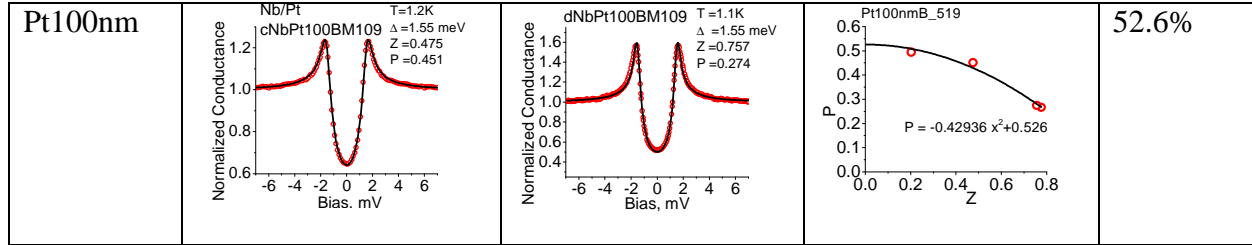
14.7.1 Spin Polarization as a function of film thickness

The measured values of spin polarization indicate that it is hard to find any dependence of P on the thickness of the samples. However, the data indicate almost linear relation with close values of P as shown in Fig. 14.11. It would be better to indicate that the intrinsic values of spin polarization are found between ~40% to ~53% for Pt samples with different thicknesses. Any concrete correlation of P with film thickness of Pt samples is not found. Any possibility of whether P values depend on their magnetization will be discussed in the following sections.
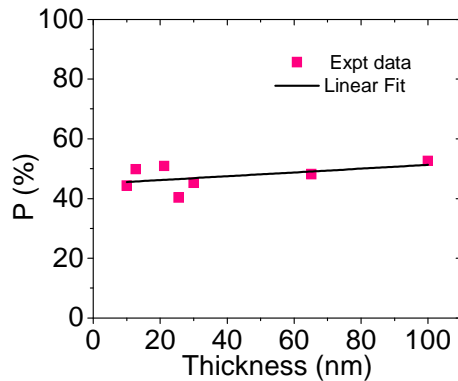
Fig. 14.11. Spin polarization data for Pt thin film samples with different thickness

14.7.2 Spin polarization as a function of Wenzel roughness (Surface area ratio)

Since the Wenzel ratio, i.e. the surface area ratio was found different for different films, it would be interesting to see the correlation of such surface roughness on spin polarization. This

will implicitly reflect the dependence of P on magnetization which might be originated from the surface roughness of the films. As shown in Fig. 14.12, the experimental data indicate that the spin polarization as a function of Wenzel roughness is almost constant within its experimental spread for different samples. This is consistent with almost constant surface magnetism of the samples with surface area ratio.
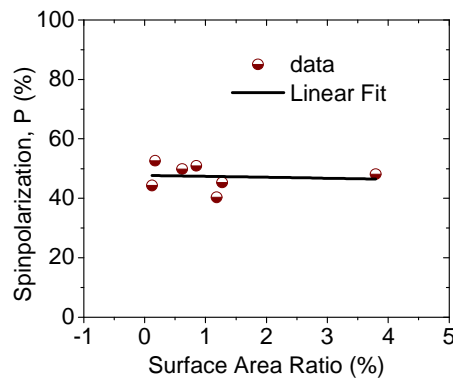
Fig.14.12. Spin polarization as a function of surface area ratio (Wenzel roughness)

14.7.3 Spin polarization as a function of magnetization

Correlation between spin polarization and magnetization is not universal; it is system dependent as explained in §15.6 in Chapter 15. So, it is important to see how they are related in Pt thin film samples. The data shown in Fig. 14.13 (a) indicate that the values of P are almost constant with the volume saturation magnetization of the films. Also, the P values are within the band between 40% and 53% as a function of surface magnetization (emu/cm^2).
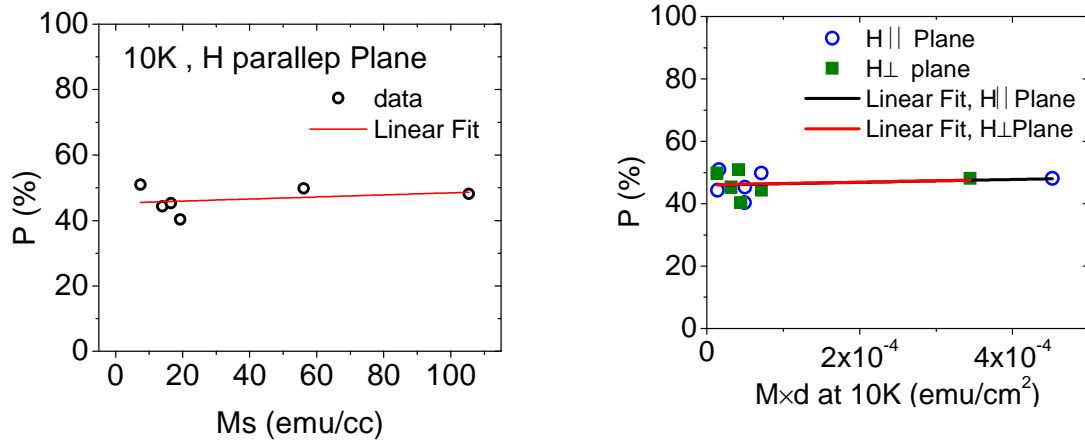
Fig. 14.13. Spin polarization as a function of saturation magnetization

14.7.4 Spin polarization as a function of Coercivity

The plots in Fig.14.14 show how the spin polarization depends on corecivity in both in parallel and perpendicular configurations. Both plots show that the spin polarization is almost constant with the coercivity of the samples.
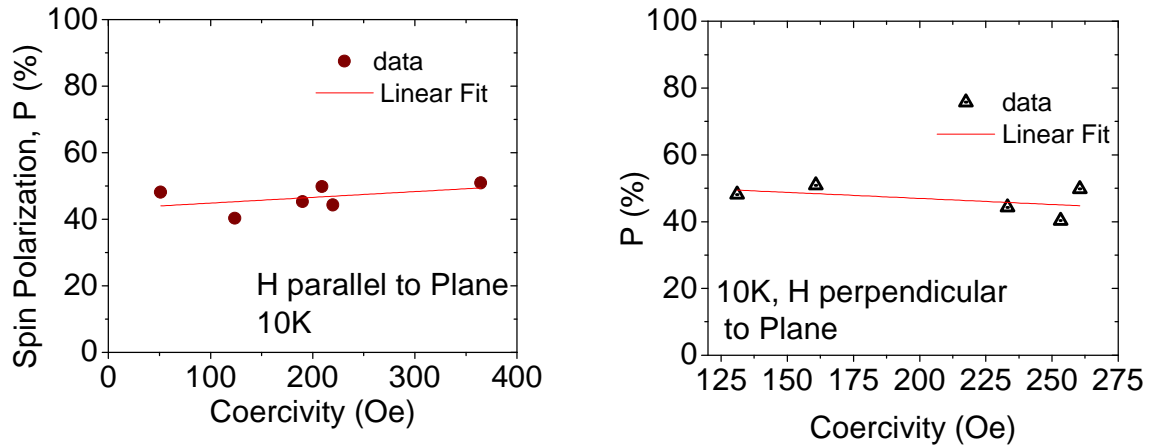
Fig.14.14. Spin polarization as a function of coercivity, (a) when the magnetizing field is parallel to the sample surface, and (b) when the magnetizing field is perpendicular to the sample surface

14.8   Conclusions

Pt thin films sputtered by e-beam evaporation or magnetron sputtering are found to be ferromagnetic. The magnetism is independent of the thickness of the films, and the surface magnetism (emu/cm^2) is more or less constant for different samples. The existence of magnetism as observed by SQUID, PCAR and neutron scattering is supported by the first principle calculation for the 3D islands in the shape of pyramid of Pt atoms. The reason for the local moment in such pyramid is related to the charge transfer from the sharp pyramid vertex to the inner Pt sites making density of states at the Fermi level higher due to the narrowing of the d-state peak. Stoner criterion is satisfied in this case causing such rough Pt surfaces ferromagnetic.

It is found that the spin polarization values of Pt thin films of thickness between 10nm and 100nm are found in between 40% and 53%. The P values do not have strong correlation with different parameters such as thickness, roughness, saturation magnetization (emu/cm^3), surface magnetization (emu/cm^2) and coercivity. It seems that the sample preparation conditions and topography of sample surfaces play some role for different values of spin polarization.

More importantly, the Pt thin films are ferromagnetic, as confirmed by series of measurements of magnetization by SQUID, and cross checking the existence of magnetization by neutron scattering. Measured finite values of transport spin polarizations also confirm that the Pt surfaces are ferromagnetic which we proposed as due to the Pt clusters in the form of pyramids of Pt atoms on the rough surfaces of Pt thin films deposited by e-beam evaporation and magnetron sputtering.

CHAPTER 15

TRANSPORT SPIN POLARIZATION OF HIGH CURIE TEMPERATURE FERROMAGNETIC MnBi FILMS BY ANDREEV REFLECTION

15.1   Introduction

Spin generation and injection are very important issues in spintronics. Especially, spin injection from ferromagnet to semiconductors is challenging due to low interface resistance [van Son et al., 2000]. Such problem can be circumvented by using the ferromagnet of high Curie temperature, high conductivity and high spin polarization. MnBi is stable in its NiAs phase and seems to be a potential candidate due to its suitable properties such as high Curie temperature [Heikes, 1955] of (628K) in stable NiAs phase at room temperature, high coercivity [Guo et al., 1993], large perpendicular room temperature anisotropy in thin films [Rüdiger et al., 2000], and high Kerr rotation (useful for magnetooptical (MO) recording) [Fasol, 1996]. These unusual magnetic and magneto-optical properties have been the main motivation for the intensive studies on the various properties of this material [Katsui et al.,1976; Shen et al.,1991; Jaswal et al., 1994; Köhler et al., 1996; Rüdiger *et al.*, 1997; Bandaru et al., 1999]. Even though MnBi in zinc blende structure is half metallic [Xu et al., 2002; Zheng et al., 2004; Kahal et al., 2010], it is difficult to grow and it may be metastable phase. But MnBi in NiAs phase is stable phase with high magnetic and structural transition temperature of 628K, and due to the possibility that the interfacial condition may be changed by the addition of Bismuth, it is particularly important to measure the transport spin polarization of MnBi in the NiAs structure [Kharel et al., 2011], which is also relevant to the understanding of MnBi junctions that show a large magnetoresistance (70% at room temperature) [Clifford et al., 2004]. Transport spin polarization of MnBi films has been measured by point contact Andreev reflection spectroscopy and the experimental values are compared with the theoretical calculations. Correlation between the

transport spin polarization and the saturation magnetization on these films has been established in this study.

15.2　MnBi samples and their structure

Four　different samples (A, B, C, D) of MnBi films were prepared on glass substrate by sequential e-beam evaporation of Bi and Mn with subsequent *in situ* annealing of bilayers immediately after the deposition. High-quality MnBi thin films can be grown by this method by maintaining the atomic ratio of Mn:Bi = 55:45 [Kharel et al., 2010]. Samples A, C, and D were 32nm thick, and sample B was 47nm thick. Two samples (A and C) were deposited at room temperature and annealed for 1 hour at $410°C$ and $400°C$, respectively; the other two samples (B and D) were deposited at $125°C$ and annealed at $350°C$ for 1.5 hours and 1 hour, respectively. All of the samples were single-phase MnBi highly textured polycrystalline films, with a hexagonal NiAs crystal structure, although small traces of elemental Bi have been detected as shown in X-ray- diffraction spectra in Fig. 15.1.
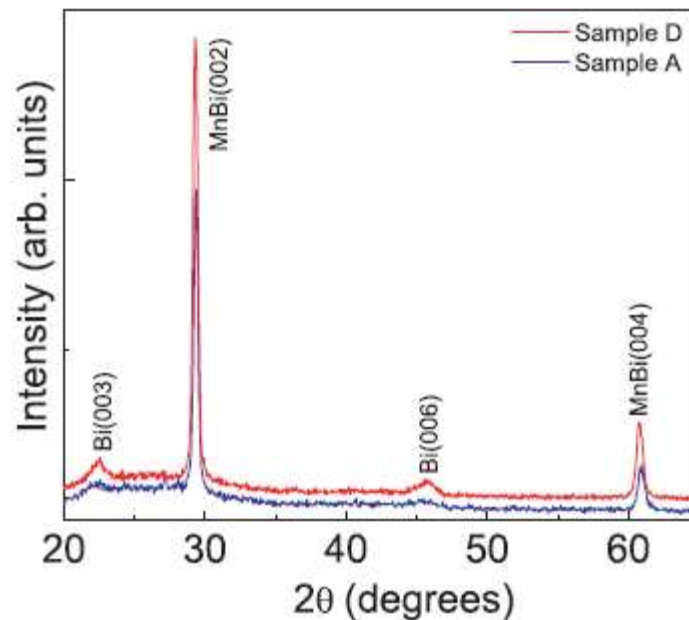
Fig. 15.1 X-ray-diffraction spectra of MnBi film (samples A and D) show strong diffraction peaks from (002) and (004) planes indicating preferred c-axis orientation of the films [Kharel et al., 2011].

15.3   Magnetization of MnBi

Magnetic hysteresis loops obtained for all samples were well-defined rectangular loops in the out of plane geometry as shown, for sample D, in Fig. 15.2. This indicates that the magnetization easy axis in perpendicular to the sample plane. The curves show that the samples are highly anisotropic with magnetization easy axis along c-axis. Saturation magnetizations measured for samples A, B, C, and D are 503, 485, 464, and 425 emu/cm3 respectively with corresponding coercivities of 8.4, 3.2, 7.9, and 5.4 KOe at 300 K. It is seen that these values are dependent on sample preparation conditions.
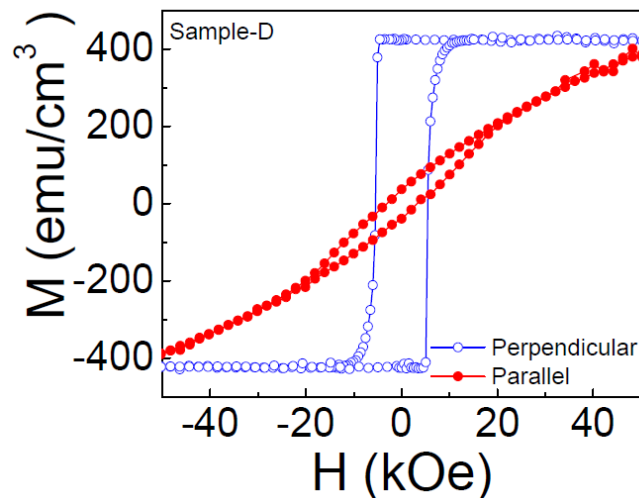
Fig. 15.2. Magnetization loops in the magnetic field parallel and perpendicular to the sample plane

15.4   Resistivity of MnBi

The resistivity as a function of temperature (Fig. 15.3) show that MnBi samples are metallic. The resistivity at 4K is ~15μΩcm with the residual resistivity ratio (rrr) of ~8.5 for all samples. Unlike the expectation of T^2 dependence of resistivity at low temperature for weak ferromagnetic materials, MnBi samples follow an anomalous power law ($\rho \sim T^m$) with m between 2.9 to 3.6, similarly to what has been observed for half -metallic film such as CrO_2 [Gupta et al., 2000]. The inset shows the power law dependence for m = 2.9 for the resistivity below 30K.
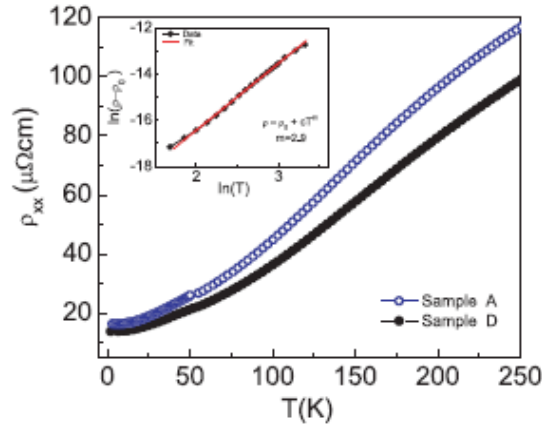
Fig. 15.3. Resistivity of MnBi films (samples A and D) as a function of temperature

15.5 Point Contact Andreev Reflection of MnBi

Transport spin polarization of MnBi was measured by using Point Contact Andreev Reflection (PCAR) spectroscopy. Electrochemically etched Nb tip was used as superconductor in contact with magnetic material MnBi thin film on Si, and the data were taken at 1.5K. Characteristic conductance curves with dip in conductance at zero bias were obtained which indicate the suppression of Andreev reflection due to spin polarization of current. For every sample A, B, C and D two of the typical conductance curves are shown in Fig. 15.4. Conductance curves (a) and (b) are for sample A; (d) and (e) for sample B; (f) and (g) are for sample C; and (i) and (j) are for sample D. Fitting of the data was done using modified BTK model. Data taken for different contact resistances show that the spin polarization value depends on interfacial barrier strength (Z) between the MnBi surface and Nb superconductor. Z dependence of P for samples A, B, C and D are shown in Fig. 15.4 (c), (f), (i), (l). For every case, intrinsic value of spin polarization have been obtained by extrapolation of the curve to Z=0 (perfectly transparent interface) [Strijkers et al., 2001]. For samples A, B, C and D, the intrinsic values are found to be $63 \pm 0.8\%$, $57.8 \pm 1.6\%$, $54.2 \pm 2.4\%$, and $51.7 \pm 1.1\%$.

Sample A
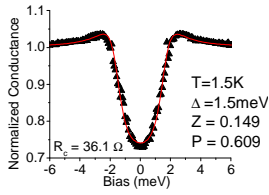
(a)
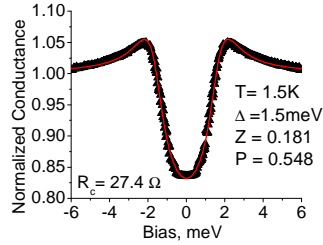
(b)
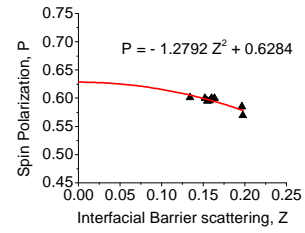
(c)

Sample B
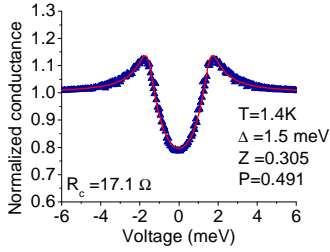
(d)
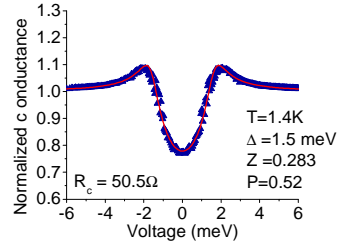
(e)
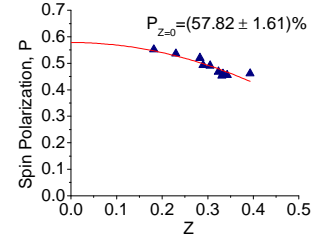
(f)

Sample C
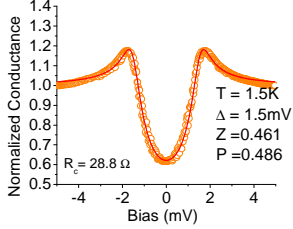
(g)
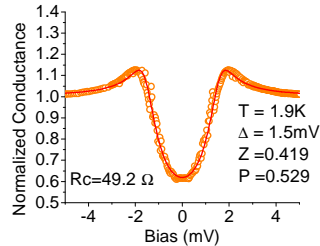
(h)
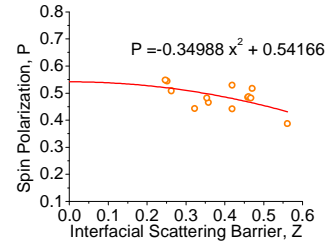
(i)

Sample D
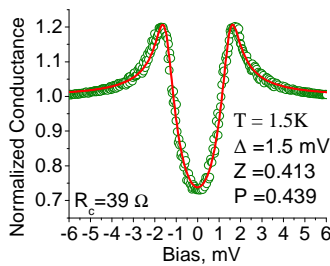
(j)
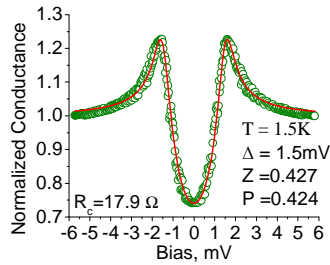
(k)
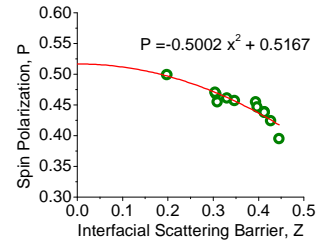
(l)

Fig. 15.4. Normalized conductance curves with mBTK fitting for samples A : figs (a,b); B: figs (d,e); C: figs (g,h); D: figs (i,j); and Z dependence of P for corresponding samples figs (c,f,i,j). Contact resistances and the fitting parameters are shown in the corresponding figures.

15.6   Correlation between spin polarization and magnetization, and transport regime

As spin polarization (P_T) is associated with the electronic states near the Fermi energy and the respective Fermi velocities, whereas the magnetic moment is associated with the algebraic sum of occupancies of all majority and minority spin states, there is no reason for these quantities to be related [Kharel et al., 2011]. However, in some case the linear relationship between P_T and M has been reported [Meservey et al., 1994], while in many other cases such as for Ni$_{1-x}$Fe$_x$ system [Veerdonk et al., 1997] as shown in Fig .15.5 (c), Co$_{1-x}$V$_x$ system and Co$_{1-x}$Pt$_x$ system [Kaiser et al., 2005] as shown in Fig 15.5 (a) and (b), and Ni$_x$Fe$_{1-x}$ system [Nadgorny et al., 2000] as shown in Fig 15.5(c), no direct relationship between the two quantities has been observed.
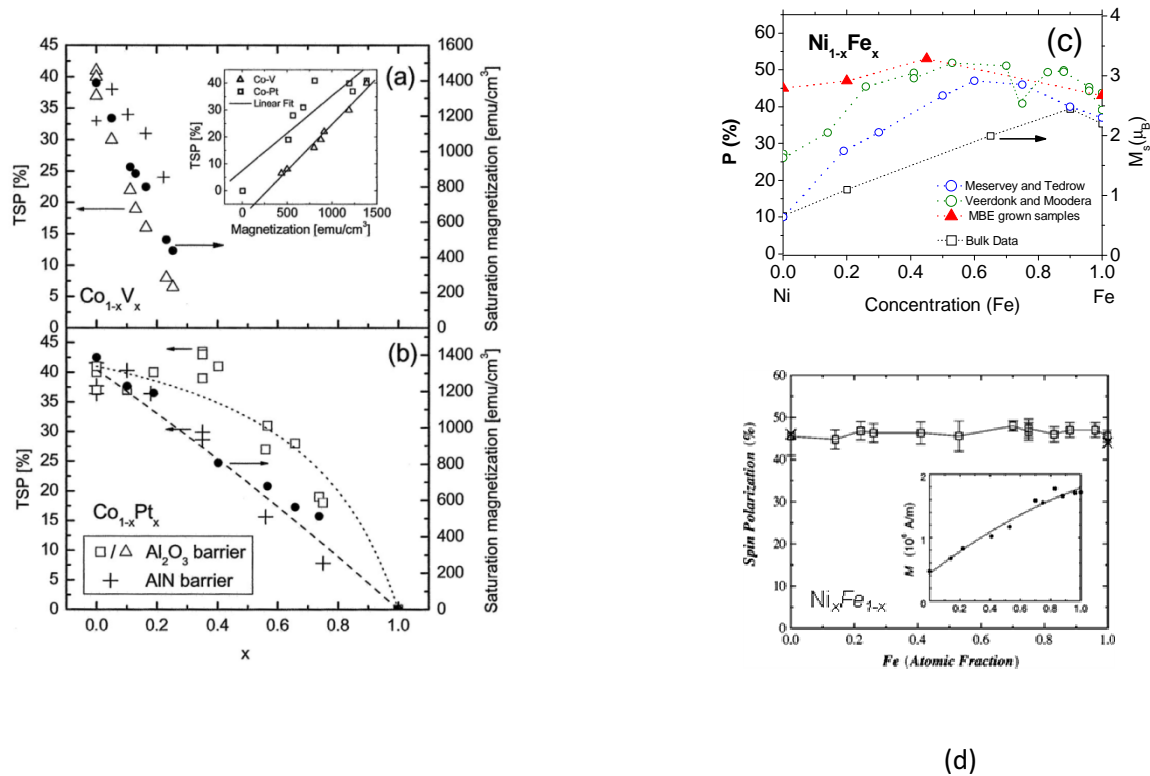
Fig. 15.5. Relation between spin polarization and magnetization in (a) Co$_{1-x}$V$_x$ system, (b) Co$_{1-x}$Pt$_x$ system, (c) Ni$_{1-x}$Fe$_x$ system, and (d) Ni$_x$Fe$_{1-x}$ system.

These works indicate that the relationship between the transport spin polarization and the magnetization is to be determined independently for different concrete material systems. In case of MnBi, the experimental values of transport spin polarization are found to be proportional to the saturation magnetization as shown in Fig. 15.6 (a). Theoretical calculations show that the spin polarizations are proportional to magnetic moment per cell, and it is further seen that the spin polarizations calculated for diffusive transport are closer to the experimental values than the spin polarizations calculated for ballistic transport, as shown in Fig. 15.6 (b).

(a)   (b)
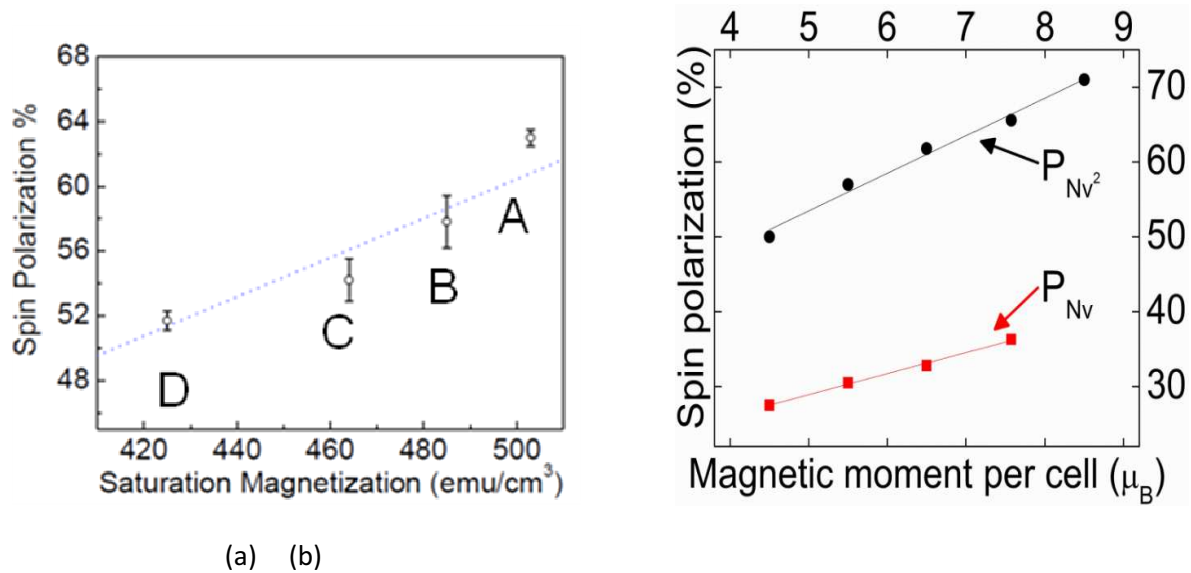
Fig. 15.6.   Correlation between spin polarization and magnetization of MnBi films (a) experimental data, (b) theoretical calculations for diffusive denoted in the graph by by P_{NV}^2 and ballistic P_{NV}.

On the other hand, it is important to know the experimental conditions to know which regime of transport was occurring during the experiment. Using the measured value of resistivity of 15 $\mu\Omega$ cm for MnBi at 4 K, and the values of calculated density of states for the majority (↑) and minority (↓) carriers, $N_\uparrow = 0.446$ and $N_\downarrow = 0.425$ states/eV/cell respectively, scattering time τ was calculated for both the carriers from Ziman formula,

$$\sigma_{\uparrow(\downarrow)} = 1/3e^2 N_{(\uparrow\downarrow)} v^2_{F(\uparrow\downarrow)} \tau, \tag{15.1}$$

where $v_{F(\uparrow\downarrow)}$ is the Fermi velocity and the conductivity $\sigma_{\uparrow(\downarrow)} = 1/\rho_{\uparrow(\downarrow)}$. The electron mean free path $L_{\uparrow\downarrow} = v_{F\uparrow\downarrow}\,\tau$ was found to be ~20nm for majority and ~10nm for minority carriers. The contact size (d) of the superconducting tip was estimated from Wexler's formula,

$$Rc \approx 4\rho L/3\pi d^2 + \rho/2d, \tag{15.2}$$

where the contact resistance R_c was changed from 10Ω to 100Ω. For these values of R_c, and for majority carriers, the contact sizes were found to be ~15nm and 5nm respectively. It is found that L>d for majority carriers and L≈d for minority carriers. This indicates that the transport is in *ballistic regime for majority, and it is in intermediate regime for minority carriers.*Though our experimental parameters show that the transport is in ballistic regime, theoretically the diffusive calculations are in better agreements (diffusive P_{nv2}= 51-66%,ballistic P_{Nv} =28-36%) with the experimental values (P_{Nv2}= 51-63%). This is possible due to the fact that P is sensitive to the interface and the termination of electrodes (there is substantial difference in electronic DOS of Mn and Bi at the Fermi energy). Bi states control the magnitude of *P (P_{Nv} = 55% and P_{Nv2} = 76%, respectively)* [Kharel et al., 2011].

15.7 Role of Spin Orbit Interaction in spin polarization

To see the effect of spin orbit (SO) coupling, band structure calculations were done for NiAs structure of MnBi. Figure 15.7 (a) and (b) show the band structure calculations for majority and minority channels without SO coupling; and (c) shows the band structure calculations for both the channels with SO coupling. Close inspection shows that there is no significant effect in dispersion relations due to inclusion of SO interaction.

(a)   (b)   (c)
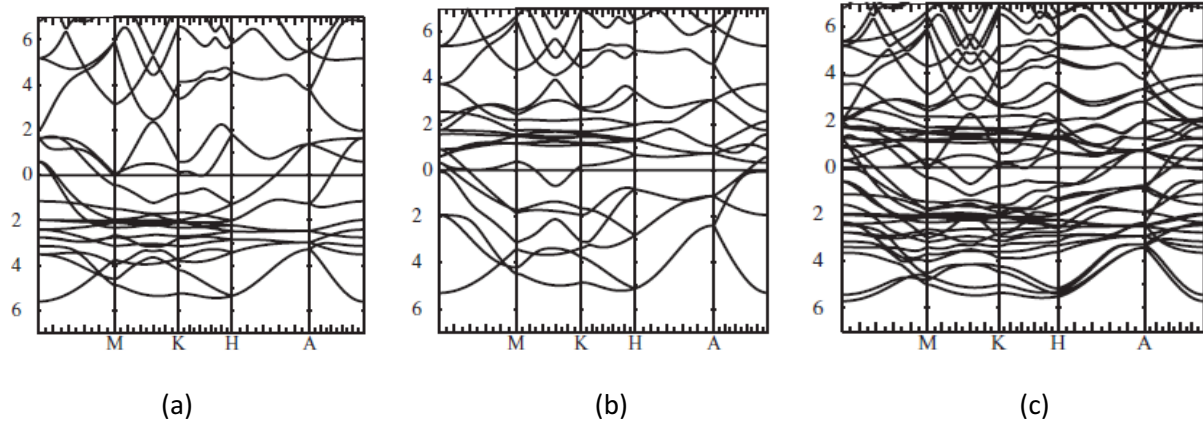
Fig. 15.7. Energy bands for (a) majority channels without SO coupling, (b) minority channels without SO coupling, and (c) both channels with SO coupling.

To further interpret our data, density of states were calculated with and without SO interaction. The comparison is shown in Fig.15.8. It shows that there is no significant difference in density of states at Fermi level due to SO coupling even though there is a slight band shift in the order of SO constant. The same DOS indicate that there is no role of SO interaction in high values of transport spin polarizations measured.
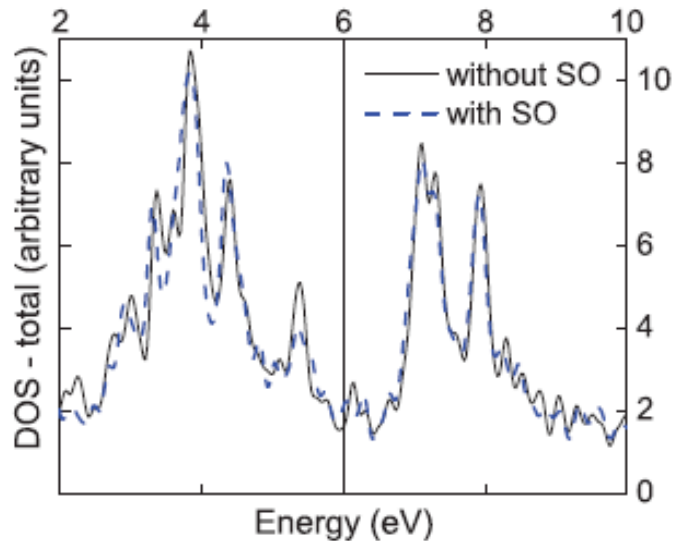
Fig. 15.8. comparison of density of states without and with SO interaction

15.8   Cause of high transport spin polarization in MnBi

The density of states at the Fermi energy are nearly equal (~0.45 states/cell/eV) for majority- and minority-spin carriers as shown in the top panel of Fig. 15.9. This results vanishing spin polarization, as shown in the bottom panel of Fig. 15.9, due to density of states as the spin polarization is defined as $P_N = (N_\uparrow - N_\downarrow) / (N_\uparrow + N_\downarrow)$, where $N_\uparrow$ and $N_\downarrow$ are the majority- and minority-spin DOS.
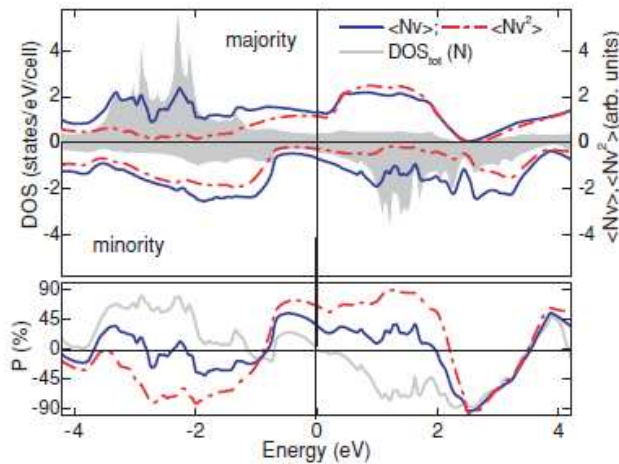
Fig. 15.9. Top panel: total DOS for majority and minority carriers (shaded region), $<Nv>\uparrow(\downarrow)$ (solid blue line), $<Nv2>\uparrow(\downarrow)$ (dashed red line); bottom panel: P near the Fermi energy for PN (DOS) (solid gray line crossing zero at 0 eV), PNv (solid blue line), and $PN\,v2$ (dashed red line) in the direction of the c axis. Inclusion of spin-orbit coupling (from fully relativistic calculations) does not practically affect the calculated DOS.

The origin of the large P_T measured in MnBi is due to the substantial spin asymmetry of the electronic bands near the Fermi energy as shown in Fig. 15.10. The Fermi velocities for the majority and minority carriers are 1.2×10^6m/s and 0.6×10^6m/s respectively. When the mobility of electrons is taken into account, a large PT is expected [Nadgorny et al., 2003; Mazin, 1999; Velev et al., 2008]. Thus the disparity in Fermi velocities is the cause of high transport spin polarization in MnBi. If the velocity is projected along c axis, the spin polarization for ballistic and diffusive transport are $P_{Nv} = 36\%$ and $PNv2 = 66\%$ respectively where as they are reduced to

$P_{Nv} = 28\%$ and $P_{Nv2} = 51\%$ when the velocity direction is considered perpendicular to ab plane. Hence, the strong anisotropy of the transport properties of MnBi can play a role for lower values of spin polarization of polycrystalline MnBi samples.
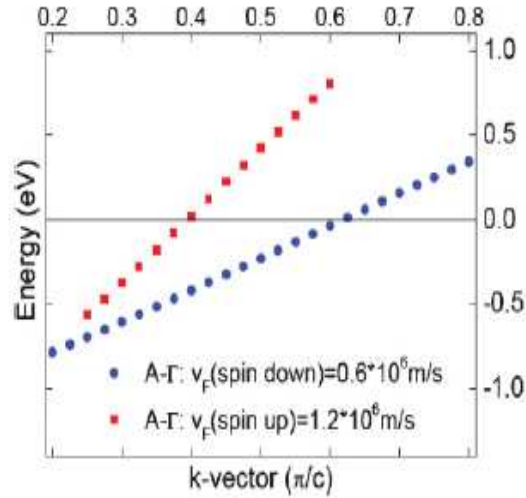
Fig. 15.10. Dispersion of the majority and minority bands near Fermi level; Red squares, majority band; blue spheres, minority band

15.9   Discussions and conclusions

Even though the experimental conditions are found to be in ballistic regime ($\lambda > d$), the first principle calculations of spin polarization ($P_{Nv2} = 51\% - 66\%$) of MnBi in diffusive regime ($\lambda < d$) agree to the experimental values (51% - 63%). This is possible due to the fact that the spin polarization can often be very sensitive to the interface, and to the termination of electrodes [Tsymbal et al., 2007]. In MnBi it is expected to be strongly dependent on the surface termination because of the substantial difference in the electronic DOS at the Fermi energy for Bi and Mn [Kharel et al., 2011].

To sum up, the structural, magnetic and transport properties of MnBi films were studied. Transport spin polarization of these films was measured by Point Contact Andreev Reflection Spectroscopy, and the values were found consistent with the results of band structure calculation

and with observation of a large magnetoresistance in MnBi contacts [Clifford et al., 2004]. The first principle calculations show that the density of states of majority and minority spin-bands at Fermi level are almost identical showing vanishing spin polarization due to the contribution of density of states. However, the disparity in Fermi velocities is the main cause of high transport spin polarization in MnBi. The transport spin polarization of MnBi was found proportional to the magnetization of MnBi.

CHAPTER 16

STUDY OF MAGNETISM AND SPIN POLARIZATION IN DEGENERATE InN AND Cr DOPED InN FILMS

16.1   Introduction

Room temperature ferromagnetism in semiconductors has been an area of interest to many researchers due to their potential spintronic application [Žutic et. al., 2004). Several dilute magnetic semiconductor (DMS) systems have been predicted theoretically by doping transition metal, for instance, Mn in GaAs, and ZnTe [Dietl et al., 2000] ; and experimentally by doping Mn on GaN [Sasaki et al., 2002], Co on ZnO [Coey et al., 2005], Co on TiO_2 [Song et al., 2006] etc. There are Oxide materials such as TiO_2 [Kim et al., 2009], In_2O_3 [Panguluri et.al. 2009], ZnO thin films [Khalid et al., 2009], and semiconductor material such as GaN [Madhu et al., 2008] which show magnetic states even without doping of 3d transition metals because of defects present in them. In some cases the weak ferromagnetism is attributed to magnetic clusters [Coey et al., 2006], impurity phases [Coey et al., 2010], or accidental contamination [Abraham et al., 2005]. In order to characterize such DMS materials for possible spintronic applications, an increasing interest in measuring their spin polarization is seen because of its insensitivity to impurity phases [Dixit et al., 2011].

Even though Oxides are the major focus for studying their room temperature ferromagnetism [Coey, 2006], materials based on III-V nitrides have attracted much interest since room temperature ferromagnetism was predicted in these materials [Dietl et al., 2000]. Transition metals such as Mn doped InN films were found to exhibit spin glass phase at low temperature, while Cr doped InN were reported to have shown room temperature ferromagnetism [Chen et al., 2004] which was confirmed by X-ray magnetic circular dichroism [Ney et al., 2006]. Recent calculations have shown that indium vacancies and nitrogen

interstitials in InN are magnetic [Duan et al., 2009]. Presence of Oxygen in InN films increases the carrier concentration, which leads to re-entrant magnetic behavior in some cases [Petukhov, et al., 2007] and might facilitate ferromagnetism via a Zener - like exchange interaction between carries and localized spins [Zener et al., 1950a, 1950b; Fröhlich et al., 1940]. At the same time, the high carrier concentration in InN leads to large conductivities which allow direct measurement of the spin polarization at low temperatures. In order to investigate the connection between spin polarization and room temperature ferromagnetism in degenerate nitride semiconducting films, we have studied pure InN and Cr substituted InN films, both having a significant oxygen content.

16.2   InN and Cr doped InN samples preparation

Indium Oxide targets were used in nitrogen rich environment to deposit InN thin films by rf magnetron sputtering. On the other hand, 2 at % and 5 at % Cr substituted InN films were deposited on c-axis oriented sapphire substrate at 475+/- 5 ^{0}C by the same technique using In_2O_3 powder (99.99% pure, Alfa Aesar) with chromium chloride ($CrCl_3$. $6H_2O$) in appropriate amounts. The sputtering was done at 475±5 ^{0}C to avoid nitrogen dissociation during the growth process. The thicknesses of these $In_{1-x}Cr_xN$ thin films were measured by cross-sectional scanning electron microscopy, and cross checked by the interference fringes in optical spectra. All thin film samples were measured approximately 1μm thick.

16.3   Structural properties of InN and $In_{1-x}Cr_xN$ films

XRD patterns of undoped InN thin films which were sputtered by using oxide target show broad reflections at 2θ = 28.96°, 30.66°, and 32.85°, consistent with an isotropic polycrystalline sample (Fig. 16.1a) [Dixit et al., 2008], and these patterns can be completely indexed to the wurtzite structure with no evidence for impurity phases [Dixit et al, 2011].

However, bcc structured In_2O_3 secondary phase but no other impurity phase have been observed in Raman spectra as shown in Fig. 16.2(a) [Dixit et al., 2008]. These films show the expected E_2 (low), E_2 (high), and A_1 (LO) modes near 90, 490, and 580 cm^{-1}, respectively, indicating a preferred c-axis orientation for the InN crystallites. Further, an unassigned phonon mode (200 cm^{-1}) is present in the Raman spectra. This band could be a disorder activated mode. These Raman studies confirm the presence of an In_2O_3 secondary phase in InN samples [Dixit et al., 2008]. Depth dependent XPS measurements show a highly oxidized surface, with the oxygen content in this InN film falling from close to 50% at the surface to approximately 25% at depths of over 4 nm [Dixit et al., 2008].

(a)   (b)
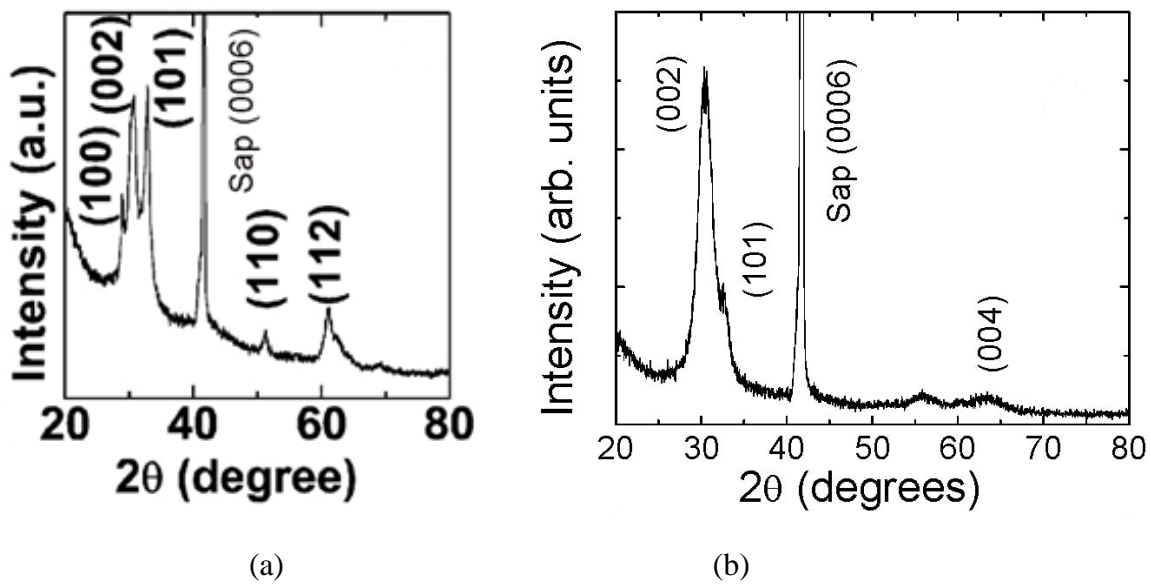
Fig.16.1. X-ray diffraction peaks for (a) the InN film sputtered using oxide target [Dixit et al., 2008], (b) the 5% Cr substituted InN films [Dixit et al, 2011]. The sapphire peak is indicated.

Figure 16.1(b) shows the XRD pattern for 5 at% Cr substituted InN films. The pattern for 2 at% films is similar. Similar to the structure of pure InN films, these peaks for 5 at% Cr substituted InN films can also be indexed to the InN wurtzite structure (JCPDS 50–1239), and are consistent with a polycrystalline sample with no impurity phases. However, similar to InN

films, 5 at% Cr samples have oxide impurity phase present which are seen in Raman spectra of these films (Fig. 16.2 (b)). These In_2O_3 peaks near 220 cm^{-1} and 300 cm^{-1} confirm that some oxide impurity phase is present in these samples, despite their apparent absence in the XRD patterns [Dixit et al, 2011].
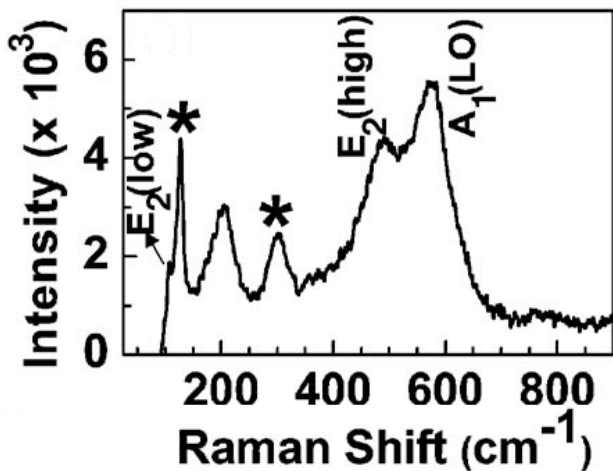
(a)
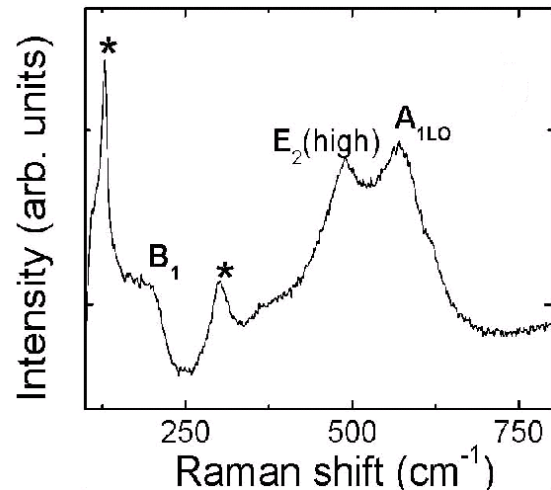
(b)
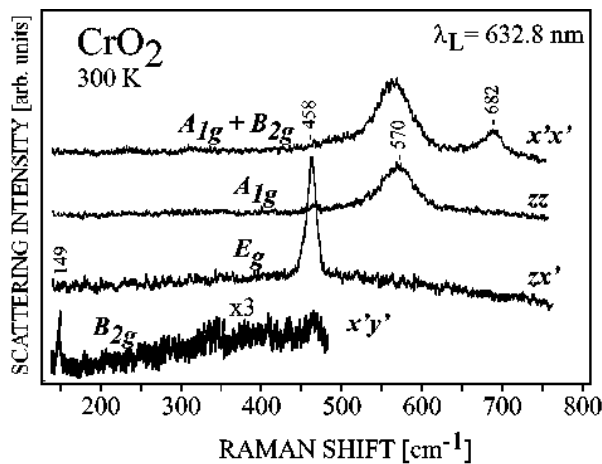
(c)
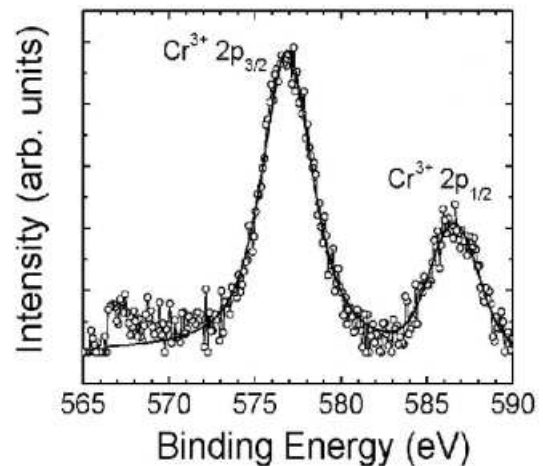
(d)

Fig.16.2. Room temperature Raman spectra for (a) InN thin film made from Oxide target. The * corresponds to the peaks at 129 and 303 cm^{-1} modes from In_2O_3 (White et al., 1972), (b) the 5% Cr substituted InN films, (c) CrO2 at 300K with 632.8 nm excitation [Iliev et al., 1999], and (d) XPS spectrum for the 5% Cr substituted InN film. The solid line is a fit indicating the presence of only the 3+ valence state.

Both XRD and Raman data did not show any evidence of ferromagnetic impurity phases. Had there been any ferromagnetic CrO_2 impurity, the Raman peak characteristics would have appeared at 149, 458, 570, and 682 cm^{-1} as shown in Fig 16.2 (c) for activation of different Raman modes at 300K with 632.8 nm excitation [Iliev et al., 1999]. But we do not see any of such Raman peaks indicating the absence of ferromagnetic CrO_2 impurity. In order to more carefully exclude the possibility of Cr-rich impurity phases, we have shown the Cr XPS spectrum for the 5 at% Cr doped InN film in Fig. 16.2 (d). This can be fit assuming that Cr is present only in the 3+ valence, consistent with substitutional doping and confirming the absence of ferromagnetic Cr in 4+ valence state.

16.4   Optical spectra and resistivity of Cr doped InN films

Hall effect measurements and plasmon absorption show that the n-type carrier concentration due to the presence of oxygen defects in InN films is found to be $3.8 \times 10^{20} cm^{-3}$, consistent with previous studies (Dixit et al., 2009). The carrier concentration for the 2 at% and 5 at% Cr substituted films were estimated to be 6.7×10^{20} cm^{-3} and 7.2×10^{20} cm^{-3} respectively. Perkin-Elmer UV-Vis spectrometer was used to find optical spectra for $In_{0.98} Cr_{0.02}N$, shown in Fig. 16.3 (a), as a plot of $(\alpha E)^2$ versus E. The spectra for $In_{0.95} Cr_{0.05}N$ sample were quantitatively similar. A large absorption peak, possibly due to plasmon excitation, was observed at the energy near 0.7 eV. At the higher energy, these curves are linear whose extrapolation gives the optical bandgap energy of approximately 1.8 eV for both samples [Dixit et al., 2011].

Figure 16.3 (b) shows the resistivity as a function of temperature for both 2% and 5% Cr substituted films. Both the films show metallic behavior at higher temperature with the resistivity of about 1 mΩcm. They show a shallow minimum in resistance at lower temperatures. The shallow minimum for 2% Cr substituted film is at about 50K, while for 5% Cr substituted sample

it is at about 150K. Such phenomena of minimum resistivity have been observed in a number of other defect-rich semiconducting films, including $ZnGa_{0.05}O$ films, which shows a metal semiconductor transition (MST): metallic conductivity above 170 K and semiconducting behavior at temperatures below it. This is explained on the basis of weak localization effects: the free electrons tend to localize at lower temperatures giving rise to minima in the resistivity. [Bhosle et al., 2006].
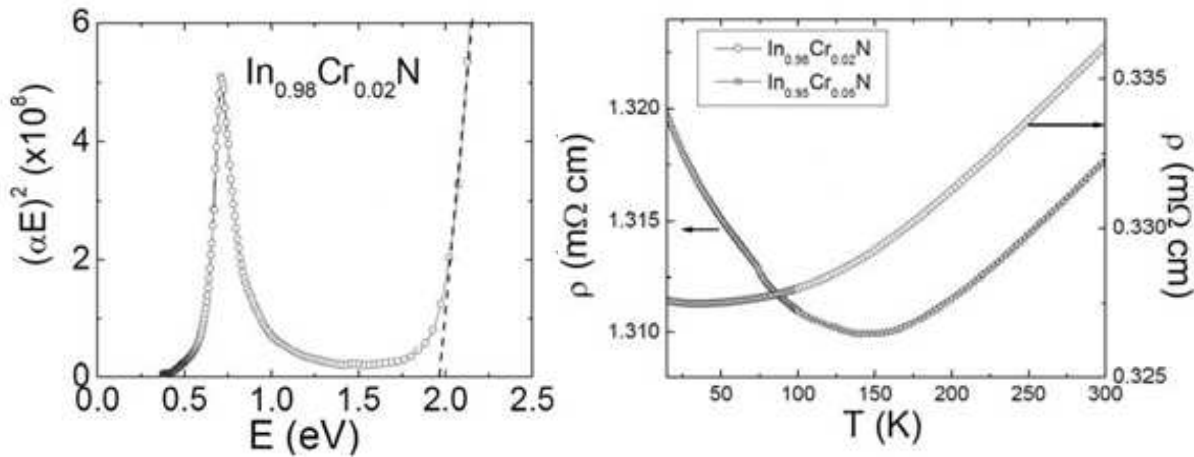
Fig.16.3. (a) Optical absorbance for the 2% Cr substituted InN film. The extrapolation of the optical band edge to zero energy is shown by the dashed line. (b) resistivity plots for the 2% Cr (circles) and 5% Cr (stars) substituted InN films.

16.5 Magnetization measurements in InN, and Cr substituted InN films

In-plane magnetizations of InN and Cr substituted (2% and 5% Cr) InN samples at room temperature were measured using SQUID magnetometer. Diamagnetic background was estimated from the high field response and it was subtracted to get the corrected magnetization curves shown in Fig. 16.4 (a). The saturation magnetization for InN sample was 0.05 emu cm^{-3}, for $In_{0.98}Cr_{0.02}N$ it was 0.15 emu cm^{-3}, and for $In_{0.95}Cr_{0.05}N$ sample it was 0.3 emu cm^{-3}. All three films show evidence of room temperature ferromagnetism with monotonically increasing saturation magnetization with Cr content. Presence of ferromagnetic signal in undoped InN samples eliminates the possibility of magnetism due solely to Cr-rich impurity phases, and

systematic dependence of saturation magnetization on Cr content diminishes the possibility of introducing magnetic impurity during sample handling. As discussed earlier, these samples contain some In_2O_3 secondary phase. However, the magnetic signal cannot develop solely in these impurity phases because the specific magnetization measured for the 5 at% Cr substituted InN film, 0.3 emu cm^{-3}, is almost as large as that measured for pure vacuum annealed In_2O_3, 0.5 emu cm^{-3} [Panguluri et. al., 2009]. Out-of-plane saturation magnetization for the 5 at% Cr substituted sample was found slightly larger than in-plane magnetization, as shown in Fig. 16.4 (b), indicating that these films have some modest anisotropy.
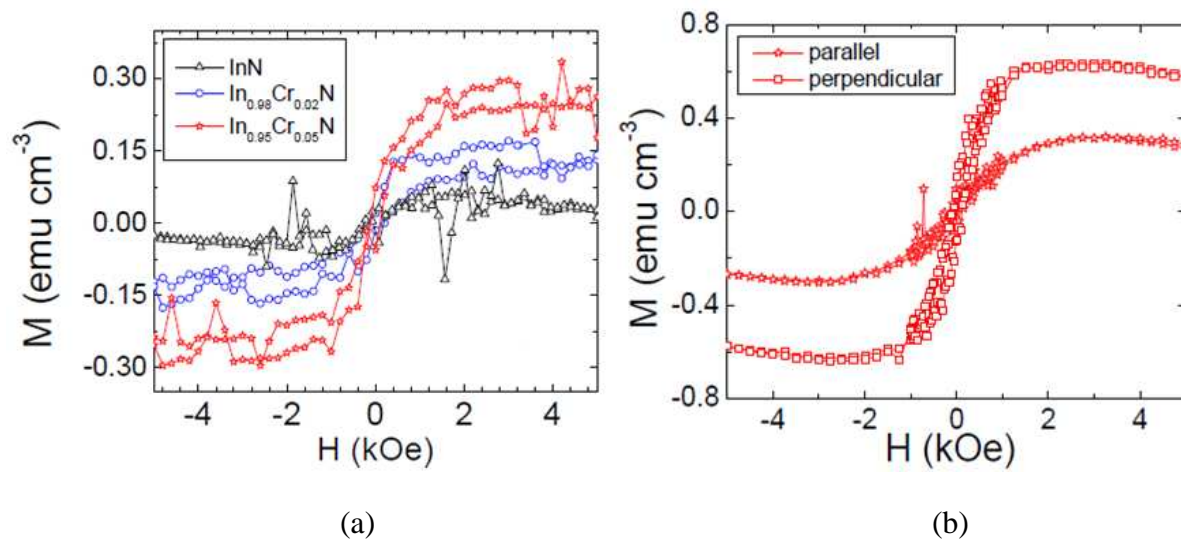
Fig. 16.4. (a) Magnetization curves for undoped InN, 2% Cr and 5% Cr substituted InN films at room temperature. (b) In-plane and out-of-plane magnetization curves for 5 at% Cr substituted film at room temperature.

Field cooled (FC) and zero field cooled (ZFC) magnetization curves (Fig. 16.5) were measured for 5% Cr substituted InN film to check whether nanoscale ferromagnetic impurity phases that were not detected by XRD or by Raman spectroscopy are responsible for room temperature ferromagnetic signals. The curves were taken at H = 500 Oe, and estimated background was subtracted for corrections. There is not significant separation between the ZFC

and FC curves, which argues against the presence of superparamagnetic impurity phases [Dixit et al., 2011]. These magnetization curves can be fit by the expression $M(T)=M_0+C/T+M_S(1-\beta T^{3/2})$, with M_0 a temperature independent background contribution, C the Curie constant, and β the spin wave stiffness. The best fit yielded a background magnetization of $M_0=0.07$ emu cm^{-3}, Curie constant C=1.3 emu K cm^{-3}, and spin wave stiffness $\beta=0.00006$. This fit to a paramagnetic plus ferromagnetic term is shown by the dashed gray line in Fig. 16.5, and yields an extrapolated ferromagnetic transition temperature of approximately 550 K [Dixit et al., 2011].
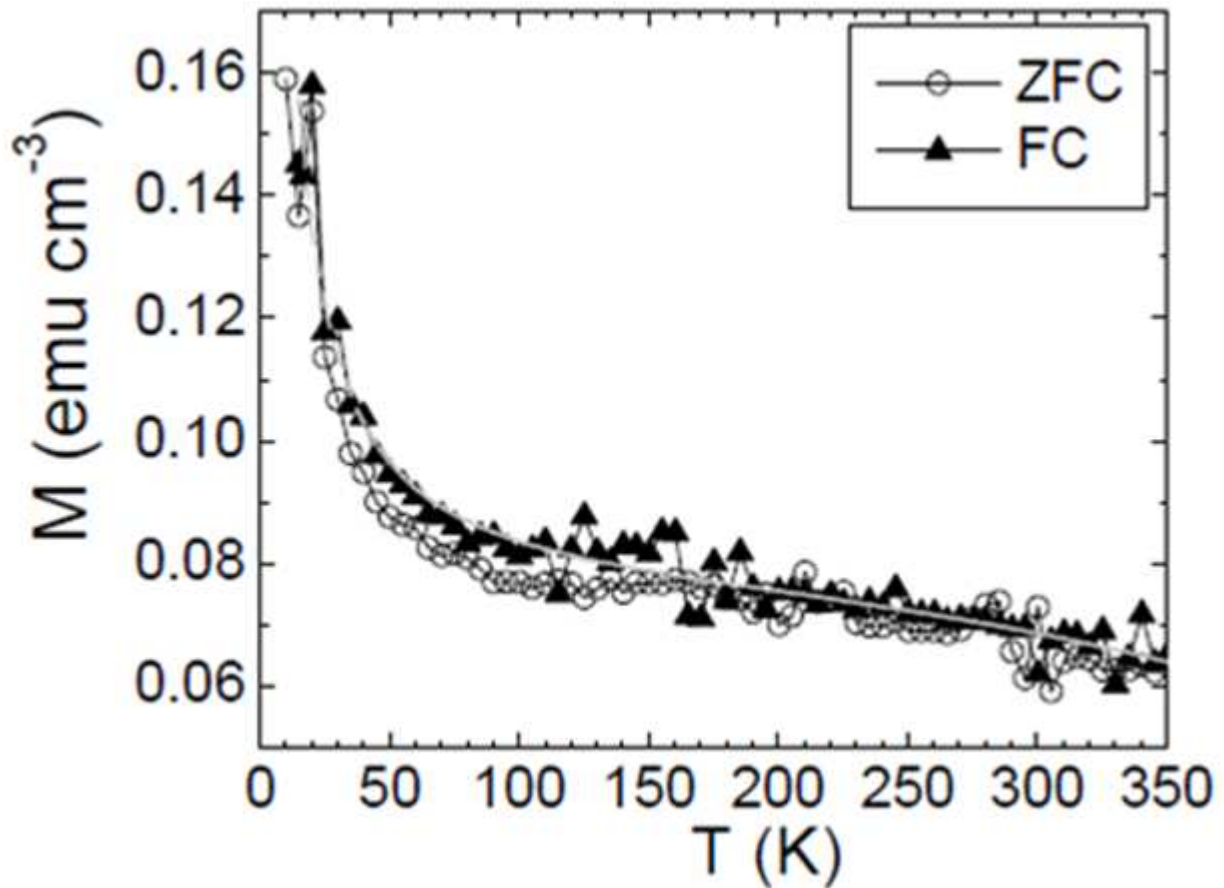
Fig. 16.5. Zero-Field Cooled (open) and Field-Cooled (closed) magnetization curves for the 5% Cr substituted InN film. The dashed line shows the fit to a paramagnetic plus ferromagnetic spin wave contribution, as discussed in the text.

16.6 Spin polarization

Spin polarization of conduction electrons in InN and Cr doped InN films were extracted by fitting using modified BTK model [Mazin et al., 2001] the conductance curves obtained by point-contact Andreev reflection (PCAR) technique (Soulen et al., 1998). Nb was used as superconducting tip to obtain conductance curves at 1.5K. The examples of conductance curves with mBTK fits for all of these samples are shown in Fig. 16.6.
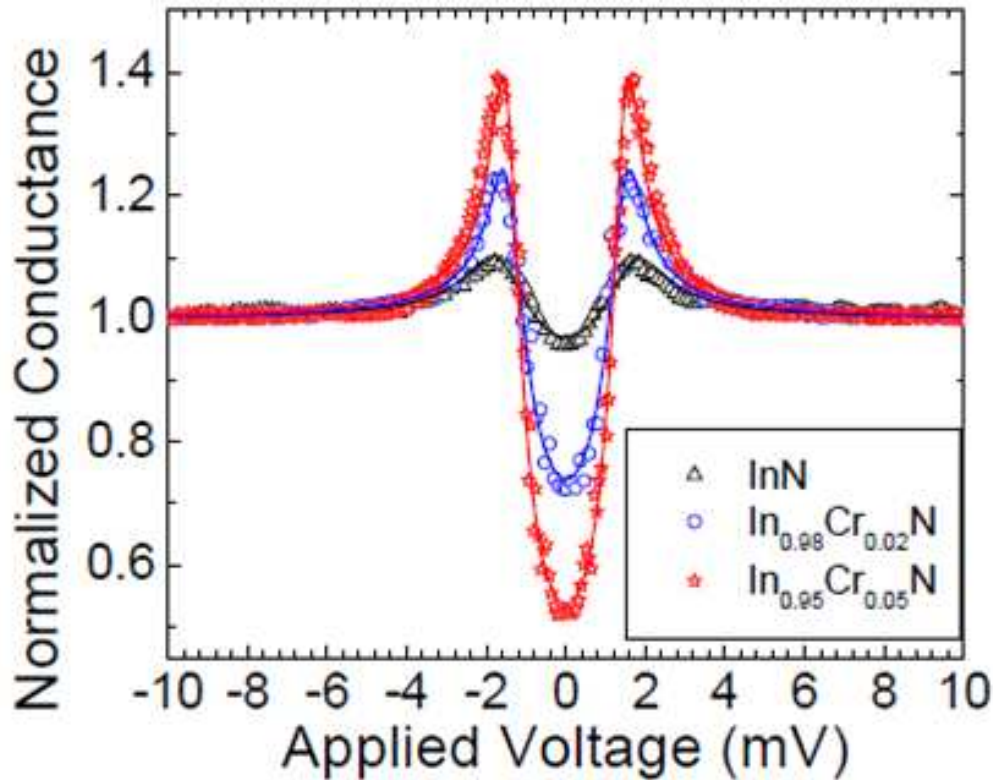
Fig. 16.6. The normalized conductance curves measured at 1.5 K using Nb superconducting tip for InN, $In_{0.98}Cr_{0.02}N$, and $In_{0.95}Cr_{0.05}N$ samples. The solid lines show the best fits by modified BTK model at 1.5K with Nb superconducting gap of $\Delta = 1.5$ meV.

The intrinsic values of spin polarization for all of these samples were found by extrapolating the Z^2 dependence of P, often encountered in PCAR measurements [Woods et al., 2004], to the case of transparent interface (Z=0). The intrinsic values of spin polarization were found to be ranging from ~ 46±2% for InN to ~50%±2% for $In_{0.95}Cr_{0.05}N$ films. Such finite

values of spin polarization suggest that the degenerate InN and Cr doped InN films may be suitable for spintronic device applications. Excess oxygen vacancies in these samples are the source of high carrier concentration which is the cause of magnetism in these samples as suggested that the ferromagnetism in certain oxide semiconductors such as In_2O_3 may be carrier mediated [Panguluri et al., 2009].

Magnetization of undoped InN films was measured after storing them under ambient conditions for approximately one year. Interestingly, the magnetization was found to be increased by a factor of about 27 to about 1.36 emu/cc (Fig. 16.7) which may reflect the effect of a larger Oxygen content on the magnetic ordering. The in-plane magnetizations in both directions were found same which indicated no magnetic anisotropy in X-and Y-directions of the plane of the film.
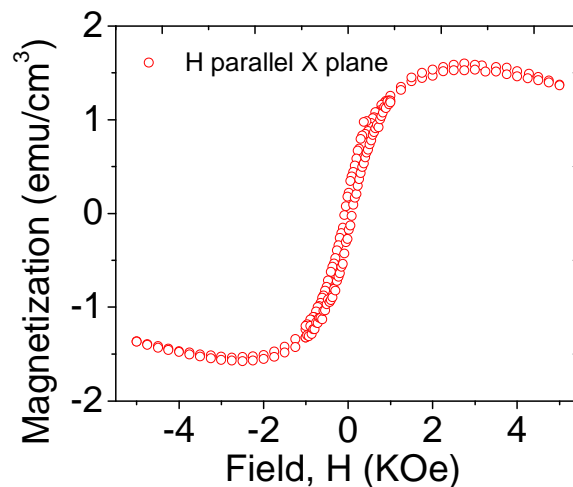
Fig 16.7 Increased magnetization of InN after storing in ambient conditions for about one year

Our studies find that incorporating Cr produces only a relatively modest increase in the magnetic moment, with an almost negligible change in the spin polarization, in agreement with the recent results indicating that the magnetic moment in Cr-doped InN is coupled to the carrier concentration, rather than Cr concentration [Kinsey et al., 2006].

16.7   Conclusions

Different properties such as structural, electrical, magnetic and spin polarization of degenerate InN and 2 at% and 5 at% Cr substituted InN films have been investigated. These samples contain considerable amount of oxygen which causes over 10^{20} cm^{-3} of high n-type carrier concentrations due to which the samples show conducting behavior down to low temperatures. Cr undoped InN and Cr doped InN thin films show room temperature magnetization, with the size of moment increasing from 0.05 emu cm^{-3} for InN to 0.30 emu cm^{-3} for 5 at% Cr doped InN samples with monotonic increase of the moment with Cr fraction. Even though the samples contain In_2O_3 impurity phase, the systematic dependence of the moment on Cr fraction excludes the possibility of other ferromagnetic impurity phases. Spin polarization was measured by PCAR technique. It was measured about 46% for undoped InN sample and about 50% for $In_{0.95}Cr_{0.05}N$ films. Room temperature ferromagnetic behavior, and finite low temperature spin polarization of these materials suggest that they may be pertinent to a number of different spintronic applications, including efficient spin injection into silicon.

CHAPTER 17

CONCLUSION AND FUTURE PROSPECT

17.1   Summary and conclusions

The first part of this dissertation (chapters 1-5) was focused on development of Si_3N_4 free-standing micromirrors with metallic coating and their torsion study by passing electric current. The torsion angles in case of Au, Ni, or Ag deposited micro structures were measured as a function of dc current passed, and their dependence was found to be quadratic. Due to negligible effects of electrostriction and Maxwell stress compression, the only effect responsible for such quadratic dependence is the Joule heating which increases the temperature of the metallic layer so that the thermal expansion of this layer constrained by Si_3N_4 layer causes non equilibrium strain which deforms the bimorph having residual stress, resulting in angular rotation [Thapa et al., 2011]. Large reproducible torsion angles with low electrical power in such electro-thermal actuation may be useful for MEMS applications. The optical detection system we have developed has high sensitivity which may be used to measure even smaller torques, such as the torque produced in heterostructures of magnetic and nonmagnetic materials, as proposed by Fulde and Kettemann [Fulde et al., 1998] and Yu [Yu et. al., 2007].

The second part of this dissertation (chap 6 onwards) was focused on spintronics, especially the development of spintronic materials and their structural, transport and magnetic properties focusing mostly on spin transport measurements by using point contact Andreev Reflection spectroscopy. A brief review of how the development of spintronics evolved was made in chapter 6. With this evolution, different spintronic devices such as GMR, TMR, MRAM, STT-RAM, SFET were developed. Their fundamental aspects and the impact in technology were briefly explained. Spin injection from ferromagnetic materials to non-magnetic

or semiconductors is efficient if nonequilibrium spins can be created at the Fermi level of such magnetic materials. Importance of knowing the degree of spin polarization is important to develop and identify such materials for their efficient and effective use in spintronics.

With this introduction, the discussion moved on to review the development of different techniques used for measuring spin polarization with more emphasis on point contact Andreev reflection (PCAR) spectroscopy in chapter 7. Spin polarization can be measured by Photoemission Spectroscopy [Johnson, 1997], Spin polarized tunneling (SPT) spectroscopy [Tedrow et al., 1971; Tedrow et al., 1973; Meservey et al., 1994], Positron Spectroscopy [Hanssen et al., 1990], and point contact Andreev reflection spectroscopy [Soulen et al., 1998]. While the values of spin polarizations measured were reported slightly different because of different sensitivity of these techniques, the values can be different depending on the regime of transport: ballistic or diffusive or intermediate. Point contact Andreev reflection spectroscopy was used throughout the study of spin polarization in this dissertation. Andreev reflection theory, BTK theory and modified BTK theory were briefly summarized in this chapter to introduce different parameters used for fitting the conductance data of the interface between superconductor and the sample in point contact experiments.

Moving on to chapter 8, it was attempted to show theoretically generated conductance curves for different cases of varying interfacial barrier strength (Z) at different temperatures for P = 0, and at different spin polarization (P) values at Z = 0. Also, such ideal curves were generated for changing Z and P both to show the possibilities of various shapes of conductance curves that are encountered in different systems while doing experiments. Conductance curves are generated for different temperature T to show how the shape of conductance curves change especially around the bias voltage equal to the superconducting gap of the tip being used. In this particular

case when P = 0 has been considered, some temperature elevation during fitting can help to achieve better fitting curve, but still retaining the same extracted value of P and almost unchanged value of Z. Uniqueness of fitting has been checked by fitting a nice experimental data with all possible changes of input fitting parameters such as temperature (T), spreading resistance (R_s), the number of data points. The test was done with change of such parameters separately or in different combinations. For the reasonably acceptable fit, the extracted values of P and Z were noted. It is found that P is dependent on Z quadratically which is similar to their correlation for different conductance curves taken for different contacts between the sample and the superconductor. It shows that the P is not only correlated with the scattering at the interface, but also it involves Z dependence that arises while fitting the data. Interestingly, the intrinsic value of P corresponding to Z = 0 for both cases are found close enough within the error bar. This indicated that even though the fittings can give some spread in P and Z values, their quadratic dependence gives unique intrinsic value of P within its error bar.

Sample preparation techniques and experimental technique of Andreev reflection spectroscopy are discussed in chapter 9. The thin film samples, viz. PdNi, Pt, MnBi, InN etc were prepared by either magnetron sputtering or e-beam evaporation. MnSi, Co doped $BaFe_2As_2$, and Ni samples with and without strain were single crystals. Magnetic properties of these samples were studied by using SQUID, transport properties were studied by using PPMS, and transport spin polarizations at low temperature were studied by lock-in technique. Superconducting tips of Nb were prepared by electrochemical etching. Various characterizing techniques such as XRD, EDX, AFM etc. were applied for some samples.

As a reliability and reproducibility test of the point contact technique, experiments were done on non-magnetic sample Cu, and highly spin polarized and known sample $La_{0.7}Sr_{0.3}MnO_3$

(LSMO). Varieties of conductance curves reported by different authors for Cu are reviewed, and the conductance curves obtained from our point contact technique are reported in chapter 10. As expected, the spin polarization for Cu samples was found to be 0. On the other hand the spin polarization of LSMO sample was measured, and its extracted value was found to be 58.4% which agrees with the reported value of P = 58% for the LSMO single crystal [Nadgorny, 2007]. These tests indicate that the point contact setup is reliable and the spin polarization values are reproducible.

After PCAR set up was found to be reliable, it was reasonable to move on exploring different new samples whose spin polarizations have not been reported so far. Manganesesilicide was chosen as one of the very interesting systems to be studied. Because of its different magnetic phases from helical to conical to induced- ferromagnetic below its critical temperature (29.5±0.5) ^{o}C, it is very interesting to know how the spin polarization of this sample changes in these phases. Magnetization measurements show that the induced ferromagnetic phase is obtained at 6.5KG at 5K. Resistivity measurements show that the transport at low temperature below critical temperature is governed by spin fluctuation (T^2 dependence), and the phase transition occurs at around 30K, the critical temperature. PCAR technique was applied by driving the superconducting tip manually, and also by driving it by squiggle piezoelectric motor. The spin polarization at 2K was measured to be 44±4% by using squiggle piezoelectric motor, and at 1.2K it was measured to be 47.8% when the tip was driven manually. The magnetic field dependent conductance curves were obtained at different magnetic phases, and their fittings gave the dependence of spin polarization with the magnetic field. It is found that the spin polarization increases with magnetic field, and it reaches to the saturation value at around 6.5KG as expected for the ferromagnetic phase, with the saturation value of P about 52%.

In another approach, e-beam lithography was done on PMMA coating on the polished surface of MnSi single crystal to open two holes each of 1 µm square at 10µm far, and Nb was deposited on the top of this surface so that Nb contact to MnSi was achieved only through these holes on PMMA. The deposited Nb film was superconducting with superconducting transition temperature of 5.5K. Conductance curves across the interface between Nb and MnSi were taken at 2K with application of different magnetic fields for both parallel and perpendicular configurations of the sample. Interestingly, the conductance curves obtained were different than conventional conductance curves. The normalized zero bias amplitude was more than 2, the maximum amplitude generally expected and encountered in Andreev reflection. Also the amplitudes were found suppressed at higher magnetic fields, disappearing completely at 38KG in the case when the plane of the sample was parallel to the applied field. In these conductance curves, another interesting feature was the oscillation of conductance curves outside the superconducting gap edge. These oscillations disappeared when the applied magnetic field exceeded 6.5KG, the field required to induce MnSi to ferromagnetic phase. This observation indicates that these oscillations arise due to helical spin fluctuation initially at no field and low field. Their fluctuations decrease with the increasing magnetic field, and disappear when the spins are aligned as MnSi is induced to ferromagnetic phase. In the same configuration of the sample, the amplitude of zero bias normalized conductance at no field decreases with temperature, and disappears at 5.5K, the same temperature as the superconducting transition temperature of Nb film being used. The conductance oscillations disappear at 4K. The systematic reduction of zero bias amplitude with temperature below T_c of Nb, and supression of conductance oscillations at temperature $T<T_c$ indicate that the spins in MnSi are taking part in the conductance features.

In case of perpendicular configuration, the conductance curves were similar with the zero bias amplitude reducing with magnetic field, and collapsing at around 30KG at 2K. The conductance oscillations disappeared at around 4KG at 2K. The temperature dependence conductance curves in this configuration also have similar features as in parallel configuration. The conduction oscillations disappear at 4K, and the zero bias amplitude disappears at 5.5K in this case also. These interesting features of conductance curves are yet to be understood in detail with the help of modeling some suitable theory.

Another interesting system studied was $Pd_{1-x}Ni_x$ alloy in which the magnetic susceptibility of nearly ferromagnetic Pd is increased by Ni impurities. Split in spin bands causes spins to polarize, and exploring the dependence of spin polarization on corresponding saturation magnetization and Curie temperature was one of the aims to work on this material. Six different thin film samples of PdNi with Ni concentrations up to 12% were sputtered. Their spin polarization, saturation magnetization and Curie temperature were measured. It was found that the Curie temperatures of all the samples were proportional to their saturation magnetization. The spin polarizations for different samples were measured from 33% to 49% with its highest value corresponding to the sample of highest Ni concentration of 12% among the samples that were studied. For bulk pure Pd the spin polarization was measured to be zero. In case of the spin polarization, it was found proportional to the saturation magnetization; and the Curie temperature as well. However, this proportional trend was found in the samples if they were sputtered in the same batch. For the samples of different batch, the proportionality of spin polarization showed different slopes. This could be due to the fact that the spin polarization is sometimes surface and termination dependent. The proportionality of Curie temperature on

saturation magnetization was valid for all samples even from different batches. The study of PdNi system has been discussed in Chapter 12 of this dissertation.

In most of the cases, superconducting tip is used to probe the spin polarization of a sample in the form of thin film or a single crystal. But an iron pnictide superconducting sample $BaFe_2As_2$ with Co doping was chosen as another interesting system. Chapter 13 discusses briefly about the historical development of superconductivity and how the development advanced to the iron pnictide superconductors. With some review of its magnetism and superconductivity, the experimental results about the field dependent and temperature dependent conductance were presented. Since the sample $BaFe_{1.8}Co_{0.1}As_2$ is suprconducting with superconducting transition temperature T_c=18K, and with superconducting gap of Δ=2.73mV, the tip for PCAR measurements was chosen to be of Au. The tips were made of 250µm thick Au wire by cutting at an angle and pulling it at the same time so that the very tip becomes sharp. The conductance curves show that a pseudogap appears at around 12 mV of bias, and this can be suppressed by applying magnetic field of 14KG whereas the main superconducting gap is still present even at 7T. Lower magnetic field was needed at higher temperature to suppress the pseudogap. Hence, evidence of pseudogap below superconducting transition temperature, and its suppression with magnetic field, was found by Point Contact Andreev Reflection (PCAR) technique.

In order to study the low magnetic system, Pt was chosen in the other study which is presented in detail in Chapter 14. Though Pt is non magnetic in bulk form, its nano-particles and nano-rods have been reported to be magnetic [Sasaki et al., 1998] experimentally and ferromagnetism in Pt nano wires has been predicted theoretically [Delin et al., 2004]. Pt clusters are also reported to have magnetic moments [Kumar et al., 2008]. Mono layer of Pt on certain substrate such as Au(001) [Blügel., 1992] and MgO [001] [Yang et al., 2010] was predicted.

However, the magnetism in its thin film was not reported by any one. So, several Pt thin films of thicknesses 10, 12.7, 21.2, 25.55, 30, 33.3, 55.5, 65.18, 74, and 100nm were deposited for the study. 10nm and 30 nm thick films were prepared by e-beam deposition and the rest of the films were deposited by magnetron sputtering. The magnetization measurements of these samples by SQUID showed that all of the Pt thin films are magnetic. The magnetism in Pt thin films was supported by neutron scattering measurements also. The magnetization per unit area of the surface of these samples was almost constant no matter what the thickness of the samples was. This indicated that the magnetism in Pt thin films is not related to volume magnetism, but it is simply the surface magnetism. The Pt thin film surfaces were images under AFM, and were found that the surfaces have roughness. In an attempt to find the correlation of surface roughness and the surface magnetization, it was noticed that the presence of roughness is the source of magnetism as predicted theoretically, but it seems that the degree of roughness has nothing to do with the degree of surface magnetism.

Beside measurement of magnetism directly, the spin polarization of these Pt thin film samples were measured by PCAR technique. The intrinsic values of spin polarization were measured between 40% and 53% for these samples. The relation of spin polarization with the thickness of the sample is hard to find. The spin polarization seems linearly dependent on the saturation magnetization of these films.

The P values do not have strong correlation with different parameters such as thickness, roughness, saturation magnetization (emu/cm^3), surface magnetization (emu/cm^2) and coercivity. It seems that the sample preparation conditions and topography of sample surfaces play some role for different values of spin polarization. More importantly, the Pt thin films are ferromagnetic. Measured values of transport spin polarization also confirm that the Pt surfaces

are ferromagnetic which may be due to Pt clusters and atomic chains on the rough surfaces of Pt thin films.

It is quite natural to look for a material that has high spin polarization. In this regard, MnBi thin films were studied because MnBi in zinc blende structure is half metallic [Xu. et al., 2002; Zheng et al., 2004; Kahal et al., 2010] though it is not stable phase, however, in NiAs structure MnBi is stable with high Curie temperature (628K). So, exploring its magnetism and spin polarization would be important in this system. Magnetization measurements show that MnBi films have perpendicular easy axis of magnetization along c-axis so that it can be used in spin injection. Transport spin polarization of MnBi thin films gave the highest P value of about 64%. Such a high value of P was found, theoretically, to be due to the disparity in Fermi velocities of majority and minority carriers at the Fermi level. The spin polarizations in different samples were found to be proportional to the saturation magnetization experimentally, which was supported by the theoretical calculations also. Due to high transport spin polarization and other suitable magnetic properties, MnBi is found to be a potential candidate in spintronic applications. Detailed description of the study of MnBi is given in Chapter 15.

Other materials needed for spintronic applications are dilute magnetic semiconductors. Room temperature ferromagnetism has been reported in such materials without or with 3d transition metal doping as reviewed briefly in Chapter 16. Degenerate InN, and 2 at % and 5 at % Cr doped InN thin films were studied. They were found to show room temperature magnetization, with the size of moment increasing from 0.05 emu cm^{-3} for InN to 0.30 emu cm^{-3} for 5 at% Cr doped InN.

Such films showing high carrier concentration and low resistivity were studied applying point contact Andreev reflection spectroscopy to probe their spin polarization. The intrinsic values of spin polarization were found to be ranging from ~ 46±2% for InN to ~50%±2% for $In_{0.95}Cr_{0.05}N$ films. Such finite values of spin polarization suggest that the degenerate InN and Cr doped InN films may be suitable for spintronic device applications. Presence of Oxygen and hence high carrier concentration in these samples is suggested to be the cause of magnetism in these samples. It is observed that the Cr doping causes relatively modest increase in magnetic moment and spin polarization. Room temperature ferromagnetic behavior, and finite low temperature spin polarization of these materials suggest that they may be pertinent to a number of different spintronic applications, including efficient spin injection into silicon.

Hence, weak ferromagnetisms of different materials were studied with the help of point contact Andreev reflection spectroscopy. These materials are potentially useful in spintronic applications.

17.2   Ongoing experiments

To answer the question of how the spin polarization of a single crystal changes if shear stress is applied to the crystal, Ni single crystals without stress and with shear stress of 11% and 25% were studied. The strain-stress relation of these single crystals is shown in Fig. 17.1.
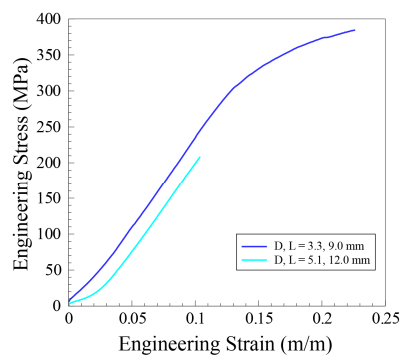
Fig.17.1. Stress-strain relation of Ni single crystals

The conductance curves after BTK fit for these crystals are shown in Fig. 17.2. The intrinsic values of spin polarizations for Ni with stress of 0%, 11% and 25% are found to be 43.6%, 38.7% and 35.7%. This trend clearly shows that the spin polarization is reduced in the sample with larger strain.

Shear	Typical conductance curves		Z dependence of P	Intrinsic value of P
0%				43.6±1.9 %
11%				38.7%
25%				35.7%
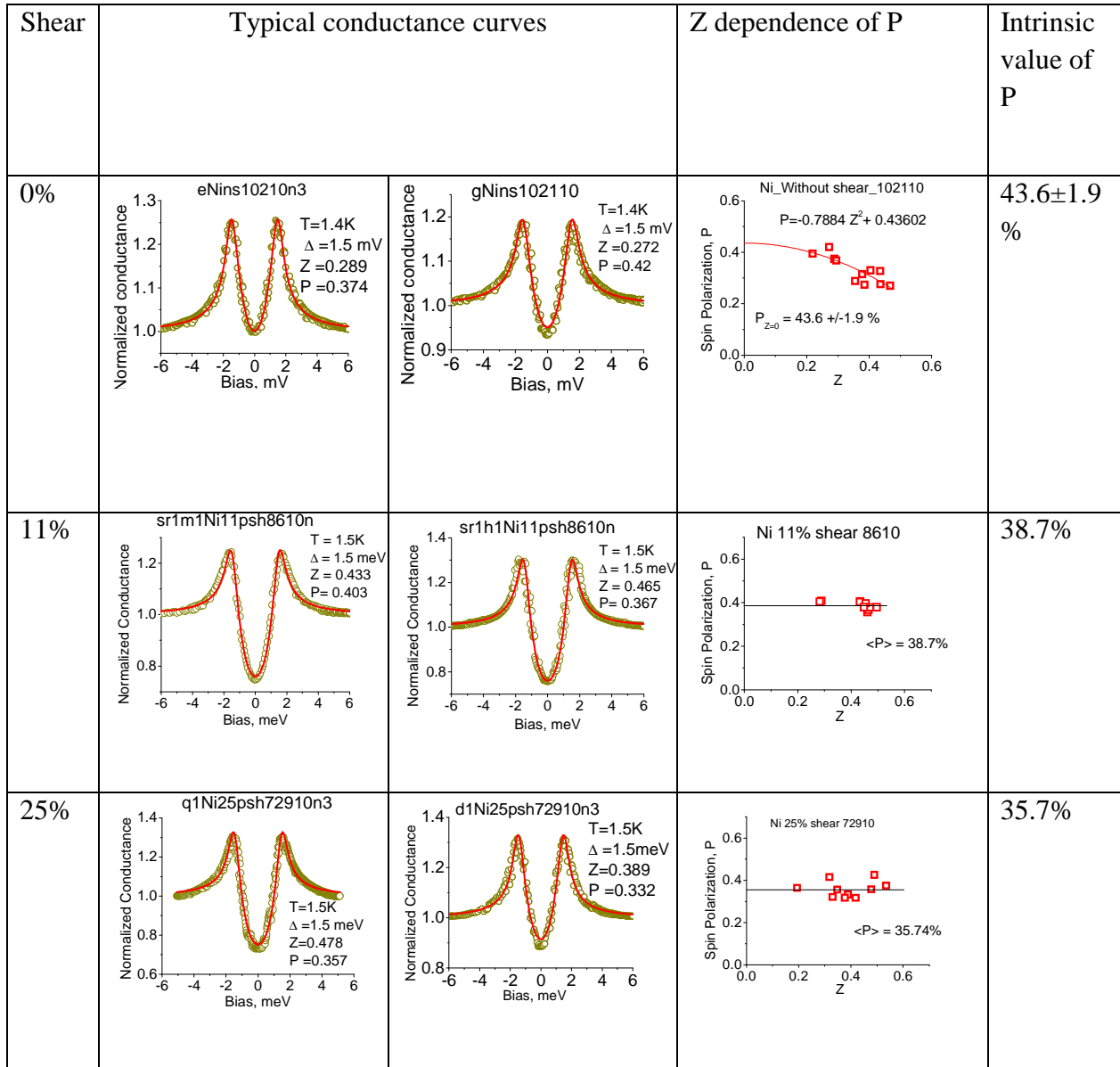
Fig. 17.2 Normalized conductance curves for Ni single crystals with shear 0%, 11% and 25%.

Out of the samples done so far, the relation of spin polarization to the shear strain of these samples is shown in Fig.17.3 (a). It seems that the spin polarization is lower for the samples with higher dislocation density caused by larger strain. This is indicated by the plot in Fig. 17.3 (b). The resistance of 25% strained sample is higher than the resistance of 11% strained sample as shown in Fig. 17.3(c). It is seen that more resistive sample has lower value of spin polarization. However, for making final conclusions, more samples with different strains are to be studied.
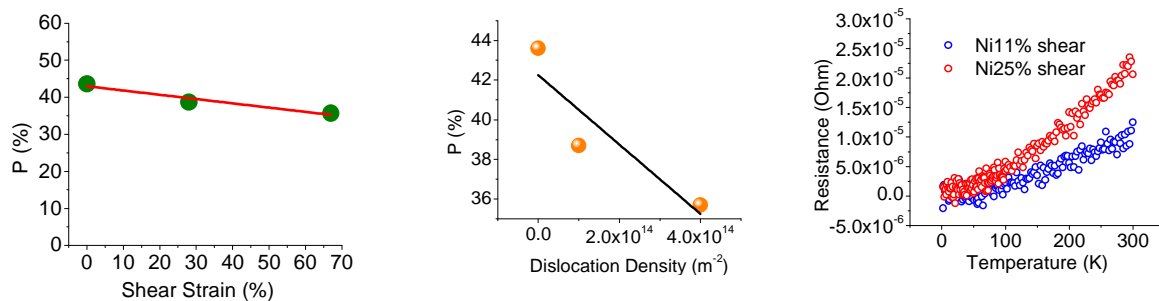
Fig. 17.3. Spin polarization as a function of (a) shear strain, (b) dislocation density, and (c) temperature dependence of resistance of strained Ni single crystals

17.3. Future perspective

One of the purposes of studying spin polarization of different low ferromagnetic materials is to find a material that is half-metallic with high spin polarization, high stability, high Curie temperature, and with other suitable properties so that it can find spintronic applications. The other importance is in understanding the fundamental aspects such as dependence of spin polarization in magnetization or in Curie temperature or in strain or in some other properties of such materials so that these properties can be tuned to control or increase the spin polarization of such materials for useful technological applications. This study can be extended to different alloys of ferromagnetic materials, e.g. CoPt with different Co concentration, or other Co based Heusler compounds, or different dilute magnetic semiconductors.

In the line of the development of bimorph thermo-electric actuators, further studies can be done in understanding the mechanism more quantitatively, and in finding the appropriate applications of the developed microstructures in MEMS technology.

APPENDIX A (I)

A.1.　　　**Moment of inertia (J) calculations for the microstructure, and the resonance frequency**

Let us consider the structure as shown in Fig. A.1. The dimensions are shown in the figure. We can calculate the moment of inertia by using the general expression for inertia tensor.
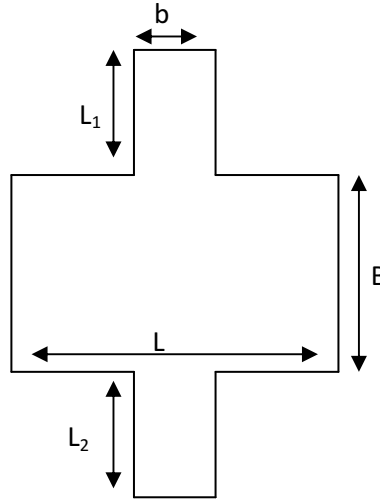
Fig. A.1. Micro electro mechanical mirror structure

$$J = \int dm \; (r^2 \delta_{ij} - r_i r_j)$$

$$= \int (r^2 \delta_{ij} - r_i r_j) \; \rho_{Si} \; dx \; dy \; dz$$

$$J_{yy} = \rho_{Si} \int (x^2 + z^2) \; dx \; dy \; dz$$

$$= \rho_{Si} \left[\frac{x^3}{3} \right]_{-b/2}^{b/2} [y]_{-L_1/2}^{L_1/2} [z]_{-h/2}^{h/2} + \left[\frac{z}{3} \right]_{-h/2}^{h/2} [x]_{-b/2}^{b/2} [y]_{-L_1/2}^{L_1/2}$$

$$J_{L_1} = \rho_{Si} \frac{b^3 L_1 h}{12} + \rho_{Si} \frac{h^3 b L_1}{12}$$

$$J_{L_2} = \rho_{Si} \frac{b^3 L_1 h}{12} + \rho_{Si} \frac{h^3 b L_1}{12} \qquad \text{(taking } L_1 = L_2)$$

$$J_{mirror} = \rho_{Si} \frac{L^3 Bh}{12} + \rho_{Si} \frac{h^3 LB}{12}$$

The expression for the angle of rotation is given by

$$\alpha_o(\varpi) = \frac{\frac{\hbar P I_o}{2q}}{\sqrt{[\frac{2k_1 G_{Si} h^3 b}{L} - \varpi^2 (\frac{1}{12} \rho_{Si} BhL^3 + \frac{1}{24} \rho_{Si} bh^3 L_F + \frac{1}{24} \rho_{Si} bh^3 L_{NM})]^2 + \frac{kJ}{Q^2} \varpi^2}}$$

The resonant frequency ω_o is found by setting the term inside the square bracket in the denominator equal to zero. This gives,

$$\omega_o = \sqrt{\frac{K}{J}} = \sqrt{\frac{\frac{2K_1 G_{Si} h^3 b}{L}}{\rho_{Si} \frac{L^3 Bh}{12} + \rho_{Si} \frac{h^3 LB}{12} + \rho_{Si} \frac{b^3 L_1 h}{6} + \rho_{Si} \frac{h^3 b L_1}{6}}}$$

Where,

$K_1 = 0.23$ = geometry factor for the ratio of h and b;

G_{Si} = silicon's shear modulus = 65 Gpa;

h = thickness of the structure = 0.5 μm;

b = width of the torsion bar; L = length of the mirror; B = width of the mirror;

ρ_{Si} = density of Si mirror = 2330 Kg/m^3;

$L_1 = L_2$ = length of the beam supporting the mirror;

P = Spin polarization of the material = 0.5 (Assumed);

Q = Quality value of the system; I_o = Amplitude of current through wire = 1 mA;

K = equivalent stiffness of the beam.

APPENDIX A (II)

MASK DESIGN

A.2.   Design of Layer 1 mask (Bottom layer)

This layer of mask as shown in Fig. A.2. is to open the window by etching into Si wafer.
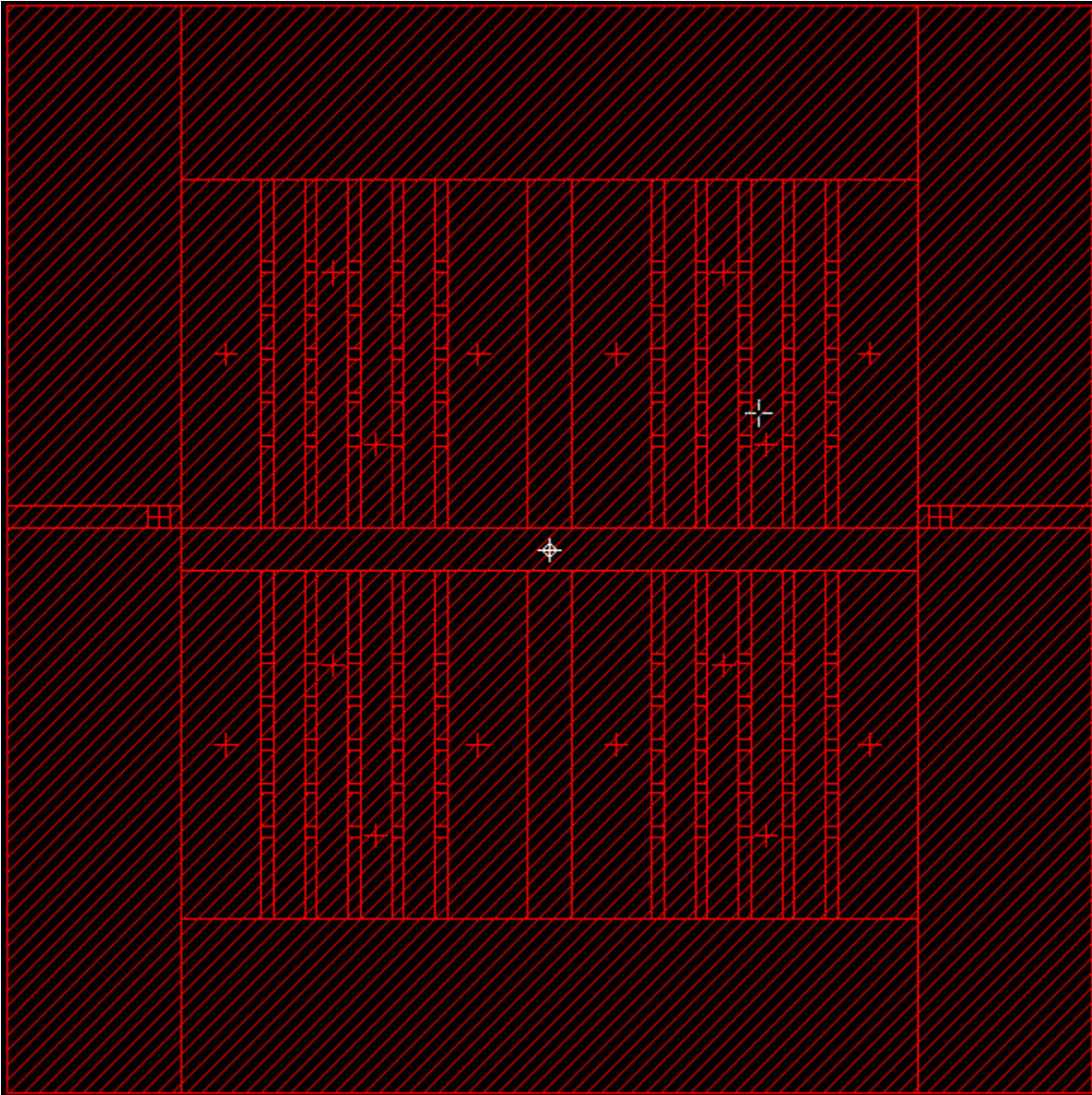
Fig. A.2. Design of Layer 1 of mask

A.3 Design of Layer 2 of mask
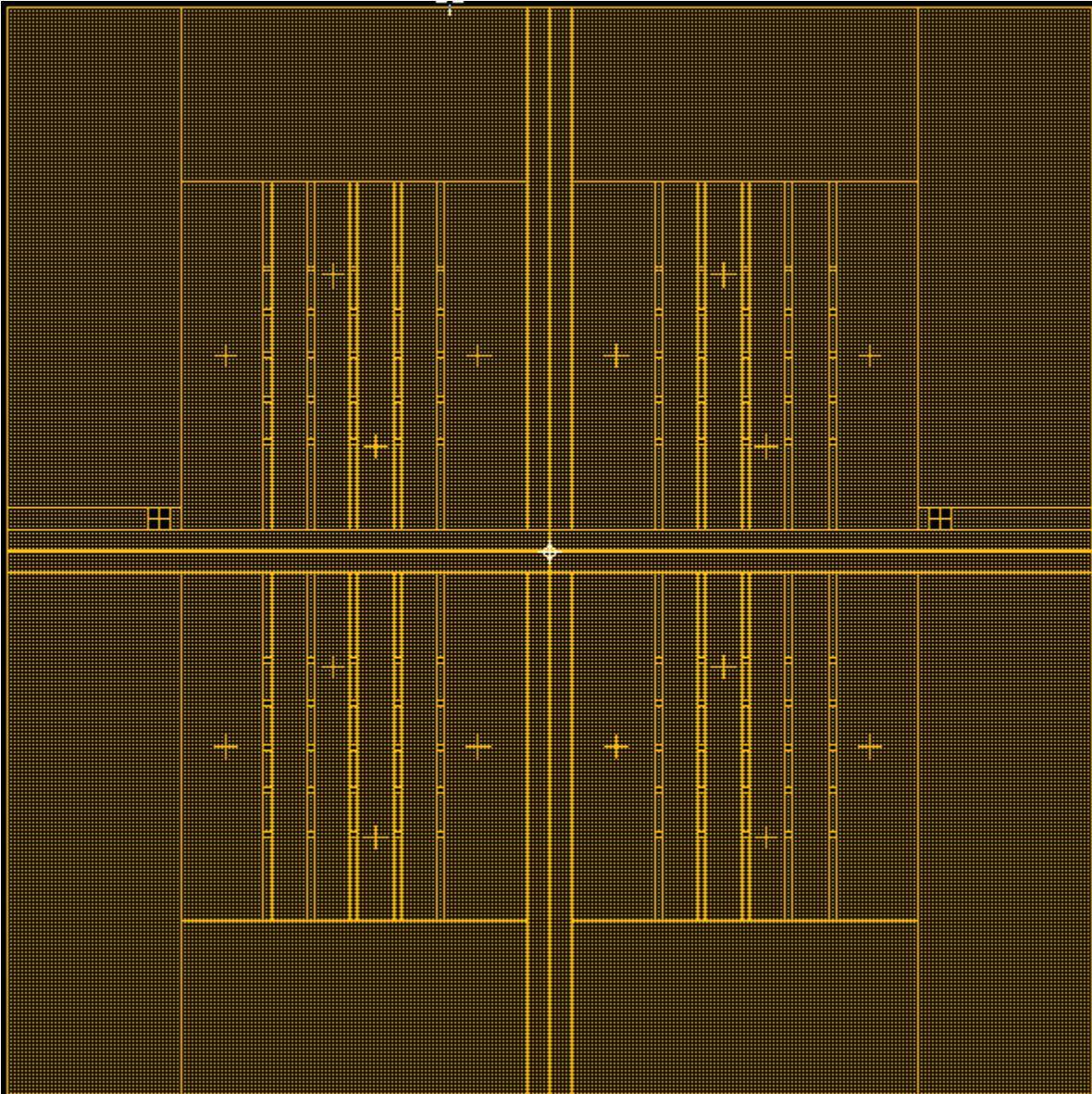
Fig. A.3. Design of Layer 2 of mask

A.4 Design of layer 3 of mask
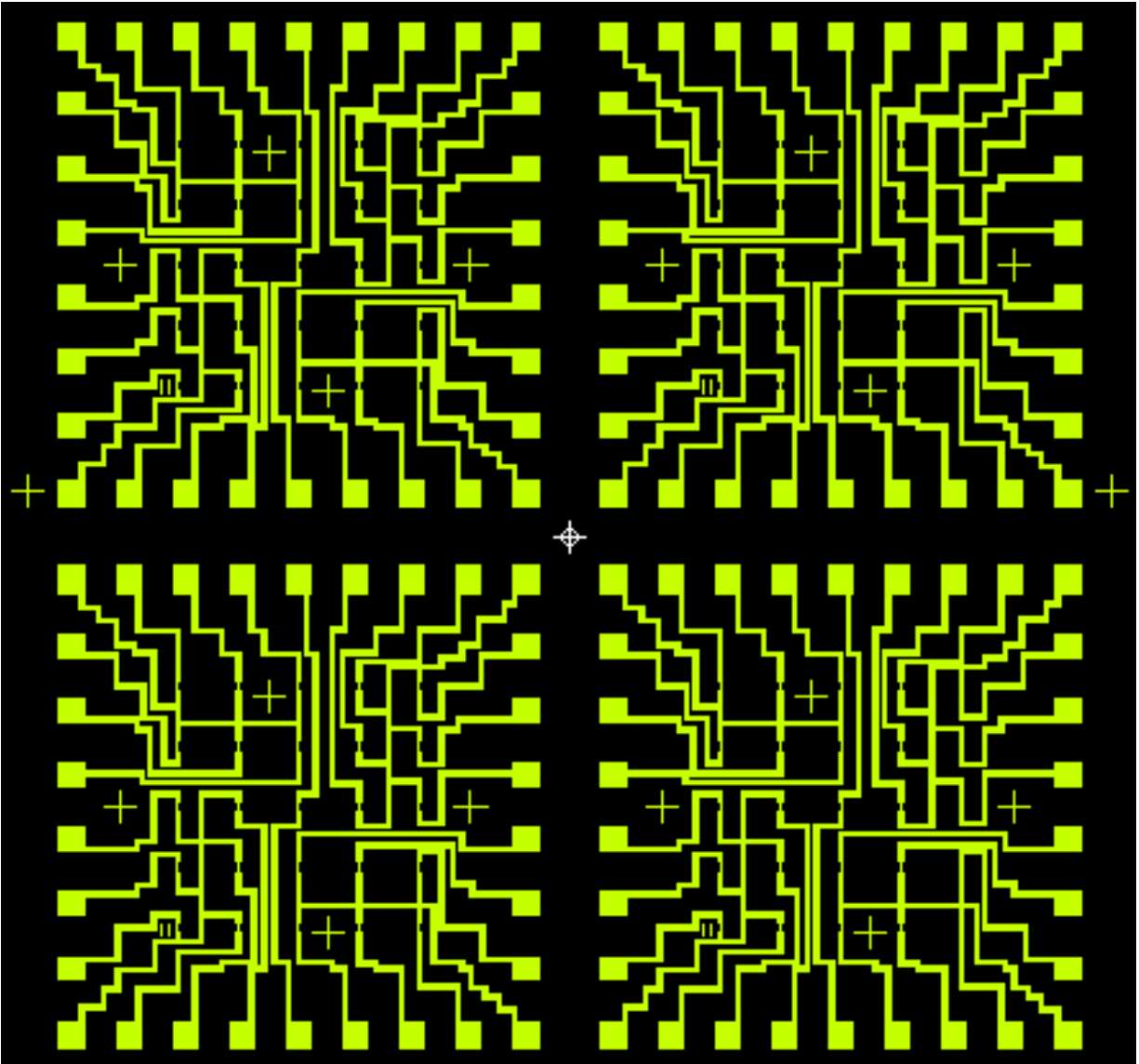
Fig. A.4. Design of Layer 3 of mask

A.5 **Single die of each layer shown separately for more clarity**
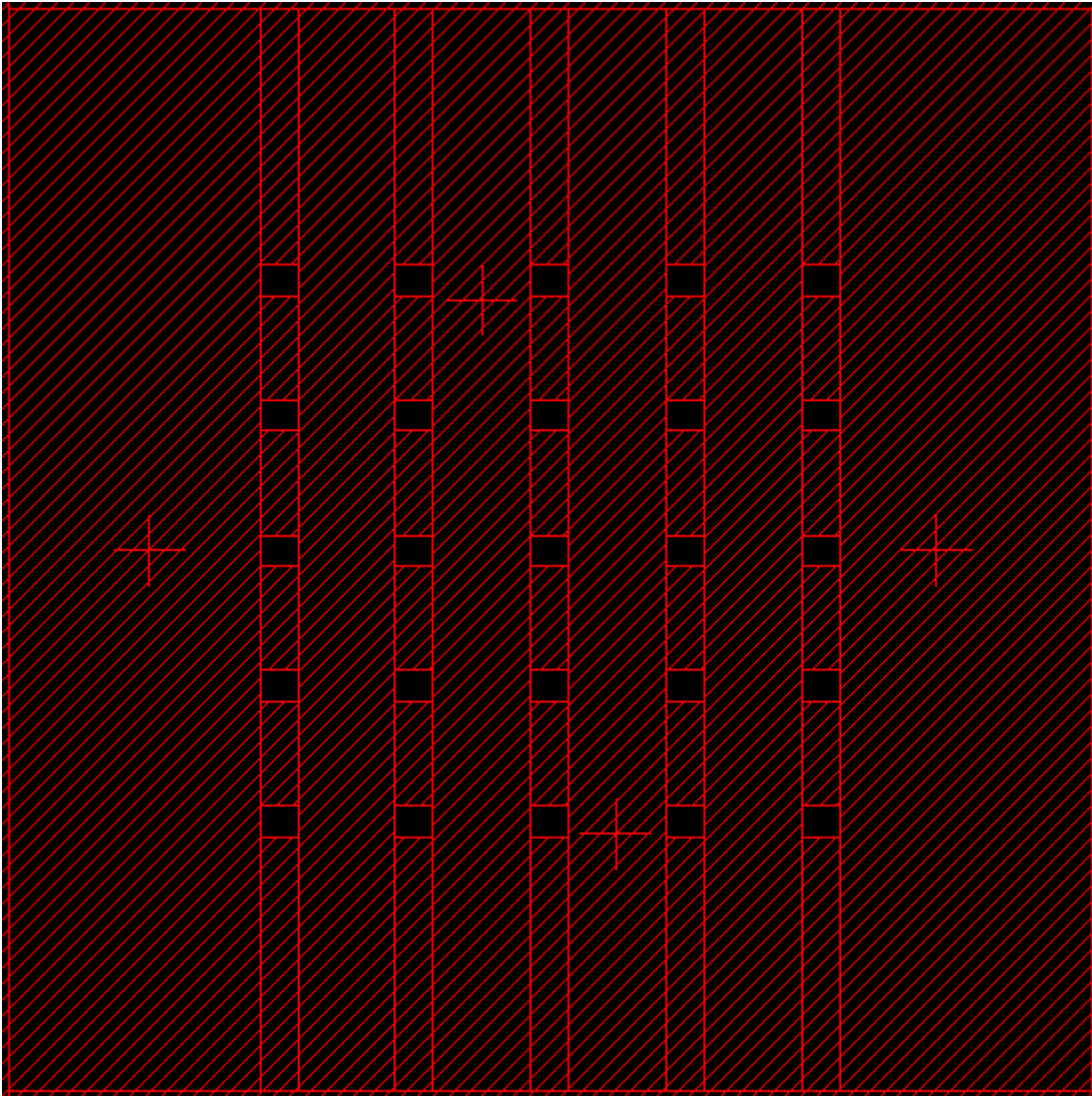
Fig. A.5a . Layer 1 of mask (single die)
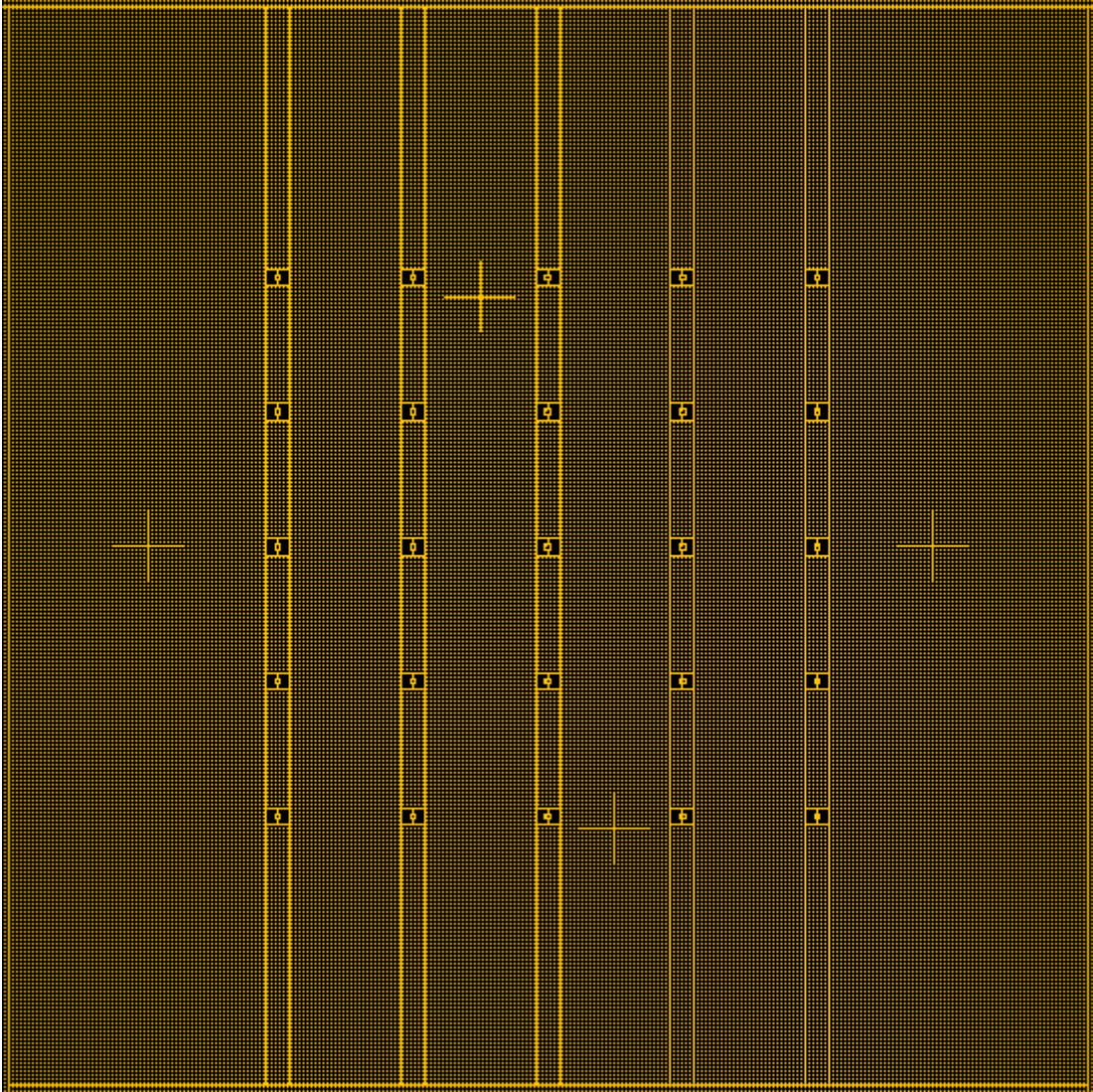
Fig. A.5b. Layer 2 of mask (single die)
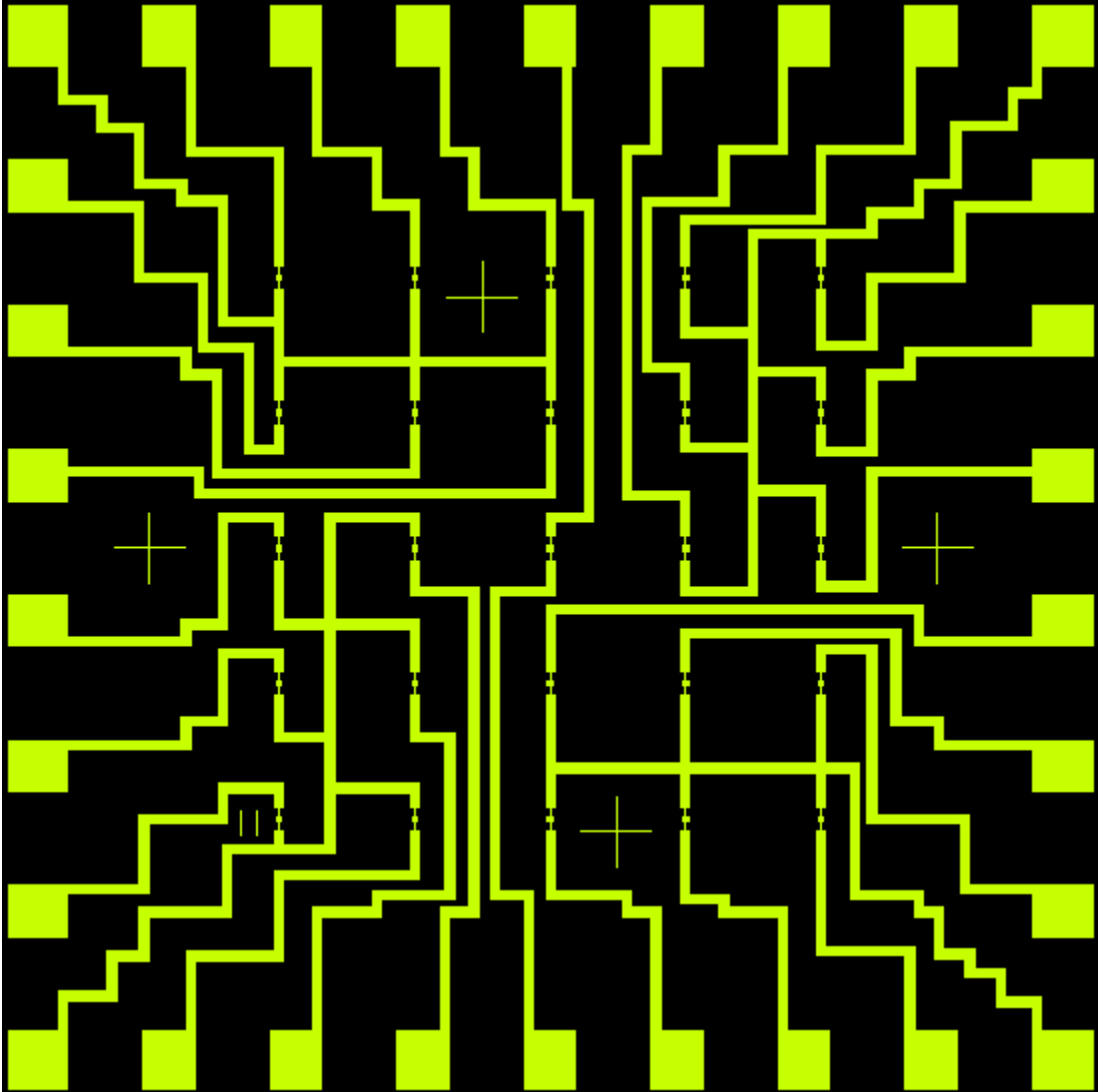
Fig. A.5c. Layer 3 of mask (single die)

A.6. Complete design of mask including alignment marks
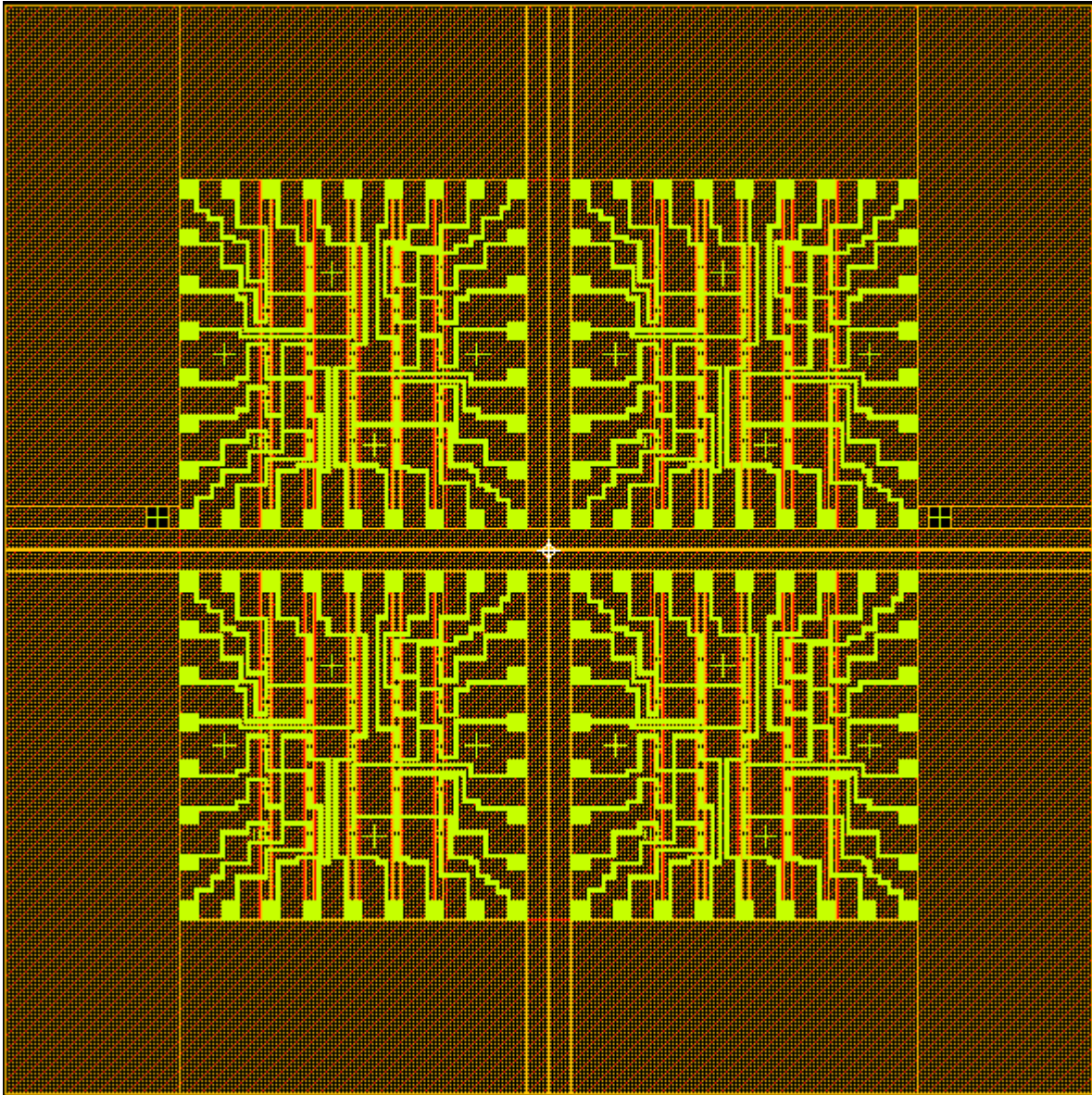
Fig. A.6. Final mask showing all layers overlapped (Fig: Top view of the design of micromirrors: the design shows four dies with box alignment marks)

APPENDIX A (III)

A.7   Fabrication Steps of Silicon Nitride freestanding mirror-beam structures with Au deposition

Photolithography was used to fabricate the freestanding structures. Several steps involved in the fabrication process are summarized below.

Step 1: Low Stress silicon nitride LPCVD (200MPa) on front and back of wafer

Fig. A.7. Schematics to show SiN layers on front and back of Si wafer

Step 2: E-beam evaporation (CHA)
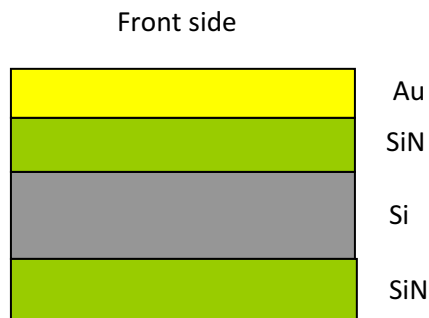
Fig. A.8. Schematics to show Au layer on SiN layers on front of Si wafer

Step 3: Contact Photolithography on back using **the layer 1 mask**

Such patterns are made on back

Trench
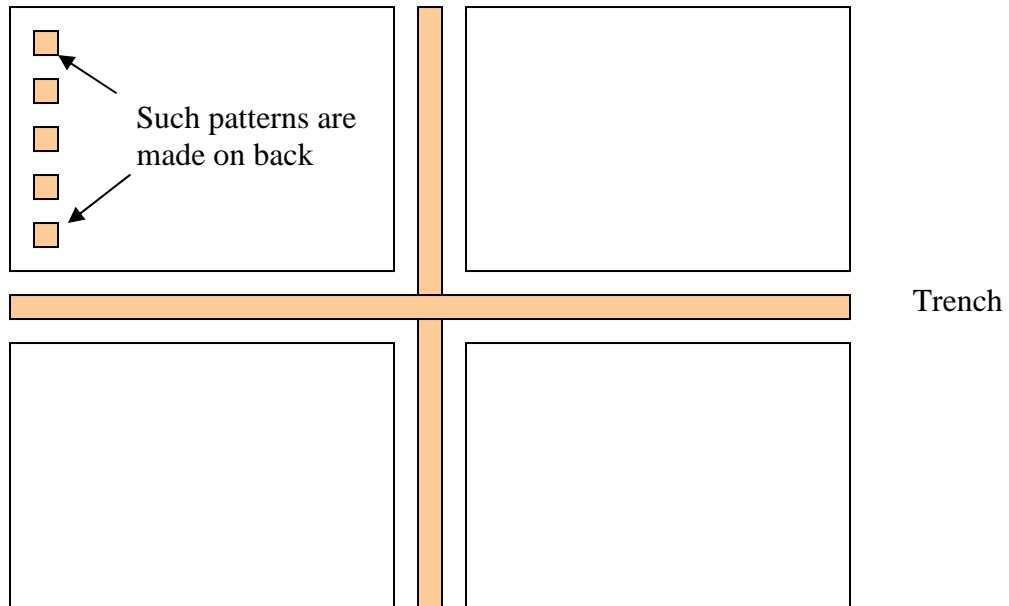
Fig A.9. Formation of pattern on SiN on the back of Si wafer by contact photolithography

Step 4: Silicon Nitride Lam 590 Etch

From back, etch the patterns ▢ and trench cross
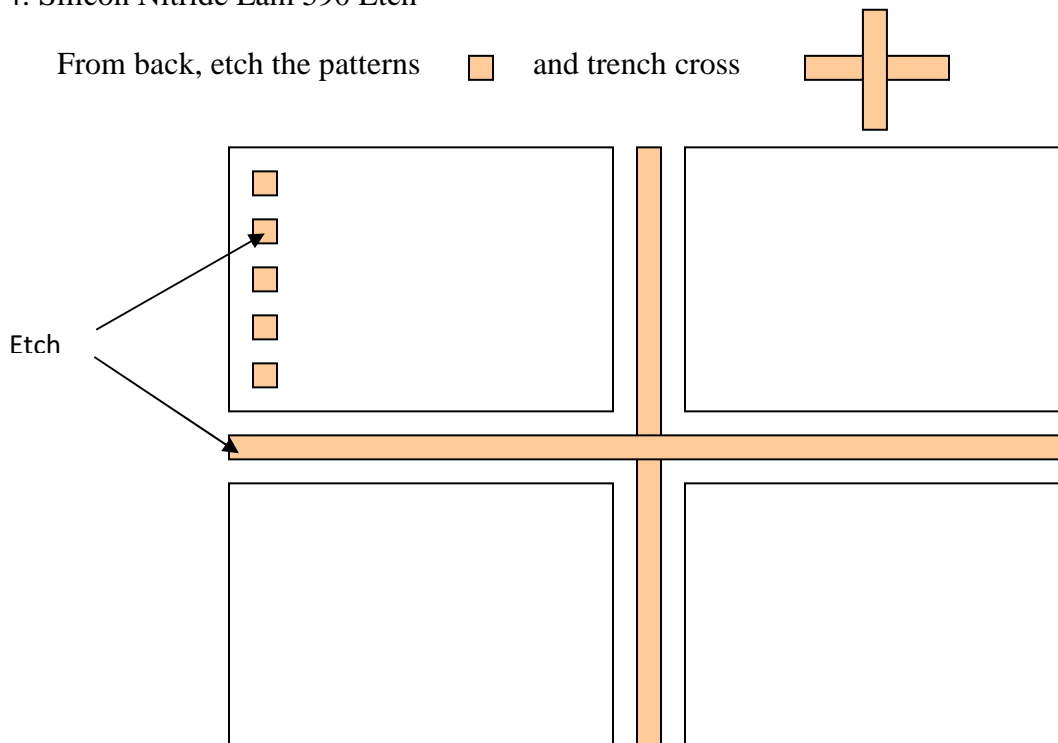
Etch

Fig. A.10. Patterns developed on SiN on the back after etching Silicon Nitride on the back

Step 5: Photoresist Stripping (Stripping left over photoresist in other areas than the pattern and trench)
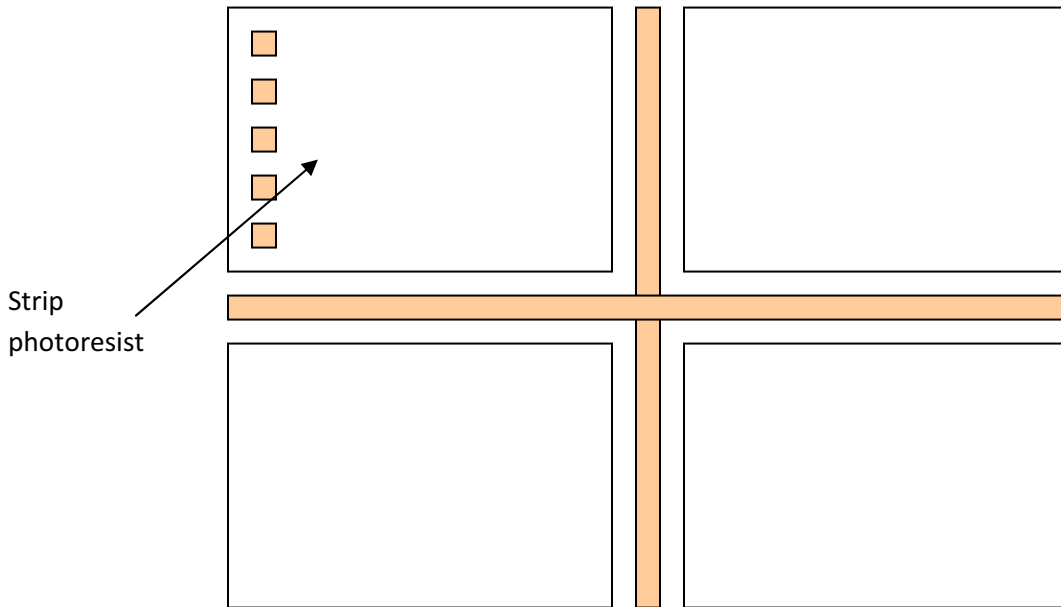
Fig. A.11. Stripping of photoresist on the top of Au in the areas except patterns and trench on the front of wafer

Step 6: KOH Silicon Etch II (from back)

 The design considers etching at 54.7 degree angle with 100 plane.
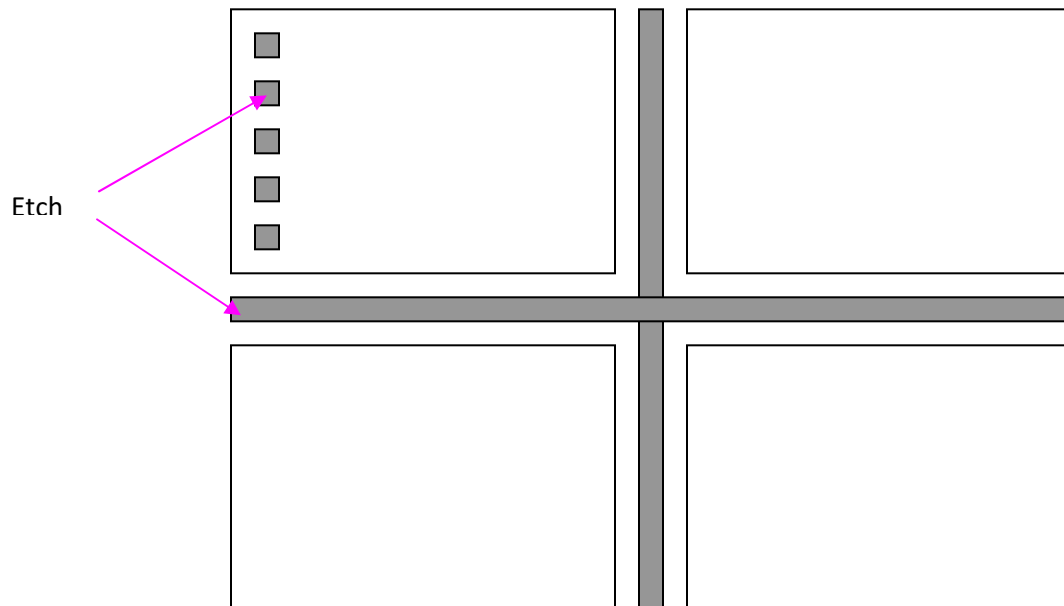
Fig. A.12. Etching of Si wafer from the back to open the square windows and dig trenches

Step 7: Contact Photolithography on front on Au surface using **mask Layer 2**

Such patterns are developed

SiN Layer
under Au
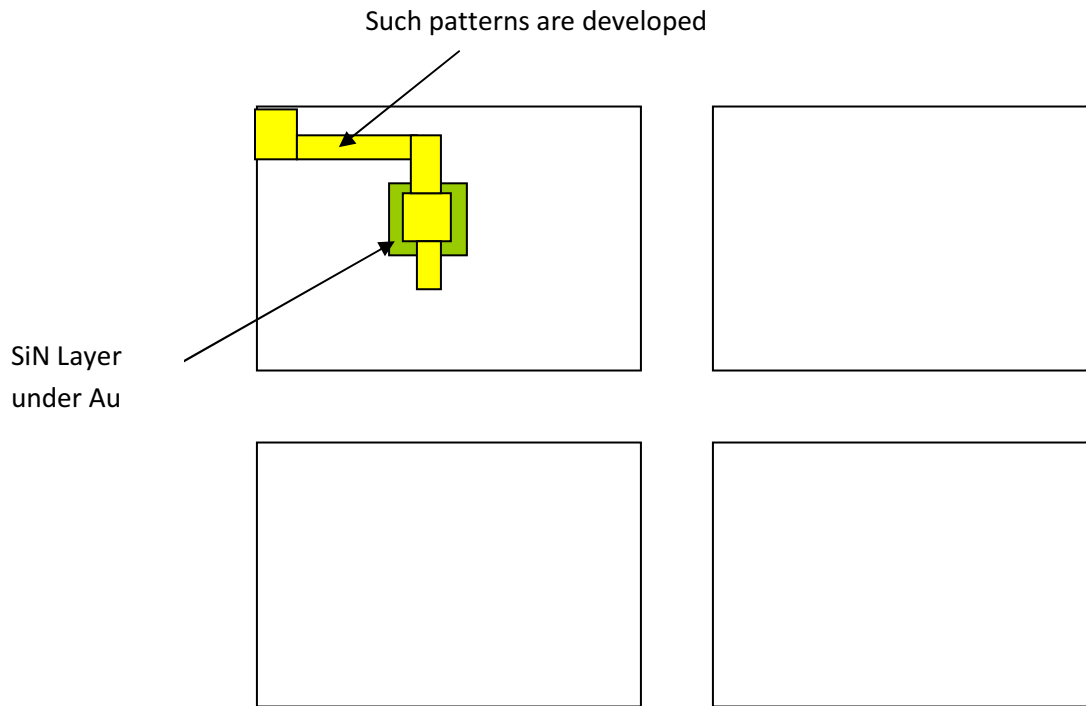
Fig.A.13. Pattern development on Au surface on the front by contact photolithography

Step 8: Gold Wet Etch (On Front)

 The pattern/ drawing of Layer 2 mask should **"remain".**

(Note: Gold patterns in this layer correspond to contact pads, wirings, and gold deposition on the surface of freestanding silicon nitride mirror-beam structures).
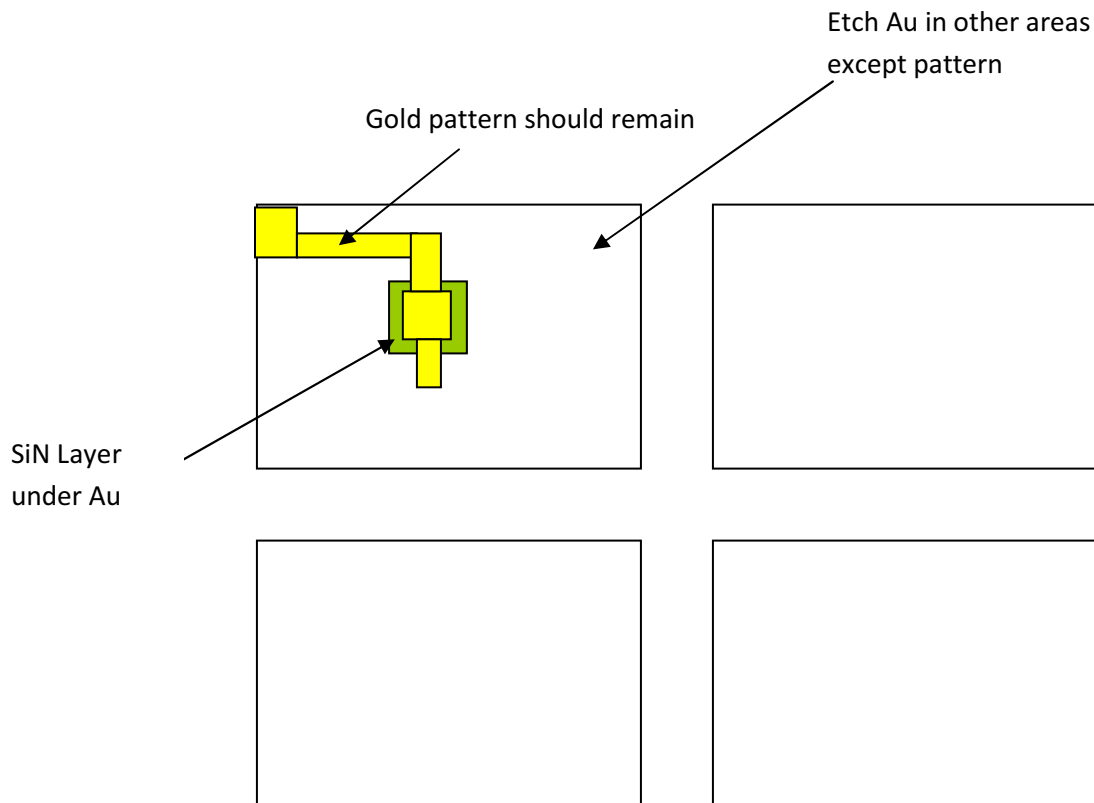
Fig. A.14. Etching Au except in the patterns on the front

Step 9: Silicon Nitride Etch on Front

(Note: Patterns of Layer 2 mask, same mask used in step 7, should remain so that we have freestanding silicon nitride mirror-beam structures with Au deposition on their front surface)

SiN Layer under Au should remain

Etch Silicon Nitride in other areas except pattern, same as Au pattern

Gold pattern should remain
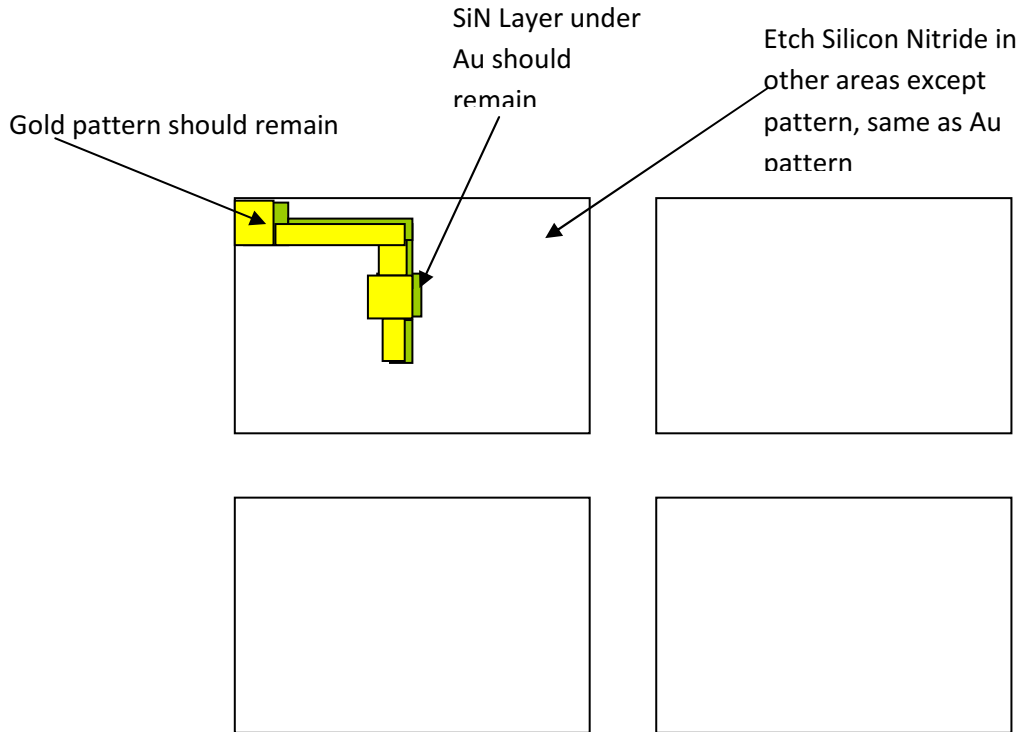
Fig. A.15. Etching SiN on the front except under Au patterns

Step 10: Photoresist Stripping: Photoresist remaining on the top of Au pattern is stripped out.

silicon nitride Layer under Au should remain

Photoresist stripped out on top of gold pattern
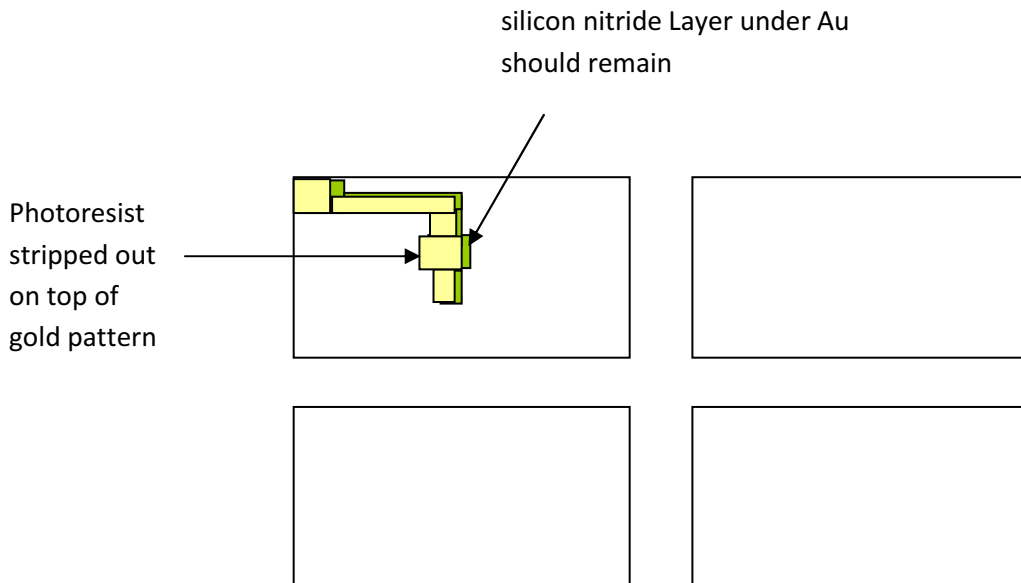
Fig. A.16. Stripping of photoresist on top of Au patterns on the front

REFERENCES

Abraham, D.W., M. M. Frank, and S. Guha, Applied Physics Letters **87** (25), 252502 (2005).

Aharoni, A., "Introduction to the theory of ferromagnetism" (Clarendon, Oxford, 1996).

Albrecht, J. D., and D. L. Smith, 2002, "Electron spin injection at a Schottky contact," Phys. Rev. B **66**, 113303.

Albrecht, J. D., and D. L. Smith, 2003, "Spin-polarized electron transport at ferromagnet/semiconductor Schottky contacts," Phys. Rev. B **68**, 035340.

Aldred, A.T., B.D.Rainford, and M.W. Stringfellow, Phys. Rev. Letters **24**, 897, 1970.

Alexandre, S. S., E. Anglada, J. M. Soler, and F. Yndurain, Phys. Rev. B **74**, 054405 (2006).

Andreev, A. F., *Zh. Eksp. Teor. Fiz.* **46**, 1823 (1964) [*Sov. Phys.ÐJ. Exp. Theor. Phys.* **19**, 1228 (1964)].

Aprili, M., M.L. Della Rocca, J. Kontos; Nano Scale devices and fundamentals edited by Rudolf Gross, Anatolie Sidorenko and Lenar Tagirov, NATO Science Series, Springer.

Aronov, A. G., 1976b, "Spin injection in metals and polarization of nuclei," Zh. Eksp. Teor. Fiz. Pisma Red. **24**, 37–39 [JETP Lett. 24, 32-34 (1976)].

Auth, N., Jakob, G., Block, T., and Felser, C., *Phys. Rev. B* **68**, 024403 (2003).

Baibich, M.N., J. M. Broto, A. Fert, F. Nguyen Van Dau, and F. Fetroff;"Giant Magnetoresistance of (001) Fe/ (001) Cr magnetic superlattices"; **61**, 2472 (1988).

Barnaś, J., and Fert, A., *Phys. Rev. Lett.* **80**, 1058 (1998).

Barnes, P.A., and Choi, A.Y., Appl. Phys. Lett. **33**, 651 (1978).

Bauer, G. E. W., Brataas, A., and van Wees, Y. T. B. J., *Appl. Phys. Lett.* **82**, 3928 (2003).

Bednorz, J. G., and K.A. Muller, Z. Phys B **64**, 189 (1986).

Beille, J. , and G Chouteau, J. Phys. F: Metal Phys., Vol **5**, 1975.

Berger, L., "Emission of spin waves by a magnetic multilayer traversed by current", Phy. Rev. B, Vol **54**, No. 13, P 9353- 9358; (1996).

Bergeret, F. S., A. F. Volkov, K. B. Efetov, " Odd Triplet Superconductivity and Related Phenomena in Superconductor-Ferromagnet Structures", arXiv:cond-mat/0506047v2 [cond-mat.super-con] 14 Jul 2005.

Bergeret, Vokov, Efetov

Berko, S., *Positron Solid State Physics*, edited by Brandt, W., and Dupasquier, A., North-Holland, pp. 64-145 (1983).

Bhosle, V., A. Tiwari, and J. Narayan, Journal of Applied Physics **100** (3), 033713 (2006).

Binasch, G., P., Grunberg, F. Saurenbach, and W. Zinn, "Enhanced magnetoresistancein layered magnetic structures with antiferromagnetic interlayer exchange", Phy. Rev. B, **39**, 4828 (1989).

Blonde , G.E., and M. Tinkham, Physical Review B, Vol **27** Number 1, 1 Jan 1983

Blonder, G. E., Tinkham, M., and Klapwijk, T. M., *Phys. Rev. B* **25**, 4515 (1982).

Blügel, S., Phys. Rev. Lett. **68** (1992) 851.

Blügel, S., Europhys. Lett. **18**, 257 (1992).

Blügel, S., Phy. Rev. B, vol **51**, Number 3 (1995).

Borèn, B., Ark. Kemi, Mineral. Geol. **11A**, 1 (1933).

Burnell, G., University of Leeds (Taken from power point Presentation) http://www.iop.org/activity/groups/subject/mag/Workshop_resources/file_30871.pdf

Carbone, F., Ph.D. dissertation, de l'Université de Genève, 2007.

Carbone, F., M.Zangrando, A. Brinkman, A. Nicolaou, F. Bondino, E. Magnano, A.A. Nugroho, F. Parmihiani, Th. Jarlborg, and D. van der Marel, Physical Review B **73**, 085114 (2006).

Chalsani, P., S.K. Upadhyay, O. Ozatay, and R.A. Buhrman; Physical review B **75**, 094417 (2007).

Chen, G.F., Z. Li, D. Wu, G. Li, D. Wu, G. Li, W.Z.Hu, J. Dong, P. Zheng, J.L. Luo, N.L. wang, arXiv:cond- mat/0803.3790.

Chen, H., N. E. Brener, and J. Callaway, Phys. Rev. B **40**, 1443 (1989).

Chen, P. P., H. Makino, and T. Yao, Journal of Crystal Growth **269** (1), 66 (2004).

Chen, X.H, T.Wu, G, Wu, R.H. Liu, H. Chen, D.F. Fang, Nature 2008, 453,761.

Cheung, T. D., J.S. Kouvel, and J. W. garland, Phys. Rev. B **23**, 1245 (1981).

Choi Wai-shing and Jan G. Smits, Dynamic Behavior of ZnO on Si_3N_4 bimorphs, Ultrasonics Symposium, IEEE, 1992.

Chouteau, G. , Physica (Amsterdam) **84B**, 25 (1976).

Ciorga, M., Pioro-Ladriere, M., Zawadzki, P., Hawrylak, P., and Sachrajda, A. S., *Appl.*

Clifford, E., M. Venkatesan, and J. M. D. Coey, J. Magn. Magn. Mater. **272–276**, 1614 (2004).

Coey, J. M. D., Current Opinion in Solid State and Materials Science **10** (2), 83 (2006).

Coey, J. M. D., P. Stamenov, R. D. Gunning, M. Venkatesan, and k. Paul, New Journal of Physics **12** (2010).

Coey, J. M. D., M. Venkatesan and C. B. fitzgerald, nature materials VOL **4** FEBRUARY 2005.

Datta, S., and B. Das, , "Electronic analog of the electrooptic modulator," Appl. Phys. Lett. **56**, 665–667, 1990.

Daughton, J. M., Pohn A. V., Fayfield R. T. and Smith C. H., J. Phy. D: Appl. Phy **32** R 169-R177 (1999).

Daughton, J., Bade P., Jenson M and Rahmati M., IEEE Trans, Magn. **28,** 2448 (1992).

Daughton, J.M. *et.al.*, IEEE Trans. Magn. **30**, 4608 (1995).

de Jong, M. J. M., and Beenakker, C. W. J., *Phys. Rev. Lett.* **74**, 1657 (1995).

Delin, A. and Tosatti, E.; Physical Review B **68**, 144434 (2003).

Delin, A., Tosatti, E.; Surface Science 566–568 (2004) 262–267.

Dieny, B., Speriosu V., Metins S., Parkin S., Guerney B., Baumgart P. and Wilhoit D., J. Appl Phys. **69**, 4774 (1991).

Dietl,T, H. Ohno, F. Matsukura, J. Cibert, D. Ferrand, SCIENCE VOL **287** 11 FEBRUARY 2000

Dixit, A., C. Sudakar, J. S. Thakur, K. Padmanabhan, Sanjiv Kumar, R. Naik, V. M. Naik, G. Lawes, J. Appl. Phys. **105**, 053104 (2009).

Dixit, A., C. Sudakar, R. Naik, G. Lawes, J. S. Thakur, E. F. McCullen, G. W. Auner, and V. M. Naik, Applied Physics Letters **93** (14), 142103 (2008).

Dixit, A., P. Thapa, C. Sudakar, R. Naik, G. Lawes, and B. Nadgorny, Submitted to Semiconductor Science and Technology, 2011.

Duan X. M., and C. Stampfl, Phys. Rev. B **79**, 174202 (2009).

Engel, B. N., J. Akerman, B. Butcher, R. W. Dave, M. DeHerrera, M. Durlam, G. Grynkewich, J. Janesky, S. V. Pietambaram, N. D. Rizzo, J. M. Slaughter, K. Smith, J. J. Sun, and S. Tehrani, BA 4-Mb toggle MRAM based on a novel bit and switching method,[IEEE Trans. Magn., vol. **41**, no. 1, pp. 132–136, Jan. 2005.

Eriksson, O., Albers, R.C., and Boring, A.M., Phys. Rev. Lett. **66**, 1350 (1991).

Esaki, L., P. Stiles, and S. von Moln´ar, 1967, "Magnetointernal field emission in junctions of magnetic insulators," Phys. Rev. Lett. **19**, 852–854.

Eschrig, M., J. Kopu, J. C. Cuevas, and Gerd Sch o¨n, "Theory of Half-Metal/Superconductor Heterostructures", Phys. Rev. Lett. **90**, Number 13 (2003).

Faiz, M. M., Ph. D. dissertation 2009, Department of Physics, Wayne State University

Fan, D. L., F. Q. Zhu, R.C. Cammarata and C.L. Chien, "Controllable highspeed rotation of nanowires", Physical Review Letters **94**, 247108-1 to 247108-4 (2005).

Fasol, G., Phys. Bl. **52**, 101 -1996.

Feder, R., Polarized Electrons in Surface Physics, World Scientific, Singapore, (1985).

Fominov, Ya. V., A. F. Volkov, and K. B. Efetov, "Josephson effect due to the long-range odd-frequency triplet superconductivity in SFS junctions with Néel domain walls", Phys. Rev. B **75**, 104509 (2007).

Fritsche, L., J. Noffke, and H. Eckardt, J. Phys. F: Met. Phys, **17**, 943 (1987).

Fröhlich, H., and F. R. N. Nabarro, Proc. R. Soc. London Ser. A **175**, 382 (1940).

Fulde, P., and A. Ferrel, Phys. Rev. 135, A550 (1964).

Fulde, P., Adv. Phys. **22**, 667 (1973c).

Fulde, P., and Kettemann, S., Spin flip torsion balance, arXiv:cond-mat/9806370v1, (1998).

Fulde, P., and S. Kettemann, "spin flip totsion balance", Ann. Physik 7, P 214-218, (1998a).

Fulde, P., and S. Kettemann, Ann Phys. (Leipzig) **7**, 214 (1998b).

Fulde, P., and Stefan Kettemann, " Spin flip torsion balance", ArXiV: cond-mat/9806370V1 30 (Jun 1998d).

Gavaler, J. R., Appl. Phys. Lett 23, 480 (1973).

Giuliani, G. et al, "Angle measurement by injection detection in a laser diode", Opt. Eng. **40** (1) p95-99 (2001).

Goldman, A. I., D.N. Argyriou, B. Ouladdiaf, T. Chatterji, A. Kreyssig, S. Nandi, N. Ni, S. L. Bud'ko, P.C. Canfield, and R. J. McQueeney, arXiv:0807.1525v2.

Griffiths, D. J., *Introduction to quantum mechanics* (Prentice Hall, 1995).

Guo, J., Z. Zhu, W. Deng and S. Sheu, "Angle measurement using surface Plasmon-resonance heterodyne interferometry: a new method", Opt. Eng. **37** (11) 2998- 3001 (November 1998).

Guo, X., X. Chen, Z. Altounian, and J. O. Str̈om-Olsen, J. Appl. Phys. **73**, 6275 (1993).

Gupta, A., X. W. Li, and G. Xiao, J. Appl. Phys. **87**, 6073 (2000).

Hanssen, K. E. H. M., P.E. Mijnarends, L. P. L. M. Rabou, and K. H. J. Buschow, Positron-annihilation study of the half metallic ferromagnet NiMnSb: Experiment, *Phys. Rev.* B **42**, 1533 (1990).

Hao, X., Moodera, J. S., and Meservey, R., *Phys. Rev. B* **42**, 8235 (1990).

Hartman (Ed.), U., 2000, Magnetic Multilayers and Giant Magnetoresistance (Springer, Berlin).

Heikes, R. R., Phys. Rev. **99**, 446 (1955).

Hirota, E., H. Sakakima, and K. Inomata, 2002, Giant Magneto-Resistance Devices (Springer, Berlin).

Hook, J.R., and H.E. Hall, second edition 1991, John Wiley & Sons.

Hosomi, M., H. Yamagishi, T. Yamamoto, K. Bessho, Y. Higo, K. Yamane, H. Yamada, M. Shoji, H. Hachino, C. Fukumoto,H. Nagao, and H. Kano, BA novel nonvolatile memory with spin torque transfer magnetization switching: Spin-RAM,[in Int. Electron Devices Meeting Tech. Digest, ashington, DC, 2005, pp. 459–462.

Huang, Q., Y. Qiu, Wei Bao, M.A. Green, J.W. Lynn, Y.C. Gasparovic, T.Wu, G. Wu, and X.H. Chen, PRL **101**, 257003 (2008).

Huger, E., and K. Osuch, Europhys. Lett. **63**, 90 (2003).

Iliev, M. N., A. P. Litvinchuk, H. G. Lee, C. W. Chu, A. Barry, J. M. D. Coey, Phys. Rev. B, **60**, 33 (1999).

Ishikawa, Y., K. Tajima, D. Bloch, and M. Roth, Solid State Commun. **19**, 525 (1976).

Ishikawa, Y., T. Komatsubara, and D. Bloch, Physica (Utr.) **86-88B**, 401 (1977).

Jeong, T., and W. E. Pickett, arXiv:cond-mat/0403442v1 [cond-mat.str-el] 17 Mar 2004.

Ji, Y., G. J. Strijkers, F. Y. Yang, and C. L. Chien, Phy. Rev. B, **64**, 224425 (2001).

Ji, Y., G. J. Strijkers, F. Y. Yang, C. L. Chien, J. M. Byers, A. Anguelouch, Gang Xiao, and A. Gupta, Phys. Rev. Lett. **86**, 5585 (2001).

Johnson, M. *et al*., "Bipolar spin switch", Science, Vol **260**, P320, (1993).

Johnson, M., *Phys. Rev. Lett.* **70**, 2142 (1993).

Johnson, M., *Science* **260**, 320 (1993).

Johnson, P. D., in *Core Level Spectroscopies for Magnetic Phenomena*, edited by P. S. Bagus et al., NATO Advanced Study Institute, Series B: Physics, Vol. 345, Plenum Press, New York, (1995).

Johnson, P.D., Spin polarized photoemission, *Rep. Prog. Phys*. **60**, 1217 (1997).

Journ. Appl. Phys. **102**, 066101 (2007).

Julliere, M., *Phys. Lett.* **54A**, 225 (1975).

Kahal, L., and M. Ferhat, J. Appl. Phys. **107**, 043910 (2010).

Kaiser, C., S.v an Dijken, S.-H. Yang, H. Yang, and S. S. P. Parkin, Phys. Rev. Lett. **94**, 247203 (2005).

Kamihara, Y., T. Watanabe, M. Horano, H. Hosono, J. Am. Chem. Soc. 2008, 130, 3296.

Kant, C. H., Kurnosikov, O., Filip, A. T., LeClair, P., Swagten, H. J. M., and de Jong, W. J. M., *Phys. Rev. B* **66**, 212403 (2002).

Kant, C. H., *Probing spin polarization: point contacts and tunnel junctions*, Ph.D. Dissertation, Eindhoven University of Technology, the Netherlands (2005).

Kasuya, T., and A. Yanase, 1968, "Anomalous transport phenomena in Eu-chalcogenide alloys," Rev. Mod. Phys. **40**, 684–696.

Katine, J. A. *et al.*, "Current induced realignment of magnetic domains in nanostructured Cu/Co multilayer pillars", Vol **76**, No. 3, P. 954, (2000).

Katsui, A., J. Appl. Phys. **47**, 4663 (1976); Shen, J. X., R. D. Kirby,band D. J. Sellmyer, *ibid.* **69**, 5984 (1991); Jaswal, S. S., J. X. Shen, R. D. Kirby, and D. J. Sellmyer, *ibid.* **75**, 6346 (1994); K¨ohler, J., and J. K¨ubler, J. Phys. Condens.Matter **8**, 8681 1996); R¨udiger, U., *et al.*, IEEE Trans. Magn. **33**, 3241 (1997); Bandaru, P. R., and T. D. Sands, J. Appl. Phys. **86**, 1596 (1999).

Kawahara, T., R. Takemura, K. Miura, J. Hayakawa, S. Ikeda, Y. M. Lee, R. Sasaki, Y. Goto, Y. Ito, T. Meguro, F. Matsukura, H. Takahashi, H. Matsuoka, and H. Ohno, B2 Mb spin-transfer torque RAM (SPRAM) with bit-by-bit bidirectional current write and parallelizing-direction current read,[in Proc. IEEE Int. Solid-State Circuits Conf., 2007, pp. 480–481.

Keizer , R.S., et al., Nature **43**, 825 (2006)

Khaire, T.S., arXiv:0912.0205.

Khaire, T.S., et. al., Phys. Rev. B **79**, 094523 (2009)).

Khaire, Trupti S., W.P. Pratt, Jr. Norman O. Birge, arXiv:0901.132v1, 2009.

Khalid, M., M. Ziese, A. Setzer, P. Esquinazi, M. Lorenz, H. Hochmuth, M. Grundmann, D. Spemann, T. Butz, G. Brauer, W. Anwand, G. Fischer, W. A. Adeagbo, W. Hergert, and A. Ernst, Physical Review B **80**, 035331(2009)

Kharel, P., P. Thapa, P. Lukashev, R. F. Sabirianov, E. Y. Tsymbal, D. J. Sellmyer, and B. Nadgorny, PHYSICAL REVIEW B **83**, 024415 (2011).

Kharel, P., R. Skomski, R. D. Kirby, and D. J. Sellmyer, J. Appl. Phys. **107**, 09E303 (2010).

Kim, D., J. Hong, Young Ran Park, and Kwang Joo Kim, Journal of Physics: Condensed Matter **21** (2009).

Kinsey, R. J., P. A. Anderson, Z. Liu, S. Ringer, S. M. Durbin, Current Applied Physics **6**, 579 (2006).

Kiselec, S. I. *et al*., "Microwave Oscillations of a nanomagnet driven by a spin polarized current", Nature **425**, 380 (2003).

Kishi, T., H. Yoda, T. Kai, T. Nagase, E. Kitagawa, M. Yoshikawa, K. Nishiyama, T. Daibou, M. Nagamine, M. Amano, S. Takahashi, M. Nakayama, N. Shimomura, H. Aikawa, S. Ikegawa, S. Yuasa, K. Yakushiji, H. Kubota, A. Fukushima, M. Oogane, T. Miyazaki, and K. Ando, BLower-current and fast switching of a perpendicular TMR for high speed and high density spin-transfer-torque MRAM,[in Int. Electron Devices Meeting Tech. Digest, 2008, pp. 1–4.

Kontos, et al., Phys. Rev. Lett., **86**, 304 (2001)

Korotkov, A. N., and Safarov, V. I., *Phys. Rev. B* **59**, 89 (1999).

Kovalev, A., , Gerrit E. W. Bauer and Brataas, Current-driven ferromagnetic resonance, mechanical torques, and rotary motion in magnetic nanostructures, Physical Review B, **75**, 014430 (2007).

Kumar, V., and Kawazoe, Y., Physical Review B **77**, 205418 (2008).

Larkin, A., and Y. Ovchinnikov, Sov. Phys. JETP 20, 762 (1965)

Lederer, P., and D. L. Mills, Phys. Rev. **165**, 837 (1968)

Li, X., "Measurements of ultrasmall current-induced rotation and magnetic properties of micro/ nano wires", Wayne State University, Master's thesis (2005).

Li, Z. *et al*., "Magnetization dynamics with a spin transfer torque", Phys. Rev. B **68**, 024404 2003).

Lim, J., Jeong, J.K., Ahn, K.H., Kim, H.J., Hwang, C.S., Park, D.Y., and Lee, D.S., J. Mater. Res., Vol. **19**, No. 2, Feb 2004.

Lin , C. J., S. H. Kang, Y. J. Wang, K. Lee, X. Zhu, W. C. Chen, X. Li, W. N. Hsu, Y. C. Kao, M. T. Liu, W. C. Chen, Y. C. Lin, M. Nowak, N. Yu, and L. Tran, B45 nm low power CMOS logic compatible embedded STT MRAM utilizing a reverse-connection 1 T/1 MTJ cell,[in Int. Electron Devices Meeting Tech. Digest, 2009, p. 279.

Litran, R., B. sanpedro, T.c. Rojas, M. Multigner, j.C. Samchez-lopez, P. Crespo, C. Lopez-Cartes, M.A. Garcia, A. Hernando, A. Fernandez; Phys. Rev. B **73**, 054404 (2006).

Loram, J. W., and K.A. Mirza, J. Phys. F 15, 2213 (1985).

Lu, Y. *et al* 1996 *Phys. Rev.* B **54** R8357

Madhu, C., A. Sundaresan, C.N.R. Rao, Phys. Rev. B **77** (2008), 201306(R).

Maeda, H., Y. Tanaka, M. Fukutumi, and T. Asano, "A New High-Tc Oxide Superconductor without a Rare Earth Element". Jpn. J. Appl. Phys. **27** (2), (1988).

Martinek, J., Barnas, J., Maekawa, S., Schoeller, H., and Schön, G., *Phys. Rev. B* **66**, 014402 (2002).

Mazin, I. I., Phys. Rev. Lett. **83**, 1427 (1999).

Mazin, I. I., Golubov, A.A., and Nadgorny, B.E., J. Appl. Phys. **89**, 7576 (2001).

Mazin, I. I., Physical Review Letters, Vol **83**, No. 7, 1999.

Meissner, W., and H. Franz, Messungen mit Hilfe von flüssigen Helium. VIII. Supraleitfähigkeit von Niobium, Physikalisch-Technische Reichsanstalt, *Mitteilung*: 558-559, 1930.

Meservey, R., and P. M. Tedrow, Phys. Rep. **238**, 173 (1994).

Meservey, R., and P.M. Tedrow, Spin-polarized electron tunneling. *Phys. Rep*. **238**, 173 (1994).

Meservey, R., Tedrow, P. M., and Fulde, P., Phys. Rev. Lett. **25**, 1270 (1970).

Minhang Bao, "Analysis and design principles of MEMS devices", ELSEVIER B.V. The Netherlands, 2005.

Miyazaki, T., and N. Tezuka, 1995, "Giant magnetic tunneling effect in Fe/Al2O3/Fe junction," J. Mag. Magn. Mater. 139, L231–L234.

Miyoshi, Y., Y. Bugoslavsky, and L. F. Cohen, PHYSICAL REVIEW B **72**, 012502 (2005)

Mohanty, P., G. Zolfagharkhani, S. Kettemann and P. Fulde, "Spin mechanical device for detection and control of spin current by nanomechanical torque", Physical Review B **70** 195301 (2004).

Moodera, J. S., Hao, X., Gibson, G. A., and Meservey, R., *Phys. Rev. Lett.* **61**, 637 (1988).

Moodera, J. S., L. R. Kinder, T. M. Wong, and R. Meservey, 1995, "Large magnetoresistance at room temperature in ferromagnetic thin film tunnel junctions," Phys. Rev. Lett. **74**, 3273–3276.

Moodera, J. S., Meservey, R., and Hao, X., *Phys. Rev. Lett.* **70**, 853 (1993).

Moore, G.E., Electronics **38**, 8 (1965).

Moriya, T., and A. Kawabata, J. Phys. Soc. Jpn. **34**, 639 (1973).

Moruzzi, V. L. , and P.M. Marcus, Physical Review B, **39**, 1989.

Mott, N. F., "The electrical conductivity of transition metals," Proc. R. Soc. London, Ser. A 153, 699–717, 1936a.

Mott, N. F., "The resistance and thermoelectric properties of the transition metals," Proc. R. Soc. London, Ser. A 156, 368–382, 1936b.

Nadgorny, B. , R. J. Soulen, Jr., M. S. Osofsky, and I. I. Mazin, G. Laprade, R. J. M. van de Veerdonk, A. A. Smits, S. F. Cheng, E. F. Skelton, and S. B. Qadri; *Phys. Rev. B (Rapid Comm.),* **61***, R3788 (2000).*

Nadgorny, B. , I. I. Mazin, M. Osofsky, R. J. Soulen, Jr., P. Broussard, R. M. Stroud, D. J. Singh, V. G. Harris, A. Arsenov, and Ya. Mukovskii, Phys. Rev. B, **63**, 184433 (2001).

Nadgorny, B., J. Phys.: Condens. Matter **19** 315209 (2007).

Nadgorny, B., R. J. Soulen, Jr., M. S. Osofsky, I. I. Mazin, G. Laprade, R. J. M. van de Veerdonk, A. A. Smits, S. F. Cheng, E. F. Skelton, and S. B. Qadri, Phys. Rev. B **61**, R3788 (2000).

Nadgorny, B., Handbook of spin transport and magnetism, 531-563 (2011).

Ney, A., R. Rajaram, E. Arenholz, Jr J. S. Harris, M. Samant, R. F. C. Farrow, and S. S. P. Parkin, Journal of Magnetism and Magnetic Materials **300** (1), 7 (2006).

Ni, N. et al., Phys. Rev. B **78**, 014507 (2008).

Norman, M. R.,   Physics 1, **21** (2008).

Nunomura, N, H. Hori, T. Teranishi, M. Miyake, S. Yamada, Phys. Letters A ,**249**, 424- 530 (1998).

Onnes, H. K., Commun. Phys. Lab. Univ. Leiden **12**, 120 (1911).

Ono, K., Shimada, H., Kobayashi, S., and Outuka, Y., *J. Phys. Soc. Jpn.* **65**, 3449 (1996).

Osipov, V. V., and A. M. Bratkovsky, 2003, "Efficient nonlinear room-temperature spin tunneling-emission in ferromagnet-semiconductor heterostructures with extended penetration depth," eprint cond-mat/0307030.

Oswald, A., R. Zeller, and P.H. Dederichs, Phy. Rev. Letters, **56**, 1986.

Panguluri, R. P., P. Kharel, C. Sudakar, R. Naik, R. Suryanarayanan, V. M. Naik, A. G. Petukhov, B. Nadgorny, and G. Lawes, Physical Review B **79** (16), 165208 (2009).

Panguluri, R. P., Ku, K. C., Wojtowicz, T., Liu, X., Furdyna, J.K., Lyanda-geller, Y.B.,Samarth, N., and Nadgorny, B., Phys. Rev. B **72**, 054510 (2005).

Panguluri, Raghava P., Pushkal Thapa, X. Zhou, Athena S. Sefat , Rongying Jin, Michael A. McGuire, Brian C. Sales, David Mandrus, I.I. Mazin, and B. Nadgorny, Unpublished data.

Park, J-H *et al* 1998 *Nature* **392** 794.

Parkin, S. S. P., 2002, "Applications of Magnetic Nanostructures," in Spin Dependent Transport in Magnetic Nanostructures, edited by S. Maekawa and T. Shinjo (Taylor and Francis, New York), 237–271.

Parkin, S. S. P., K. P. Roche, M. G. Samant, P. M. Rice, R. B. Beyers, R. E. Scheuerlein, E. J. O'Sullivan, S. L. Brown, J. Bucchigano, D. W. Abraham, Y. Lu, M. Rooks, et al., 1999, "Exchange-biased magnetic tunnel junctions and application to nonvolatile magnetic random access memory," J. Appl. Phys. **85**, 5828–5833.

Parkin, S., More N. and Roche K., Phys. Rev. Lett. **64,** 2304 (1991).

Petukhov, A.G., Igor Zutic, Steven C. Erwin, Phys. Rev. Lett. **99**, 257202 (2007).

Phys. Lett. **80**, 2177 (2002).

Prins, M. W. J., H. van Kempen, H. van Leuken, R. A. de Groot, W. van Roy, and J. De Boeck, 1995, "Spindependent transport in metal/semiconductor tunnel junctions," J. Phys.: Condens. Matter **7**, 9447–9464.

Pufall, M. R., W. H. Rippard, and T. J. Silva, BMaterials dependence of the spin-momentum transfer efficiency and critical current in ferromagnetic metal/Cu multilayers,[Appl. Phys. Lett., vol. **83**, pp. 323–325, Jul. 14, 2003.

R¨udiger, U., and G. G¨untherodt, J. Appl. Phys. **88**, 4221 (2000).

Rabou, L. P. L. M., Ph.D. Thesis, University of Amsterdam (1983).

Rattikorn Yimnirun, Paul J. Moses, Robert E. Newnham & Richard J. Meyer, Jr., Electrostrictive Strain in Low-Permittivity Dielectrics, Journal of Electroceramics, **8**, 87-98, 2002.

Redinger, J., Blügel, S., Podloucky, R., Phys. Rev B, vol **51**, Number 19 (1995).

Remo, J. L., "Reduced-noise- displacement measurements with a correlated differential photodiode sensor", Applied Optice, **36**, No 22, P 5488 (1997).

Ren, Z.A., J.Yang, W.Lu, W. Yi, X.L. Shen, Z.C. Li, G.C. Che, X.L. Dong, L.L.Sun, F. Zhou, Z.X. Zhao, Europhys. Lett. 2008, **82** ,57 002.

Rotter, Marianne, Marcus Tegel, and Dirk Johrendt, PRL **101**, 107006 (2008).

Ryazanov, V. , et al., Phys. Rev. Lett. **86**, 2427 (2001)

S M Stishov, S M, A E Petrova, S khasanov, G Kh Panova, A A Shikov, J C Lashley, D Wu and T A Lograsso, J. phys.: Condens. Matter **20** (2008).

Santos, T. S., and Moodera, J. S., *Phys. Rev. B* **69**, 241203 (2004).

Sasaki, M., Mai Osada, Noriaki Sugimoto, Shinji Inagaki, Yoshiaki Fukushima, Atsushi Fukuoka, Masaru Ichikawa, Microporous and Mesoporous Materials **21** (1998) 597-606.

Sasaki, T., Saki Sonoda, Yoshiyuki Yamamoto, Ken-ichi Suga, Saburo Shimizu, Kouichi Kindo, Hidenobu Hori, JOURNAL OF APPLIED PHYSICS VOLUME **91**, NUMBER 10 15 MAY 2002

Sefat, Athena S., Rongying Jin, Michael A. McGuire, Brian C. Sales, David J. Singh, and David Mandrus, Phys. Rev Lett. **101**, 117004 (2008).

Servagent, N., F. Gouaux, and T. Bosch, "Measurements of displacement using the self mixing interference in a laser diode", J. Opt. **29**, 168-173 (1998).

Shinoda , D., and S. Asanabe, J. Phys. Soc. Jpn. **21**, 555 (1966).

Shinohara, T., and T. Sato, Phy. Rev. Letters, **91**, 2003.R

Siegel, R.W., Ann. Rev. Mater. Sci. 10: 393-425 (1980).

Sigalas, M. M., and D. A. Papaconstantopoulos, Phys. Rev. B **50**, 7255 (1994).

Similar to SrRuO3, e.g., Nadgorny, B. *et al.*, Appl. Phys. Lett. **82**, 427 (2003).

Singh, D. J., and M. H. Du, Phys. Re. Lett. **100**. 237003 (2008)

Slonczewski, J. C., BCurrent-driven excitation of magnetic multilayers,[J. Magn. Magn. Mater., vol. 159, pp. L1–L7, Jun. 1996.

Slonczewski, J.C., "Current driven excitation of magnetic multilayers", J. Magn, Magn. Mater, Vol **159**, issue 1-2, P L1-L7, (2000).

Smogunov, A., Dal corso, A., Delin, A., Weht, R., and Tosatti, E.; nature nanotechnology Vol **3** January 2008.

Song, C., K. W. Geng, F. Zeng, X. B. Wang, Y. X. Shen, F. Pan, Y. N. Xie, T. Liu, H. T. Zhou, and Z. Fan, Physical Review B **73** (2), 024405 (2006).Song et al., 2006]

Soulen Jr, R. J.; Byers, J. M.; Osofsky, M. S. ; Nadgorny, B. Ambrose, T.;   Cheng, S. F.; Broussard, P. R. ;   Tanaka, C. T.; Nowak, J.; J. S. Moodera, J. S. ; Barry, A. ; J. M. D. Coey, J. M. D.; SCIENCE VOL **282** 2 OCTOBER 1998.

Stewart, D. A., stewart@cnf.cornell.edu, Nov 10, 2006.

Strijkers, G. J., Ji, Y., Yang, F. Y., Chien, C. L., and Byers, J. M., *Phys. Rev. B* **63**, 104510 (2001).

Su Ji, Tian-Bing Xu, Shujun Zhang, Thomas R. Shrout, and Qiming Zhang, A Hybrid Actuation System Demonstrating Significantly Enhanced Electromechanical Performance, Smart Structures and Materials 2004: Electroactive Polymer Actuators and Devices (EAPAD). Edited by Bar-Cohen, Yoseph. Proceedings of the SPIE, Volume 5385, pp. 461-467 (2004).

Sun, J Z *et al* 1997 *Appl. Phys. Lett.* **70** 1769–71

Suzuki, T., Nakamura, H., Sasaki, O., and Greivenkamp, J., "Small rotation-angle measurement using an imaging method", Opt. Eng. **40**(3) 426-432 (March 2001).

Taillefer, L., G.G. Lonzarich, and P. Strange, J. Magn. Magn. Mater. 54-57, 957 (1986).

Takahashi, H., K. Igawa, K. Arii, Y. Kamihara, M. Hirano, and H. Hosono, Nature **453**, 376 (2008).

Tanaka, Y. , Y. Asano, A. A. Golubov, and S. Kashiwaya, "Anomalous features of the proximity effect in triplet superconductors", Phys.Rev. B **72**, 140503(R) (2005).

Tedrow, P. M. and Meservey, Phy. Rev. Lett. Vol **26**, No.4 (1971).

Tedrow, P. M. and Meservey, R., Phy. Rev. B, Vol **7**, No.1, (1973).

Tedrow, P.M., and R. Meservey, "Spin dependent Tunneling into Ferromagnetic Nickel", Physical Review Letter, **26**, 192 (1971).

Tehrani, S., B. Engel, J. M. Slaughter, E. Chen, M. De- Herrera, M. Durlam, P. Naji, R. Whig, J. Janesky, and J. Calder, 2000, "Recent developments in Magnetic Tunnel Junction MRAM," IEEE Trans. Magn. **36**, 2752–2757.

Thapa, Pushkal; Ivan Avrutsky, Raghava Panguluri, Boris Nadgorny, "Development of low power large torsion angle bimorph electro-thermal actuators", Sensor Letter, in press 2011.

Tomash, McMillan & Anderson PRL **16**, 85 (1966)

Tsymbal, E. Y., K. D. Belashchenko, J. Velev, S. S. Jaswal, M. van Schilfgaarde, I. I. Oleynik, and D. A. Stewart, Prog. Mater. Science **52**, 401 (2007).

Uhlenbeck, G.E., and S. Goudsmit, naturwissenschaften , **13**, 953 (1925).

Upadhyay, S. K., Palanisami, A., Louie, R. N., and Buhrman, R. A., *Phys. Rev. Lett.* **81**, 3247 (1998).

van der Marel, D., A. Damascelli, K. Schulte, and A.A. Menovsky, Physica B **244**, 138 (1998).

van Son, P. C., H. van Kempen, and P. Wyder, Phys. Rev. Lett. **58**, 2271 (1987); G. Schmidt *et al.*, Phys. Rev. B **62**, R4790 (2000).

Veerdonk, R. J. M., J. S. Moodera, andW. J. M. de Jonge, *Conference Digest of the 15th International Colloquium on Magnetic Films and Surfaces*, Queensland, Australia, Aug. 1997.

Velev, J. P., P. A. Dowben, E. Y. Tsymbal, S. J. Jenkins, and A. N. Caruso, Surf. Sci. Rep. **63**, 400 (2008).

Wang, X. F., T Wu, G, Wu, R H Liu, H. Chen, Y L Xie and X H Chen, New Journal of Physics **11** (2009) 045003.

Wegrowe, J. E. *et al.*, "Spin Polarized current induced magnetization switch: Is the modulus of magnetic layer conserved?", J. Appl. Phys. **91**, Vol 91 (10), P6806, 2002.

Weidinger, A., Ch. Niedermayer, A. Golnik, R. Simon, E. Recknagel, J. I. Budnick, B. Chamberland and C. Baines Phys. Rev. Lett. **62** 102 (1989).

Wen, H. H., G. Mu, L.Fang, h. Yang, X. Y. Zhu, Europhys. Lett. 2008, **82**, 17 009.

Wen, Hai-Hu; Adv. Mater. **20** 3764-3769 (2008).

Wernick, J H, Wertheim G K and Sherwood R C 1972 Mater. Res. Bull. **7** 1431

Wernick, J. H., G. K. Wertheim, and R. C. Sherwood, Mat. Res. Bull. **7**, 1431 (1971).

Wexler, G., Proc. Phys. Soc. London **89**, 927 (1966).

White, W. B., and V. G. Keramidas, Spectrochim. Acta, Part A **28**, 501 (1972).

Williams, H. J., J. H. Wernick, R.C. Sherwood, and G. K. Wertheim, J. Appl. Phys. **37**, 1256 (1966).

Wolf S.A., D.D. Awschalom, R.A. Buhrman, J.M.Daughton, S. Von Molnar, M.L.Roukes, A.Y. Chtchelkanova, D.M. Tregor, "Spintronics: A spin based electronics vision for future" 16 November 2001 vol **294** Science.

Wolf S.A., Lu J., Stan M.R., Chen E., Treger D.M., "The promise of nanomagnetics and spintronics for future logic and universal memory", Proceedings of the IEEE, Vol **98**, No. 12, December 2010.

Woods, G. T., Soulen, R. J. Jr., Mazin, I. I., Nadgorny, B., Osofsky, M. S., Sanders, J.,Srikanth, H., and Egelhoff, W. H., *Phys. Rev. B* **70**, 54416 (2004).

Worlege, D C and Geballe T H 2000 *Appl. Phys. Lett.* **76** 900

Wu, M.K., J. R. Ashburn, and C.J. Torng, Phys. Rev. Lett. **58** (1987).

Wu, R. and Freeman, A.J. Phys. Rev. B **45**, 7222 (1992).

XEI Software manual, version 1.7.6., Park System Corporation.

Xia, K., Kelly, P. J., Bauer, G. E. W., and Turek, I., *Phys. Rev. Lett.* **89**, 166603 (2002).

Xu, Y. Q., B. G. Liu, and D. G. Pettifor, Phys. Rev. B **66**, 184435 (2002).

Yamanouchi, M. *et al*., "current induced domain wall switching in a ferromagnetic semiconductor structor", Nature Vol 428 P539 (2004).

Yang, L.H., Park, J., Yu, B.D., and Jang, Y.R., Journal of the Korean Physical Society, Vol. **56**, No. 3, March 2010, pp. 791~795.

Yin, Y., M. Zech, T. L. Williams, X. F. Wang, G. Wu, X. H. Chen, and J.E. Hoffman, Phys. Rev. Lett. **102**, 097002 (2009).

You, C.-Y., and Bader, S. D., *J. Appl. Phys.* **87**, 5215 (2000).

Yu Hao and J.–M. Liu, "Current-induced mechanical torsion of a magnetic nanowire", JOURNAL OF APPLIED PHYSICS **102**, 066101 (2007).

Zener, C., Phys. Rev. **81**, 440 (1950a); Phys. Rev. **83**, 299 (1950b).

Zheng, J., and J. W. Davenport, Phys. Rev. B **69**, 144415 (2004).

Zhu, M.J., Bylander, D.M, and Kleinman, L., Phys. Rev. B **43**, 4007 (1991).

Zolfagharkhani Guiti, Alexei Gaidarzhy, Pascal Degiovanni, Stefan Kettemann, Peter Fulde and Pritiraj Mohanty, Nanomechanical detection of itinerant electron spin flip, nature 720 nanotechnology, Vol **3**, December 2008.

Zutic, I., J. Fabian, and S.Das Sarma, "Spintronics: Fundamentals and applications," Reviews of modern Physics, Vol **76**, April 2004.

Zvezdin, A. K., Mishchenko, A. S., and Khval'kovskii, A. V., *Zh. Tekh. Fiz.* **48**, 53 (2003); *Tech. Phys.* **4**, 431 (2003).

Zwart, P., Rabou, L. P. L. M., Langedijk, G. J., Jeavons, A. P., Kaan, A. P., Akkerman, H. J. M., and Mijnarends, P. E., *Positron Annihilation*, edited by Jain, P. C., Singru, R. M., and Gopinathan, K. P., World Scientific, Singapore, p. 297 (1985).

Zwierzycki, M., K. Xia, P. J. Kelly, G. E. W. Bauer, and I. Turek, 2003, "Spin injection through an Fe/InAs interface", Phys. Rev. B **67**, 092401.

ABSTRACT

THE STUDY OF WEAK FERROMAGNETISM BY ANDREEV REFLECTION SPIN SPECTROSCOPY AND DEVELOPMENT OF BIMORPH ELECTRO-THERMAL ACTUATORS

by

PUSHKAL THAPA

December 2011

Advisor: Prof. Boris Edward Nadgorny

Major: Physics (Condensed Matter)

Degree: Doctor of Philosophy

It is well accepted that spin polarization of materials has a major role in spintronics to improve the efficiency of spintronic devices. Point contact Andreev reflection (PCAR) spectroscopy, one of the popular and reliable techniques, was used to study the spin polarization of various materials, generally with low ferromagnetism, in order to understand the transport properties of spin polarized current and find the relation of spin polarization with other parameters such as saturation magnetization or the Curie temperature so that better spintronic materials can be identified and developed.

With brief review of the work in spintronics, Andreev reflection theory and spectroscopy, and data analyzing by modified BTK model, we have studied various weak ferromagnetic single cryatals such as MnSi and Co doped $BaFe_2As_2$, and various thin film materials such as $Pd_{1-x}Ni_x$,

MnBi, Pt, InN etc. By applying PCAR we have investigated how the spin polarization of itinerant ferromagnet Manganese monosilicide changes as it undergoes magnetic phase transition from helical to conical to induced ferromagnetic when external magnetic field is applied. When Nb contacts on MnSi were set up by e-beam lithography and sputtering on PMMA coated on polished MnSi surface, conductance curves with amplitude more than 2 and with conductance oscillations for the bias more than superconducting gap were obtained. The suppression of these oscillations at around 6.5KG indicated quite an interesting observation of the presence of triplet superconductivity in Nb/MnSi interface.

Because of magnetocrystalline anisotropy PdNi was chosen as another interesting system to study. The spin polarization, magnetization and the Curie temperature of $Pd_{1-x}Ni_x$ samples with different concentration of Ni were studied. The Curie temperature was found proportional to the saturation magnetization. But in case of spin polarization, the values were found proportional to the saturation magnetization if the samples were sputtered in the same batch otherwise there was some spread in spin polarization possibly due to its surface sensitivity.

PCAR spectroscopy of superconducting sample: Co doped iron pnictide ($BaFe_2As_2$) was performed. The conductance curves showed the presence of pseudogap at around 12 meV, and these could be suppressed by applying magnetic fields of ~14 KG perpendicular to the ab-plane.

The existence of magnetism in isolated Pt clusters is known, however, whether the Pt thin films are magnetic or not was unknown. For finding this, Pt thin films of various thicknesses were studied. PCAR spectroscopy revealed that all thin films of Pt show spin polarization, indicating that the films are magnetic. SQUID measurements also gave finite value of saturation magnetization of such films, and neutron scattering measurements confirmed the existence of

ferromagnetism in Pt thin films. First principle calculations show that the magnetism could arise due to surface roughness of the film. The charge transfer from the sharp pyramid vertex to the inner Pt sites of 3D islands, which can be viewed as supported clusters, makes the density of states at the Fermi level higher due to the narrowing of the d-state peak. This satisfies Stoner criteria and hence exhibiting local moments. The surface magnetization (emu/cm^2) is more or less constant and it is independent of the thickness of the films.

Spin injection into semiconductors needs a ferromagnet with high Curie temperature, high conductivity and high spin polarization. Though MnBi in unstable zinc blende structure is predicted to be half metallic, MnBi thin films in NiAs structure were studied due to their stable phase. The study showed that MnBi thin films have perpendicular magnetic anisotropy with easier magnetization along c-axis, and PCAR study revealed that these films have high transport spin polarization consistent with band structure calculation and their high magnetoresistance. The high spin polarization was not because of density of states at Fermi level due to almost identical values in spin bands but it was accounted due to the disparity in Fermi velocities in these bands. The transport spin polarization of MnBi correlates proportionally with their saturation magnetization. MnBi seems to be a potential candidate for spin injection to semiconductors.

Room temperature ferromagnetism in semiconductors is another property useful for spintronic devices. Magnetism and spin polarization of dilute magnetic semiconductors: degenerate InN, and Cr doped InN were studied. Undoped and Cr doped InN thin films showed room temperature magnetization with monotonic increase of the moment with Cr fraction. Finite low temperature transport spin polarization was measured in these samples. These materials have

potential application in spintronics due to their room temperature ferromagnetism and finite low temperature spin polarization.

Motivated with the spin torque initially in hybrid structure of magnetic and non magnetic structure, free standing microstructures were fabricated and coated with magnetic and non magnetic materials Au, or Ag or Ni separately. While passing dc current through the structure, a torque was produced even in non magnetic single material. The torque produced was found proportional to the square of the dc current. The expansion of metallic layer due to Joule heating, and residual strain on Si_3N_4 free standing microstructure together cause the torque. Such developed bimorph electro-thermal actuators may find application in MEMS technology.

AUTOBIOGRAPHICAL STATEMENT

PUSHKAL THAPA

Education: | **Ph.D.** | 2011, Wayne State University, Detroit, MI, USA
| **M. S.** | 2005, Bowling Green State University, Bowling Green, OH, USA
| **M. Sc.** | 1994, Tribhuvan University, Kathmandu, Nepal
| **B. Sc.** | 1989, Amrit Science College, Kathmandu, Nepal

Recent Publications, papers submitted/in preparation, and conference talks:

- "Development of low power large torsion angle bimorph electro-thermal actuators", **accepted** to Sensor Letters, Ref. SL1731968_1648, (2011).
- "Transport Spin Polarization of High-Curie Temperature MnBi Films", Physical Review B **83**, 024415 (2011).
- "Robust Room Temperature Persistent Photoconductivity in Polycrystalline Indium Oxide Films", Applied Physics Letters **94**, 252105 (2009).
- "Pressure Distributions in a static physical model of hemilarynx: measurements and computations", Journal of Voice, Vol **24**, Issue 1, Pages 2-20, 2010.
- "Ferromagnetism and spin polarization in degenerate InN and $In_{1-x}Cr_xN$ films", submitted to Semiconductor Science and Technology.
- "Evidence of pseudo gap in superconducting $BaCo_{0.1}Fe_{1.8}As_2$ single crystals by point contact Andreev reflection spectroscopy" in preparation for submission to PRL.
- "Surface ferromagnetism in Pt thin films", in preparation for submission to Nature Materials.
- "Signature of triplet superconductivity at the interface of Niobium MnSi" in preparation for submission to Science.
- "Magnetic properties of a weak ferromagnet $Pd_{1-x}Ni_x$", in preparation for submission to PRB.
- "The effects of strain on spin polarization in Ni single crystals", in preparation for submission to APL.
- "Transport spin polarization of high-Curie temperature MnBi films", American Physical Society March Meeting, March 23, 2011, Dallas, Texas.
- "Andreev Reflection Spin Polarization measurements of a weak ferromagnet $Pd_{1-x}Ni_x$", American Physical Society March Meeting, May 1, 2010, Flint, Michigan.
- "Point contact Andreev Reflection Spin Spectroscopy in MnSi single crystals", American Physical Society March Meeting, Mar 16, 2009, Pittsburgh, Pennsylvania.

Honors and Awards

- Robert Gretchen and Overman Scholarship Award, Dept. of Phys., BGSU, OH, USA (2004).
- Best thesis award for M. S. thesis, Department of Physics, BGSU, OH, USA (2005).
- Distinguished graduate thesis award nominee for Master's thesis, BGSU, OH, USA (2005).
- Industrial and Manufacturing Research Assistant (IMR) award, WSU, MI, USA (2009).
- American Association of Physics Teachers (AAPT) Graduate Teaching Assistant Award, Wayne State University, MI, USA (2011).
- Graduate research best poster presentation award, Wayne State University, Detroit, MI, USA (2011).